UNIVERSITE DE LYON

UNIVERSITE DE SHERBROOKE

STMicroelectronics

Developing Ultrasensitive and CMOS Compatible ISFETs in the BEOL of Industrial UTBB FDSOI Transistors

---

A thesis submitted to Université de Sherbrooke and Université de Lyon (co-supervised) in partial fulfillment of the requirements of the degree of Doctor of Philosophy

Getenet Tesega AYELE

Jury:

COHEN-BOUHACINA, Touria	Université de Bordeaux	Rapporteur
GUIDUCCI, Carlotta	EPFL	Rapporteur
CANVA, Michael	Université de Sherbrooke	Rapporteur
CLEMENT, Nicolas	Université de Tokyo	Examinateur
DROUIN, Dominique	Université de Sherbrooke	Directeur de thèse
SOUIFI, Abdelkader	INSA-LYON	Co-directeur de thèse
CLOAREC, Jean-Pierre	Ecole Central de Lyon	Invité
MONFRAY, Stephane	STMicroelectronics	Invité
ECOFFEY, Serge	Université de Sherbrooke	Invité

Lyon, France **May, 2019**

Abstract

The sensor market has recently seen a dramatic growth fueled by the remarkable application of sensors in the consumer electronics, automation industry, wearable devices, the automotive sector, and in the increasingly adopted internet of things (IoT). The advanced complementary metal oxide semiconductor (CMOS) technology, the nano and micro fabrication technologies, and the innovative material synthesis platforms are also driving forces for the incredible development of the sensor industry. These technological advancements have enabled realization of sensors with characteristic features of increased accuracy, miniaturized dimension, integrability, volume production, highly reduced cost, and fast response time.

Ion-sensitive field-effect transistors (ISFETs) are solid state (bio)chemical sensors, for pH (H^+), Na^+, K^+ ion detection, that are equipped with the promise of the highly aspired features of CMOS devices. Despite this, the commercialization of ISFETs is still at the stage of infancy after nearly five decades of research and development. This is due mainly to the limited sensitivity, the controversy over the use of the reference electrode for ISFET operation, and because of stability issues. In this thesis, ultrasensitive and CMOS compatible ISFETs are integrated in the back end of line (BEOL) of standard UTBB FDSOI transistors. A capacitive divider circuit is employed for biasing the front gate for stable performance of the sensor.

Exploiting the intrinsic amplification feature provided by UTBB FDSOI transistors, we demonstrated ultrahigh sensitive ISFETs. The amplification arises from the strong electrostatic coupling between the front gate and the back gate of the FDSOI, and the asymmetric capacitances of the two gates. A change in voltage at the front gate appears at the back gate as an amplified shift in voltage. The amplification, referred to as the coupling factor (γ), is equal to the ratio of the gate oxide capacitance and the buried oxide (BOX) capacitance. Therefore, functionalizing the pH sensing at the front gate of FDSOI devices, the change in surface potential at the front gate is detected at the back gate amplified by the coupling factor (γ), giving rise to an ultrahigh-sensitive solid state chemical sensor.

Integration of the sensing functionality was made in the BEOL which gives the benefits of increased reliability and life time of the sensor, compatibility with the standard CMOS process, and possibility for embedding a capacitive divider circuit. Operation of the MOSFETs without a proper front gate bias makes them vulnerable for undesired floating body effects. The capacitive divider circuit addresses these issues by biasing the front gate simultaneously with the sensing functionality at the same gate through capacitive coupling to a common BEOL metal. Therefore, the potential at the BEOL metal would be a weighted sum of the surface potential at the sensing gate and the applied bias at the control gate.

The proposed sensor is modeled and simulated using TCAD-Sentaurus. A complete mathematical model is developed which provides the output of the sensor as a function of the solution pH (input to the sensor), and the design parameters of the capacitive divider circuit and the UTBB FDSOI transistor. In that case, consistent results have been obtained from the modeling and simulation works, with an expected sensitivity of 780 mV/pH corresponding to a sensing film having Nernst response.

The modeling and simulation of the proposed sensor was further validated by a proof of concept extended gate pH sensor fabrication and characterization. These sensors were developed by a separated processing of just the pH sensing component, which is electrically connected to the transistor only during characterization of the sensor. This provides faster and simpler realization of the sensor without the need for masks and patterning by lithography. The extended gate sensors showed 475 mV/pH sensitivity which is superior to state of the art low power ISFETs.

Finally, integration of the sensing functionality directly in the BEOL of the UTBB FDSOI devices was pursued. An experimental sensitivity of 730 mV/pH is obtained which is consistent with the mathematical model and the simulated response. This is more than 12-times higher than the Nernst limit, and superior to state of the art sensors. Sensors are also evaluated for stability, resolution, hysteresis, and drift in which excellent performances are demonstrated.

A novel pH sensing architecture is also successfully demonstrated in which the detection is functionalized at the gate protection diode rather than the front gate of UTBB FDSOI devices. The abrupt current switching, as low as 9 mV/decade, has the potential to increase the fixed bias sensitivity to 6.6 decade/pH. We experimentally demonstrated a sensitivity of 1.25 decade/pH which is superior to the state of the art sensitivity.

Key words—Back end of line (BEOL), capacitive coupling, CMOS, fully-depleted silicon-on-insulator (FDSOI), ion-sensitive field-effect transistor (ISFET), pH sensor, ultrathin body and buried oxide (UTBB)

Résumé

Le marché des capteurs a récemment connu une croissance spectaculaire alimentée par l'application remarquable de capteurs dans l'électronique de consommation, l'industrie de l'automatisation, les appareils portables, le secteur automobile et l'internet des objets de plus en plus adopté. La technologie avancée des complementary metal oxide semiconductor (CMOS), les technologies de nano et de micro-fabrication et les plateformes de synthèse de matériaux innovantes sont également des moteurs du développement incroyable de l'industrie des capteurs. Ces progrès ont permis la réalisation de capteurs dotés de nombreuses caractéristiques telles que la précision accrue, les dimensions miniaturisées, l'intégrabilité, la production de masse, le coût très réduit et le temps de réponse rapide.

Les ion-sensitive field-effect transistors (ISFETs) sont des capteurs à l'état solide (bio) chimiques, destinés à la détection des ions H^+ (pH), Na^+ et K^+. Malgré cela, la commercialisation des ISFETs est encore à ses balbutiements, après près de cinq décennies de recherche et développement. Cela est dû principalement à la sensibilité limitée, à la controverse sur l'utilisation de l'électrode de référence pour le fonctionnement des ISFETs et à des problèmes de stabilité. Dans cette thèse, les ISFETs ultrasensibles et compatibles CMOS sont intégrés dans le BEOL des transistors UTBB FDSOI standard. Un circuit diviseur capacitif est utilisé pour polariser la grille d'avant afin d'assurer des performances stables du capteur.

En exploitant la fonction d'amplification intrinsèque fournie par les transistors UTBB FDSOI, nous avons présenté des ISFET ultra sensibles. L'amplification découle du fort couplage électrostatique entre la grille avant et la grille arrière du FDSOI et des capacités asymétriques des deux grilles. Un changement de tension au niveau de la grille avant apparaît sur la grille arrière sous la forme d'un décalage amplifié de la tension. L'amplification, représentée par le facteur de couplage (γ), est égale au rapport de la capacité de l'oxyde de grille et de la capacité de le buried oxide (BOX). Par conséquent, en fonctionnalisant la détection du pH sur la grille avant pour les dispositifs FDSOI, la modification du potentiel de surface sur la grille avant est détectée par la grille arrière et amplifiée du facteur de couplage (γ), donnant lieu à un capteur chimique à l'état solide à sensibilité ultra-élevée.

L'intégration de la fonctionnalité de détection a été réalisée en back end of line (BEOL), ce qui offre les avantages d'une fiabilité et d'une durée de vie accrues du capteur, d'une compatibilité avec le processus CMOS standard et d'une possibilité d'intégration d'un circuit diviseur capacitif. Le fonctionnement des MOSFETs, sans une polarisation appropriée de la grille avant, les rend vulnérables aux effets de grilles flottantes indésirables. Le circuit diviseur capacitif résout ce problème en polarisant la grille avant tout en

maintenant la fonctionnalité de détection sur la même grille par un couplage capacitif au métal commun du BEOL. Par conséquent, le potentiel au niveau du métal BEOL est une somme pondérée du potentiel de surface au niveau de la grille de détection et de la polarisation appliquée au niveau de la grille de contrôle.

Le capteur proposé est modélisé et simulé à l'aide de TCAD-Sentaurus. Un modèle mathématique complet a été développé. Il fournit la réponse du capteur en fonction du pH de la solution (entrée du capteur) et des paramètres de conception du circuit diviseur capacitif et du transistor UTBB FDSOI. Dans ce cas, des résultats cohérents ont été obtenus des travaux de modélisation et de simulation, avec une sensibilité attendue de 780 mV / pH correspondant à un film de détection ayant une réponse de Nernst.

La modélisation et la simulation du capteur proposé ont également été validées par une fabrication et une caractérisation du capteur de pH à grille étendue avec validation de son concept. Ces capteurs ont été développés par un traitement séparé du composant de détection de pH, qui est connecté électriquement au transistor uniquement lors de la caractérisation du capteur. Ceci permet une réalisation plus rapide et plus simple du capteur sans avoir besoin de masques et de motifs par lithographie. Les capteurs à grille étendue ont présenté une sensibilité de 475 mV/pH, ce qui est supérieur aux ISFET de faible puissance de l'état de l'art.

Enfin, l'intégration de la fonctionnalité de détection directement dans le BEOL des dispositifs FDSOI UTBB a été poursuivie. Une sensibilité expérimentale de 730 mV/pH a été obtenue, ce qui confirme le modèle mathématique et la réponse simulée. Cette valeur est 12 fois supérieure à la limite de Nernst et supérieure aux capteurs de l'état de l'art. Les capteurs sont également évalués pour la stabilité, la résolution, l'hystérésis et la dérive dans lesquels d'excellentes performances sont démontrées.

Une nouvelle architecture de détection du pH est également démontrée avec succès, dans laquelle la détection est fonctionnalisée au niveau de la diode de protection de la grille plutôt que de la grille avant des dispositifs UTBB FDSOI. La commutation de courant abrupte, aussi basse que 9 mV/decade, pourrait potentiellement augmenter la sensibilité de polarisation fixée à 6,6 decade/pH. Nous avons démontré expérimentalement une sensibilité de 1,25 decade/pH supérieure à la sensibilité reportée à l'état de l'art.

Mots-clés: Back end of line (BEOL), couplage capacitif, CMOS, fully depleted silicon on insulator (FDSOI), ion-sensitive field-effect transistor (ISFET), capteur de pH, ultrathin body and buried oxide (UTBB)

Table of Contents

Abstract iii

Résumé v

List of Figures xi

List of Tables xv

List of Abbreviations and Acronyms xvi

List of Symbols xix

Acknowledgement xxi

CHAPTER ONE 1

INTRODUCTION 1

1.1 pH Sensors 2

1.2 Context 5

1.3 Objective 6

1.4 Outline of the Thesis 7

CHAPTER TWO 10

LITERATURE REVIEW 10

2.1 Early Developments on ISFETs 10

2.2 Floating Gate ISFETs 13

2.3 Super Nernstian Sensitivity ISFETs 17

2.4 Nanowire, TFET and FinFET based ISFETs 21

2.5 BioFET Sensors 23

2.6 Backside Contact ISFETs 25

2.7 pH-Sensing Films 25

2.8 Drift and Hysteresis 27

2.9 The Reference Electrode 29

2.10 Conclusion 33

CHAPTER THREE 36

MODELING AND SIMULATION 36
3.1 The EI Interface 37
3.2 The Capacitive Divider Circuit 41
3.3 UTBB FDSOI Devices 42
3.4 The pH Sensor with a Capacitive Divider Circuit 50
3.5 Simulation of the Sensor 52
3.5.1 Sensing the Surface Charge 53
3.5.2 Sensing the Surface Potential 55
3.6 Sensing at the Gate Protection Diode 58
3.7 Conclusion 62
CHAPTER FOUR 65
FABRICATION OF THE SENSORS 65
4.1 Layout of the Devices on the Die 65
4.2 The Proof of Concept Sensors 66
4.3 Integration of the Sensors in BEOL 68
4.3.1 Process Flow 68
4.3.2 Mask Design 71
4.3.3 Fabrication Process 74
4.4 Fabrication of Mixed-type Sensors on a Die 80
4.4.1 Process Flow 82
4.4.2 Mask Design 84
4.4.3 Fabrication Process 87
4.5 Conclusion 93
CHAPTER FIVE 95
CHARACTERIZATION 95
5.1 Figures of Merit 95
5.2 Characterization Protocol 99

5.3 The Proof of Concept EG pH sensor ... 102
5.4 The Sensor Integrated in BEOL ... 105
5.5 Sensing at the Gate Protection Diode ... 115
5.6 Conclusion ... 118
CHAPTER SIX ... 120
CONCLUSION ... 120
6.1 Summary of the Thesis ... 121
6.1.1 Modeling and Simulation ... 122
6.1.2 EG pH Sensor ... 122
6.1.3 Sensor in BEOL of FDSOI ... 123
6.1.4 Sensing at Diode ... 123
6.2 Original Contribution ... 123
6.3 Perspective ... 124
APPENDIX-I ... 126
RÉSUMÉ ÉTENDU ... 126
A1. Introduction ... 126
A2. Etat de l'art ... 127
A3. Modélisation et simulation ... 132
A4. Capteur de pH EG ... 134
A5. Capteur en BEOL de FDSOI ... 136
A6. Détection à la diode ... 139
A7. Conclusion ... 142
APPENDIX-II ... 147
SIMULATION CODES ... 147
APPENDIX-III ... 150
MASKS USED FOR FABRICATION ... 150
APPENDIX-IV ... 158

PUBLICATIONS 158

References 160

List of Figures

Figure 1. 1 Illustration of the internet of things and big data [GSMA, web] 1
Figure 1. 2 An Ag/AgCl glass electrode [12] 2
Figure 1. 3 Different components of sensors 3
Figure 1. 4 Structure of an ISFET 4
Figure 2. 1 Cross sectional view of the ISFET reported by P. Bergveld in 1970 11
Figure 2. 2 Schematic diagram of the ISFET reported by Matsuo and Wise in 1974 12
Figure 2. 3 Schematic diagram of floating gate ISFET 14
Figure 2. 4 Diagram of sensor used for DNA sequencing [59] 16
Figure 2. 5 Schematic diagram of the ISFET reported by [74] 17
Figure 2. 6 Schematic diagram of the SiNW/CMOS hybrid ISFET [75] 18
Figure 2. 7 Sensitivity scaling with capacitance ratio and schematics of the dual gate ISFET [76] 19
Figure 2. 8 Schematic diagram of dual gate SOI ISFET with a back-side sensing [78] 20
Figure 2. 9 Silicon nanowire (SiNW) chemical sensor [97] 22
Figure 2. 10 Schematics of a penicillin-sensitive EnFET (PenFET) [116] 23
Figure 2. 11 pH sensitivities of ISFETs having different sensing films [39] 26
Figure 2. 12 Long term drift as a function of temperature [139] 28
Figure 2. 13 pH dependent drift in amorphous tungsten oxide [40] 29
Figure 2. 14 Schematic diagram of the sensor with interdigitated architecture [70] 31
Figure 2. 15 Schematics of a supercapacitor (C_1 and C_2 stand for capacitances) [164] 32
Figure 2. 16 Illustration of electro-osmosis [166] 33
Figure 3. 1 The electrical double layer. 38
Figure 3. 2 Schematic diagram of the capacitive divider circuit (left), and its equivalent circuit (right).... 41
Figure 3. 3 Cross section of the UTBB FDSOI transistor 42
Figure 3. 4 Schematic diagram of industrial n-type flip-well UTBB FDSOI transistors 43
Figure 3. 5 The electrical connection diagram for characterization of the electrostatic coupling between the front gate and the back gate (NFET SLVT) 45
Figure 3. 6 Measured I_D-V_{BG} characteristics of the UTBB FDSOI devices 45
Figure 3. 7 Measured I_D-V_{BG} characteristics of the LVT PFET UTBB FDSOI device 46
Figure 3. 8 Measured I_D-V_{BG} characteristics of LVT NFET UTBB FDSOI devices 47
Figure 3. 9 Attenuated shift in threshold voltage at the front gate induced by a change in back gate voltage 48

Figure 3. 10 Tuning of the linear operating regime to the left (negative V_{BG}) for higher potentials at the front gate. 49
Figure 3. 11 Tuning of the linear operating regime to the right for negative potentials at the front gate ... 50
Figure 3. 12 Schematics of the pH sensor integrated in BEOL of UTBB FDSOI (left) and its equivalent electrostatic model (right) 50
Figure 3. 13 Potential profile (left), charge distribution (middle), and major parameters (right) of the simulated sensor 53
Figure 3. 14 Simulated I_D-V_{BG} characteristics of the FDSOI ISFET at different surface charges at the sensing gate (SG)........ 54
Figure 3. 15 Simulated I_D-V_{BG} characteristics of the FDSOI ISFET at different surface potentials at the sensing gate (SG)........ 56
Figure 3. 16 Simulation result showing reduced sensitivity at comparable dimensions of the sensing gate capacitor. 57
Figure 3. 17 Simulation result showing no response to change in control gate voltage........ 58
Figure 3. 18 Schematic diagram of the sensor in which sensing is made at the gate protection diode. 58
Figure 3. 19 Schematics of the sensor with FDSOI and NPN connection. 59
Figure 3. 20 Drain current switching due to the DIBL effect........ 59
Figure 3. 21 Dependence of the DIBL effect on device gate length 60
Figure 3. 22 Dependence of the DIBL effect on drain voltage 61
Figure 3. 23 Simulation result showing the potential distribution in short UTBB FDSOI devices. 61
Figure 3. 24 Shift of the I_D-V_{BG} curve depending on the diode bias 62
Figure 4. 1 Layout of the block of transistors on the (2.5 cm x 2.9 cm) die 65
Figure 4. 2 Schematic diagram of the proof of concept extended gate pH sensor 67
Figure 4. 3 SEM cross sectional image of the transistors........ 68
Figure 4. 4 XPS characterization of ALD deposited aluminum oxide 69
Figure 4. 5 Process flow for integration of the pH sensors in the BEOL [199] 70
Figure 4. 6 Top down schematic diagram of the sensor 71
Figure 4. 7 Overall layout of the mask 72
Figure 4. 8 Optical measurement of the dimensions and spacing of the pads at 20X (left) and 50X (right) magnifications 73
Figure 4. 9 Layout and dimensions of the sensing gate and the control gate 73
Figure 4. 10 Optical image of the sensor after UV-1: opening for S, D, G, BG pads 75
Figure 4. 11 Temperature profile of the HD-4104 curing process 75

Figure 4. 12 Optical image of the sensor at the end of Ti/Al deposition and patterning (SG is the sensing area, also called sensing gate; CG is the control gate) 78
Figure 4. 13 SEM cross sectional image of the sensor 79
Figure 4. 14 outline of the fabricated sensors, with the optical image as an inset and a pH droplet dispensed on the sensing area [38] 80
Figure 4. 15 The modified dicing scheme to place the block of transistors at the center of the die........ 81
Figure 4. 16 The selected rows of transistors (left), and outline of sensors on the surface of the die (right) 82
Figure 4. 17 Process flow indicating the integration of pH sensor in the BEOL. 83
Figure 4. 18 Process flow indicating fabrication of the pH sensor with extended sensing area........ 84
Figure 4. 19 Overall outline of the mask 85
Figure 4. 20 Layout of the control gate and sensing gate of BEOL integrated sensors (red: control gate, black: sensing area) 86
Figure 4. 21 The control gate design of the extended gate sensors 87
Figure 4. 22 Optical image of the sample after pad opening (UV-1) 88
Figure 4. 23 Optical image of the sample after UV-2 for metallic extension 89
Figure 4. 24 XPS characterization of the aluminum oxide deposited by sputtering 90
Figure 4. 25 Optical image of the sensor after control gate deposition and patterning (UV-4) 91
Figure 4. 26 Top down SEM image of the mixed type sensors in the vicinity of extended sensing areas.. 92
Figure 4. 27 Top down SEM image of the mixed type sensors in the vicinity of electrical contacts 92
Figure 5. 1 The characterization bench 95
Figure 5. 2 Calibration curve of a sensor [205] 96
Figure 5. 3 Illustration of accuracy and precision using analogy with game of darts [210]........ 98
Figure 5. 4 Illustration of hysteresis behavior of a sensor [205] 99
Figure 5. 5 pH sensitivity of the extended gate pH sensor 103
Figure 5. 6 Repeatability of the I_D-V_{BG} characteristics of the extended gate sensor at pH 8 104
Figure 5. 7 Chronogram of the extended gate pH sensor’s response 104
Figure 5. 8 Stability characterization with and without a bias at the control gate........ 105
Figure 5. 9 Sensitivity of the BEOL integrated pH sensors 106
Figure 5. 10 Modulation of the BEOL integrated pH sensors’ output through control gate........ 107
Figure 5. 11 Chronogram of the BEOL integrated sensors’ response........ 107
Figure 5. 12 pH response of sensors, before (left) and after (right) normalization function, with drain leakage current through cured AZ-1512 resist 108

Figure 5. 13 Measured currents of the pH sensor through the drain, source, control gate and back gate in dry condition 109
Figure 5. 14 Measured currents of the pH sensor through the drain, source, control gate and back gate in pH 10 110
Figure 5. 15 Measured pH response of sensors developed based on p-type FDSOI devices 111
Figure 5. 16 Attenuated sensitivity of a pH sensor 111
Figure 5. 17 Response time of the BEOL integrated sensors 112
Figure 5. 18 Diagram showing the response for resolution computation of the BEOL integrated sensors 113
Figure 5. 19 Diagram showing the hysteresis of the BEOL integrated sensors 114
Figure 5. 20 Measured response of the sensor for drift study 114
Figure 5. 21 pH response at lower drain voltage (V_{DD}=0.1 V) 115
Figure 5. 22 Sensitivity and linearity of pH response at lower drain voltage (V_{DD}=0.1 V) 116
Figure 5. 23 pH response at higher drain voltage (V_{DD}=0.6 V) 116
Figure 5. 24 pH response of short devices 117
Figure 5. 25 Chronogram of sensors based on very short devices 117
Figure 6. 1 Sensitivity benchmark of the sensor for fixed current readout 120
Figure 6. 2 Sensitivity benchmark of our sensor for fixed bias readout 121

List of Tables

Table 2. 1 Hysteresis results of different sensing films [143] 28
Table 3. 1 Calculated changes in floating gate voltage for different changes in control gate voltage 57
Table 4. 1 Deposition recipe of the ALD aluminum oxide 74
Table 4. 2 Photolithography process with AZ1512 photoresist 76
Table 4. 3 Deposition recipe of Ti/Al deposition by sputtering 77
Table 4. 4 Deposition parameter of the PVD deposited aluminum oxide 89

List of Abbreviations and Acronyms

ALD	Atomic Layer Deposition
BEOL	Back End of Line
BG	Back Gate
BOX	Buried Oxide
cm	Centimeter
CMOS	Complementary Metal Oxide Semiconductor
CVD	Chemical Vapour Deposition
DG	Dual Gate
DG ISFET	Dual Gate Ion-Sensitive Field-Effect Transistor
DI	Deionized
DIBL	Drain Induced Barrier Lowering
DL	Double Layer
EDL	Electrical Double Layer
EG	Extended gate
EI	Electrolyte-Insulator
EIS	Electrolyte Insulator Semiconductor
fA	Femtoampere
FDSOI	Fully Depleted Silicon on Insulator
FET	Field-Effect Transistor
FEOL	Front End of Line
FG	Floating Gate
FG ISFET	Floating Gate Ion-Sensitive Field-Effect Transistor
FinFET	Fin Field-Effect Transistor
GP	Ground Plane
IC	Integrated Circuit
ILD	Inter Layer Dielectric
IMOS	Impact Ionization Metal Oxide Semiconductor Field-Effect Transistor
IoT	Internet of Things
IPA	Isopropanol
IR	Infrared
ITRS	International Technology Roadmap for Semiconductors
LVT	Low Threshold Voltage

min	Minute
MIS	Metal Insulator Semiconductor
mm	Millimeter
MOS	Metal Oxide Semiconductor
MOSFET	Metal Oxide Semiconductor Field-Effect Transistor
mV	Millivolt
NFET	N-channel Field-Effect Transistor
nm	Nanometer
NMOS	Negative Channel Metal Oxide Semiconductor
NW	Nanowire
NWFET	Nanowire Field-Effect Transistor
PFET	P-channel Field-Effect Transistor
PMMA	Poly(methyl methacrylate)
PMOS	p-type Metal Oxide Semiconductor
PVC	Polyvinyl chloride
PVD	Physical Vapor Deposition
REF	Reference Electrode
REFET	Reference Field-Effect Transistor
RF	Radio Frequency
RIE	Reactive Ion Etching
SBFET	Schottky Barrier Field-Effect Transistor
SCE	Short Channel Effect
SEM	Scanning Electron Microscope
SG-FET	Suspended Gate Field-Effect Transistor
SiGe	Silicon Germanium
SiNW	Silicon Nanowire
SLVT	Super Low Threshold Voltage
SNR	Signal to Noise Ratio
SoC	System on Chip
SOI	Silicon on Insulator
SS	Subthreshold Swing
SW-CNT	Single Walled Carbon Nanotube
TFET	Tunnel Field-Effect Transistor
UTB	Ultrathin Body

UTBB	Ultrathin Body and BOX
UV	Ultraviolet
XPS	X-ray Photoelectron Spectroscopy

List of Symbols

α	pH Buffer Capacity
σ	Surface Charge Density
ΔV	Change in Voltage
k_B	Boltzmann Constant
µA	Microampere
µl	Microliter
µm	Micrometer
µs	Microsecond
µV	Microvolt
φ	Surface Potential
γ	Coupling Factor
A	Ampere
A	Area
C	Coulomb
C_{BOX}	BOX Capacitance
C_{CG}	Capacitance of Control Gate
C_{OX}	Gate Oxide Capacitance
C_{SG}	Capacitance of Sensing Gate
C_T	Total Capacitance
D	Drain
f	Femto
F	Farad
G	Gate
I	Current
L	Length
m	Milli
m	Meter
n	Nano
q	Elementary Charge
Q	Charge
s	Second
S	Source

S	Subthreshold Slope
Si	Silicon
t	Time
T	Temperature
V	Voltage
V_{BG}	Back Gate Voltage
V_{CG}	Control Gate Voltage
V_g	Gate Voltage
V_{SG}	Sensing Gate Voltage
W	Width

Acknowledgement

I am very thankful to my thesis supervisors Abdelkader SOUIFI, Dominique DROUIN and Jean-Pierre CLOAREC for their advice, guidance and help throughout the three years of my PhD study. My sincere gratitude goes also to Stephane MONFRAY and Serge ECOFFEY whose contribution is huge for the successful completion of this research work.

Special thanks is for Juliana CHAWICH. I would also thank students and colleagues at ST Crolles, INL and 3IT, with whom my stay was enjoyable. I generally thank all the people who contributed to this work one way or another.

I would like to thank the examiners and all the jury members of this PhD defense for their precious time. Last but not least, many thanks to STMicroelectronics for their generous financing of this PhD thesis through a CIFRE program.

CHAPTER ONE

INTRODUCTION

The modern age marks the beginning of the fourth industrial revolution (Industry 4.0) which is characterized by the integration of the computing network and the physical world (cyber-physical system), commonly referred to as the internet of things (IoT) [1]–[4]. Artificial intelligence (AI), big data, machine learning, and deep learning are the other emerging technologies constituting the majority of the technological developments of the near future [5], [6]. Sensors form the corner stone of all these technologies ensuring the data streaming from the physical world to the computing network.

Figure 1. 1 Illustration of the internet of things and big data [GSMA, web]

In broader terms, the essence of sensors goes as far as the very existence of living things as it is through biological sensors that cells, organs and organisms function in a healthy metabolic condition, and toxic free environment. Such sensors detect or measure oxygen level, hormones, nutrients, light, motion, temperature, toxins, and other internal and environmental chemical, bio, and physical property. Other than the biological sensors, we use sensors in our daily lives ranging from the traditional temperature and touch sensitive devices to more sophisticated smart objects.

The sensor market has recently seen a dramatic growth fueled by the remarkable application of sensors in the consumer electronics, automation industry, wearable devices, the automotive sector, and the increasingly

adopted internet of things (IoT) [1], [7]. It is also driven by innovative material synthesis and processing along with fabrication technologies such as complementary metal oxide (CMOS) and micro electromechanical systems (MEMS) [8], [9]. These advanced technologies enabled development of sensors with characteristic features of increased accuracy, miniaturized dimension, highly reduced cost, and fast response time.

The global sensor market is forecasted to grow exponentially at a compound annual growth rate (CAGR) of 11.3 % during the period 2016 – 2022, reaching $241 billion by 2022 [8]. The worldwide IoT market which encompasses not only the sensors but also the connectivity equipments and IoT platforms, is on the other hand predicted to grow at a 20% CAGR hitting $7.1 trillion in 2020 [10], [11].

1.1 pH Sensors

Glass electrode, the first chemical sensor ever developed, is a pH sensor which is the most widely used equipment for acidity measurement [9]. Nevertheless, it has severe limitations such as bulky size, fragility, toxicity (in the case of saturated calomel electrode), and CMOS incompatibility. In addition, large volume of sample is required for pH testing with glass electrodes. Acidity measurement in food processing plants is risky with glass electrodes─ if the fragile instrument breaks, the whole inventory in the process line would be thrown away due to strict quality control and security requirements. pH measurement of soil requires rugged instruments due to the harsh environment. Miniaturized sensors can also be hardly met with the glass electrode. Basic components of an Ag/AgCl electrode are shown on figure 1.2.

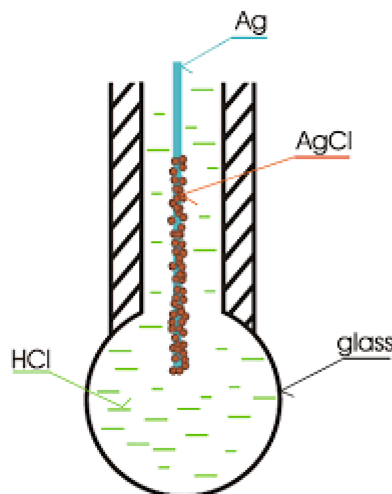

Figure 1. 2 An Ag/AgCl glass electrode [12]

The alternative pH measuring mechanisms involve optical [13]–[16], acoustic [17], magnetic [18], [19], MEMS [20], light addressable potentiometric sensing (LAPS) [21]–[24], and field-effect transistor [25], [26] detection or transduction methods. Figure 1.3 shows the block diagram of the reception, transduction, and signal processing stages of such sensors. The optical pH sensors are based on the shift in photonic absorption spectrum depending on the pH value, while the change in velocity of surface acoustic waves is used for acoustic pH sensors. In the cases of magnetic and MEMS pH sensors, the change in vibration speed and deflection of the microcantilever respectively are recorded for the pH sensing. The electronic pH sensing techniques, LAPS and ISFET, rely on a pH dependent shift in potential.

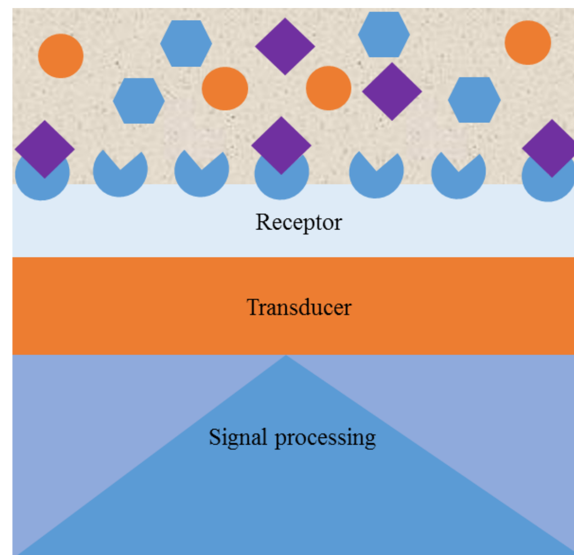

Figure 1. 3 Different components of sensors

ISFETs (ion-sensitive field-effect transistors) are solid state ion sensors in which the drain current is modulated by the ion activity of an aqueous solution. The schematic diagram of the basic ISFET structure is shown on figure 1.4. Such CMOS chemical sensors provide immense benefits over the other pH sensing alternatives. Some of the benefits are the high input impedance, dc and low frequency bandwidth, small size, reliability, fast response time, and multi-sensor chip [26], [27]. They also enable on-chip signal processing to achieve high to low impedance transformation, temperature compensation, and signal multiplexing [27]. In addition, they are useful for in situ impedance transformation, relatively easy possibility of manufacturing small and rugged multi-probes [28]. MOS based sensors have also the potential to detect minute traces of charge, 10^{10} charges/cm^2, or few tens of charges in a device of 1 µm by 100 nm dimension [29].

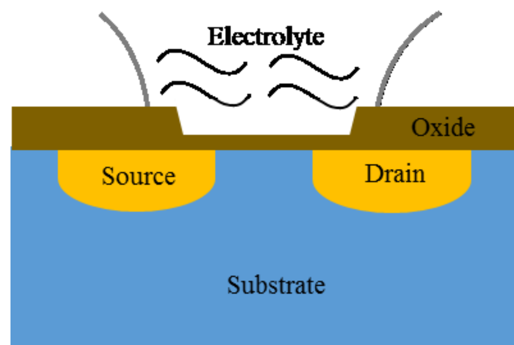

Figure 1. 4 Structure of an ISFET

The global pH sensor market is predicted to gain an exponential growth, at ~4% of a CAGR during 2017 - 2023, reaching $1.8 billion in 2023 [30]. This market of the pH sensors range from consumer use drink water acidity/alkalinity monitoring to large scale industrial process controls. Below is a list of the main potential industries deploying the largest share of pH sensors.

The ever increasing world population, the highly rising rate of urbanization and industrialization, the alerting climatic change all call for wider use of pH sensors for tighter monitoring of water pH and wiser use of the depleting water resource [30]. The advanced CMOS technology and nanotechnology are also driving forces towards providing affordable solutions for end user water quality measurement systems which in turn widens the market of these sensors. Therefore, water acidity measurement both at central water treatment plant level and end user level, is a big future market for the pH sensors.

Agriculture is one of the fore front industries to be boosted by the fourth industrial revolution- the internet of things. This is through continuous data collection, automation and fast decision making. pH sensors play a key role in such smart agriculture by providing data on soil acidity and pH value of the rain water. The rugged nature of solid state pH sensors is also suited for soil acidity measurement in the harsh environments of farming fields.

Pharmaceuticals, and chemical industries in general, can control quality of their products and monitor their fabrication processes using pH sensors. Correlating the pH value of the semi product with its process step, application of these sensors help for monitoring of industrial processes. Acidity measurement of chemicals in chemical research laboratories is also a big market for these sensors.

In food processing industries, breweries, and dairy, acidity measurement constitute a crucial method for

controlling quality of products. Acidity level of the food or drink indicate not only the planned processing of the semi product, but also the compatibility of the intake with the user's health condition.

The health industry, which takes the lion's share of the overall global market, is not an exception for wide use of pH sensors. The humans' body fluids such as the gastric juice, intestinal fluid, urine, blood, saliva, and sweat carry ample amount of information about the health condition of the person. Therefore, pH sensors are applicable in the health industry for collecting data about the person's health.

1.2 Context

Integrating ultrasensitive pH sensors in the BEOL of industrial UTBB FDSOI devices, the context of this research can be presented from several dimensions. The main points of interest are the miniaturization and the ruggedness provided by the solid state sensor over the widely used glass electrode, the signal amplification in FDSOI transistors, the biasing functionality of the capacitive divider circuit, the benefits provided by the BEOL integration, and the advantages of developing sensors based on industrial devices.

Acidity measurement with glass electrodes does not meet the requirements of several industries. The fragile nature of the glass makes the instrument a less attractive option in agriculture and food processing industries. The big dimension of this device is a constraint towards implantables and small test-volume applications. These and other limitations of the contemporary technology, and the potential attractive features of the highly advanced CMOS technology led to intensive investigation of the solid state solution- the ISFETs.

The commercialization of ion-sensitive field-effect transistors, solid state pH sensors, is still at the stage of infancy after nearly 5-decades of research and development. This is due mainly to the constraint imposed by the use of reference electrode. The miniaturized solid state sensor operated with a large reference electrode does not allow to exploit the potential attractive features of ISFETs. Consequently, operation of such sensors without reference electrode provides full exploitation of the long aspired advantages of the highly matured CMOS technology.

Several times, development of certain technological solutions are driven not only by demands but also opportunities provided by complementing technological advancements. The introduction of UTBB FDSOI devices is not an exception to this trend that such device architectures provide special features for sensing applications. Although these FDSOI transistors were developed mainly for logic applications, the strong electrostatic coupling between the front gate and back gate of FDSOI provide an intrinsic amplification

feature for sensing applications enabling fabrication of ultrasensitive sensors.

When an MOSFET is operated without a bias applied to the front gate (electrically floating), its potential is determined by stochastic factors such as trapped charges and potentials coupled through parasitic capacitances [31]. The presence of peak doping near the back interface, for the ground plane of SOI devices, introduces existence of neutral region in the film which in turn results in floating body effect [32]. This kind of device operation results in instabilities in drain current and threshold voltage. It may also result in formation of a parasitic bipolar transistor in the MOS structure, which creates impact ionization and reduced drain breakdown voltage [33]. It can also cause anomalous I-V characteristics, transients, and hysteresis [33]. Despite the presence of all the above listed problems, most of the ISFETs reported on literature do not have effective front gate biasing connection. Therefore, a mechanism such as a capacitive divider circuit should be employed in ISFETs to enable both sensing and biasing functionalities at the front gate of the transistor.

Noise has been mentioned in several literature reports of solid state pH sensors as one of the main bottlenecks. However, the exact sources of such noises have not been well investigated, except some intuitive anticipations that the noise arises from the electrolyte-insulator interface. Nevertheless, transistors alone that are fabricated by non-standard processes can give I-V characteristics of relatively high variability and noise. Indeed, in [34] it is reported that the ISFET noise is dominated by the FET transistor noise. Thus, developing pH sensors based on industrial transistors is an excellent approach for developing sensors that have highly reduced noise levels.

Summarizing the discussion, the context of this work encompasses surpassing the Nernst limit of pH sensitivity employing UTBB FDSOI transistors, enabling stable performance of the sensor by applying a front gate bias through a capacitively coupled control gate, and ensuring CMOS compatibility by substituting the conventional reference electrode by a simple capacitive divider circuit. Last but not least, the BEOL integration helps to achieve volume production of the sensors with the advanced CMOS platform, and provides better life time for the sensors.

1.3 Objective

The general objective of this PhD thesis is to demonstrate integration of ultrasensitive and CMOS compatible pH sensors in the BEOL of industrial UTBB FDSOI devices. Such goal of integration encompasses the following specific objectives.

- To demonstrate ultrasensitive pH sensors exploiting the special features of UTBB FDSOI transistors,
- To enable CMOS compatibility of the sensors replacing the reference electrode with a capacitively coupled control gate,
- To employ a capacitive divider circuit at the front gate for sensing and front gate biasing simultaneously,
- To functionalize the sensing film on top of the BEOL gate metal, and
- To pursue the signal recording at the back gate.

The above mentioned general and specific objectives encompass experimental demonstration and validation through modeling. More specifically, this includes the following major tasks:

- Mathematical modeling,
- TCAD simulation,
- Proof of concept demonstration, and
- Final prototype fabrication and characterization.

1.4 Outline of the Thesis

This thesis is organized into 6-chapters. The first chapter is introduction of the research topic in which the overall review of the sensors, the market trend and applicability of the pH sensors, the context of the research work, the open research question, and the objectives are described.

The second chapter comprises the literature review in which a brief history and developmental research works on the solid state pH sensor are presented. Major reports on modifications of the sensor architectures, derivatives of the ISFETs, sensors based on recent transistor technologies, explored ion sensing materials, and non-idealities in ISFETs are highlighted. Analysis and comparison are also provided on the state of the art sensors to indicate the pros and cons of the different approaches.

Modeling and simulation work of the proposed sensor is presented in the third chapter. This chapter consists of a rigorous modeling and analysis of the different components of the sensor, mainly the FDSOI transistor, the capacitive divider circuit, and the electrolyte-insulator interface. TCAD simulation is also included to endorse the mathematical model of the sensor.

Chapter four discusses the detail fabrication processes carried out in this PhD research project. Thus, the

mask design, the layout of the transistors and sensors on the die, the process flow, and each fabrication process step are discussed in this chapter. It includes discussion of fabrication processes of the extended gate sensor, the sensor integrated in the BEOL, and the mixed-type sensors.

The fifth chapter provides the experimental result and discussion part of the project. This characterization chapter starts with a concise description of the parameters (figures of merit) used for evaluation of the sensors' performances, followed by a description of the protocols employed for measurement of each figure of merit. Finally, the experimentally measured performances of the extended gate and the BEOL integrated sensors are provided. Results of sensors' performances while sensing through the gate protection diode are also presented in the last section of this chapter.

At last, a concise summary of the thesis is provided on the sixth chapter. Summarizing the core points of the research work, the major original contributions and the perspectives suggested for future work are mentioned in this last chapter.

CHAPTER TWO

LITERATURE REVIEW

Solid state ion sensors, that are also commonly called ion-sensitive field-effect transistors (ISFETs), have received extensive research and development since their first invention in 1970 [25]. After nearly 5-decades of research, they are still at their stage of infancy towards commercialization due mainly to the limited sensitivity, the reference electrode, and stability issues [35]–[38]. In this chapter, we review and analyze the major literature reports on different aspects of such sensors that are published since the first inception of FET based ion sensors.

2.1 Early Developments on ISFETs

In 1970, P. Bergveld reported the ion-sensitive field-effect transistor, in which he explained the possibility of modulating the drain current through the double layer that is formed at the electrolyte-oxide interface [25]. Removing the gate metal of the MOSFET, he exposed the gate oxide of the transistor to an aqueous solution to probe the molar concentration of sodium ion (Na^+) in the electrolyte (schematic diagram is shown on figure 2.1). Without use of reference electrode, a linearly increasing drain current was demonstrated as a function of logarithmic molar concentration of sodium chloride (NaCl).

The motivation came from the observation that recording of ion activities in electrochemical and biological environments through measurement of potential differences between two electrodes suffers from noise contributed by several non-specific phenomena. According to Bergveld, this can be mitigated through probing of the local surface charge density at the interface of a double layer [25]. From the MOSFET theory that the threshold voltage (V_{th}) changes depending on trapped charges at the Si-SiO_2 interface, such V_{th} modulation can be obtained due to double layer charges arising from exposure of the gate oxide to the electrolyte. Exploiting this, a solid state ion sensor can be developed by immersing the gate oxide of an MOSFET into the electrolyte and monitoring the drain current.

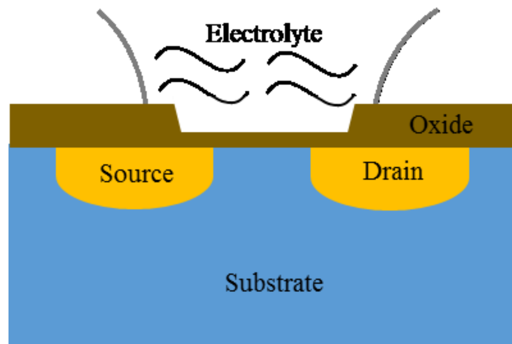

Figure 2. 1 Cross sectional view of the ISFET reported by P. Bergveld in 1970

This work is impressive as a first demonstration of an MOSFET based chemical sensor. However, the short communication didn't include sufficient explanation of repeatability, reliability, stability and selectivity so that this work received lots of criticisms especially from the perspective of the reference electrode. Use of silicon oxide as a sensing film is also another drawback of that work as this material is poorly selective and unstable [39], [40].

Two years later (in 1972), the inventor of the ISFET published his work on measurement of Na^+ and H^+ ion activities employing field-effect device without use of reference electrode for the sensor operation [41]. In this work also, he emphasized on probing of the local electric field rather than the overall potential difference between the two electrodes. Nevertheless, an erroneous principle of operation is provided by making an analogy with that of a glass electrode. Such operation of ISFETs which is based on ion exchange of hydrated gel has later been proved incorrect by using non-hydrating materials such as silicon nitride as pH sensing layer.

Basing their work as later development of microelectrodes, Matsuo and Wise reported in 1974 a slightly modified ISFET [26]─ having a reference electrode, and silicon nitride (Si_3N_4) pH sensing film on top of the gate oxide (SiO_2). Consequently, they applied a bias through the reference electrode for their device operation. The schematics is as shown below on figure 2.2. Although the use of silicon nitride as pH sensing material is better than silicon oxide, the use of the reference electrode has been an issue of controversy to date. Besides, the use of the conventional reference electrode restricts the attractive features of the CMOS chemical sensors such as small size, fast response time, and cheaper and volume production.

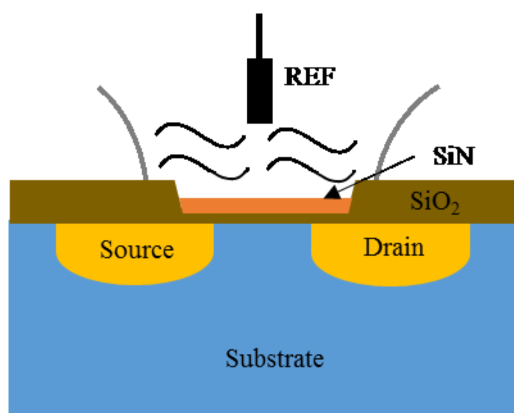

Figure 2. 2 Schematic diagram of the ISFET reported by Matsuo and Wise in 1974

On a review paper by JN Zemel, in 1975, operation of sensors without the reference electrode has been endorsed by justifying the principle of operation of the sensors with the observed threshold voltage shift of MOSFETs induced by oxide charges. Thus, he described the possibility of modulating the inversion layer as a function of in-diffusion of ions or out-migration of charges to the EI interface [42]. Although this paper described better the overall principle of operation of the sensors, the ion-diffusion based pH sensing mechanism accepted at that time is proved wrong later, following the introduction of site binding model by D. Yates, et al [43].

In the same year (1975), SD Moss et al developed a potassium sensitive solid state device using a valinomycin/plasticizer/poly(vinylchloride) membrane placed over the gate region of a field-effect transistor [44]. Although the principle of operation described resembles that of Bergveld's analysis, measurements were made applying a bias through an Ag/AgCl reference electrode. In addition to the use of reference electrode, stability, reliability, repeatability and response time were not satisfactory in this work.

Besides the components and architectures of the ISFETs, different materials have also been explored for usage as pH sensing material. At the end of the 1970s, T. Matsuo and M. Esashi published their work on pH sensing characteristics of different materials [45]. Even though they used LPCVD for the deposition (at around 800°C which is not compatible with some of the state of the art BEOL CMOS processes), their characterization of silicon oxide (SiO_2), silicon nitride (Si_3N_4), aluminum oxide (Al_2O_3), and tantalum oxide (Ta_2O_5) was very important. From this work, we could observe the poor performance of silicon oxide (in terms of both sensitivity and selectivity) and the instability of silicon nitride, for pH sensing. On the contrary, aluminum oxide and tantalum oxide have near-Nernstian sensitivities (53 - 57 mV/pH) and very good selectivities (2 mV for Na^+ and K^+ ions) [45]. This work is very useful from the point of view of comparing performances of some pH sensing films. On the contrary, their sensors have limitations as they were

developed based on conventional bulk MOSFET, and since calomel reference electrode was used for front gate biasing.

Not so long after the invention of the ISFET, the instability of SiO_2 and Si_3N_4 sensing films have been studied by RM Cohen et al, in 1978 [46]. Intrigued by previous literature reports on instability of SiO_2 sensing films due to hydration or gel formation at its surface [47], they studied the reliability of SiO_2 and Si_3N_4 sensing films. They attributed the earlier breakdown of SiO_2 films due to microcrack formation, recommending Si_3N_4 to be better sensing dielectric than SiO_2.

SD Moss et al (1978), reported hydrogen, calcium, and potassium sensitive FET transducers in which Si_3N_4 is used as hydrogen ion sensing film while PVC membranes loaded with liquid ion exchangers (dodecyl phosphonate for calcium, valinomycin for potassium) and solution cast were employed for calcium and potassium ion sensing [27]. Near Nernstian responses and fast response times have been reported although the operation included use of reference electrode. The reported pH sensing performance was also limited in a narrow range, and small sensitivity compared to the Nernst response. The demonstrated sensitivity plot of the drain current vs pH is linear which is another limitation of the report compared to the state of the art semi-log response in the subthreshold regime.

To summarize, tens of publications have been made on ISFETs during the first decade from its first invention. These early research works emphasized on performance comparison among a few sensing films, and on demonstration of detecting different cations, such as Na^+, K^+, and Ca^{++}. A few attempts on elaboration of the principle of operation of the ISFET have also been made. The work from the perspective of exploring different pH sensing materials was successful as near Nernstian responsive dielectrics such as aluminum oxide and tantalum pentoxide have been reported.

2.2 Floating Gate ISFETs

Starting from the 1980s, the sensitive film could also be integrated on top of a floating gate metal, giving rise to either of a floating gate (FG) or an extended gate (EG) ISFET. This provides better isolation of the electronics part from the hostile liquid environment, helps further miniaturization [48], and is suited for easier sensor encapsulation. It also provides the opportunity for capacitive divider circuit where front gate biasing voltages and sensing-film surface potential can be capacitively-coupled to the common floating gate metal. The schematics of floating gate ISFET is shown below on figure 2.3.

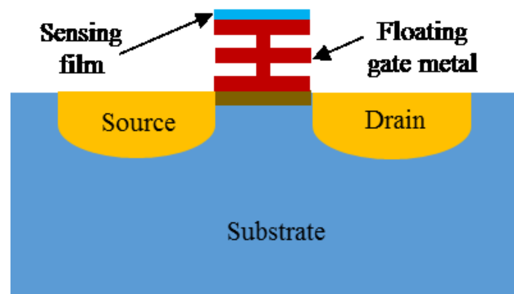

Figure 2. 3 Schematic diagram of floating gate ISFET

A. K. Covington, et al., patented the extended gate ISFET in 1984, labelling it as "offset-gate chemical-sensitive field-effect transistor" [49]. They pointed that their invention is a development of the ion-selective-electrode (ISE), which is basically based on an extended conductor. The sensor was claimed to be applicable for detection and measurement of ion activity and concentration [50]. Although it was a great step towards promoting the floating gate ISFET architecture, this specific device was not effective compared to the state of the art BEOL integrated floating gate ISFET. Moreover, it does not have the gate biasing functionality.

J Spiegel, et al., have developed a multi-species microprobe using extended gate chemically sensitive field-effect transistor [51]. Structure of this sensor consistes of a coaxial line which is an extension of the gate metal of the transistor. Depositing IrOx, AgCl and LaF_3 thin films on the extended gate, they reported a solid state sensing of H^+, Cl^-, and F^- ions respectively. Unfortunately, their device's sensitivity was very small (less than 50 mV/pH), and the setup lacks front gate biasing.

L. Bousse, et al., have also published their works on floating gate ISFET, following the standard 2-µm CMOS process, which is modified only starting from the metal interconnect step [52]. With this work, they demonstrated the feasibility of fabricating ISFETs and associated circuits with a standard CMOS process with small modifications. As in the standard CMOS process, they used a polysilicon gate as a floating gate metal which was also used to define the source and drain regions. It was in turn covered with an LPCVD deposited silicon nitride which served as the pH-sensitive layer. Despite such CMOS compatible fabrication of the ISFET, this work had the limitations of front-gate biasing, limited sensitivity, and less-performing pH-sensing material (silicon nitride).

J. Bausells et al (1999) also reported pH sensing ISFETs developed on the second metal layer of standard CMOS [53]. Therefore, the sensor consisted of a floating electrode of the polysilicon and two metal layers on top of which an oxynitride layer exists serving as a pH sensing material. The use of standard CMOS

process helped them integrate the signal processing circuitry along with the ISFET on the same die. The floating gate architecture was crucial for the integrated sensor fabrication as the polysilicon was required for defining the source and drain (self-aligned) regions of the standard MOS device. The presence of the electrically floating polysilicon layer on the gate region had an additional benefit of reduced light sensitivity.

In 2003, A. Minch et al., published their work on FET-based sensors based upon chemoreceptive neuron MOS transistor which was the combination of chemicapacitors, and neuron MOS (MOS) transistors, with an extended floating gate structure for molecular and chemical sensing [54]. Mentioning the possibility of fabricating their sensor by a simple post-processing of conventional CMOS integrated circuits, they also pointed that the MOS area of their ISFET had very similar fabrication requirements to those of commercial Flash EEPROM, in which the FG is primarily adapted for nonvolatile storage. They emphasized, their work on the FG ISFET to be based on the characteristic feature of the floating gate MOS transistor that such devices can be constructed with any number of control-gate electrodes, which couple into the FG capacitively. The floating gate voltage is then established through charge sharing or capacitive voltage addition, as a weighted sum of the voltages that are applied at the control gates (CGs). The coefficient of each input signal is directly proportional to the capacitance of the corresponding control gate or sensing gate, and is normalized by the total capacitance seen by the floating gate. But their work uses the control gate for signal recording, which highly attenuates the sensitivity of the ISFET.

A. Cohen et al (2004) reported the recording of neuron activity using depletion mode floating gate ISFET developed by a post processing of 0.5 µm standard CMOS technology [55]. They pointed that the floating gate approach is preferable to protect the most delicate channel area of the device from the liquid environment, and due to the design flexibility provided by the architecture. They also mentioned the benefit of using depletion mode transistors in order to avoid application of bias which in turn results in ion migration and a consequent drift.

P. A. Hammond et al (2004) also reported the integration of a pH sensor on a 0.6 µm standard CMOS process [56]. The sensor circuit designed for differential measurement consisted of an ISFET and REFET (reference field-effect transistor) in the floating gate architecture. The silicon nitride passivation layer was used as the pH sensing dielectric in which a sensitivity of 43 mV/pH is obtained. Large threshold voltages were observed on the fabricated sensors which were postulated by the authors to arise from trapped charges on the floating gate. Ultraviolet radiation and substrate biasing have been employed to correct the undesired deviation.

M. J. Milgrew, et al (2005) developed a 16 x 16 pixel array of floating gate ISFETs along with signal acquisition and processing circuitry for imaging cultured cell population [57], [58]. Employing a standard CMOS device, and using the passivation layer as a pH sensitive film, they demonstrated the pH sensing functionality of their sensor array chip. A sensitivity of 46 mV/pH is achieved. A conventional Ag/AgCl reference electrode was used for the sensor operation.

Ion Torrent is one of the pioneer developers of ISFETs, especially for non-optical genome sequencing. In 2011, they published their DNA sequencing work, utilizing the floating-gate architecture which they claimed as a move to get a better protection of the electronics part from the liquid environment [59]. Capability to sequence bacterial genomes and even a human genome, has been reported. Nevertheless, operation of the ISFET without proper bias at the front gate raises the stability issue. On the other hand, use of state of the art FDSOI devices instead of bulk transistors is recommended to enhance the sensitivity of the ISFETs. Figure 2.4 shows the floating gate sensor utilized for DNA sensing.

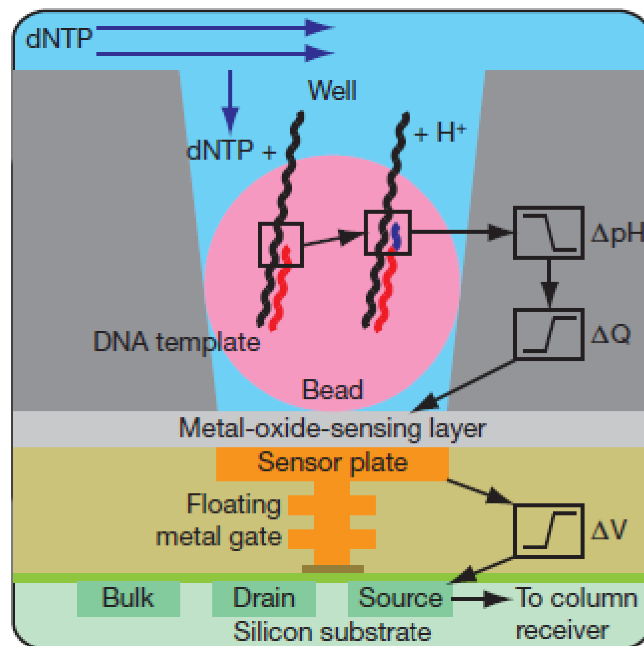

Figure 2. 4 Diagram of sensor used for DNA sequencing [59]

The integration of the pH sensing functionality as an extended gate ISFET has also gained immense research and development [60]–[69]. This technique enables miniaturized sensing at catheter tips, separation of electronics and liquid environment, simpler and cheaper encapsulation, development on commercial CMOS with a simple post processing, and cleaner sensing area due to reduced fabrication process on top of the sensing film.

As a conclusion, from the first invention of the ISFET by P. Bergveld in 1970, several research and development works have been carried out on this solid state sensor. The possibility of integrating the pH-sensing film on top of a floating gate, instead of direct exposure of the gate oxide, is one of these developments which is very important for better electronics-liquid isolation, compatibility with standard CMOS process, and simpler encapsulation. Most of the recent works on solid state chemical and bio sensors are based on such architecture [59], [70]–[73].

2.3 Super Nernstian Sensitivity ISFETs

After almost 30 years of research and development on ISFETs, enhanced sensitivities surpassing the Nernst limit were reported by different groups. In 2012, K. B. Parizi et al., reported a sensitivity of 130mV/pH [74] which is higher than twice the Nernst response. They attributed the sensitivity increment to an enlarged sensing gate of an extended-gate ISFET. They also avoided utilization of reference electrode by using a differential sensing circuit which consisted of a pair of matching n channel and p channel ion sensitive sensors connected in parallel and biased at a matched transconductance bias point [74]. The drawback of this work is that the theoretical explanation of the amplified sensitivity is not satisfactory, and the sensing area is too large— in cm^2 dimension.

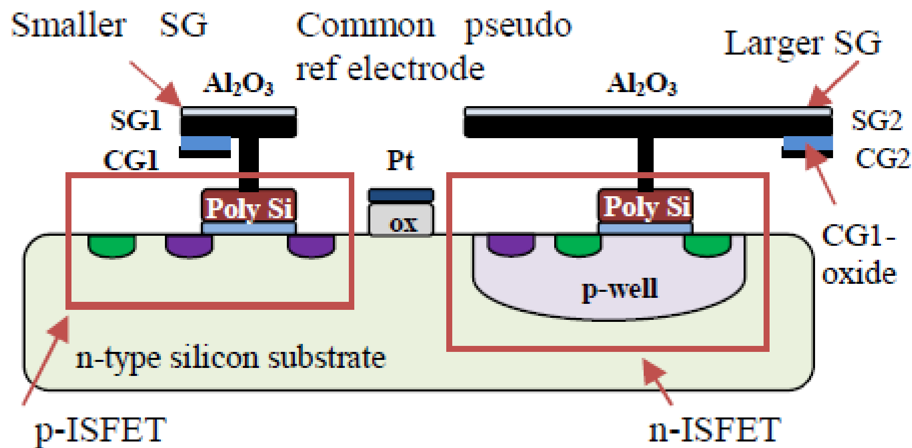

Figure 2. 5 Schematic diagram of the ISFET reported by [74]

In 2013, J. Lee et al., published their work on SiNW/CMOS hybrid biosensor circuitry with two functional stages [75]. The 1st stage consisted of a series connected complementary (n-/p-type) SiNW block, which senses the target biomolecules and amplifies the bio-signal, yielding high sensitivity. The 2nd stage is composed of a CMOS circuit block, which further amplifies the bio-signal and eliminates noise without

sacrificing sensitivity [75]. This work had high sensitivity compared to the contemporary state-of-the-art ISFETs, in spite of the fact that it totally comprises four devices. Therefore, this sensor is more of a circuit than a device which increases the overall sensor complexity (which also decreases the reliability) and dimension by more than four times. It had the noise cancellation feature also which is seen as an additional strong side. A common liquid gating of all the devices was used for the sensor operation.

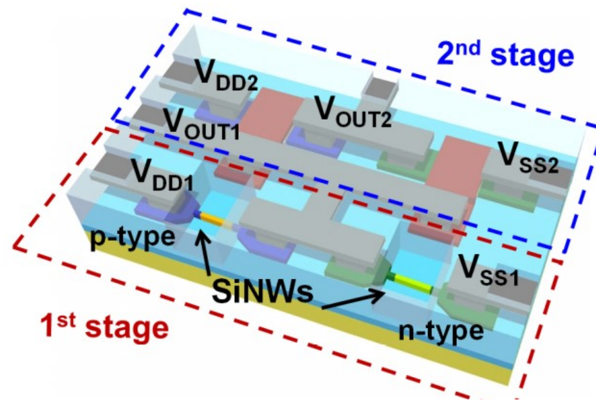

Figure 2. 6 Schematic diagram of the SiNW/CMOS hybrid ISFET [75]

On the other hand, M. Spijkman, et al., utilizing the capacitive coupling feature of dual-gate ISFETs, reported an enhanced sensitivity that scales linearly with a capacitive coupling factor of C_{top} /C_{bottom} [76]. The enhancement was attained by using a self-assembled monolayer (SAM) of octadecylphosphonic acid as a top gate dielectric, and a 1.2 µm SiO_2 layer of the bottom-gate dielectric [76]. The sensitivity scales linearly with the ratio C_{top} /C_{bottom} which is a special feature of SOI devices for sensing applications. Despite this important feature of the work, it has a couple of serious short comings. The first one is the very low subthreshold slope of the I_D-V_{BG} characteristics (less than 1-decade of drain current for a voltage range of more than 15 V) of the device that makes the sensor vulnerable to noise, and requires stringent readout circuit. Secondly, the SAM layer is directly exposed to the electrolyte which raises the reliability and stability issues of the sensor. Moreover, the reported high sensitivity is obtained at the cost a very thick bottom-gate dielectric which makes the sensor not-suited for low power state-of-the-art sensing applications. Last but not least, the bias voltage at the front gate side was applied though Ag/AgCl reference electrode which makes the sensor not suited to realize miniaturized sensors. The schematics of the dual-gate ISFET is shown as an inset on figure 2.7.

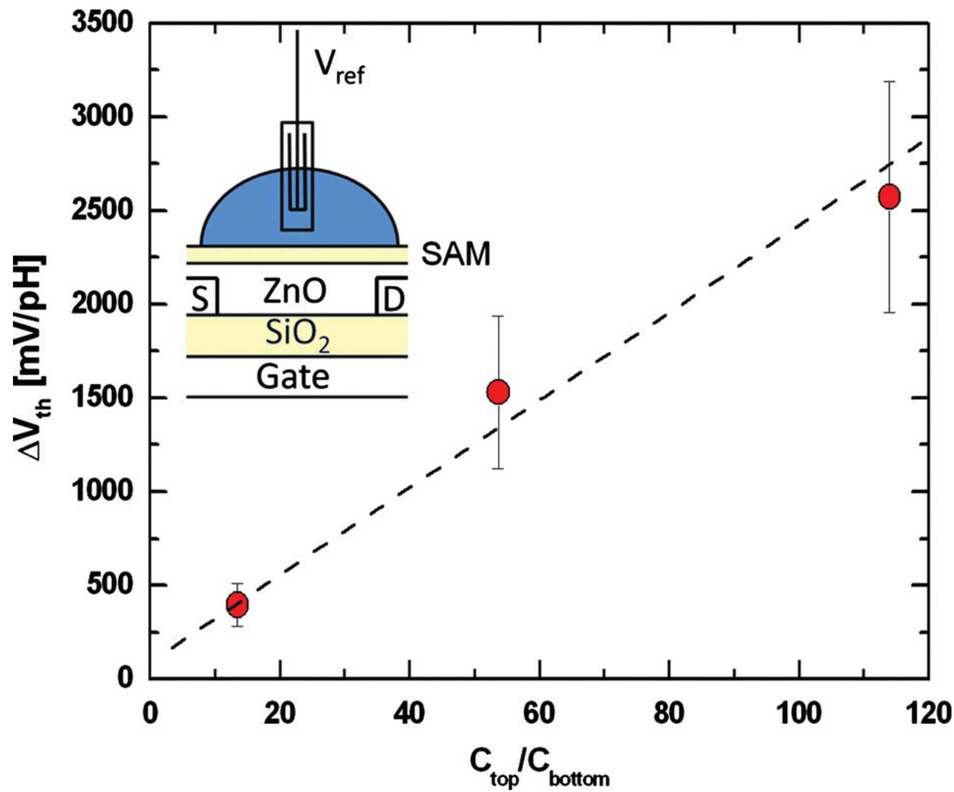

Figure 2. 7 Sensitivity scaling with capacitance ratio and schematics of the dual gate ISFET [76]

The capacitive-coupling feature that arises from the DG structure was also exploited by Hyun-June Jang & Won-Ju Cho in order to beat the Nernst limit of ISFETs' sensitivity. In 2014, they reported their work on ultra-thin body (UTB) based DG ISFET by which the authors claim not only a well increased sensitivity, but also a strongly suppressed leakage component that gives the ISFET a better stability [77]. They argued that thick body produces non-ideal factors, such as unstable coupling ratio and leakage components, in the capacitive-coupling relationship, rendering serious degradation in the device performance. By that, they also mentioned that the sensitivity of a 4.3-nm-thick UTB device is increased by more than twice, compared to an 85 nm body device, and greater stability improvements can be obtained. Although this work sounds great, it over emphasized on the study of body thickness. It could investigate effect of front gate and back gate oxide thicknesses, as the intrinsic amplification depends more on the ratio of the front-gate and back-gate capacitances. More importantly, they also utilized commercial Ag/AgCl reference electrode for front gate biasing (through the electrolyte), which makes their UTB based ISFET limited from the point of view of miniaturization.

Y. -J. Huang et al., published their works on dual gate ISFET that is based on a 0.18 μm SOI-CMOS SoC

platform with the back-side sensing structure (schematics shown on Fig. 2.8) [78]. In contrary to the commonly used approach of pH-sensing at the front gate, they employed back side etching deep into the buried oxide in order to use the BOX membrane as a sensing film. A sensitivity of 453 mV/pH is reported although it is not clear how amplification can be obtained while sensing from the backside. For drift minimization, a pulse-modulated biasing technique is used.

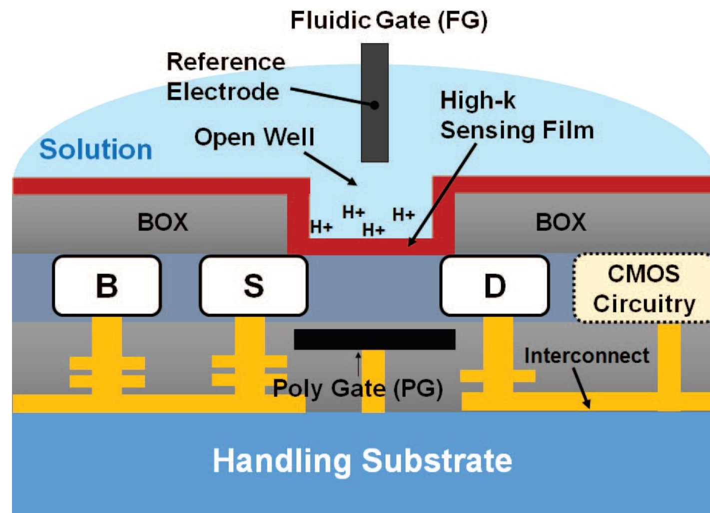

Figure 2. 8 Schematic diagram of dual gate SOI ISFET with a back-side sensing [78]

Al-Aidal A., et al., in 2012, published a paper on high gain ISFET based υMOS chemical inverter. It is based on the idea that using floating gate MOS concepts, a complementary pair of ISFETs (n and p devices) can share the same ion sensitive membrane forming an ISFET based chemical switch [79]. The technique is that through properly sizing the coupling capacitor, it is possible to enhance pH sensitivity referred to its input more than a hundredfold which forms an ISFET based υMOS chemical inverter with enhanced input referred sensitivity. But this sensor is a circuit consisting of several devices and it relies exclusively on the capacitive weighted-addition of electrical signals. In that case, it needs to gradually increase the input voltage at a given electrical input, which is capacitively coupled to a floating metal through a very small capacitor compared to other inputs.

L.Rahhal, et al., showed pH sensing demonstration of UTBB FDSOI transistors with a PECVD deposited silicon nitride in the BEOL [80]. However, the reported experimental sensitivity- 250 mV/pH is much less than the theoretically expected performance. The demonstrated linearity and the I_D-V_{BG} window of the sensor for uniform sensitivity were also not satisfactory. This may be because of the vulnerability of silicon nitride for instability upon contamination [45], side reaction of the electrolyte with the AZ-5214E

passivation material, and lack of capacitive divider circuit for front gate biasing.

To sum up the discussion on enhanced-sensitivity ISFETs, the amplification provided by dual gate transistors helped to surpass the Nernst limit. Nevertheless, it is not only the amplified shift in voltage that makes the device better, but also a reasonable amount of shift in current (steeper subthreshold slopes). Otherwise, the accompanying small shift in current would be vulnerable to noise. In addition, higher changes in current enable the sensor to be suited both for fixed bias and fixed current readout circuit. Most of the high-sensitivities reported on literature rely exclusively on change in voltage, which can easily be achieved just by lowering the subthreshold slope of transistors. Therefore, ISFETs of high sensitivity (in terms of change in voltage for a certain change in pH) which also have steep subthreshold slopes are better performing sensors.

2.4 Nanowire, TFET and FinFET based ISFETs

ISFETs have also been developed based on nanowire FETs (NW FETs), tunneling FETs (TFETs), and FinFETs. Each transistor type has its own attractive features, which may provide a correspondingly interesting performance to develop the desired sensor. The ultrathin gate oxide is attractive feature for single charge resolution detection, while steep subthreshold slopes provide better detectable changes in output current for a certain amount of change in pH.

Several reports have been produced on NW based ISFETs [81]–[95], in a search for more sensitive detection. The transport characteristics of NW devices are modified in liquid environment by the charging of surface functional groups due to the protonation or deprotonation phenomenon of the sensing process [96]. However, these alternative options did not demonstrate neither super-Nernstian response nor CMOS compatibility. The reported sensitivities include 18 mV/pH [92], 40 mV/pH [90], and 60.2 mV/pH [91]. Therefore, SOI based dual gate ISFETs would be much preferred options towards highly sensitive and CMOS compatible sensors.

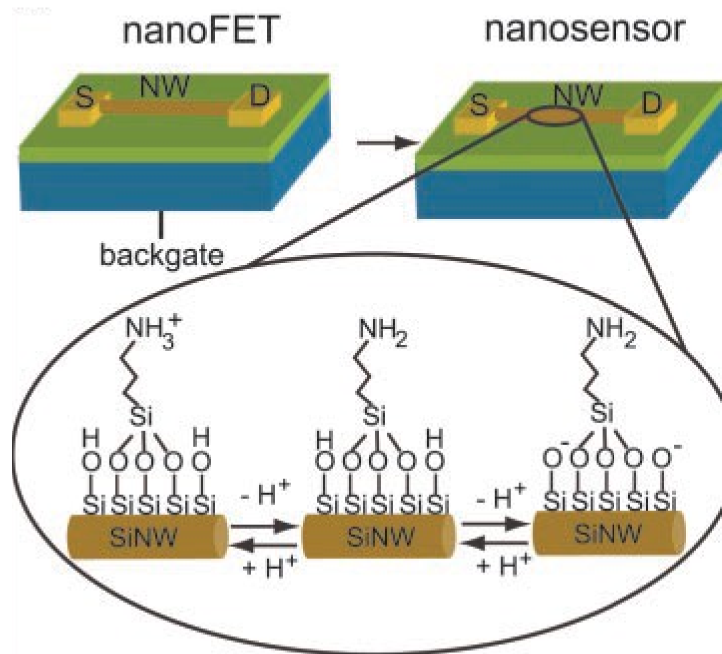

Figure 2. 9 Silicon nanowire (SiNW) chemical sensor [97]

The subthreshold swing (SS) of TFET that can possibly go below 60 mV/decade provides a potential for high sensitivity detection at fixed bias readout. Chemical and biosensors based on such devices have been reported by several groups [98]–[103]. For fixed current applications, however, the sensitivity of these sensors are limited to the Nernst limit (59.6 mV/pH) as in conventional FET sensors. In addition, the SS of TFETs depends on the gate bias [104] which degrades its use for low power sensing applications. More transistor alternatives are reported that have below (kT/q) subthreshold slopes, such as impact ionization MOSFET (I-MOS), feedback FET (FB-FET), Schottky barrier FET (SBFET), and nano electromechanical FET (NEMFET) [104]–[109]. Although the promising subthreshold slope of these transistors, which goes well below (kT/q) to 5 and 2 mV/decade, no ISFETs have been reported on these transistors yet.

The steep switching performance of IMOS devices comes from an avalanche breakdown of a gated p^+-i-n^+ structure. In SBFETs, the abrupt switching arises from modulation of the contact resistance instead of the channel [110]. Integrating biased Schottky barriers into FinFET devices, very steep switching is reported in [108] in which combined effects of impact ionization and Schottky barriers are exploited. The weak impact ionization generates an electron hole pair, by which the accumulated holes in the potential well lower the barrier, which in turn provides more electrons for more impact ionization. The resulting positive feedback effect helps for achieving highly steep switching. NEMFETs on the other hand rely on mechanical movement of the gate electrode for achieving the sub-60 mV/decade swing. Therefore, such transistors have the shortcomings of speed and reliability associated with the mechanically moving component.

Chemical and biosensors based on FinFETs are not as common as other types such as NW and TFET ISFETs. S. Rigante, et al., developed FinFET based ISFETs for ionic and biological sensing applications [111]–[114]. In [113], it was reported a sensitivity of 56 mV/pH utilizing HfO_2 pH-sensing film on FinFET device. M. Zaborowski, et al., have also reported FinFET based pH sensors, which had a Nernstian-limited sensitivity [115]. Reference electrode was employed in this work for the application of front gate voltage that gave rise to a very low subthreshold slope (less than 1-decade of change in drain current for a voltage sweep of -6V to 4V). In this gate-voltage sweep, the drain current had a range between 1 μA and 10 μA which makes the device not suited for state of the art low power applications. We can also see the lack of the intrinsic amplification in FinFET based sensors, unlike in FDSOI based ISFETs.

2.5 BioFET Sensors

The rapid advancement of the silicon technology has enabled fabrication of analytical systems such as micro total analysis system (μTAS), lab-on-chip systems, electronic tongues and artificial noses [116]. BioFETs are sensors realized by integrating bioreceptors such as antibodies, enzymes, proteins or nucleic acids onto field-effect transistors. The integration most commonly relies on an ISFET based local detection of pH change that arises from the bioreceptor-analyte conjugation.

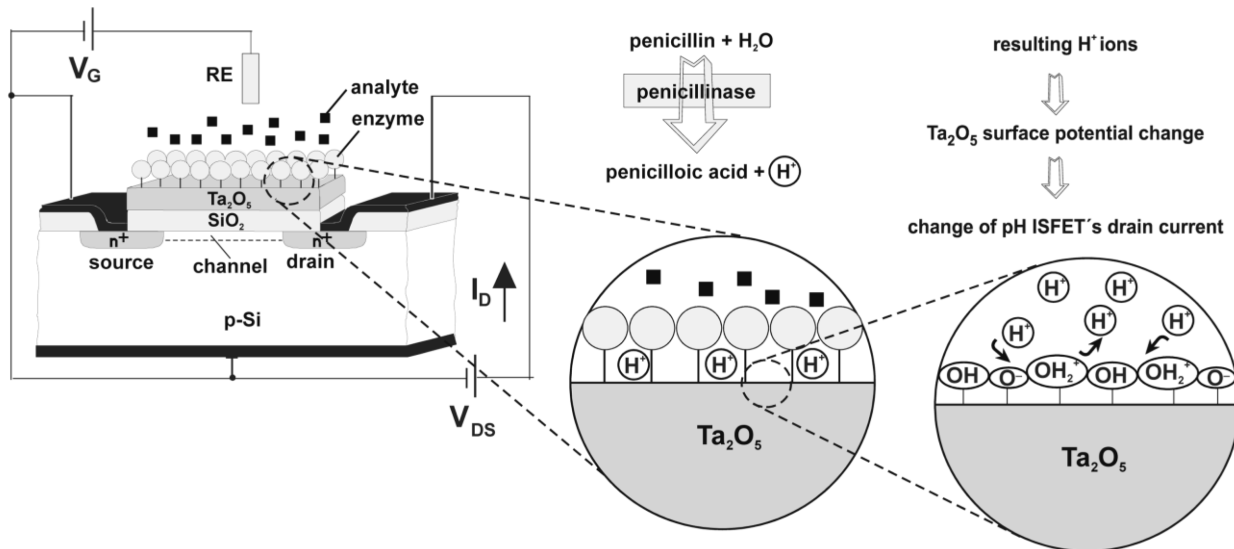

Figure 2. 10 Schematics of a penicillin-sensitive EnFET (PenFET) [116]

S. Caras and J. Janata (1980) developed an enzyme coupled FET for sensing penicillin. Using a differential

circuit of two ISFETs, one with a membrane of cross-linked albumin- penicillinase and the other having only cross-linked albumin on the gate, they realized penicillin sensing [117]. In the presence of penicillin, the penicillinase enzyme catalyzes hydrolysis of penicillin to penicilloic acid releasing hydrogen ions which changes the local pH on the sensing area of the ISFET. The small size of the sensing area helps to use a very small amount of the enzyme for the sensing purpose.

Glucose sensing bioFETs have also been developed utilizing the ISFET mechanism. Catalysis of glucose with a glucose oxidase enzyme yields gluconolactone whose further hydrolysis give gluconic acid. This in turn results in a change in pH giving rise to an ISFET based glucose sensing. A. Shul'ga, et al (1992) reported such an ENFET with glucose oxidase immobilized in polyacrylamide gel (PAAG) and by crosslinking with bovine serum albumin (BSA) [118].

D. G. Pijanowska, et al (1997) developed a biosensor for urea detection. Hydrolysis of urea catalyzed by urease produces hydroxyl ions (OH^-) which results in a local change of the pH. Immobilizing urease on the silicon nitride pH sensing surface of an ISFET, a pH-based indirect determination of urea concentration is reported [119].

S Schütz et al (2000), reported a BioFET based on a bioelectronic interface between a field-effect transistor and an insect exploiting their natural capability to detect volatiles released by damaged plants [120]. The antenna of the insect was connected to the gate of the FET device by means of a hemolymph ringer solution. The developed "bioelectronic nose" provided a very high sensitivity in a wide dynamic range [120].

A. B. Kharitonov, et al (2001) published their work on ISFET based detection of lactate [121]. Reduction of $NAD(P)^+$ or oxidation NAD(P)H result in a change in pH. NADH is a cofactor of the enzyme lactate dehydrogenase. The aminosiloxane-functionalized gate oxide is modified with pyrroloquinoline quinone (PQQ) that acts as a catalyst for the oxidation of NADH.

The operation of enzyme FET devices is based on the detection of the hydrogen ion that is released during the enzymatic catalyzed reaction. Nevertheless, this indirect probing through pH measurement has its own challenges as the performance becomes affected by the sample pH and buffer capacity [122]. As a possible solution for the buffer capacity effect, a coulometric system was suggested by [122].

2.6 Backside Contact ISFETs

Encapsulation is one of the bottlenecks mentioned for the immature industrialization of ISFETs. This is because of the difficulty of effectively protecting the circuitry from the liquid environment. A. Neidig, et al., patented the technique of making electrical contacts on the opposite side of the substrate in 1980, so that the encapsulation process becomes easier [123].

Driven by the challenge that the sensing layer of the ISFET can hardly approach the detectable surface of the human enamel, H. Vlekkert et al (1988) developed an ISFET with a back source and drain contact for dental plaque pH measurement [124]. With this technique, the increased gap between the active surface of the ISFET and the encapsulation atop the bonding wires was reduced.

The silicon on sapphire (SOS) and silicon on insulator (SOI) technologies have given rise to ISFETs of backside contact in which the source and drain connections are made on one side while the sensing gate area on the opposite side of the device [78], [124]–[126]. In [78], based on SOI devices, instead of making back side contacts, back side sensing has been reported. Etching into the buried oxide for using the BOX membrane as pH sensing film, a very high sensitivity has been presented. However, from the amplification characteristic of SOI devices, no explanation is provided how high sensitivity was obtained at the BOX while signal recording was carried out at the front gate.

2.7 pH-Sensing Films

The very first ISFET, reported in 1970, was based on SiO_2 sensing layer even though it was sensing sodium ion (Na^+) activity. In the next work of the same person, after 2 years, the same sensing material (SiO_2) was employed for detecting both H^+ and Na^+ ion activities. From this later work, we can clearly see the poor selectivity of SiO_2 for pH sensing applications.

In 1974, Matsuo et al., deposited a layer of silicon nitride on top of the gate oxide for probing the pH. In 1979, H. Abe, et al., have studied the sensitivity and selectivity of ISFETs having sensing films of silicon oxide, silicon nitride and aluminum oxide (sensitivity comparisons are presented on Fig. 2.10) [39]. They obtained a result which showed that silicon oxide has much less performance in terms of sensitivity, selectivity and stability. The silicon oxide film has a relatively low sensitivity compared to the Nernst response, and yet its pH sensitivity is unstable. In addition, SiO_2 showed significant response for changes in concentration of Na^+ and K^+ ions, showing its poor selectivity. Relatively high amount of long term drift

was also recorded with the silicon oxide film. On the other hand, silicon nitride showed a better pH-sensing performance than silicon oxide- better selectivity and sensitivity. But still, it has stability issues that trace amount of oxygen content in the nitride makes its performance worse than silicon oxide [39].

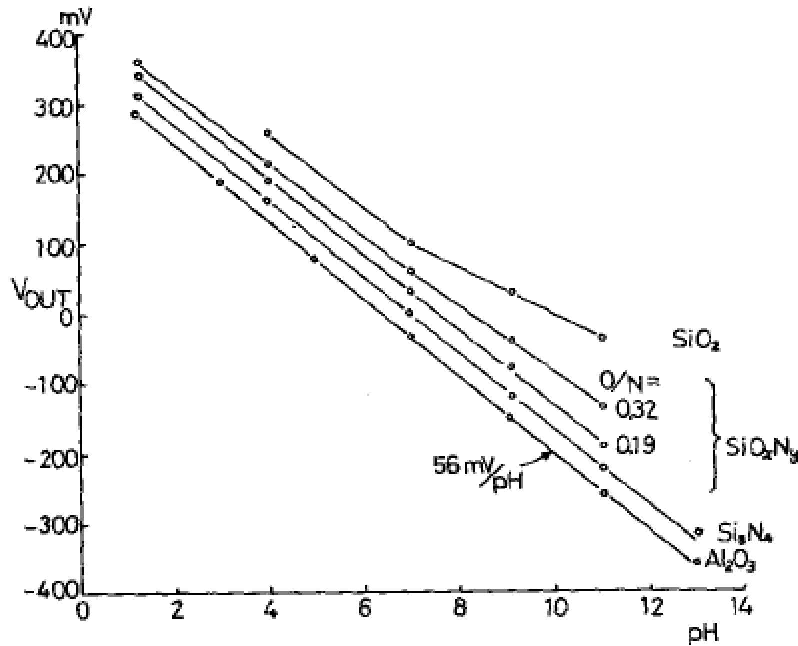

Figure 2. 11 pH sensitivities of ISFETs having different sensing films [39]

Few years later, other dielectric materials were also investigated, such as hafnium oxide (HfO_2), and tantalum pentoxide (Ta_2O_5) for better sensitivity, stability and selectivity. Aluminum oxide and tantalum pent oxide gave high sensitivities, high selectivities, and low hysteresis [45].

T. Katsube, et al., have studied the pH sensing behavior of iridium oxide films [127]. The pH response of this material suffered from initial instability and drift. The authors attributed the observed drift to an increased hydration of the film with time. Its response to interfering ions is also significant, close to 10 mV response at 0.1 M of Na^+ ion.

T. Fu Lu, et al., investigated pH sensing performance of hafnium oxide (HfO_2) with and without SF6 plasma treatment [128]. Although near Nernstian sensitivity is claimed, significant response to interfering ions (9.8 to 3.5 mV/pNa), high levels of hysteresis (more than 20 mV) and drift are observed which makes the device non-preferable over aluminum oxide and tantalum oxide.

Titanium dioxide (TiO_2), tin oxide (SnO_2), erbium oxide (Er_2O_3), praseodymium oxide (Pr_2O_3), and other

high-k materials have been investigated for pH sensing material [129]–[135]. Sensitivities are variable depending on the deposition mechanism in most of these sensing films.

Therefore, aluminum oxide has better performances in terms of sensitivity, selectivity and stability as a pH-sensing material. Tantalum pentoxide has also great performances, but aluminum oxide is preferable over tantalum pentoxide for its well-developed fabrication processes and facilities (deposition and patterning) [136]. Aluminum oxide has also been employed for commercial pH measuring instruments developed by Cordis R&D and Sentron [126], [137].

2.8 Drift and Hysteresis

The non-ideal effects such as drift, hysteresis and dependence of sensitivity on temperature have been mentioned as factors for the immature commercialization of ISFETs. Drift, in this case, is described as a long term, monotonic change in ISFET output under the same pH and measurement condition. On the other hand, hysteresis is the offset in sensor's output at the same pH, but depending on the previous pH to which the sensor was exposed. In [138], the hysteresis behavior is attributed to slow response of sites that are located under the surface in which the surface site model was used for the description.

Qualitative descriptions have been provided for the potential physico-chemical phenomena behind the drift effect [139]–[141]. Slow mass transfer, field enhanced ion migration, slow pH response of the sensing film, hydration, and gradual chemical modification of the surface of the sensing film are some of the reasons mentioned for drift behavior [140], [142].

L. Bousse, et al., described the hysteresis and drift as limiting factors for accuracy of pH sensor devices based on insulator/electrolyte interfaces that originate from the slow response of such sensors [138], [143]. In [138], they reported a modeling of the hysteresis phenomenon describing the sensor's output to be a summation of several first order exponential responses of different time constants. Such non idealities exist, however, to different extents in different pH sensing materials. It is reported that aluminum oxide and tantalum oxide have smaller drift and hysteresis compared to silicon nitride. The result is shown on table 2.1 below.

Table 2. 1 Hysteresis results of different sensing films [143]

Material	Ta_2O_5	Al_2O_3	Si_3N_4
Hysteresis acid side (mV)	1.68	3.73	6.29
Hysteresis basic side (mV)	1.72	4.40	10.92

P. Hein et al., on the other hand, defined drift as the temporal shift of the output voltage under constant conditions like temperature, pH value and concentration of the buffer solution [139]. They mentioned that pH measurements with ISFETs are falsified by a drift rate of about 1 mV/h, which means a pH change of 0.02 pH/h. They also studied rate of drift dependence on temperature, which is shown on Fig. 2.11.

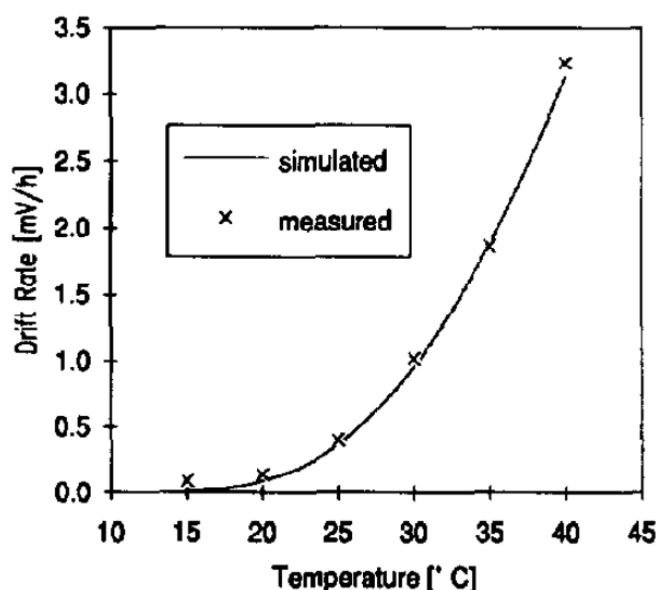

Figure 2. 12 Long term drift as a function of temperature [139]

S. Jamasb, et al., postulated that the origin of drift is associated with the relatively slow chemical modification of the sensing film surface as a result of exposure to the electrolyte [144]. It is also mentioned that the chemical modification of the dielectric is assumed to result from a transport limited reaction. They modeled the rate of the reaction by a hopping and/or trap limited transport mechanism for a quantitative analysis of the drift phenomenon. The change in the chemical composition of the dielectric surface leads to a change in the insulator capacitance with time, which gives rise to a long term drift [144].

J. L. Chiang, et al., studied the temperature effect, drift and hysteresis of amorphous tungsten oxide based ISFETs [40]. By this, they reported that pH sensitivity increases with increasing temperature, while hysteresis effect is dependent on the measuring loop time and measuring path. They also reported that drift increases with increasing pH, as illustrated on Fig. 2.12. Finally, benchmarking the hysteresis and drift in amorphous tungsten oxide, they confirmed that aluminum oxide and tantalum oxide have better performances.

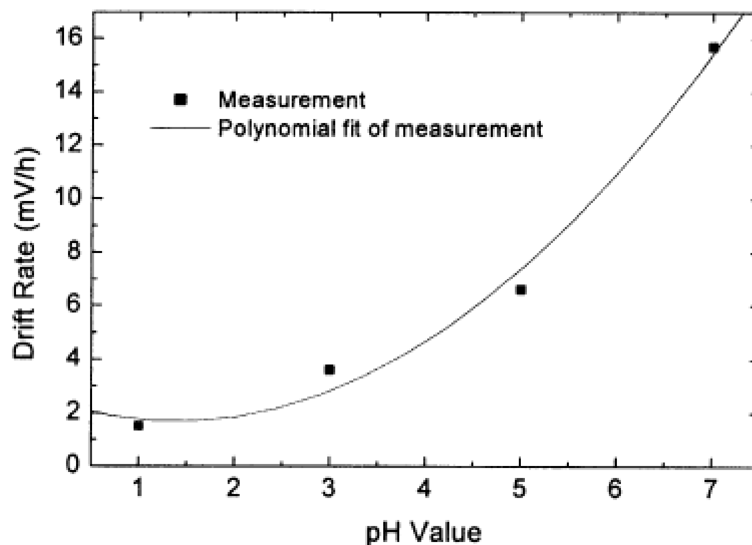

Figure 2. 13 pH dependent drift in amorphous tungsten oxide [40]

To minimize the non-idealities in ISFETs, the first measure would be a proper choice of the pH sensing material, such as Al_2O_3 and Ta_2O_5, instead of silicon oxide and silicon nitride. Recently, Y. J. Huang, et al, have also pointed utilization of pulse wave modulated biasing for significant reduction of drift in ISFETs [78]. The pulse wave modulated biasing is not, however, required for the ISFETs having a control gate biasing scheme as the control gate bias is usually grounded. Moreover, there is no applied external voltage at the electrolyte in such kinds of sensors, opposed to the case of Ref-electrode biased ISFETs. As in other types of sensors, compensation and correction would also be proper measures to address the above discussed non-ideal factors in pH sensors.

2.9 The Reference Electrode

The controversy over the use of reference electrode for ISFET operation started just after 4 years from the first report of the ISFET, and by the second group who worked on the field next to the inventor [25], [26].

When the concept of the ISFET was introduced at the very beginning, the principle of operation was based on the property of MOSFETs that ionic species incorporated in the device during fabrication of MOSFETs introduce variations in the threshold voltage (V_{th}) [145], so that it didn't have reference electrode. Bergveld endorsed his stance towards unnecessity of the reference electrode for ISFETs in his later work [41] by explaining the capability of the localized field to modulate the threshold voltage of MOSFETs.

Different reasons are given by different groups for the utilization of reference electrodes in their ISFETs. In [146], the necessity of the reference electrode is attributed to the completion of the electric circuit from the MOS body to ground through the electrolyte. In other works, the purpose of the reference electrode is mentioned to be for suppressing noise that would otherwise get enormous from the electrolyte bulk. Still other works gave different reasons─ to bias the electrolyte bulk [129]. Some other groups mentioned that the reference electrode's purpose is for biasing the front gate side of the ISFET.

Research and development works have been carried out to miniaturize the reference electrode so that a correspondingly scaled ISFET would be realized [146]. In some works, the conventional structure of the reference electrode is preserved while shrinking down its size, but such electrodes had a very limited lifetime. This is because the period over which the content of the interior solution remained constant depended on the rate of the mass transport through the junction and on the volume of the interior compartment [146]. Another attempt was to realize a solid state reference electrode, which is also known as a reference field-effect transistor (REFET) which resembles an ISFET except that it is coated with an ion insensitive material at the sensing area [146].

PA Comte and J Janata have reported in 1978 the possibility of substituting the conventional reference electrode with an integrated reference field-effect transistor [28]. In this work, they compared the differential output drain current of the sensor using a conventional reference electrode and using just a bare conductor or an exposed part of the silicon substrate for biasing the solution. Having obtained equivalent performance in all cases, they explicitly mentioned the unnecessity of employing reference electrodes for the ISFET operation [28].

This was followed by several research and development works on REFETs [147]–[152], [152]–[157]. Such works tried to address the challenges of impedance matching, synthesis of materials insensitivity to ions, and developing robust readout circuit [158]. For instance, Matsuo et al (1986) deposited a parylene film on the Si_3N_4 gate of the ISFET to obtain a pH insensitive REFET [159].

Instead of developing ion insensitive materials, another approach is proposed as a pseudo REFET. This is through engineering the response time of the sensing film [160]. Therefore, such materials act as insensitive compounds at the beginning until their response time is reached, acting both as an REFET and as an ISFET before and after their response time respectively.

Very recently, in 2018, R. Zeng et al proposed an interdigitated architecture for sensing and biasing of the electrolyte eliminating the use of the reference electrode [70]. Nonetheless, a closer observation of this architecture and its electrical layout, equivalent electrostatic functionality can be provided by the passivated metallic extensions of the control gate that pass underneath the electrolyte in the pH sensor that we developed in the BEOL of FDSOI devices. Thus, this work endorses our approach of using the capacitive divider circuit to bias capacitively not only the transistor, but also the electrolyte.

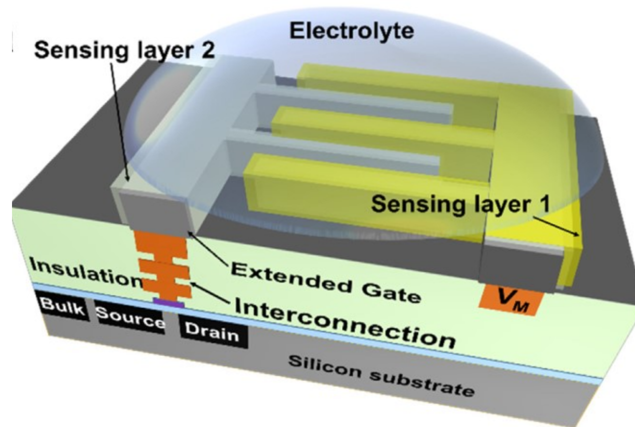

Figure 2. 14 Schematic diagram of the sensor with interdigitated architecture [70]

On the contrary, there are groups who demonstrated operation of their ISFET without the reference electrode[26]. Qi Zhang, et al., reported the possibility of avoiding the reference electrode in the case of floating gate ISFETs where biasing can be applied through a control gate [161]. On the other hand, it is also reported that for the actual measurement of threshold voltage with the grounded gate electrode no reference electrode is necessary in the electrolyte [162]. The electrolyte is only contacting the gate and can react with the gate material, but is not a part of the actual chain of measurement.

Beside the sensing application such as ISFETs, the electrical double layer formation is exploited in other applications such as supercapacitors and electro-osmosis. Both of these applications operate without use of reference electrodes. Therefore, it would be very important to consider broader applications for assessing the necessity of the reference electrode in ISFET operation.

The principle of operation of supercapacitors is based on the separation of charge at the electrochemical interface between the electrodes and the electrolyte [163], [164]. During the charging process, negative and positive charges are attracted to the positive and negative plates of the capacitor respectively. Therefore, the energy storage is achieved in an electrical double layer capacitance with a pure electrostatic charge accumulation at the electrode-electrolyte interface [163]–[165]. It is very interesting that each electrode is treated as a single capacitor of a corresponding capacitance (C_1 and C_2 for the two electrode on figure 2.15) [164]. This shows the reliance of the principle of operation on a local electrical double layer formation. The schematics of supercapacitors, with the main components such as electrodes and separators, are shown below on figure 2.15.

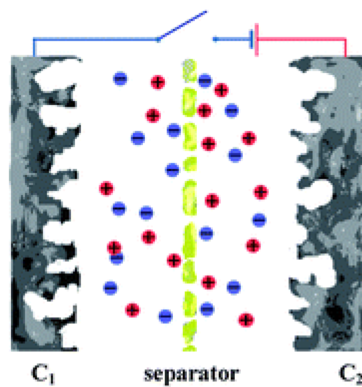

Figure 2. 15 Schematics of a supercapacitor (C_1 and C_2 stand for capacitances) [164]

Electro-osmosis is the flow of liquid induced by an applied electric field across a capillary tube or a microchannel through a Coulomb force. The chemical equilibrium between a solid surface and an electrolyte gives rise to an electrical double layer or Debye layer that consists of a firmly anchored layer of charge and a diffuse layer of mobile counter ions. Hence, application of electric field in a transvers direction (parallel to the solid surface) drags those counter ions resulting in a flow of the liquid. Such an electro-osmosis effect is illustrated below on figure 2.16 which operates without the necessity of a reference electrode.

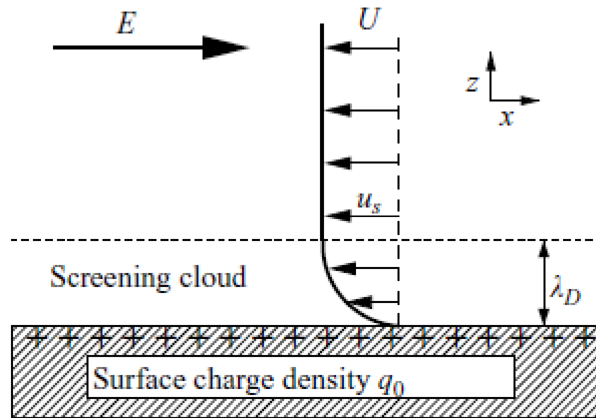

Figure 2. 16 Illustration of electro-osmosis [166]

To summarize the issue on the reference electrode, there still has no consensus upon it. Publications are still being produced from both sides: employing reference electrodes and without use of reference electrodes. Our suggestion is to endorse the approach with a thorough scientific analysis, and find better options so as to enjoy the aspired attractive features of the solid state chemical sensors.

2.10 Conclusion

For its attractive characteristic features such as miniaturized dimension, CMOS integrability, and fast response time, solid state (bio)chemical sensors have been extensively studied for the last nearly 5 decades. ISFETs were first reported by Piet Bergveld in 1970 exposing the gate oxide of an MOSFET (gate metal removed) to electrolyte. Only after 4 years, in 1974, a slightly modified ISFET was introduced which included an additional silicon nitride layer for pH sensing and a reference electrode for biasing the sensor. From that time on, the necessity of the reference electrode for ISFET operation has been an issue of controversy.

Exploring different organic and inorganic materials, for detection of H^+, Na^+, K^+, Ca^{++} ions, ISFETs adapted for sensing different ion have been reported. Studies for finding better performing pH sensing materials are somehow successful. With extensive characterization of such films, SiO_2, Si_3N_4, Al_2O_3, Ta_2O_5 for instance, Al_2O_3 and Ta_2O_5 have demonstrated near Nernstian response with highly reduced drift and hysteresis. The sensitivity is however vulnerable for attenuation due to several factors.

Starting from the 1980s, ISFETs have been realized following the floating gate architecture, in which the sensing film is integrated on top of the gate metal instead of exposing the ultrathin gate oxide to the hostile

liquid environment. This approach provides not only longer sensor life time, but also easier fabrication using the well developed standard CMOS platform. The floating BEOL metal is also advantageous for realizing the capacitive divider circuit which enables front gate bias through a capacitively coupled control gate.

ISFETs have been reported on different advanced transistors such as FinFETs, TFETs, and SiNW FETs. But they all suffer from the same constraint as in ISFETs based on conventional MOSFET─ Nernst limited pH response. On the other hand, UTBB FDSOI transistors have special features─ strong electrostatic coupling and asymmetric capacitances between the two gates which provide intrinsic amplification for sensing applications. Exploiting such performance of the devices, ultrasensitive sensors can be developed based on UTBB FDSOI transistors. However, CMOS compatible ultrasensitive chemical sensors based on UTBB FDSOI devices were not developed yet. Thus, the theme of this PhD thesis is towards demonstrating a viable solution towards sensitivity, stability, and CMOS compatibility.

Despite the transistor options for sub (kT/q) subthreshold swing, such as TFET, I-MOS, FB-FET, NEMFET, SB-FET, which have below 5 and 2 mV/decade subthreshold slopes, no ISFET exceeding the Nernst limit (0.99 decade/pH for conventional MOSFET) has been reported to date based on such transistors. Such steep current switching behaviors, in which sensing is functionalized at the gate protection diode, have been exploited in this PhD work for demonstrating ultrahigh sensitive pH sensors at fixed bias readout.

BioFETs have also been realized by integrating bioreceptors such as antibodies, enzymes, proteins or nucleic acids onto ion-sensitive field-effect transistors. Detection of urea, penicillin, and glucose have been reported based on such field-effect devices.

After nearly five decades of research and development on these solid state chemical and biosensors, they are still at their infancy stage of commercialization. The principle of operation and the necessity of the conventional reference electrode are still subject to controversy. To enable the advancement of these sensors, and to ensure exploitation of the attractive features provided by the advanced CMOS technology, dependable solutions should be investigated for full integration of the sensors in the CMOS IC.

CHAPTER THREE

MODELING AND SIMULATION

Several publications have been produced on development of chemical sensors and biosensors based on state of the art transistors such as TFETs, FDSOI and FinFETs [113], [114], [167], [168]. In the "Lab-on-Skin™" sensing platform developed by Xsensio SA, using FDSOI devices, a maximum sensitivity of 52 mV/pH is reported [168]. A sensitivity of just 56 mV/pH is also reported by [114] using FinFET based ISFETs. In such literature reports, neither the motivation for the use of such advanced transistors nor the aspired enhanced performances over conventional MOSFETs are not clear. The reported performances, such as sensitivity, can equivalently be achieved using just ordinary bulk MOSFETs that can provide up to 59.6 mV/pH sensitivity (Nernst response).

In this chapter, not only a clear indication of the benefits of integrating the sensors based on UTBB FDSOI devices, but also a crisp mathematical modeling is provided which helps explain every possible experimental response of the sensors. The modeling is also crucial for the designing process of the sensors so that the potential sources of signal attenuation would be properly addressed. Moreover, we developed a model for explaining the response of ISFETs that are developed based on any transistor type with the only requirement that the sensor is operated in the subthreshold regime with a logarithmic I_D-V_g characteristics.

Since a novel approach is followed to enable CMOS compatibility, ultrahigh sensitivity, and stable performance of the pH sensor, a rigorous analysis and modeling is performed in which the output of the sensor is mathematically described as a function of the solution pH (input variable to the sensor). The developed mathematical model of the sensor is also validated by a numerical simulation of the sensor utilizing TCAD-Sentaurus.

Due to the multidisciplinary nature of the CMOS pH sensor, and since the recognition component and the transduction component of the sensor work based on different physical phenomena, the modeling and analysis of the sensor can be carried out at the level of individual components. Finally, the input output characteristics of the components (subsystems) are combined to describe the performance of the sensor as a function of the pH value, mainly for the study of sensitivity. Hence, the sensor can be divided in to the following subsystems.

- The electrolyte-insulator (EI) interface,
- The capacitive divider circuit, and
- The FDSOI transistor

At the electrolyte-insulator interface, the recognition aspect of the pH sensing takes place where a pH dependent surface potential builds up. The capacitive divider circuit enables capacitive coupling of this surface potential and the bias applied at the control gate to the floating BEOL gate metal of the transistor. The UTBB FDSOI transistor provides an amplified signal of the front gate voltage which is recorded at the back gate as a shift in threshold voltage.

3.1 The EI Interface

When an object is immersed in a liquid, an electrical double layer (EDL) forms at the interface of the object and the liquid. The object can be a solid material, a droplet of an immiscible liquid, or a gaseous bubble. Formation of the interfacial potential difference is due to charge transfer occurring across the interface, ionization of active surface groups, and/or orientation of permanent or induced dipoles [169].

Hermann von Helmholtz modeled the EDL simply as a differential capacitor [170] which is analogous to a parallel plate capacitor. It is assumed that the double layer consists of two layers of charges of opposite sign which are separated by a fixed distance. However, this model lacks several considerations such as dependence of the capacitance on charge density, and diffusion of ions in the solution. The Helmholtz model also fails to explain dependence of the measured capacitance on voltage.

Based on the observation that the capacitance was dependent on the applied potential and on the ionic concentration, the Gouy-Chapman model was introduced that has the commonly used diffuse model of the EDL. According to Gouy and Chapman, ions in the electric double layer are subjected to electrical and thermal energy so that the distribution of ions follows Maxwell-Boltzmann statistics as a function of distance from the interface [169]. The model explains that the double layer consists of an inner layer of adsorbed surface charges and a diffuse layer of counter charges electrically screening the adsorbed charges. The inner charges are firmly attached to the object through adsorption, while the diffuse charges are loosely held by a Coulomb attraction. The distribution of diffuse ions varies as a function of distance from the surface following the Boltzmann distribution. This results in an exponentially decreasing electrical potential from the solid-liquid interface to the bulk of the liquid. Nevertheless, the Gouy-Chapman model also fails to explain the electrical double layer of highly charged interfaces.

The Stern layer accounts for ions' finite size and consequently an ion's closest approach to the electrode is on the order of the ionic radius [171]. In Stern's model, some ions adhere to the electrode as suggested by Helmholtz, giving an internal Stern layer, while some form a Gouy-Chapman diffuse layer [169]. The Stern model has its own limitations, namely that it effectively treats ions as point charges, assumes all significant interactions in the diffuse layer are Coulombic, and assumes dielectric permittivity to be constant throughout the double layer [169].

D. C. Grahame proposed that some ionic or uncharged species can penetrate the Stern layer, forming specifically adsorbed ions [172]. Grahame's model describes three regions viz the inner Helmholtz plane (IHP), the outer Helmholtz plane (OHP), and the diffuse layer. The electrical double layer, which considers the Stern modification of Gouy-Chapman layer (including Helmholtz capacitance), and Graham's specifically adsorbed ions is shown on Fig. 3.1 below.

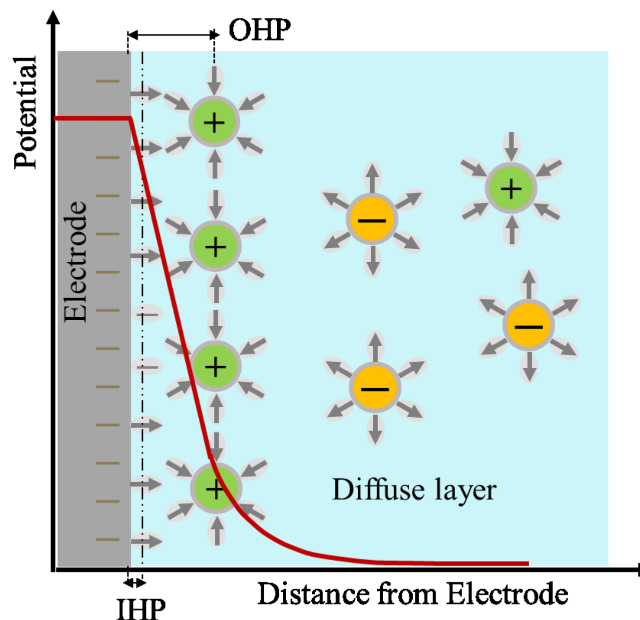

Figure 3. 1 The electrical double layer.

According to the widely accepted site binding theory, the surface charging mechanism at pH-sensing metal oxides comes from the unequal adsorption of protons (H^+) and hydroxyl ions (OH^-) by surface hydroxyl groups to form positive or negative sites respectively [173]. The adsorption phenomena of H^+ and OH^- ions is attributed to the amphoteric reaction of the surface hydroxyl groups which are schematically represented as follows (*M stands for metal*).

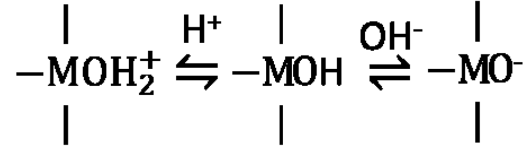

Thus, the resulting surface charge, which depends on an excess of one type of charged site over the other, is a function of the solution pH. The adsorption of positive or negative ions result in a diffuse layer of counter negative or positive ions respectively.

A detailed treatment of the EI interface describing the charging mechanism, the density of charges, and the pH sensitivity have been reported in [174]–[179]. In our model, though, it suffices to obtain a simplified expression of the pH response relating the surface potential as a function of pH. Therefore, simplified versions of the EI interface treatments are considered here.

The distribution of counter ions in the electrolyte which forms a proton concentration gradient between the electrolyte bulk and surface is mathematically described by Boltzmann equation as in (3.1) [174].

$$[H^+]_S = [H^+]_B e^{\frac{-q\varphi}{k_B T}} \tag{3.1}$$

where $\boldsymbol{k_B}$ is the Boltzmann constant, $\boldsymbol{q}$ is the elementary charge, T is temperature, φ is surface potential, $[H^+]_B$ is the proton concentration in the bulk, and $[H^+]_S$ is the proton concentration at the surface (dielectric-electrolyte interface).

Rearranging (3.1), the surface potential φ is expressed as a function of the proton concentrations at the dielectric-electrolyte interface and in the bulk as given by (3.2) below, which is also referred to as the Nernst equation.

$$\varphi = \frac{k_B T}{q} ln \frac{[H^+]_B}{[H^+]_S} \tag{3.2}$$

The pH sensitivity of the dielectric films, which is the change in surface potential per unit change in pH, is derived from (3.2) and is given mathematically as follows in (3.3):

$$\frac{d\varphi}{dpH} = -2.3 \frac{K_B T}{q} \alpha \tag{3.3}$$

where α is the proton buffer capacity whose value lies in the range, $0 < \alpha < 1$.

From equation (3.3), we can observe that the pH sensing film gives a maximum sensitivity of 59.6 mV/pH at room temperature which is known as the Nernstian limit of sensitivity [180]. In literature, depending on direct derivation from the Nernst equation, the maximum sensitivity of conventional ISFETs has also been given to be equal to the Nernst limit (59.6 mV/pH). But the maximum attainable sensitivity of ISFETs, in terms of change in drain current per unit change in pH, is not elucidated on literature to date.

Nonetheless, the sensors can be embedded in either of fixed bias or fixed current readout circuits, so that the pH dependent output variable of the ISFET can be either of the change in drain current or the shift in threshold voltage respectively. In this regard, it is very important to drive the maximum theoretical sensitivity of ISFETs, in terms of change in drain current per unit change in pH, for fixed bias applications. Hence, we drive such an expression which indicates clearly the expected outputs of sensors that are developed based on different types of transistors.

Equation (3.2) indicates that the surface potential developed at the EI interface is a logarithmic function of the ion activity, H^+ ion activity for instance. Since pH is also a logarithmic function of the H^+ ion activity, equation (3.3) illustrates that a change in pH results in a buildup of a linearly changing surface potential. This surface potential will in turn act at the gate of field-effect devices in the operation of ISFETs. From MOSFET theory, it is known that the drain current changes with gate voltage logarithmically in the subthreshold region. The expression of the subthreshold slope is given below on equation (3.4) [181].

$$S = \frac{dV_g}{d(log(I_D))} \tag{3.4}$$

where S is the subthreshold slope

With the well-established optimal operation in the subthreshold regime [182], the fixed bias sensitivity ($\Delta I_D/\Delta pH$) of ISFETs can be given by equation (3.5), which is derived from equations (3.3) and (3.4). Therefore, ISFETs developed based on conventional MOSFETs, which have a thermionic subthreshold slope (more than 60 mV/decade), can give a maximum fixed bias sensitivity of 0.99 decade/pH.

$$\frac{\Delta I_D}{\Delta pH} = \left(-2.3\ \frac{K_B T}{q} \alpha\right)\left(\frac{1}{S}\right) \tag{3.5}$$

The 0.99 decade/pH fixed bias sensitivity described above is an equivalent of the well-known Nernst limit which describes the maximum value of change in surface potential per unit change in pH. Nevertheless, for sensors based on sub 60 mV/decade transistors such as TFETs and IMOS, this sensitivity can go beyond the 1 decade/pH sensitivity. This enhanced sensitivity is equivalent to the signal amplification obtained in FDSOI devices for fixed current sensing applications.

Equation (3.3) gives the mathematical description of the change in surface potential at the pH sensing film, for a unit change in electrolyte pH. From this model of the electrolyte-insulator interface, we obtained the expected response of the EI component as a function of the solution pH which is the input variable to the sensor under development. The pH dependent surface potential, which is the output of the EI interface, serves as an input to the capacitive divider circuit.

3.2 The Capacitive Divider Circuit

The capacitive divider circuit, the electrical circuit for applying a front gate bias while achieving the pH detection simultaneously at the front gate, is crucial for stable operation of the sensor which also enables CMOS compatibility of the chemical sensor. The schematic diagram of such capacitive divider circuit along with the equivalent circuit is presented on figure 3.2.

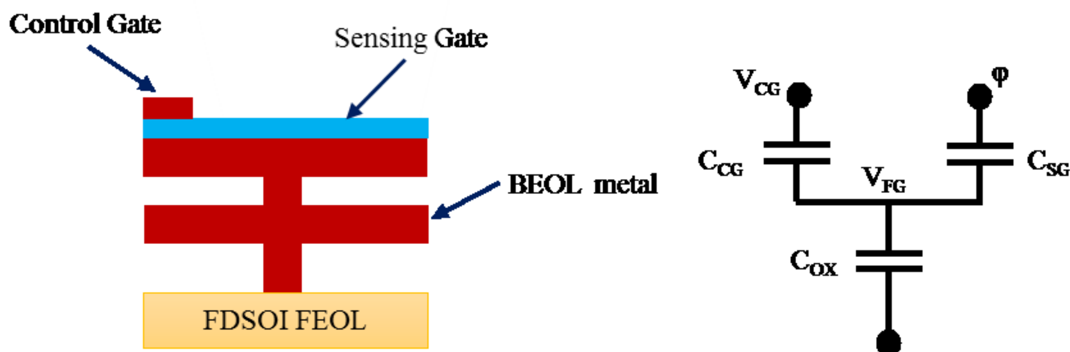

Figure 3. 2 Schematic diagram of the capacitive divider circuit (left), and its equivalent circuit (right)

The potential that can be recorded at the back gate after amplification through electrostatic coupling, in the UTBB FDSOI devices, is the voltage which appears at the floating BEOL metal (V_{FG}). This voltage is in turn a weighted sum of the sensing gate voltage and the control gate voltage which is mathematically given by equation (3.6) below.

$$V_{FG} = \frac{C_{CG}}{C_T} V_{CG} + \frac{C_{SG}}{C_T} \varphi \tag{3.6}$$

where V_{FG} is the voltage at the floating BEOL metal, φ is the surface potential at the sensing gate, and C_T is the sum of gate oxide capacitance, control gate capacitance (C_{CG}) and sensing gate capacitance (C_{SG}).

The ratio between V_{FG} and φ lies between 0 and 1 which means that the capacitive divider circuit introduces an attenuation factor unless the control gate and sensing gate capacitances are properly designed. Therefore, the sensing gate capacitance should be designed to be much higher than the control gate capacitance and the gate oxide capacitance in order to avoid (decrease) the signal attenuation.

3.3 UTBB FDSOI Devices

The CMOS integrated circuits have been almost exclusively fabricated on bulk silicon substrates until the bulk planar technology reached the limit of pursuing the scaling [33]. The evolution from bulk to fully depleted SOI on thick box was a way to reduce the electrostatic integrity although the integration on a thick buried oxide led to electrostatic coupling within the BOX due to the lateral electrical field penetration [183]. This challenge is addressed by the introduction of ultrathin body and buried oxide (UTBB) FDSOI architecture in which a very thin BOX and a highly doped ground plane are used. Figure 3.3 below shows the cross section of such FDSOI transistors.

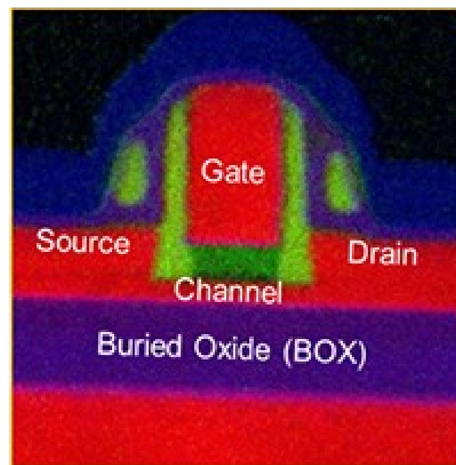

Figure 3. 3 Cross section of the UTBB FDSOI transistor

Figure 3.4 shows the schematic diagram of n-type flip-well UTBB FDSOI transistors, indicating the source, drain, gate, back gate and gate-protection diode. The wire connection between the front gate and the N-terminal of the protection diode is also indicated.

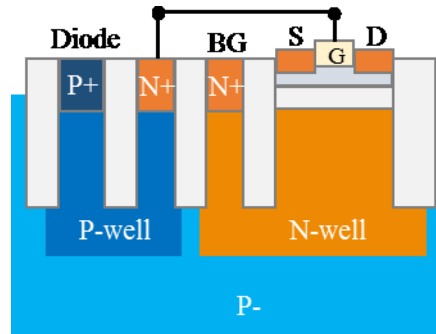

Figure 3. 4 Schematic diagram of industrial n-type flip-well UTBB FDSOI transistors

The tuning (multi V_{th}) capability provided by the thin BOX and highly doped ground plane of UTBB architecture is also accepted to solve some issues such as electrostatic control, operating power consumption, and standby energy dissipation in the 28 nm and below FDSOI technology [184], [185]. This is highly important to develop miniaturized, portable and ultralow power applications.

The UTBB FDSOI transistors provide promising technological platform for emerging markets beyond logic applications because of their special back biasing feature through the highly doped ground-plane which is also called the back gate (BG) as it acts as a second gate to control the threshold voltage of the transistor. The back biasing feature is beneficiary from two main perspectives. The first one is the multi V_{th} performance which gives tuning of the linear operating regime, and for ultralow power operation. The second advantage is to use one gate for modulating the drain current while using the other gate for other functionalities such as detection (sensing) purposes.

A sensitivity amplification is obtained in the case of UTBB FDSOI devices that arises from the strong electrostatic coupling and asymmetric capacitance between the two gates of the transistor. In this case, a change of front gate voltage results in an amplified shift in threshold voltage at the back gate.

The coupling factor (γ) between the front gate and the back gate of the FDSOI devices is given as follows [183], [186], [187].

$$\gamma = -\left(\frac{\Delta V_{th}}{\Delta V_g}\right) = \left(\frac{C_{Si}C_{OX}}{C_{BOX}(C_{OX}+C_{Si})}\right) \tag{3.7.1}$$

where ΔV_{th} is the shift in threshold voltage at the back gate, ΔV_g is a change in voltage at the front gate, C_{OX} is the gate oxide capacitance, and C_{BOX} is buried oxide capacitance.

Equation (3.7.1) can be expressed in terms of the thicknesses of the oxide and the silicon as in below, on equation (3.7.2) [187]:

$$\gamma = \left(\frac{3t_{BOX}}{3t_{OX}+t_{Si}}\right) \tag{3.7.2}$$

For the sensor which is developed based on UTBB FDSOI devices, the above equations can be approximated as follows, given by (3.7.3) [186]–[188].

$$\gamma = -\frac{\Delta V_{th}}{\Delta V_g} = \frac{C_{OX}}{C_{BOX}} \tag{3.7.3}$$

The electrostatic coupling between the front gate and back gate is effective only in FDSOI transistors where the channel is ultrathin [189], [190]. Therefore, both the ultrathin body and buried oxide architecture of the devices are crucial for the ultrasensitive performance of the sensors integrated on UTBB FDSOI devices.

We characterized the coupling between the two gates of the transistors. The source was grounded while a fixed bias was applied at the drain. Then I_D-V_{BG} sweeps were taken at different applied voltages at the front gate. The electrical connection of the transistor for such characterizations is shown on figure 3.5. During these characterizations the gate protection diode was not connected to any bias.

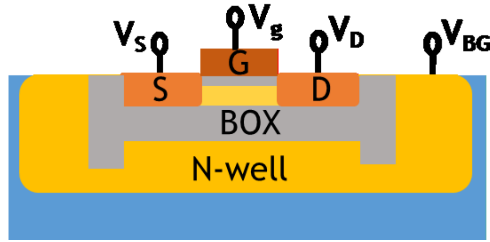

Figure 3. 5 The electrical connection diagram for characterization of the electrostatic coupling between the front gate and the back gate (NFET SLVT)

Below is a measured I_D-V_{BG} characteristics of NMOS SLVT (super low threshold voltage) or flip-well UTBB FDSOI transistors having gate oxide and BOX thicknesses of 1.8 nm and 25 nm respectively. The devices are manufactured by STMicroelectronics.

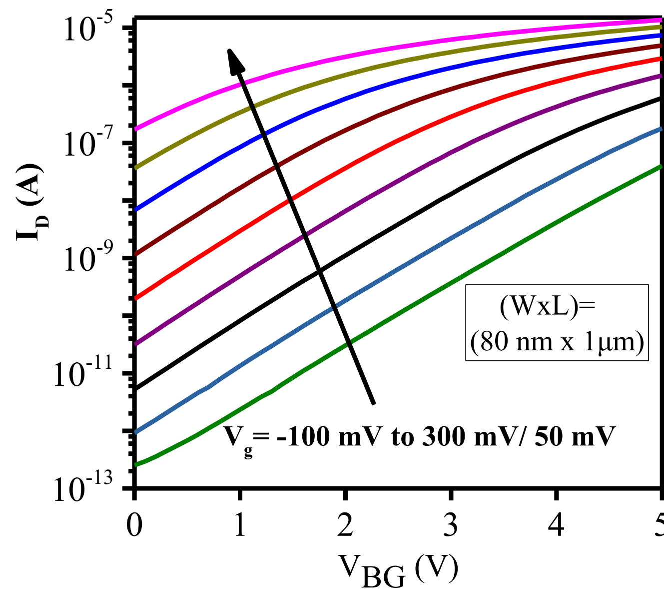

Figure 3. 6 Measured I_D-V_{BG} characteristics of the UTBB FDSOI devices

As can be observed from figure 3.6, a 50 mV change in front gate voltage results in a 650 mV shift of voltage at the back gate. This provides a built in amplification of 13-times which helps to obtain an ultrasensitive pH sensor. The measurement results are in confirmation with the mathematical model given by equation (3.7) that the shift in threshold voltage at the back gate is 13 times the change in front gate voltage which is equivalent to the ratio of gate oxide capacitance and BOX capacitance.

The same characterizations have also been undertaken on low threshold voltage (LVT) or regular-well PFET and NFET devices which are available on the same die with the NFET SLVT devices. The results are shown on figures 3.7 and 3.8 respectively.

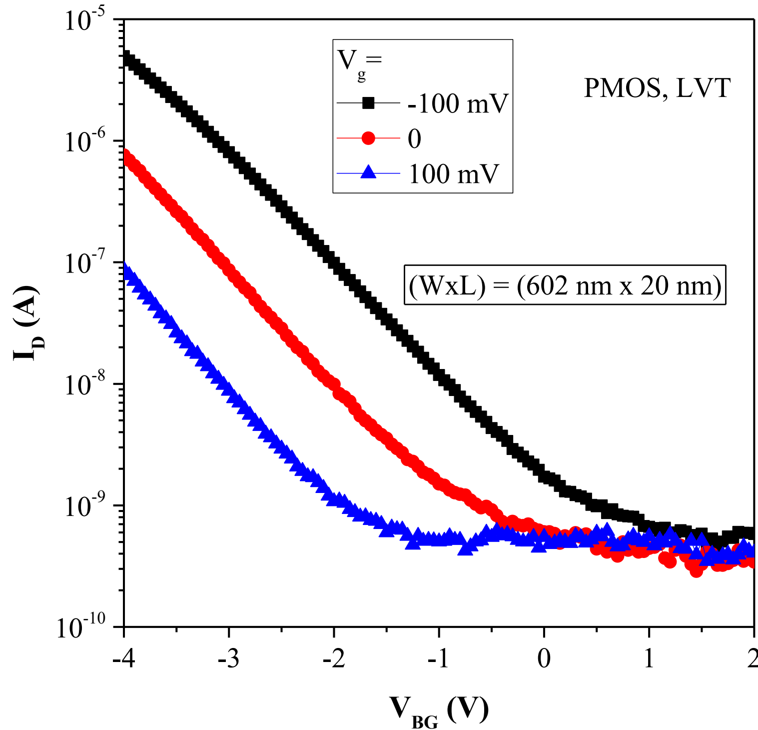

Figure 3. 7 Measured I_D-V_{BG} characteristics of the LVT PFET UTBB FDSOI device

Since the amplification depends on the ratio of gate oxide capacitance and buried oxide capacitance, for a change in 100 mV at the front gate, a 1.3 V shift is obtained at the back gate in the cases of all the flip well and regular well NFET and PFET devices.

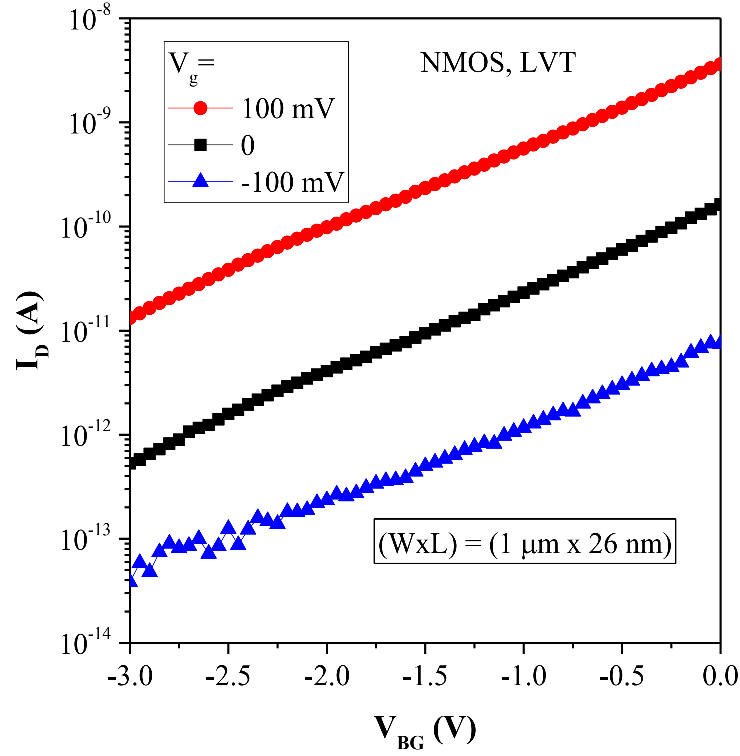

Figure 3. 8 Measured I_D-V_{BG} characteristics of LVT NFET UTBB FDSOI devices

In the contrary, a change in voltage at the back gate results in an attenuated shift in threshold voltage at the front gate given by the relation below, on equation 3.8.

$$\Delta V'_{th} = -\frac{C_{BOX}}{C_{OX}} \Delta V_{BG} \tag{3.8}$$

where $\Delta V'_{th}$ is the shift in threshold voltage at the front gate which can also be expressed as ΔV_g, as the shift is the same in the subthreshold region (the region where the sensing functionality is performed). ΔV_{BG} is the change in applied voltage at the back gate.

A measured characteristics of such attenuated coupling between the two gates of NMOS SLVT UTBB FDSOI device is presented below on figure 3.9. The transistor had a gate length and width of 2 µm and 80 nm respectively.

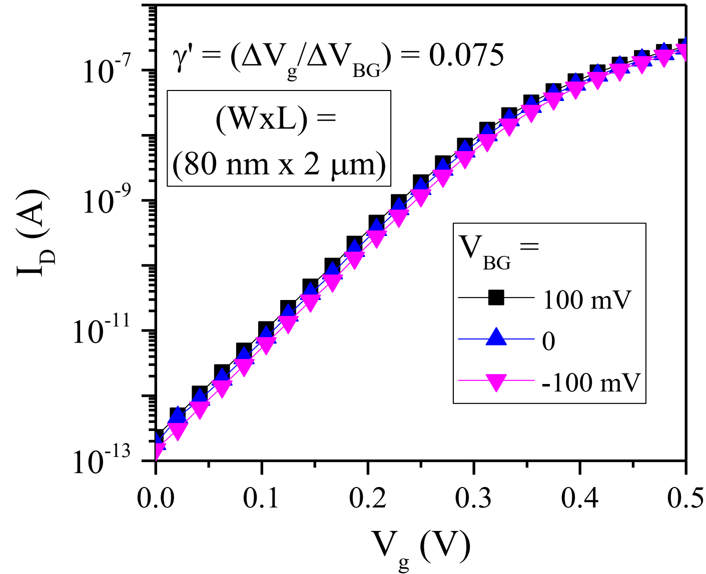

Figure 3. 9 Attenuated shift in threshold voltage at the front gate induced by a change in back gate voltage

From the characteristics presented on figure 3.9, a 100 mV change in back gate voltage results in only a 7.5 mV shift in the threshold voltage at the front gate. This is equivalent to a coupling factor ($\gamma' = \Delta V_g/\Delta V_{BG}$) of 0.075. Therefore, pursuing the sensing functionality at the front gate provides an intrinsic signal amplification for developing ultrasensitive sensors, while the reverse introduces a signal attenuation.

In addition to the amplification, the back biasing feature of UTBB FDSOI devices provide a significant advantage of tuning. The tuning capability addresses the challenge of saturation that would arise because of the high sensitivity and the wide pH range. On figures 3.10 and 3.11 the measured tuning characteristics of NFET SLVT devices are provided.

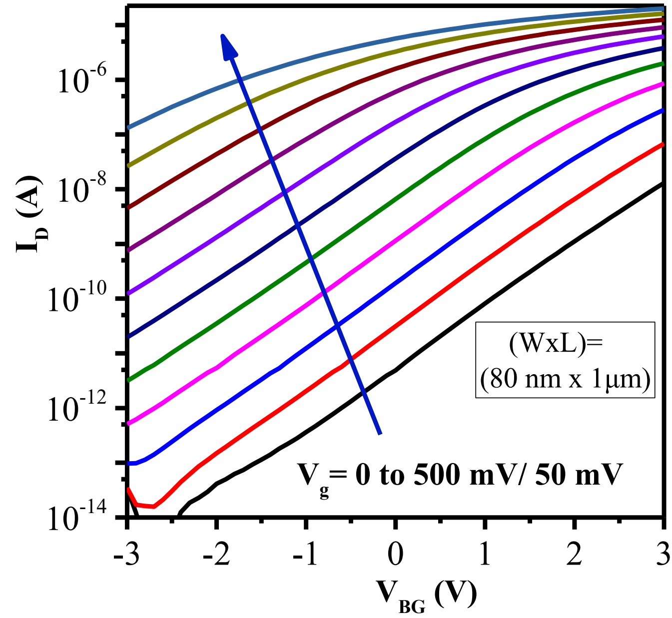

Figure 3. 10 Tuning of the linear operating regime to the left (negative V_{BG}) for higher potentials at the front gate.

The result shows that, for potentials less than 0 (which corresponds to higher pH) at the front gate, the linear operating regime at the back gate shifts to the right. On the other hand, higher potentials at the front gate (more acidic pH), the back gate voltage needs to be decreased. This way, the whole pH range (pH 0 to 14) can be measured without saturation problem.

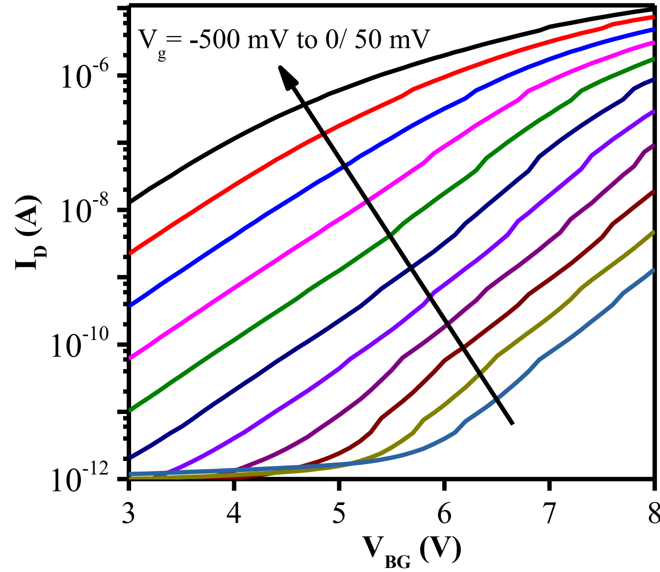

Figure 3. 11 Tuning of the linear operating regime to the right for negative potentials at the front gate

3.4 The pH Sensor with a Capacitive Divider Circuit

The pH sensor is integrated in the BEOL of industrial UTBB FDSOI transistors with a capacitive divider circuit for front gate biasing through a capacitively coupled control gate. Figure 3.12 shows the schematics of the pH sensor where detection of the pH is pursued at the front gate while the signal is recorded at the back gate. The equivalent electrostatic model of the sensor is also provided on figure 3.12.

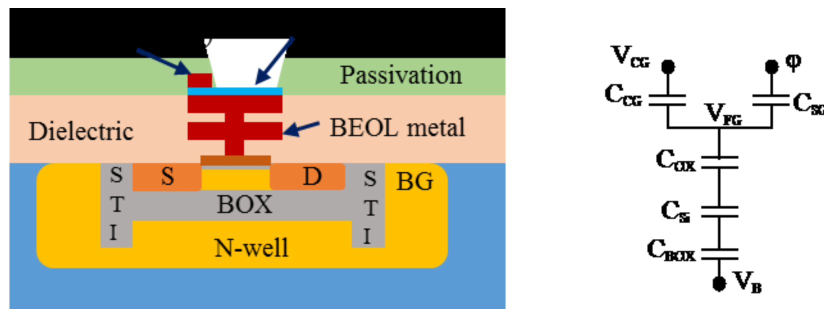

Figure 3. 12 Schematics of the pH sensor integrated in BEOL of UTBB FDSOI (left) and its equivalent electrostatic model (right)

Consequently, functionalizing the pH sensing at the front gate of FDSOI devices, the change in surface potential at the front gate is detected at the back gate amplified by the coupling factor (γ), giving rise to an ultrahigh-sensitive solid state chemical sensor. Combining the input output characteristics of the sensor's

components, the shift in threshold voltage (for NMOS devices) at the back gate is mathematically shown below on equation (3.9) as a function of the solution pH.

$$\Delta V_{th} = \left(2.3\ \frac{K_B T}{q} \alpha\right)\left(\frac{C_{OX}}{C_{BOX}}\right)\left(\frac{C_{CG}}{C_T} \Delta V_{CG} + \frac{C_{SG}}{C_T} \Delta pH\right) \tag{3.9}$$

For computing the sensitivity of the pH sensor, which is the ratio of change in threshold voltage to the change in pH, the control gate voltage should be kept constant so that the term containing (ΔV_{CG}) on equation (3.9) becomes zero. As a result, the sensitivity is derived as follows given by equation (3.10). This is a complete description of the sensitivity of such sensors in which the effects of the sensing film, the capacitive divider circuit, and the FDSOI coupling factor are all included in one equation.

$$\frac{\Delta V_{th}}{\Delta pH} = \left(\frac{C_{SG}}{C_T}\right)\left(\frac{C_{OX}}{C_{BOX}}\right)\left(2.3\ \frac{K_B T}{q} \alpha\right) \tag{3.10}$$

On equations (3.9) and (3.10), the term $\left(\frac{C_{SG}}{C_T}\right)$ comes from the capacitive divider circuit which takes a value between 0 and 1. The circuit should be designed in such a way that $C_{SG} << C_T$, so that the $\left(\frac{C_{SG}}{C_T}\right)$ term is very close to unity, otherwise it introduces a sensitivity attenuation.

Depending on the desired application of the sensors, modeling the drift may also be required for some continuous pH monitoring uses. S. Jamasb, et al developed physical models for quantitative evaluation of drift phenomena in ISFETs having sensing films of silicon nitride and aluminum oxide [141], [142], [144]. It is postulated that the drift is generally associated with a gradual modification of the surface of the sensing film due to its exposure to the electrolyte. According to the model of S. Jamasb, et al, the drift comes from the change in insulator capacitance which arises from the surface modification.

In the case of ISFETs which have silicon nitride sensing films, S. Jamasb, et al explained that drift is caused by a gradual hydration of the silicon nitride surface forming silicon oxide or oxynitride layer [141], [144]. Comparing the time scales of the drift phenomena and transport in insulators, they correlated the rate of hydration with dispersive transport mechanism. The same correlation to dispersive transport mechanism is

made for evaluating a drift behavior in the case of aluminum oxide sensing films [144]. The exponential temporal sensing film modification, proposed by S. Jamasb, et al, which results in a correspondingly exponential drift is presented on equation (3.11).

$$x_{SG}(t) = x_{SG}(\infty)\{1 - exp[-(t/\tau)^{\beta}]\} \tag{3.11}$$

where x_{SG} (t) is the thickness of the modified sensing film at time t, x_{SG} (∞) is the final modified film thickness, τ is the time constant, and β is a dispersion parameter (0< β<1). A time constant of 1.20 hour and dispersion parameter of 0.713 are reported in [144] *for aluminum oxide sensing film at pH 4.*

Therefore, inserting equation (3.11) into the C_{SG} term of equation (3.10), a sensitivity mathematical model which depends not only on the sensor parameters but also on the duration of measurement, can be obtained. However, we would like to stress that the model presented by S. Jamasb, et al, needs more rigorous analysis and experimental validation before accepting it as a well-established theory.

The pH sensor has been designed in which no reference electrode is needed due to the incorporation of a BEOL metal and a capacitively coupled control gate. Hence, the front gate bias is applied through a control gate rather than a reference electrode. Therefore, this sensor is highly sensitive and CMOS compatible which is suited for low-power and low-cost ultrasensitive applications expected for the IoT market. The proposed approach has been validated by the consistent results obtained from the modeling, simulation and experimental characterization.

3.5 Simulation of the Sensor

We simulated the performance of the pH sensor that we developed utilizing TCAD Sentaurus. The UTBB FDSOI transistor which is used as building block of the sensor is built using Sentaurus process emulating the standard fabrication process. Deposition and patterning of the pH sensing film and the control gate are also undertaken in Sentaurus process. Finally, the source, drain, back gate, the floating BEOL metal, and the control gate contacts were defined in Sentaurus device for the electrical simulation of the sensor. Figure 3.13 shows the simulated sensor along with the simulating parameters.

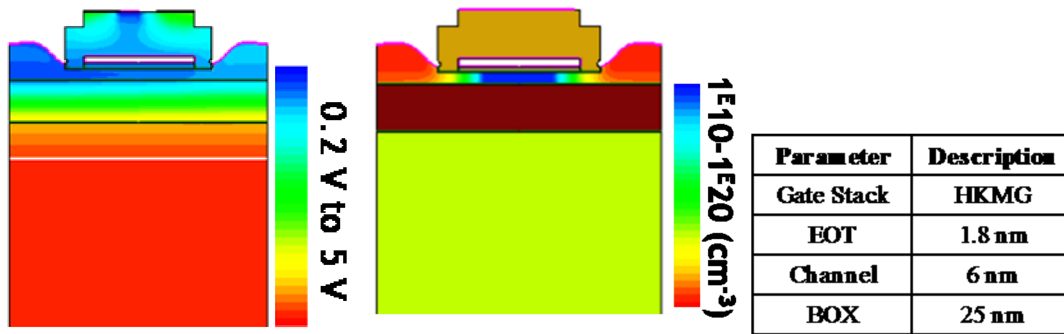

Parameter	Description
Gate Stack	HKMG
EOT	1.8 nm
Channel	6 nm
BOX	25 nm

Figure 3. 13 Potential profile (left), charge distribution (middle), and major parameters (right) of the simulated sensor

Different physical models are employed for computation of charge carrier density, current density, potential profile, and electron/hole mobility. Considering the Fermi-Dirac distribution function, which is valid at all energy levels, unlike the Boltzmann approximation which is valid only at high energy region, the Fermi statistics was chosen over the Boltzmann statistics for n and p density description. This ensures validity of the model at all regions including high carrier density regions such as active parts of the transistor. The Poisson equation is solved to compute the electrostatic potential which is interdependent with both mobile and stationary charges.

The drift-diffusion carrier transport model, which is the default carrier model in Sentaurus device, is utilized for current density computation. This model takes into account the current due to the gradient in electrostatic potential and carrier concentration, and the current due to spatial variation in the electron affinity, the band gap, and carrier effective masses. The mobility degradation at the semiconductor-insulator interface was also accounted for through the Lombardi model [191]. The Coulomb scattering which is apparent in thin devices [192], and the remote phonon scattering due to the HfO_2 high-K material [193] are also accounted for in the calculations.

In order to widen the potential application area of the simulated sensor, the electrolyte-insulator interface is modeled in two different ways in Sentaurus device. They are sensing the surface potential and sensing the surface charge. Developing the sensor in the BEOL of the 28 nm industrial UTBB FDSOI transistors, we demonstrated a single charge sensitivity (a shift of 7 mV for 30 elementary charges), and 780 mV/pH. The modelling and simulation are validated by experimental fabrication and characterization.

3.5.1 Sensing the Surface Charge

Q. Zhang, *et al*. have modeled the ion sensitive floating gate field-effect transistor, in such a way that a

certain amount of surface charge (Q_s) is adsorbed at the electrolyte-insulator interface of their sensing probe [161]. The adsorbed surface charge, Q_s induces a counter charge (Q_i) in the floating gate metal, with a maximum value of Q_s = -Q_i at perfect induction. Mathematically, modulation of the voltage at the floating BEOL metal with the adsorbed surface charges is given by equation 3.12.

$$V_{FG} = \frac{1}{C_T} Q_i + \frac{C_{CG}}{C_T} V_{CG} \tag{3.12}$$

where V_{FG} is the voltage at the floating gate, V_{CG} is the applied voltage at the control gate, C_T is summation of gate oxide capacitance (C_{OX}) and C_{CG}, and Q_i is the induced charge at the floating gate due to surface charge on top of the sensing dielectric.

Modeling the adsorption of ions on the sensing film as distributed surface charges, the shift in voltage at the back gate is simulated as a function of change in density of surface charges at the sensing gate. The result is presented below on figure 3.14.

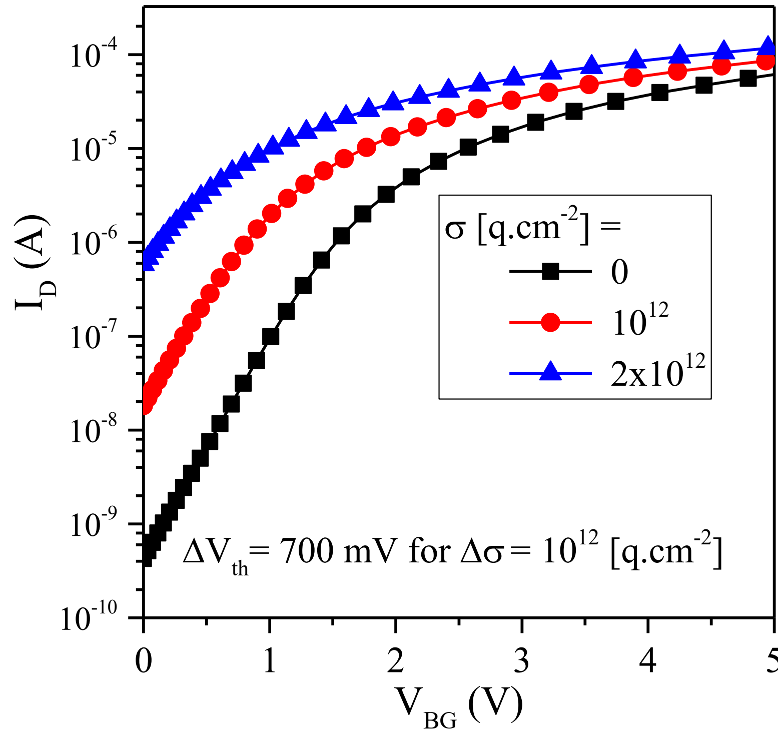

Figure 3. 14 Simulated I_D-V_{BG} characteristics of the FDSOI ISFET at different surface charges at the sensing gate (SG).

From the given change in charge density of $\Delta\sigma = 10^{12}$ [q.cm^{-2}] and from the sensing area of (296 nm) x (1 μm), we calculated the total deposited charges to be 0.47 fC. The simulation was run for $C_{OX} = 5.7$ fF and $C_{CG} = 3.8$ fF. Calculating for ΔV_{FG} from the above variables, using equation (3.12), we obtain $\Delta V_{FG} = 50$ mV for $\Delta\sigma = 10^{12}$ [q.cm^{-2}]. Therefore, by adding the amplification factor ($\gamma = 13$), we get a change in threshold voltage, $\Delta V_{th} = 650$ mV for $\Delta\sigma = 10^{12}$ [q.cm^{-2}]. Crosschecking the simulation result (given on figure 3.14) with the mathematical model given by equation (3.12), we obtained that the simulation result is consistent with the mathematical model. We also observed that, even a few number of elementary charges produce a substantial amount of shift in the threshold voltage of the sensor─ 30 elementary charges result in a shift of the threshold voltage equal to 7 mV. Therefore, this ISFET which has a deeply scaled down effective oxide thickness, is able to detect charges at a sensitivity of single elementary charge.

3.5.2 Sensing the Surface Potential

For operation of the ISFET in chemical and biological environments, we can also model the system by considering the surface potential due to electrolyte-insulator interaction as a variable source of potential. According to D. L. Harame, *et al*., from the point of view of the field-effect transistor, φ is a variable voltage source in series with the gate electrode [194]. The simulation result modeling the sensor in this approach is presented below on figure 3.15.

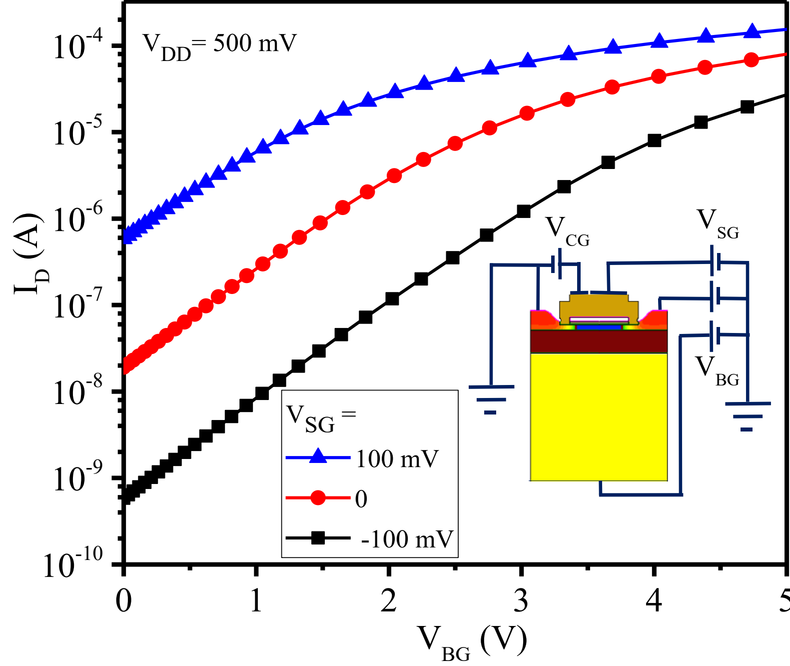

Figure 3. 15 Simulated I_D-V_{BG} characteristics of the FDSOI ISFET at different surface potentials at the sensing gate (SG).

From equation (3.6), it can be observed that the sensitivity scales down by a factor of $\frac{C_{SG}}{C_T}$. However, for BEOL ISFETs, the sensing gate has much larger area so that it has much larger capacitance even compared to the gate oxide capacitance. The simulation was run at C_{CG} = 23 pF, C_{SG} = 23 nF, and C_{OX} = 1.16 fF. Substituting these values in equation (3.6), we obtain $\frac{C_{SG}}{C_T}$ = 0.99 which gives ΔV_{th} = (0.99) * (γ) * (ΔV_{SG}). For ΔV_{SG} = 100 mV, the calculation gives ΔV_{th} = 1.386 V while the simulation result yields ΔV_{th} = 1.3 V which is a very close conformity. Therefore, a pH sensitivity reaching 780 mV/pH (corresponding to a change in surface potential of 60 mV per unit pH) is obtained with our simulated ISFET.

The simulation was run at different conditions, such as different ratios of dimensions of the sensing gate capacitance. The theoretically expected maximum sensitivities have been obtained when the simulation was run for sensing gate area of large area compared to its separation distance. However, when the order of dimensions of the capacitance area are comparable with the separation distance, the simulated sensitivity is smaller than the calculated sensitivity. This is because of the fringing fields indicating that the BEOL is more suited for the sensing functionalization. Below, on figure 3.16, is a simulation result showing such an attenuation effect by 26%.

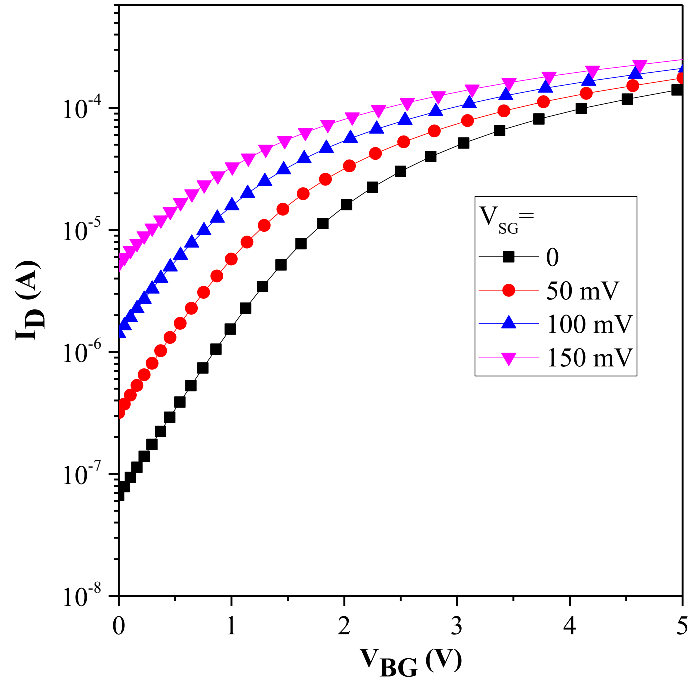

Figure 3. 16 Simulation result showing reduced sensitivity at comparable dimensions of the sensing gate capacitor.

Equation (3.6) shows the mathematical relation showing the shift in voltage at the back gate as a weighted sum of the voltages at the control gate and the sensing gate. However, for a properly designed capacitive divider circuit, in such a way as to minimize the sensitivity attenuation, the coefficient of the control gate voltage is close to zero. This results in a negligible modulation of the floating gate metal voltage through the control gate voltage.

Below is the mathematical result indicating the small modulation effect of the control gate voltage (V_{CG}) at sensing gate, control gate, and gate oxide capacitances of 23 pF, 23 fF, and 1.16 fF resepectively. In this case, the modulation capacity of the control gate voltage is only 0.1%.

Table 3. 1 Calculated changes in floating gate voltage for different changes in control gate voltage

ΔV_{CG} (mV)	-150	-100	-50	0	50	100	150
ΔV_{FG} (mV)	-0.15	-0.10	-0.05	0	0.05	0.10	0.15

This reduced effect is also simulated using the TCAD Sentaurus, where the mathematically computed result is validated. The simulation result is presented on figure 3.17 below.

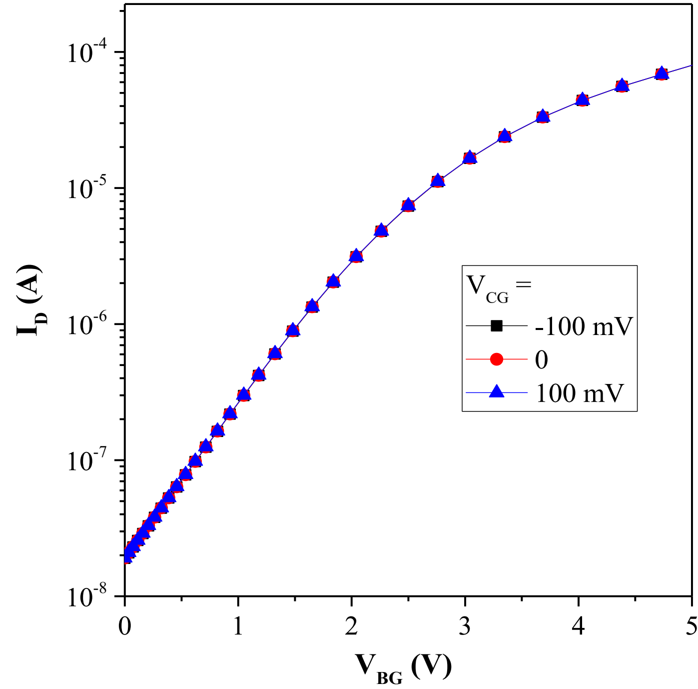

Figure 3. 17 Simulation result showing no response to change in control gate voltage.

3.6 Sensing at the Gate Protection Diode

We also developed a novel pH sensor in which the pH sensing is made through the protection diode of the transistor in the BEOL. The schematic diagram of the sensor and the equivalent electrical connections are given on figure 3.18 and figure 3.19 respectively, based on flip well (SLVT) n-type FDSOI transistors.

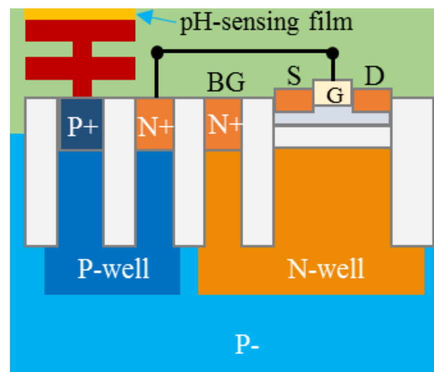

Figure 3. 18 Schematic diagram of the sensor in which sensing is made at the gate protection diode.

The pH detection is carried out at the P-terminal of the gate protection diode, whereas the opposite terminal of the diode is tied to the front gate. The diode-front gate connection provides an NPN junction with the back gate (in case of N-well FDSOI devices). When the back gate voltage (V_{BG}) << 0, the NPN junction becomes conductive and the back gate bias appears at the front gate of the FDSOI NMOS transistor. Such negative biases both at the front gate and at the back gate turn off the FDSOI.

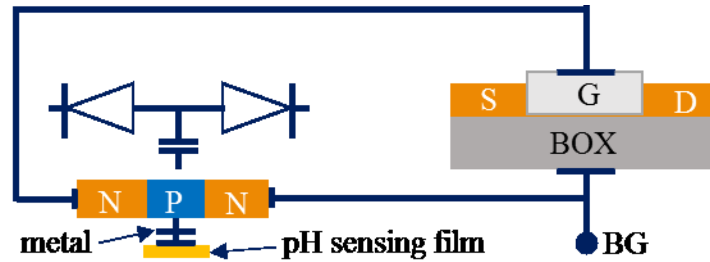

Figure 3. 19 Schematics of the sensor with FDSOI and NPN connection.

At small negative voltages and for positive biases at the back gate, the NPN junction gets turned off. In this condition, the front gate of the FDSOI becomes floating and if the drain voltage (V_D) increases, the FDSOI transistor becomes turned on very abruptly due to the drain induced barrier lowering (DIBL) effect in very short devices. Such steep switching, reaching as small as 9 mV/decade, is illustrated below on figure 3.20. This figure shows the drain current switching while the voltage at the back gate is swept from -0.8 V to 0.2 V (at an SLVT NFET device).

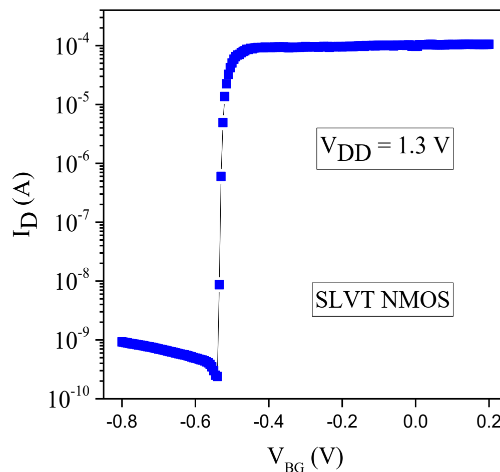

Figure 3. 20 Drain current switching due to the DIBL effect

DIBL is a short-channel effect referring to a number of phenomena encompassing a simple change of

threshold voltage at higher drain voltages, change of the subthreshold slope, and entire failure of the gate to turn the device off at extremely short gate lengths [195], [196]. Figure 3.21 shows the dependence of the drain current switching on the gate length of devices.

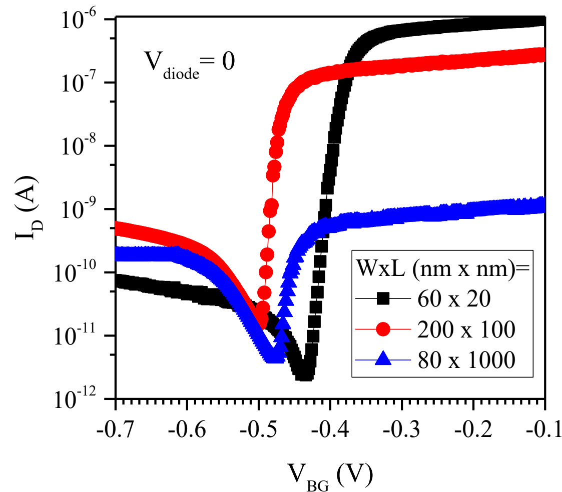

Figure 3. 21 Dependence of the DIBL effect on device gate length

Validating the DIBL theory that such effects are more sound in short gate length devices, figure 3.21 illustrates that the 20 nm gate length device has the steepest drain current switching, compared to those of 100 nm and 1000 nm devices. The longest device, at gate length of 1000 nm, has the least steep switching of the drain current.

The DIBL effect depends not only the gate length, but also on the drain voltage. It becomes more significant with an increasing drain voltage. Figure 3.22 shows such dependence, indicating that steepest change in drain current is obtained at the maximum drain voltage.

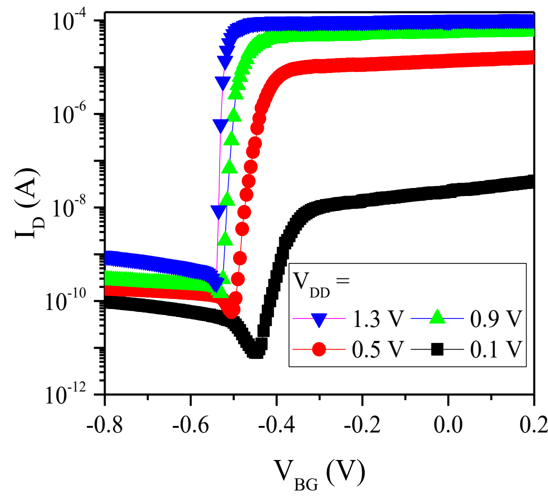

Figure 3. 22 Dependence of the DIBL effect on drain voltage

In short devices, the height of the barrier for the carriers at the source is lowered by the drain electric field flux at increased drain voltages [197]–[202]. The simulated profile of the potential at the different regions of the FDSOI and the NPN structure is shown below on figure 3.23. It illustrates the barrier degradation between the source and drain.

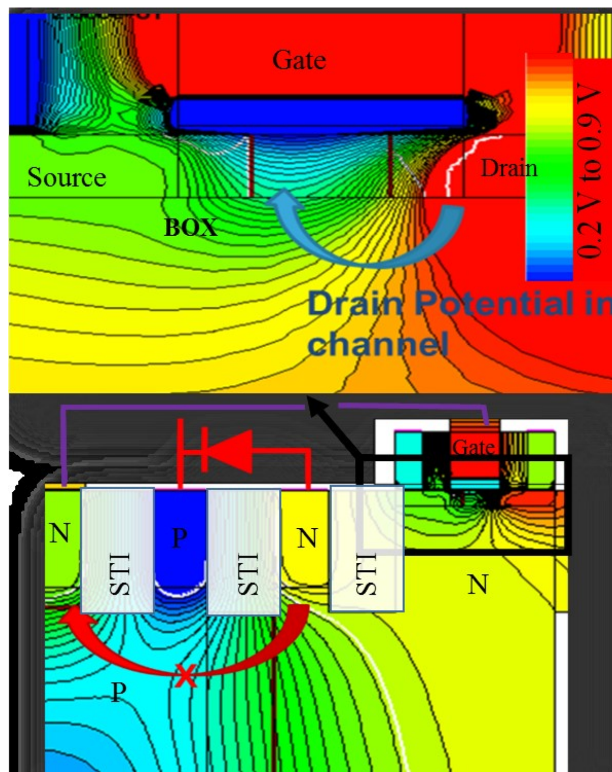

Figure 3. 23 Simulation result showing the potential distribution in short UTBB FDSOI devices.

By changing slightly the potential at P area of the NPN junction, the entire I_D-V_{BG} curve shifts. As the I_D-V_{BG} curve is extremely steep, any small change of the potential at the diode P-area leads to large variation in the drain current providing an extremely sensitive detection. Figure 3.24 below presents the shift in the back gate voltage at which switching of the drain current takes place, depending on the bias at the diode.

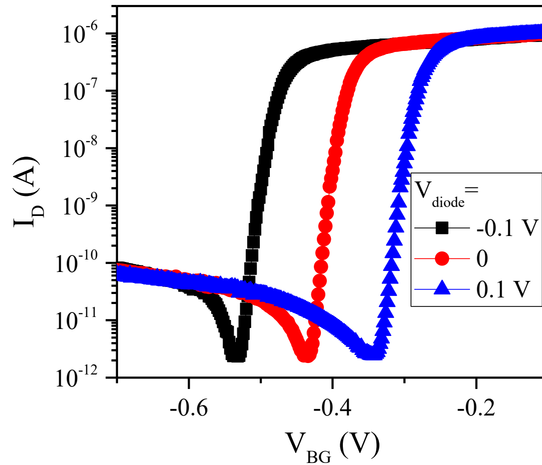

Figure 3. 24 Shift of the I_D-V_{BG} curve depending on the diode bias

This effect is used to sense small pH variation on an electrode connected to this P-area. Consequently, integrating the pH sensing film on the BEOL metal of the diode, the back gate voltage at which the drain current switches depends on the pH value of the electrolyte. By changing the pH value, the potential at P area of the NPN junction changes and the entire I_D-V_{BG} curve shifts.

3.7 Conclusion

With a thorough analysis of the individual components of the sensor— the UTBB FDSOI, the capacitive divider circuit, and the EI-interface, a rigorous mathematical model of the sensor is developed. The developed model relates the output of the sensor as a function of the sensor input and the design parameters of the capacitive divider circuit and the UTBB FDSOI transistor.

At the EI interface, the maximum change in surface potential per unit change in pH is 59.6 mV/pH which is commonly referred to as the Nernst response. This signal is coupled to the BEOL metal of the FDSOI through the capacitive divider circuit. The potential seen at the BEOL metal, a weighted sum of the control gate bias and the sensing gate potential, is recorded at the back gate amplified by the coupling factor of the

UTBB FDSOI.

Numerical simulations have been carried out using TCAD-Sentaurus to validate the proposed approach and the mathematical model. Considering the adsorption of ions onto the sensing film as distributed surface charges, the shift in voltage at the back gate is simulated as a function of change in density of surface charges at the sensing gate. The simulation is also carried out modeling the surface potential at the EI interface as a variable voltage. Consistent results have been obtained from the simulation with a sensitivity of 780 mV/pH and single charge detection. All simulation results are in confirmation with theoretical expectation and mathematical modeling.

CHAPTER FOUR

FABRICATION OF THE SENSORS

Fabrication of the sensors was carried out on a general purpose die in which the UTBB FDSOI transistors and other active components exist. Hence, the fabrication process includes process steps for passivating the undesired active areas of the die. The required transistors were inscribed somehow far from the center of the die (when diced following the dicing streets), so that two different designs have been employed for the sensor fabrication. Initially, the dicing was made following the dicing streets which imposed constraint towards exploiting more devices, because of the location of the transistors away from the center of the die. Because of this, a modified dicing was later employed to center the transistors which enables exploitation of 4-times more devices per die.

4.1 Layout of the Devices on the Die

The layout of the block of transistors, shown in green on the (2.5 cm x 2.9 cm) die, is presented hereunder on figure 4.1. The block contains totally 414 PFET and NFET transistors, of both regular well (LVT) and flip well (SLVT) architectures. This block, which has 46 rows of transistors named DSD-01 to DSD-46, spans an area of 2 mm by 5 mm on the die.

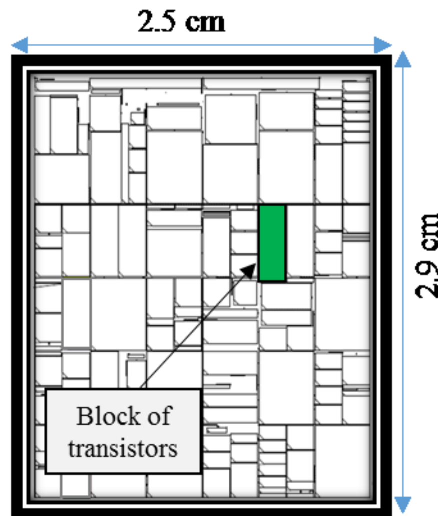

Figure 4. 1 Layout of the block of transistors on the (2.5 cm x 2.9 cm) die

In the first integration of the sensors, in the BEOL of the transistors, only 9-devices of SLVT NFET type were chosen due to space constraint for the electrical contact extension and the electrolyte dispensing area. Since the transistors are close to the edge of the die, the metal extension for S, D, BG contact cannot be made to the right— all extensions need to be made to the left. This poses a space constraint for including more devices for the sensor fabrication. Regarding the electrolyte dispensing area, a 20 µl or 30 µl of electrolyte spans an area of 2 to 3 mm diameter. This means that although more than 9 neighboring transistors are used for the sensor integration, they will all be exposed to the electrolyte during characterization of 1-sensor. This creates a challenge against systematic characterization of the sensor in which each sensor would preferably contact the solution only when it is planned for characterization. In addition, the characterization bench can characterize only 1 sensor at a time. Therefore, characterization of several sensors of the same die, at the same time after dispensing the pH solution, is not possible. This challenge is addressed in the improved design, with a modified dicing of the wafer, which is presented in section 4.4.

4.2 The Proof of Concept Sensors

Validating the proposed approach and the mathematical model with a numerical simulation on TCAD-Sentaurus, a proof of concept extended gate (EG) pH sensor was developed. This extended gate operation of the sensor is very important for two main reasons. The first purpose is the simpler and faster processing of the sensor. The second and equally significant benefit is that larger sensing areas, compared to the area covered by the pH solution during characterization, can be obtained. This enables to avoid interfering side reactions with the passivation material, so that abnormalities on the output signal of the sensor would be reduced. It is also an advantage that in the case of extended gate sensors, additional processes are not pursued on top of the sensing film which provides cleaner sensing area.

These proof of concept EG sensors were developed by a separated processing of just the pH sensing components, which are electrically connected to the transistors only during characterization of the sensors. This provides faster and simpler realization of the sensor without the need for masks and patterning by lithography. In contrary, the external electrical connection during the characterization brings in more inconvenience and signal attenuation.

The pH sensing components of the EG pH sensors were processed on 750 µm Si substrates which had a thermally grown 500 nm oxide (SiO_2). A Ti/Pt layer of 10 nm/80 nm thickness was then deposited by e-beam evaporation [180] that serves as an extension of the FDSOI floating BEOL gate metal for the extended

gate operation of the sensor. For the sensing film, 50 nm aluminum oxide (Al_2O_3) was deposited by atomic layer deposition (ALD) on the Ti/Pt metal layer. Finally, we applied silver paste to complete the external electrical connections between the Ti/Pt metal layer of the sensing component and the floating metal gate of the FDSOI. The schematic diagram of the electrical connection and system layout for pH sensing characterization is shown on figure 4.2.

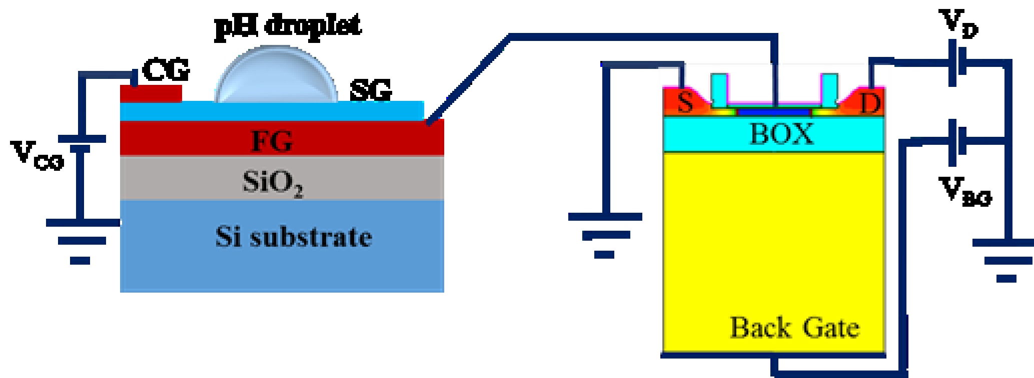

Figure 4. 2 Schematic diagram of the proof of concept extended gate pH sensor

The proof of concept sensors were realized utilizing n-type flip-well (SLVT) FDSOI transistors that are manufactured by STMicroelectronics. The transistors have a channel of thickness (t_{Si}) = 6 nm, buried oxide (BOX) = 25 nm, and equivalent gate oxide thickness = 1.8 nm. The devices have also a gate width and gate length of 80 nm and 1 µm respectively. The SEM cross sectional image of the FDSOI transistors is shown below on figure 4.3.

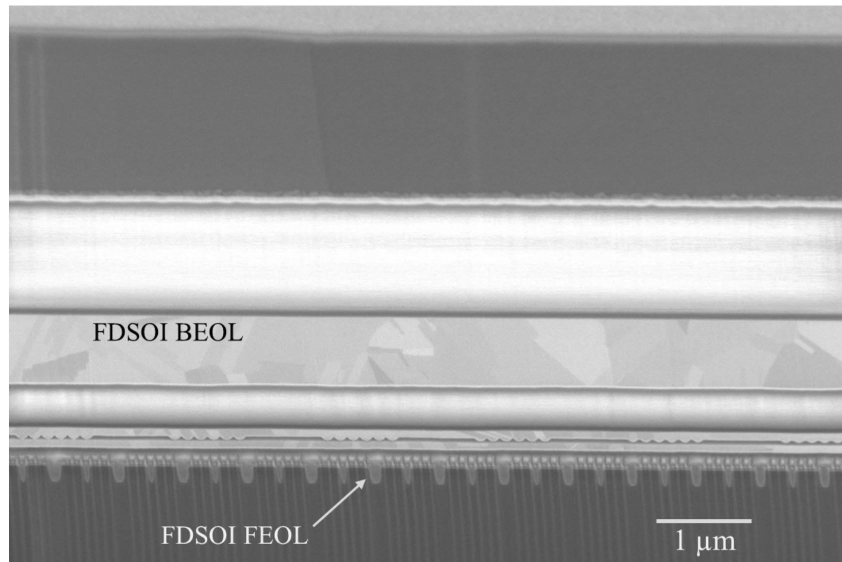

Figure 4. 3 SEM cross sectional image of the transistors.

4.3 Integration of the Sensors in BEOL

Following the validation of the proposed sensor with the mathematical modeling, simulation using TCAD Sentaurus, and with fabrication and testing of the extended gate pH sensor, we integrated the pH sensors in the BEOL of UTBB FDSOI transistors.

Dicing the general purpose wafer following the company dicing streets, the layout of the pH sensors was prepared in such a way that the maximum number of pH sensors would be integrated on a die. This is because of the space constraint for electrical contact extension and considering the area covered by the pH droplet while measurement, and the optimum number of sensors that can be characterized with the available characterization bench.

4.3.1 Process Flow

With the metallic pads of the transistors available (exposed) on the die, the process flow was designed as to fabricate the sensor with the cleanest possible sensing film in the shortest number of process steps. From this point of view, the deposition of the pH sensing film was carried out at the very beginning. Thus, deposition of aluminum oxide with atomic layer deposition (ALD) was made on an acetone-IPA-DI water

cleaned surface of fresh dies. The XPS characterization result of the ALD deposited Al_2O_3 film is given below on figure 4.4.

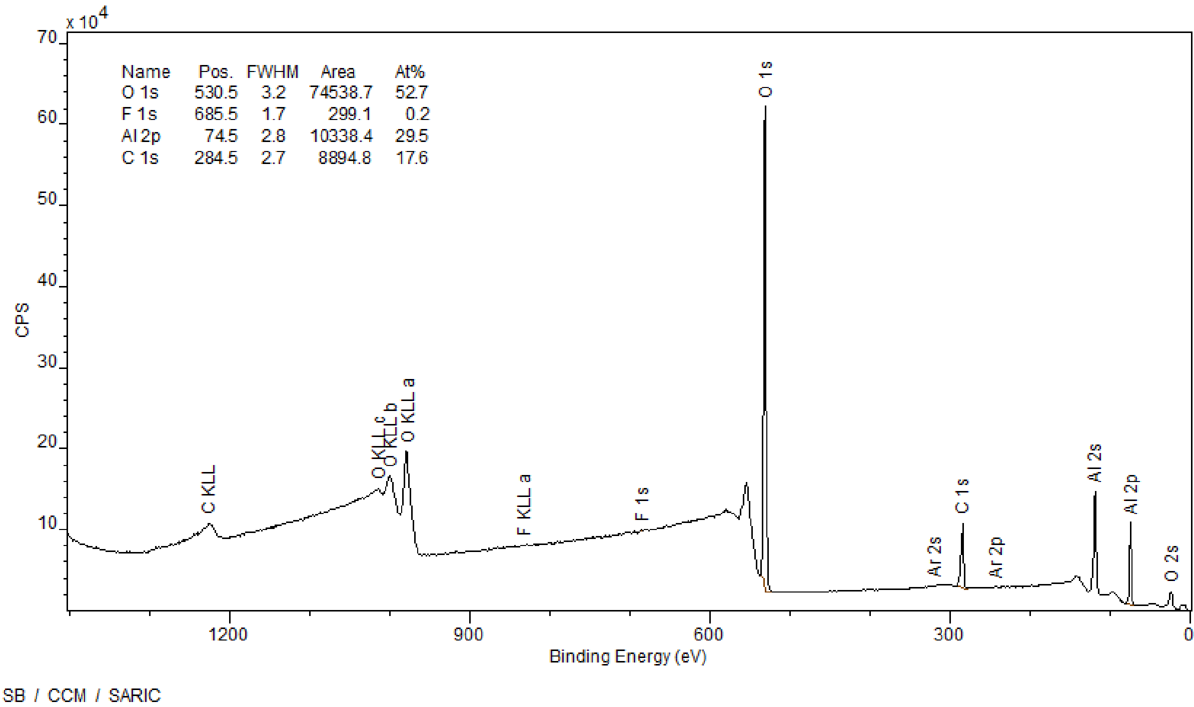

Figure 4. 4 XPS characterization of ALD deposited aluminum oxide

For the sensing application, stoichiometry of the sensing film and the level of purity (contaminants) constitute the major parameters [39]. On the XPS characterization result presented above on Fig. 4.4, very good stoichiometry (1.78) of aluminum oxide is obtained. The major contaminant observed on the result is carbon which can also come from the environment during the XPS characterization. Hence, the ALD deposition of the sensing film gave very good level of the requirement.

The sensing film deposition was followed by an HD-4104 deposition, patterning and curing. This deposition and patterning of the passivation layer before patterning and etching the sensing film was made to combine the two metal deposition and patterning steps required for the control gate and for the source (S), drain (D), back gate (BG) contacts. The passivation layer could alternatively be made with a thick (around 1.2 µm) silicon oxide layer. However, HD-4104 was chosen over SiO_2 for its equivalent passivation performance obtainable at lesser process steps. Unlike in SiO_2, in the case of HD-4104 there is no need neither for PECVD or PVD deposition nor for etching.

After curing the HD-4104, the patterning and etching of the aluminum oxide is made to open the source, drain, and back gate contacts. At this step, metal deposition and patterning is carried out for the combined extension of the source, drain, and back gate contacts, and for the control gate.

Finally passivation layer is deposited and patterned to delimit the sensing area from the rest of the sensor's surface. The summarized process flow is presented diagrammatically on figure 4.5 below.

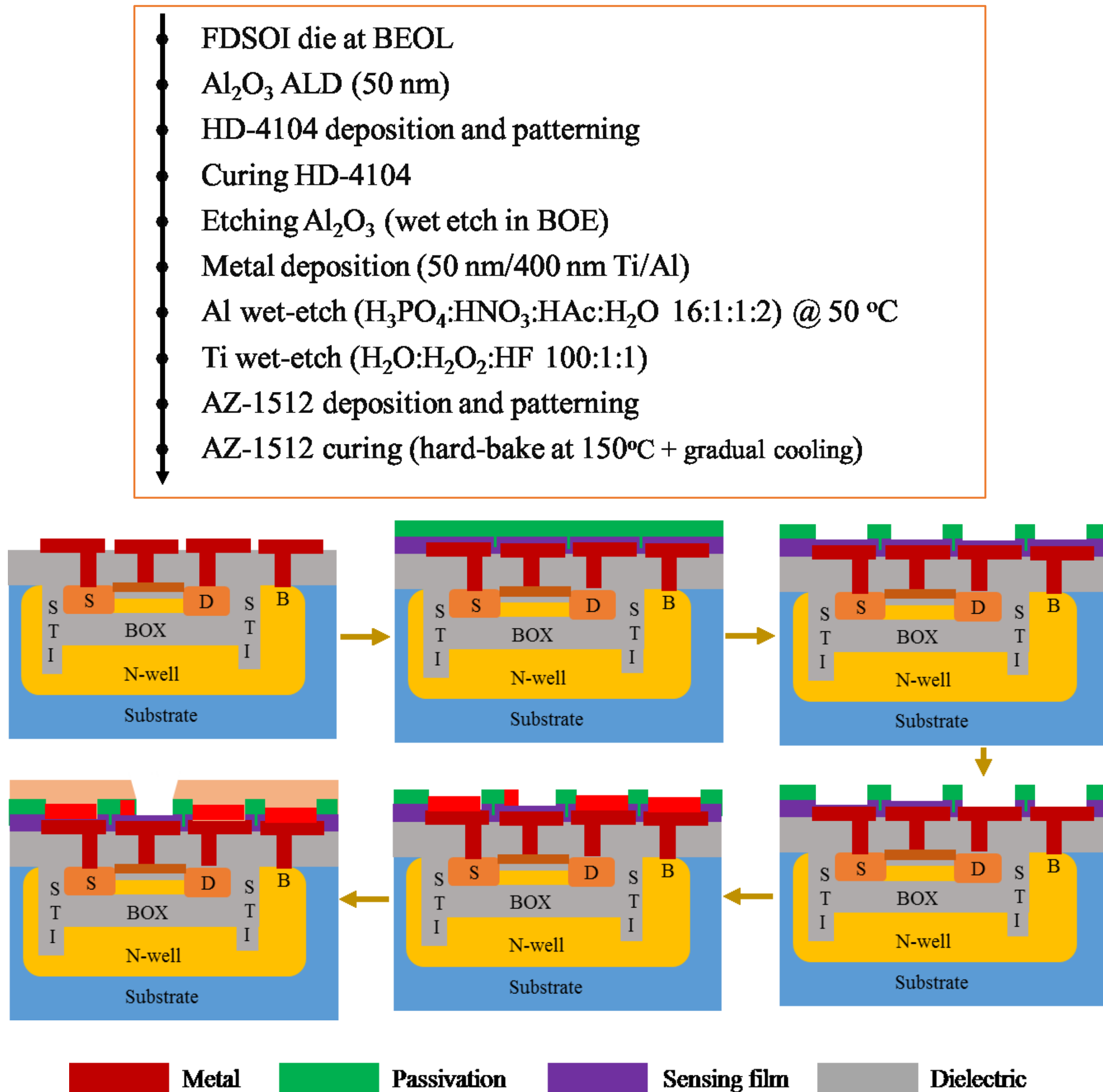

Figure 4. 5 Process flow for integration of the pH sensors in the BEOL [203]

The top down schematic diagram of the sensor which is integrated following the above process flow is presented hereunder on figure 4.6. The extended electrical connection pads are 5 mm away from the sensing

zone which gets covered by the pH solution during characterization. This is sufficient spacing considering the area of nearly 1 mm radius which is usually covered by the pH droplet.

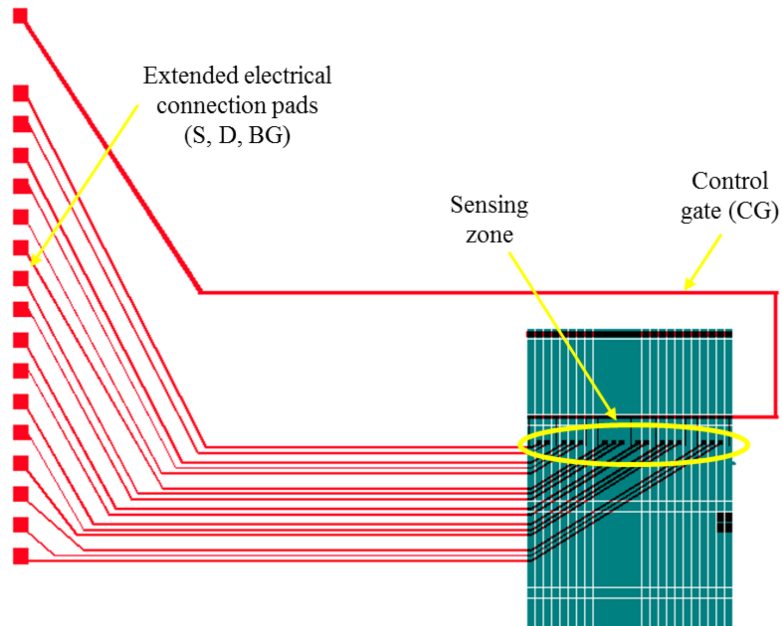

Figure 4. 6 Top down schematic diagram of the sensor

4.3.2 Mask Design

With the space constraint for the metallic extension and droplet coverage, only 9-transistors which constitute a single row of 25 pads were chosen for the integration of the pH sensing. The overall layout of the mask with the 9 sensors, on a (2.5 cm x 2.9 cm) die looks like below on figure 4.7. All the mask designs have been carried out using CleWin 5.1 layout editor, of version 5.1.1. Not only the basic structures of the sensors and the alignment marks, but also verniers and resolution keys were included in the mask design.

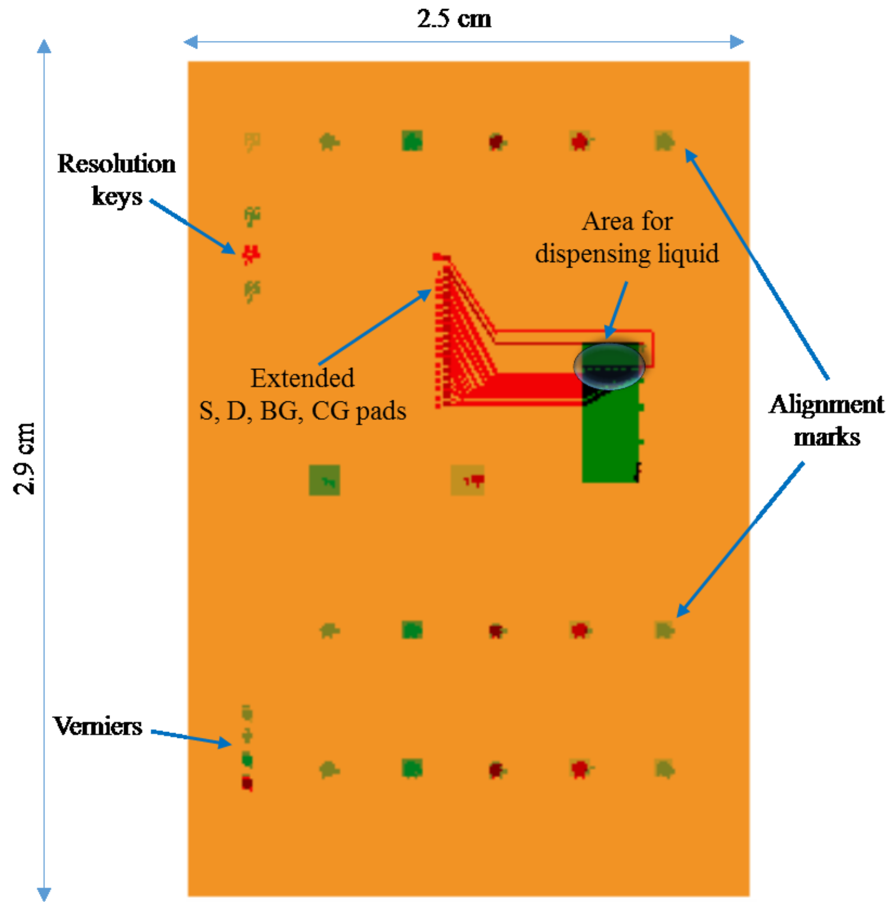

Figure 4. 7 Overall layout of the mask

The area of the metallic pads and their horizontal and vertical spacings were measured using optical microscope at several magnifications, for better accuracy. Figure 4.8 below shows the optical image taken during measurement of the dimensions and spacing of the pads.

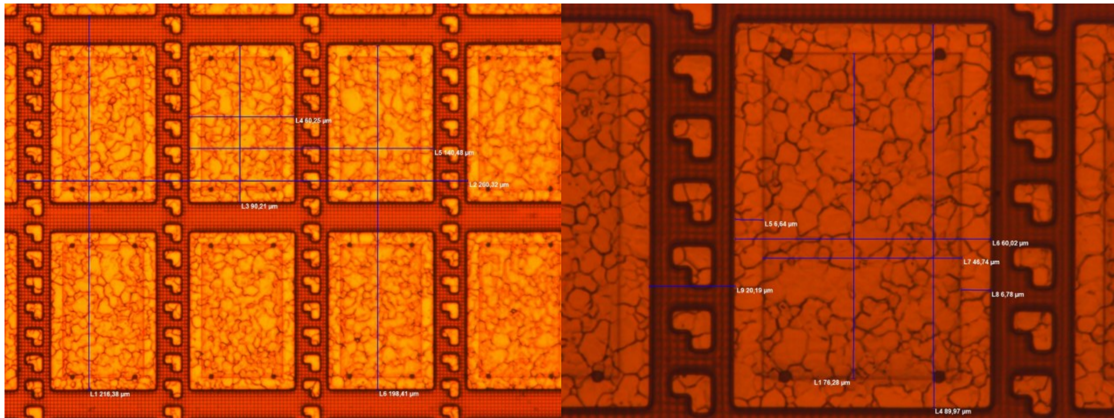

Figure 4. 8 Optical measurement of the dimensions and spacing of the pads at 20X (left) and 50X (right) magnifications

From these measurements, each pad had (60 µm x 90 µm) area, with a horizontal and vertical spacing of 20 µm and 18 µm respectively. This measurement is very important not only for partitioning of the pad into sensing gate and control gate areas, but also to accurately locate the designed mask structures on the selected rows of transistors.

The sensing gate – control gate design looks like below, shown on figure 4.9. As described in the modeling and simulation of the sensor, the control gate capacitance should be much smaller than the sensing gate capacitance for reducing the sensitivity attenuation introduced by the capacitive divider circuit. Therefore, the width of the control gate is set to be 10 µm, considering the alignment accuracy and precision of the process steps also. Consequently, the length of the control gate is shortened from 70 µm to 64 µm instead of decreasing further the width below 10 µm.

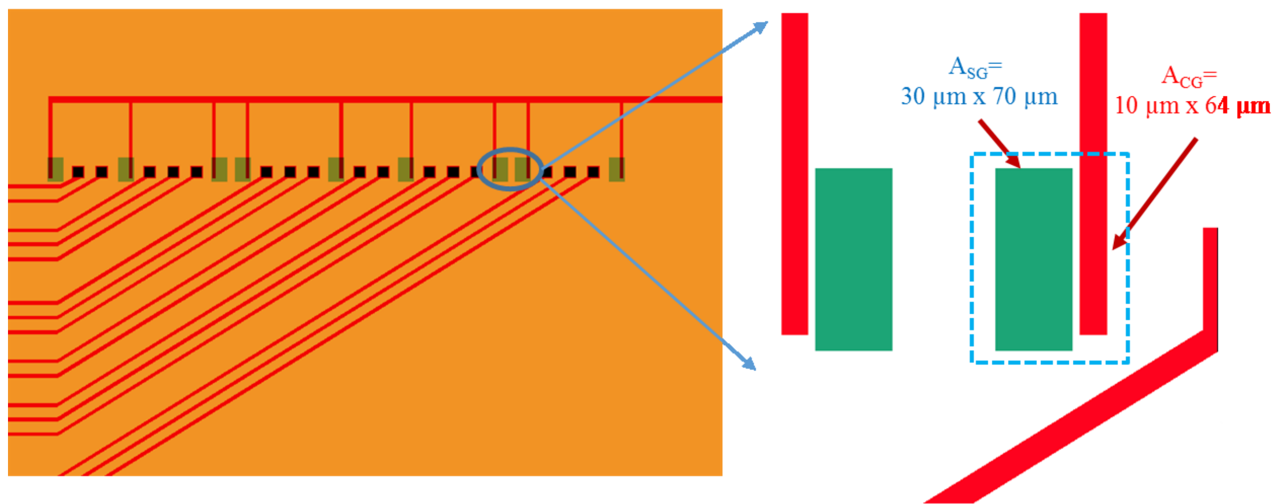

Figure 4. 9 Layout and dimensions of the sensing gate and the control gate

4.3.3 Fabrication Process

The fabrication process of the sensors starts with atomic layer deposition of the sensing film, which is aluminum oxide, on an acetone-IPA-DI water cleaned die. The deposition recipe of the aluminum oxide is given below on table 4.1 for a 50 nm ALD deposition of aluminum oxide.

Table 4. 1 Deposition recipe of the ALD aluminum oxide

Parameter	Description	Parameter	Description
GPC (Å/cycle)	1	Purge time	3 s
Boost	non	Prec. Temperature (°C)	18
Temp. TE2 (°C)	10	Carrier gas	200 sccm
Stabilization time	10 minutes	IMS	400
Precursor 1	TMA	Line 1 (TEMAHF)	50
Pulse time	100 ms	Line 2 (SAM.24)	50
Purge time	2 s	Line 3 (H_2O)	200
Prec. Temperature (°C)	amb	Line 4 ($TiCl_4$)	50
Carrier gas	150 sccm	Line 5 (TMA)	150
Precursor 2	H_2O	Line 6 (NH_3)	50
Pulse time	100 ms	Line 7 (O_2)	80

This is followed by coating and patterning of HD-4104, a self-priming, negative tone, photo definable, polyimide precursor [204], for passivating the active parts on the die's surface. As this resist is highly viscous, the dispensing was made gently followed by half a minute of waiting before starting to spin. This helps for bubble free coating of the HD-4104. Then the spin coating was made at a speed of 4000 rpm for 60 seconds. The acceleration was 500 rpm for 5 seconds. A soft bake was employed at 90°C for 90 seconds, followed by 100°C for another 90 seconds. The exposure step had a broadband exposure for 20 seconds at 12 mW/cm^2 intensity. The developing step consisted of an immersion in PA-401D for 50 seconds, a rinse in PA-400R for 15 seconds, drying with nitrogen gun, and finally a 2-minutes of cleaning with oxygen plasma at 100 W. The purpose of the plasma cleaning is for removing residual resists which may remain on the developed areas. The optical image of the samples at this step, with openings for source, drain, gate, and back gate pads is provided below on figure 4.10.

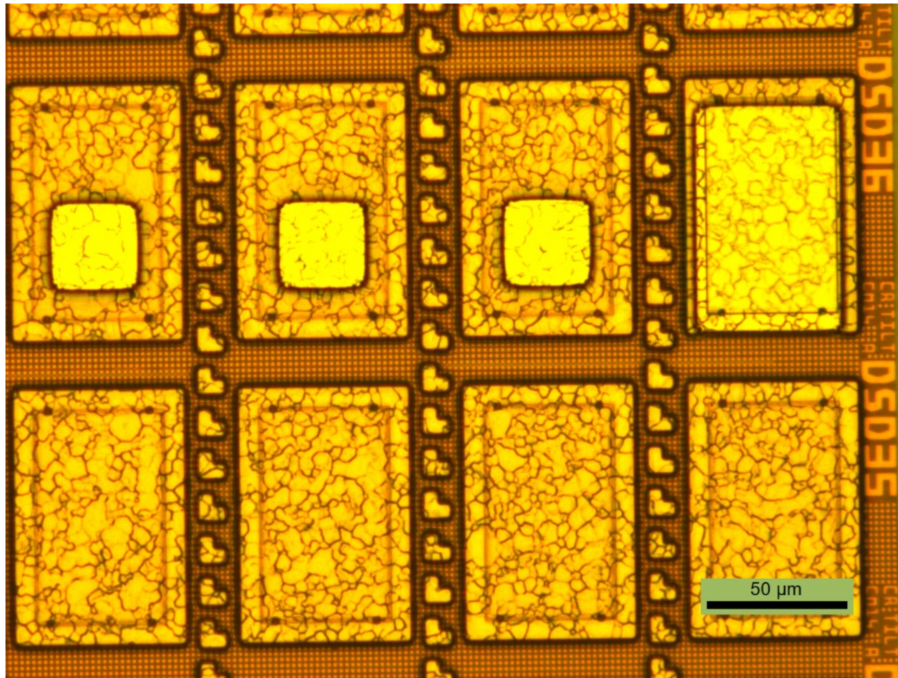

Figure 4. 10 Optical image of the sensor after UV-1: opening for S, D, G, BG pads

At this stage, the samples are ready for curing of the deposited and patterned HD-4104. The requirement of the curing, which should be performed in nitrogen environment, is for removing residual solvents and photosensitive ingredients. It is also important for completing the imidization and the adhesion processes. The temperature profile of the curing process is depicted below on figure 4.11.

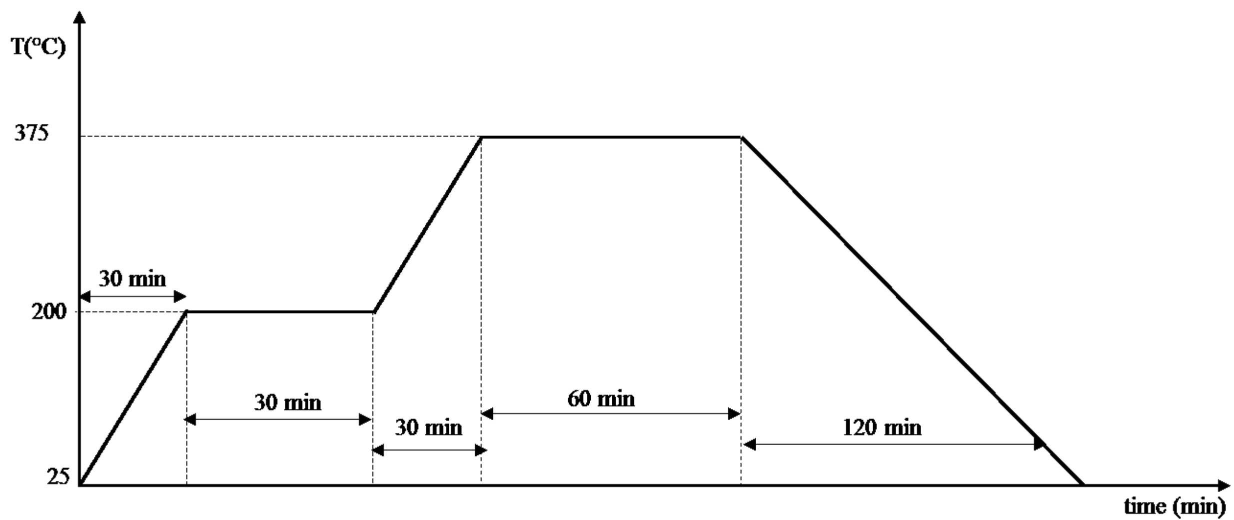

Figure 4. 11 Temperature profile of the HD-4104 curing process

After completion of the curing step, etching of the aluminum oxide was carried out to open for metal contact of the source, drain, and back gate metallic pads. The positive photoresist AZ 1512 was employed for the photolithography patterning. This resist was chosen for its great adhesion to the substrate which is suited for the wet etching processes, optimum film thickness (1.2 µm at 4000 rpm), compatibility with common developers and strippers, and broad process parameter window [205].

The resist was coated on the samples at a speed of 4000 rpm for 30 seconds, with an acceleration of 1000 rpm for 3 seconds. The soft bake is done at 100 °C for 50 seconds. Then the samples were exposed for 15 seconds at an intensity of 12 mW/cm^2. The developing step was made with an immersion in MF319 developer for 45 seconds, followed by a 15-minutes of rinsing in deionized (DI) water, and drying with nitrogen gun. Finally, a post bake at 115 °C for 50 seconds, and cleaning in oxygen plasma at 100 W for 2-minutes was carried out. This process is summarized on table 4.2 below.

Table 4. 2 Photolithography process with AZ1512 photoresist

Process	Description
Spin-coating	At a speed of 4000 rpm for 30 seconds, with an acceleration of 1000 rpm for 3 seconds
Soft bake	at 100 °C for 50 seconds
Exposure	Intensity (broadband) = 12 mW/cm^2, for 15 seconds
Develop	Developer: MF319 (immersion) for 45 seconds, followed by a 15-minutes of rinsing in deionized (DI) water, and drying with nitrogen gun
Post bake	115 °C for 50 seconds
Plasma cleaning	100 W for 2-minutes

Following the patterning, the aluminum oxide was etched in buffered oxide etch (BOE) 6:1. The etchant was chosen considering the optimum etching rate and the very good selectivity of the oxide with respect to the underlying aluminum metallic pads. It took between 30 and 45 seconds to etch the 50 nm of atomic layer deposited aluminum oxide. Etching rates on different batches of samples have been determined from a calibration with the dummy samples.

Striping of the resist has been done employing immersion in Microposit™ remover 1165 at 65°C for 5-minutes followed by a cleaning in acetone/IPA/DI water for 2-minutes in each solvent. At last plasma cleaning has been added at 100 W for 2-minutes.

Soon after completion of the cleaning, to reduce the growth of native oxide on the aluminum metal pads, Ti/Al metal deposition was made with a sputtering machine. As the die has hills and valleys of ±1.2 μm, the Ti adhesive layer had a thickness of 50 nm so that it could easily adhere to the steps. For reliable conductivity, the deposited aluminum layer was 500 nm thick. The recipe for deposition of the Ti/Al metal layer is provided below on table 4.3.

Table 4. 3 Deposition recipe of Ti/Al deposition by sputtering

Parameter	Description	Parameter	Description
Layer 1		**Layer 2**	
Target	Ti	Target	Al
Duration	33 minutes and 20 seconds	Duration	2:00 hours
Thickness	50 nm	Thickness	500 nm
Power	100 W	Power	150 W
Pressure	2.9 mTorr	Pressure	8.3 mTorr
Mode	RF	Mode	DC
Gas	Argon	Gas	Argon

The photolithography patterning has been undertaken with the same procedure as described on table 4.1 for etching the Ti/Al layer. The top metallic layer, which is aluminum, was etched with a commercial Al-etch [206] that has a composition of (H_3PO_4:HNO_3:HAc:H_2O 16:1:1:2), at 50°C. The 500 nm of Al layer was etched in 1 minute and 30 seconds. The etching rate of this step is however very sensitive to stabilization of temperature, so that it needs nearly 10 minutes of waiting (while heating the solution on hot plate) to obtain stable etch rate. Next to the Al-etching, etching of the adhesive Ti layer was made in a highly diluted Ti-etch chemical [206], which is given by (H_2O: H_2O_2: HF 100:1:1). The 50 nm Ti is completely etched in 10 seconds at this level of dilution. Finally, striping of the resist has been done employing immersion in Microposit™ remover 1165 at 65°C for 5-minutes followed by a cleaning in acetone/IPA/DI water for 2-minutes in each solvent. 2-minutes of plasma cleaning at 100 W is also made.

At the end of this step, extension of electrical connections for the source, drain, and back gate of the transistor is achieved. The process flow was designed in such a way that the control gate is also obtained at

this step combined with the source, drain, and back gate extension. The optical image of the sensor at the end of this process step is depicted on figure 4.12.

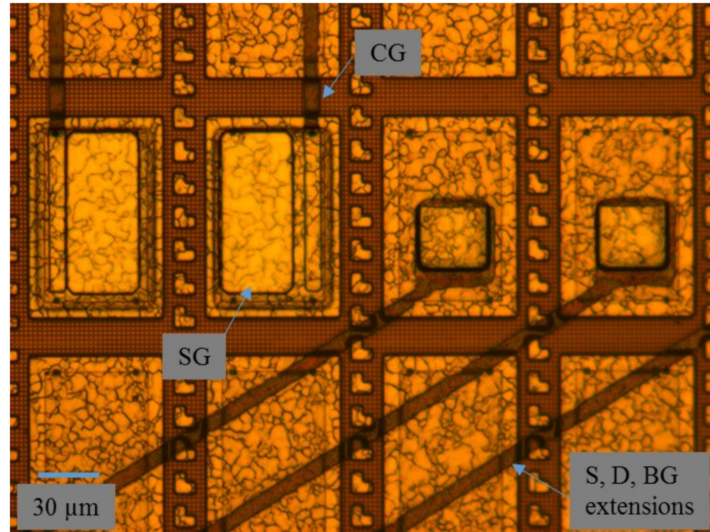

Figure 4. 12 Optical image of the sensor at the end of Ti/Al deposition and patterning (SG is the sensing area, also called sensing gate; CG is the control gate)

The last process step is passivation─ to protect the die's surface from the liquid environment except the sensing area. Therefore, this is achieved with a photoresist deposition, patterning and curing. Negative resists are preferred for this purpose as they have cross-linking molecules during the curing process which help for more chemically strong (inert) passivation. Since the fabricated mask was positive tone (dark field) intended for AZ-5214E resist, AZ-1512 resist was used for the passivation as the first one was not available in the laboratory. The same photolithography process was employed as in table 4.2. At the end of the photolithography, however, the resist was cured with a hard bake at 150°C for 5-minutes followed by a gradual cooling. The optical image of the sensor with all process steps completed looks exactly like figure 4.12 above since the resist is transparent. On figure 13 below, SEM cross sectional image of the fabricated sensor is provided.

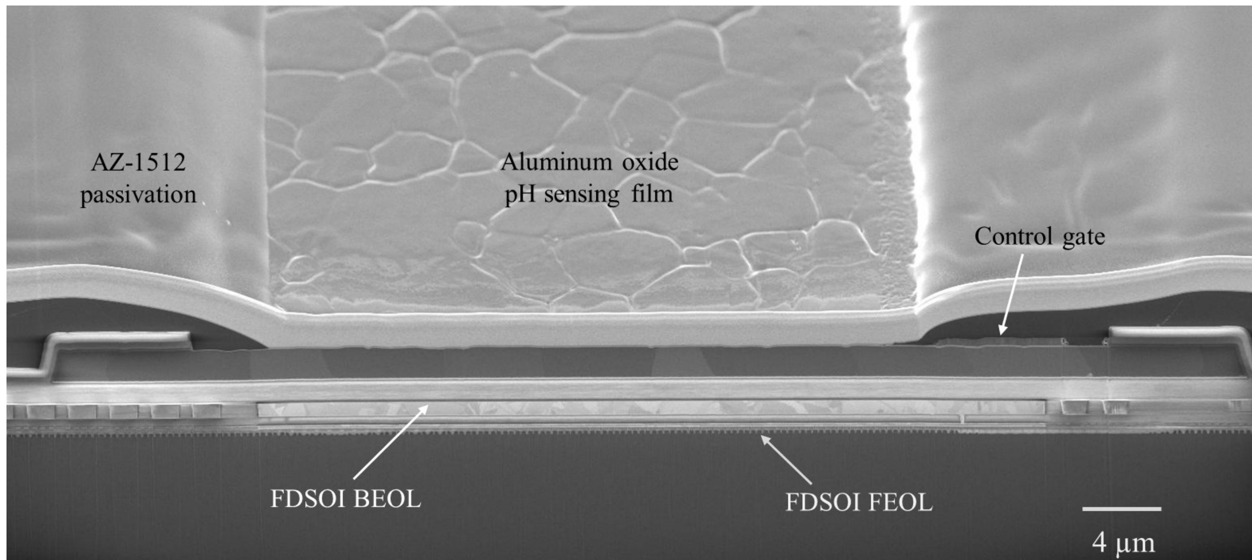

Figure 4. 13 SEM cross sectional image of the sensor

The outline of the fabricated sensors that are ready for characterization, with the optical image as an inset and a pH droplet dispensed on the sensing area is provided below on figure 4.14. Each sensor has a sensing area of (29 μm x 70 μm).

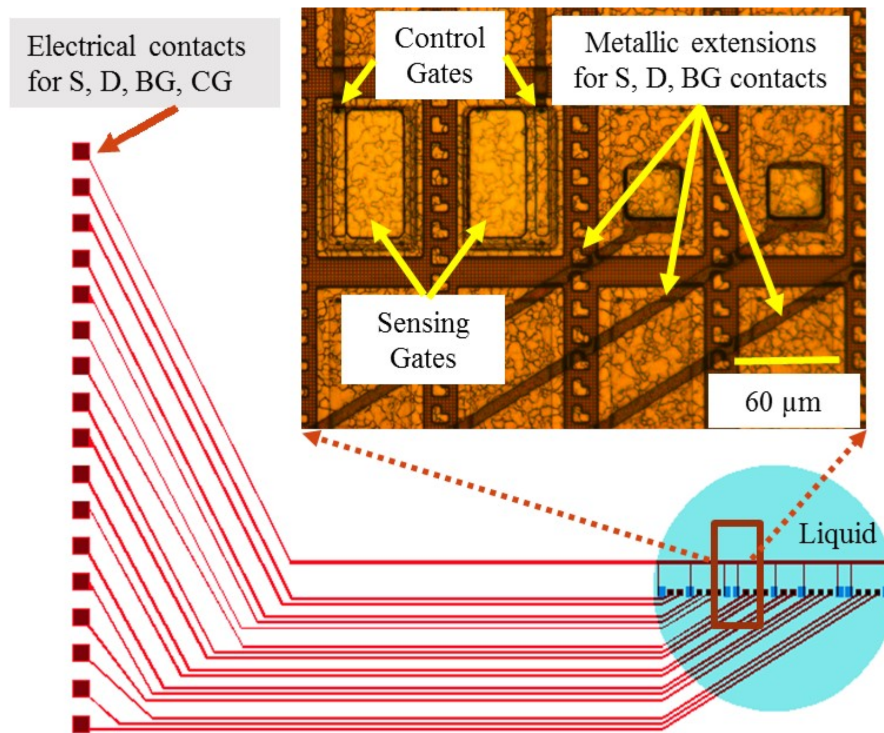

Figure 4. 14 outline of the fabricated sensors, with the optical image as an inset and a pH droplet dispensed on the sensing area [38]

4.4 Fabrication of Mixed-type Sensors on a Die

The fabrication process discussed in section 4.3 provided a successful first test of the proposed pH sensor. However, as the passivation layer at the last process step was not suited for longer period characterizations, revisions were made on the mask design. In the process, changes have been introduced not only on this last mask, but also on the dicing of the wafer and on the types and number of sensors per die. Therefore, in this section, we describe the new design, process flow and fabrication process in which the number of sensors is increased from 9 to 36 per die. Moreover, sensors are developed on both LVT and SLVT PFET and NFET devices. 18 of the devices are designed to be able to sense the pH either of at the sensing gate or at the protection diode. Figure 4.15 shows the modified dicing scheme.

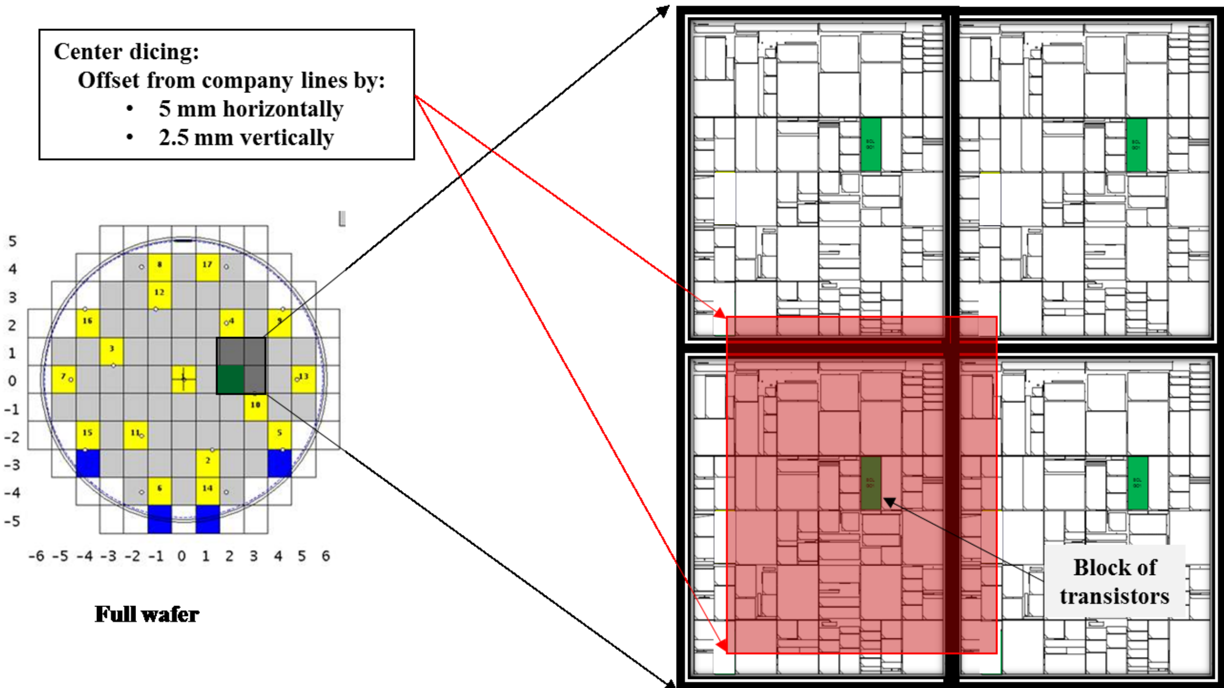

Figure 4. 15 The modified dicing scheme to place the block of transistors at the center of the die

Placing the desired block of transistors at the center of the 2.5 cm x 2.9 cm die, we have now much more space for extending the source, drain, and back gate pads of more devices. Additionally, there is also space to enlarge sensing areas of some sensors.

Figure 4.16 below shows the selected four rows of transistors, and outline of resulting sensors on the surface of the die. Sensing areas of DSD-04 and DSD-42 rows are extended away, while sensing areas of DSD-20 and DSD-36 rows of sensors are integrated directly on top of the gate pad. In addition, sensors based on DSD-04 and DSD-42 transistors have additional sensing functionality through the gate protection diode.

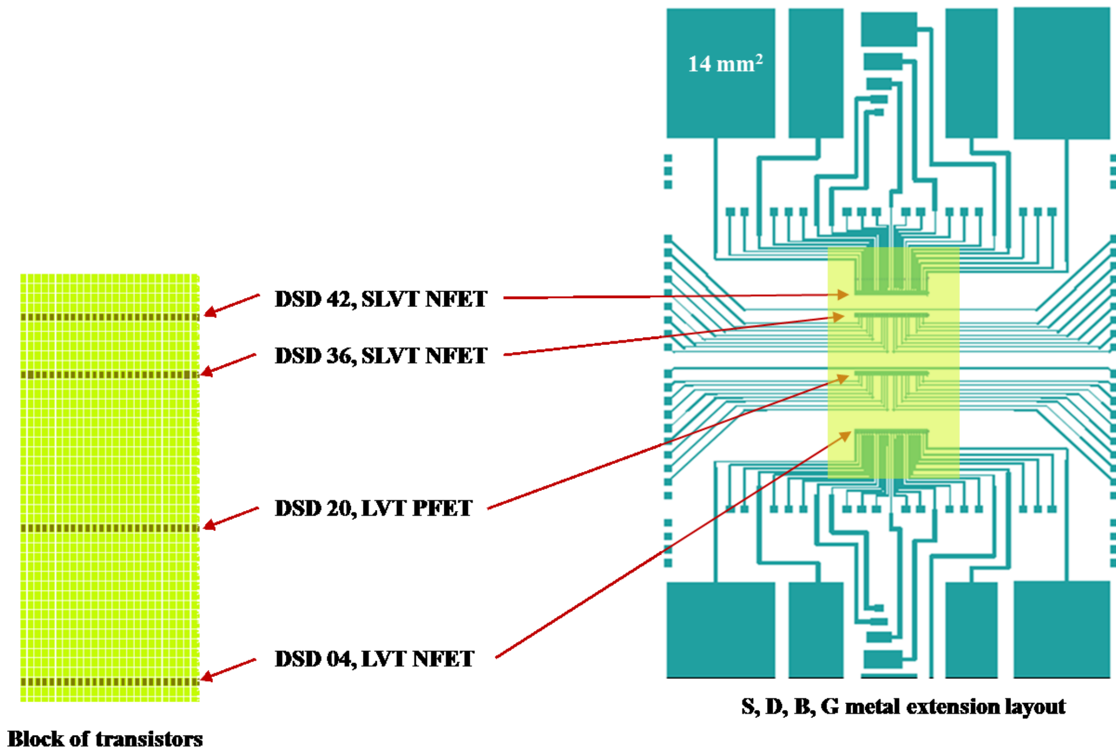

Figure 4. 16 The selected rows of transistors (left), and outline of sensors on the surface of the die (right)

4.4.1 Process Flow

In this revised design, the fabrication process starts with passivation of the die's surface except the source, drain, gate, back gate and diode contacts of the 36 transistors selected for fabrication of the sensor. A cured HD-4104 is utilized for the passivation which was attained following the same patterning and curing procedures as described in section 4.3 of this chapter. This is followed by metallic deposition and patterning for extending the source, drain, back gate and diode pads of the transistors. The gate pads of DSD-42 and DSD-04 transistors were also extended at this process step in order to obtain larger sensing areas. The third process step comprises physical vapor deposition (PVD) of aluminum oxide for the sensing film, and etching only from the electrical contacts. At the fourth step, control gate has been deposited and patterned. The last process step was passivation, in which HD-4104 was patterned and cured. Therefore the sensor is passivated with a cured HD-4104 except the sensing areas and electrical connection points. The process flow is summarized diagrammatically as follows on figure 4.17 and figure 4.18.

- FDSOI die at BEOL
- HD-4104 deposition and patterning
- Curing HD-4104
- Metal deposition (50 nm/500 nm Ti/Al)
- Al wet-etch (H_3PO_4:HNO_3:HAc:H_2O 16:1:1:2), Ti wet-etch (H_2O:H_2O_2:HF 100:1:1)
- Al_2O_3 deposition (sputtering)
- Etching Al_2O_3 (wet-etch in BOE)
- Metal deposition (50 nm/500 nm Ti/Al)
- Al wet-etch (H_3PO_4:HNO_3:HAc:H_2O 16:1:1:2), Ti wet-etch (H_2O:H_2O_2:HF 100:1:1)
- HD-4104 deposition and patterning
- HD-4104 curing

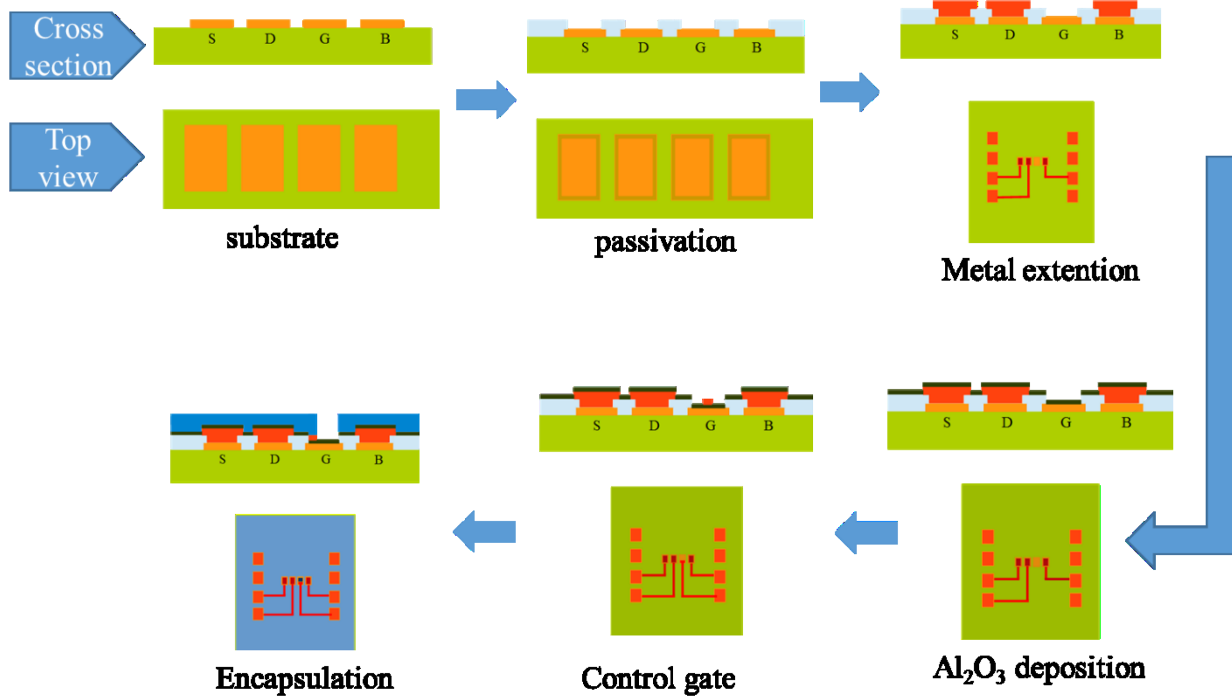

Figure 4. 17 Process flow indicating the integration of pH sensor in the BEOL.

In this new approach of fabricating mixed types of sensors, a single set of process flow cannot illustrate the fabrication steps. This is because the cross section at the different sensor types is different even after the same process steps. For this reason two process flows are employed for description of this fabrication

process. Figure 4.18 shows the summarized process flow, indicating the top view and the cross section of the sensors across the pads.

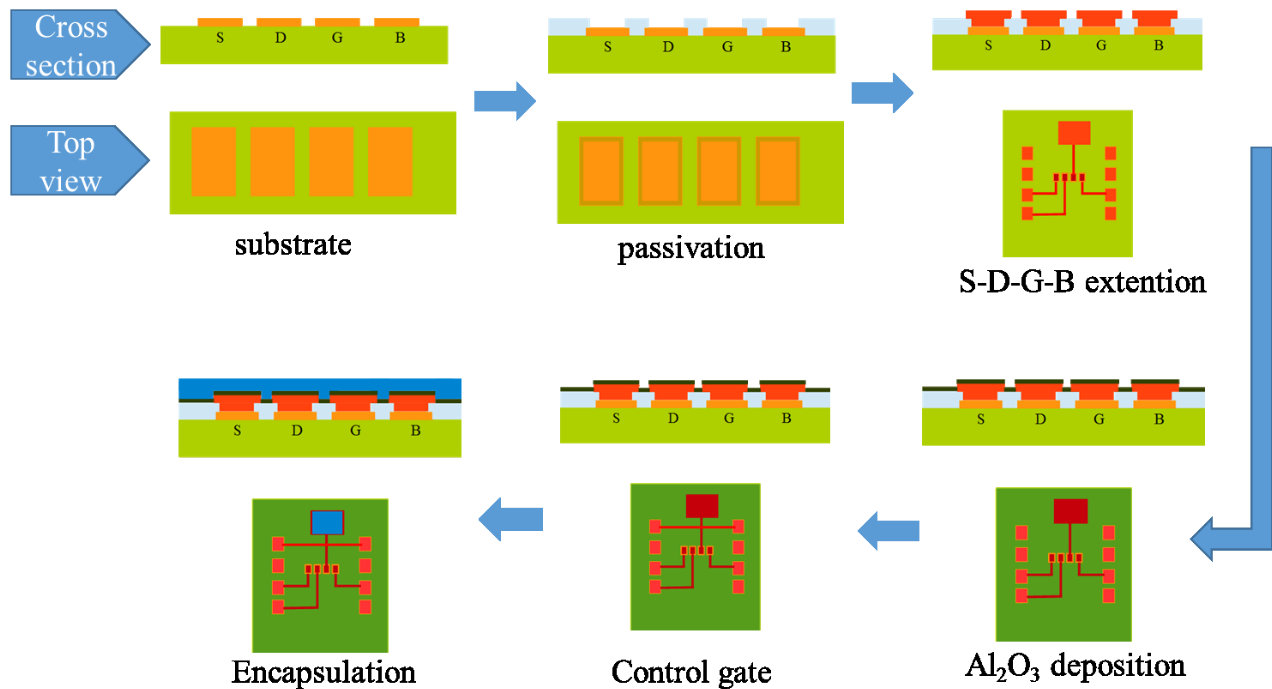

Figure 4. 18 Process flow indicating fabrication of the pH sensor with extended sensing area

4.4.2 Mask Design

The overall outline of the new mask is given below on figure 4.19. A pair of alignment marks, for each process step starting from second process, are included at the top and bottom of the mask. A backup pair of the same alignment marks are also added at the right and left parts of the mask. In addition, resolution keys and verniers are included for each process step.

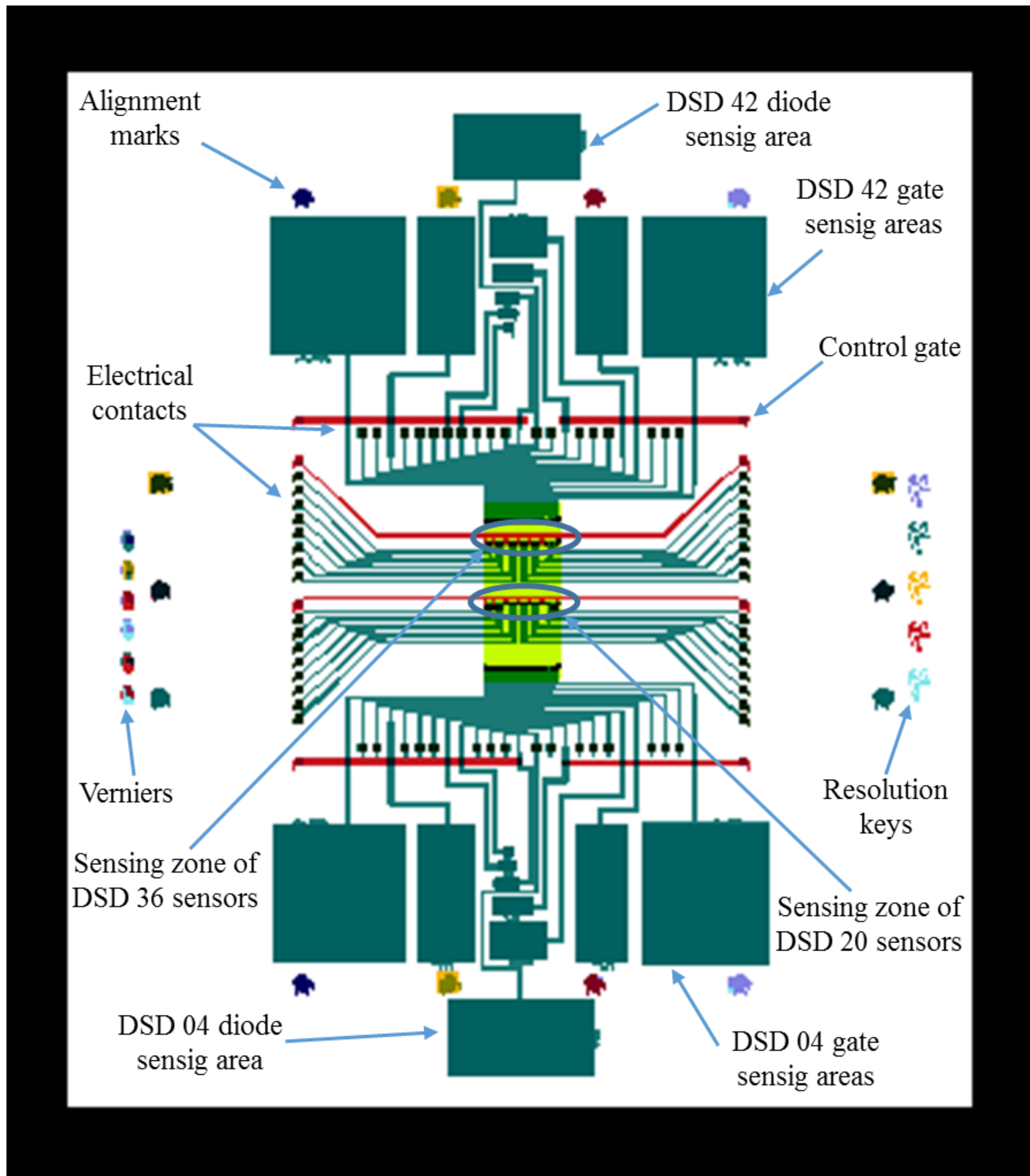

Figure 4. 19 Overall outline of the mask

The first mask, used for pad-opening from the passivation, is designed as a negative tone (bright field) mask. Alignment of this UV-1 process was made with the existing pad structures of the die whose dimensions were already measured and known. At the end of UV-1 process, alignment marks are inscribed on the sample for the next process steps.

The mask for UV-2 is used for extending the source, drain, gate, back gate, and diode pads. The gate and diode pads are extended for obtaining larger sensing areas. Unlike in the case of the process employed for

the integration of the 9-sensors per die, which is discussed in section 4.3, the control gate deposition and patterning is processed separately (not combined with the source, drain, and back gate extension).

The mask for the third process step is utilized for patterning and etching aluminum oxide from the electrical contacts (extended source, drain, and back gate contacts).

The control gate deposition and patterning comes at the fourth (UV-4) process step in this design. For the DSD-04 and DSD-42 sensors whose sensing gates are extended, a single control gate is designed which passes on top of the gate extension line. But for DSD 20 and DSD 36 sensors, the control gate is applied individually on top of each sensor's floating BEOL gate metal. Modification of the control gate design so that it lies along the shorter width of the pad helps to reduce further the control gate capacitance. This in turn is important for decreasing the attenuation factor introduced by the capacitive divider circuit as discussed in chapter 3. Figure 4.20 shows the control gate-sensing gate outline of the sensors that are directly integrated on top of the BEOL metal.

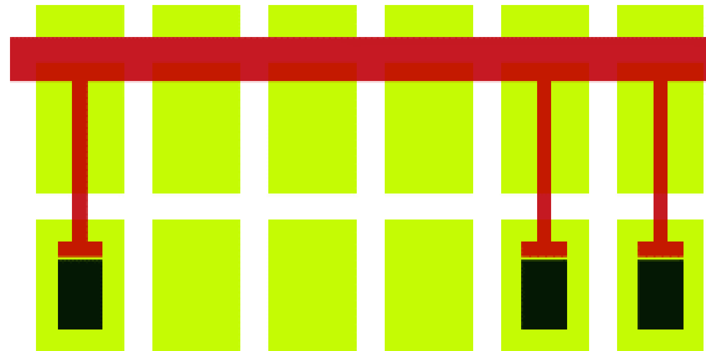

Figure 4. 20 Layout of the control gate and sensing gate of BEOL integrated sensors (red: control gate, black: sensing area)

In contrary, the control gate for DSD 04 and DSD 42 sensors is applied as shown below on figure 4.21. A metallic bar passes on top of the extension metallic lines (which goes from the BEOL gate metal to the extended sensing area). Between the control gate metal and the gate extension metals, there is the sensing film which serves as the dielectric for this capacitive structure.

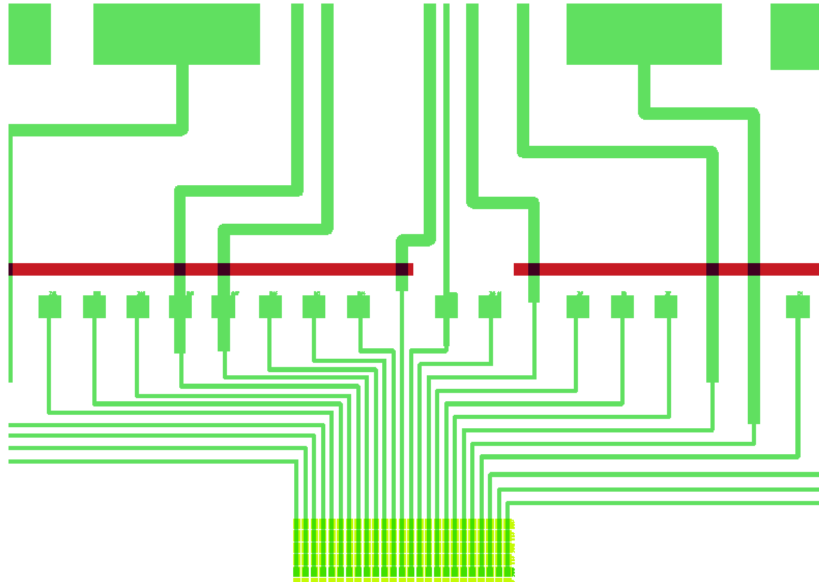

Figure 4. 21 The control gate design of the extended gate sensors

The mask for the last process step (UV-5) is used for opening the sensing areas and the electrical contacts from the passivation layer.

4.4.3 Fabrication Process

The fabrication starts with passivation of the die's surface except the source, drain, gate, back gate and diode contacts of the 36 transistors chosen for developing the sensors. The passivation was done with a cured HD-4104. The patterning and curing procedure is the same as described in section 4.3 of this chapter. Optical image of the sensor after HD-4104 patterning and curing is shown on figure 4.22 below.

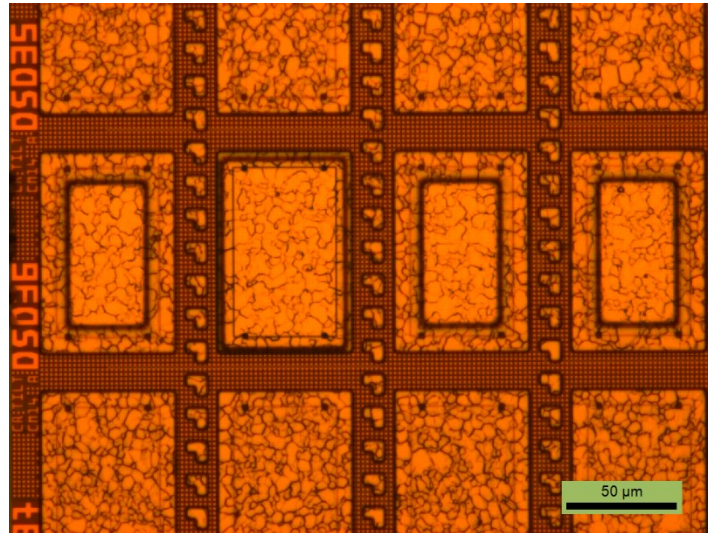

Figure 4. 22 Optical image of the sample after pad opening (UV-1)

The larger opening of the second pad of DSD-36 is for better alignment of the first process step with the existing pads of the die. It wouldn't affect the performance of the sensor as this pad is a drain contact and the area of pad opening wouldn't introduce changes.

The deposition of 50 nm/500nm Ti/Al metal was pursued following the passivation step. The deposition and patterning of the metal layer is the same as the one described in section 4.3. The same deposition parameters as indicted on table 4.2 have been followed. Optical image of the sensor after this step is shown below on figure 4.23.

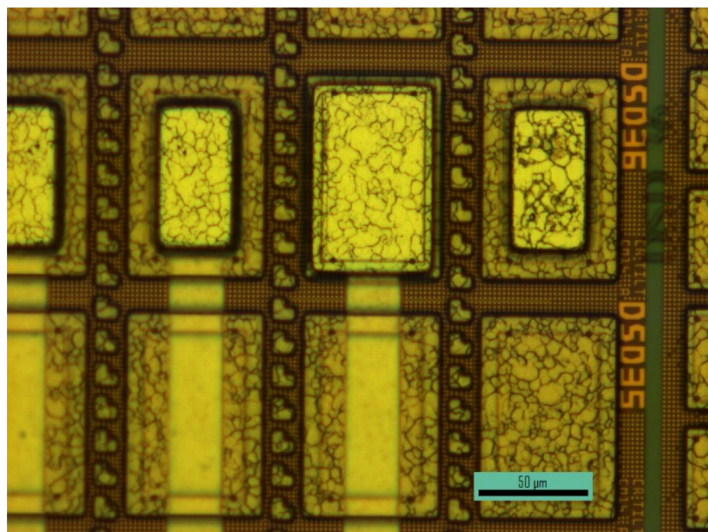

Figure 4. 23 Optical image of the sample after UV-2 for metallic extension

Next to this, deposition of the sensing film was carried out. In this case, the pH sensing aluminum oxide was deposited by sputtering. The change of the deposition method from ALD to sputtering is because of the incompatibility of the passivating HD-4104 with the ALD machine. The sputtering deposition parameters are provided hereunder on table 4.4.

Table 4. 4 Deposition parameter of the PVD deposited aluminum oxide

Parameter	**Description**
Target	Al_2O_3
Duration	2:00
Thickness	50 nm
Power	80 W
Pressure	2.4 mTorr
Mode	RF
Gas	Argon

Cross checking the stoichiometry and level of contamination of the aluminum oxide deposited by sputtering with that of the ALD deposited oxide, very close similarity is obtained. Figure 4.24 below shows an XPS characterization result of the aluminum oxide deposited by sputtering.

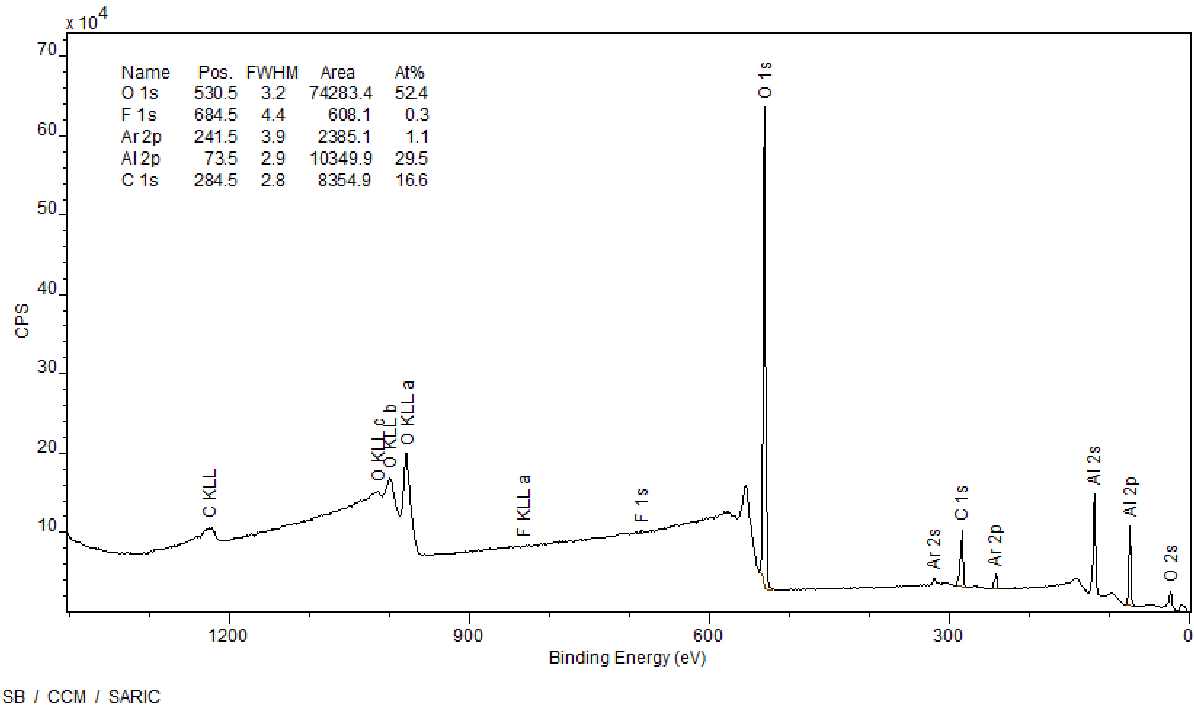

Figure 4. 24 XPS characterization of the aluminum oxide deposited by sputtering

The etching of the aluminum oxide was carried out utilizing buffered oxide etch (BOE) 6:1. After this step, deposition and patterning of the control gate followed. Figure 4.25 shows the optical image of the sensor at this stage.

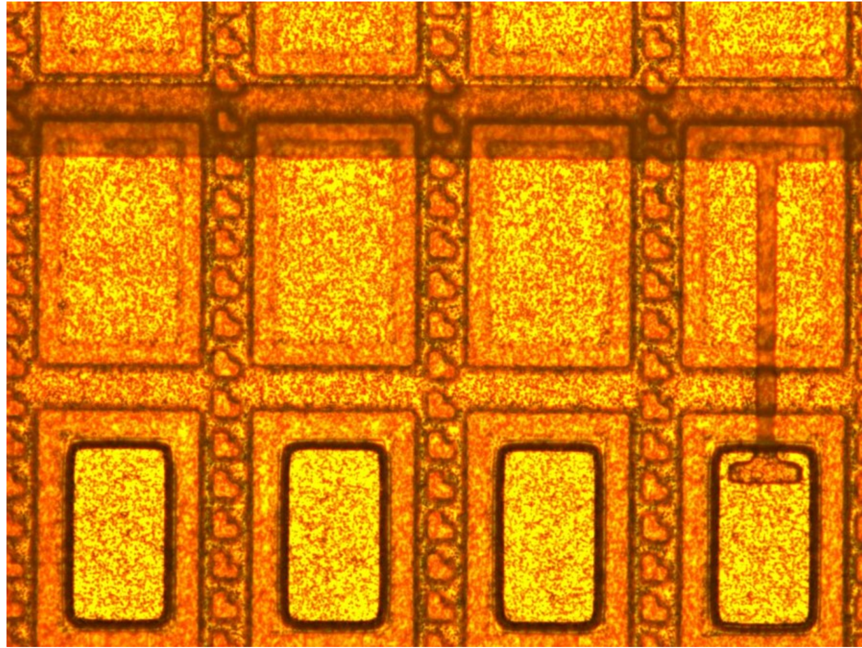

Figure 4. 25 Optical image of the sensor after control gate deposition and patterning (UV-4)

At last, passivation of the sensors surface was accomplished with a cured HD-4104. As in the case of sensors described in section 4.3, this passivation layer serves for protection of the sensors' structures from the liquid environment. Consequently, only the sensing areas and the electrical contacts are exposed, the rest passivated by a cured HD-4104. Figures 4.26 and 4.27 present the top down SEM images of the fabricated sensors which are ready for characterization.

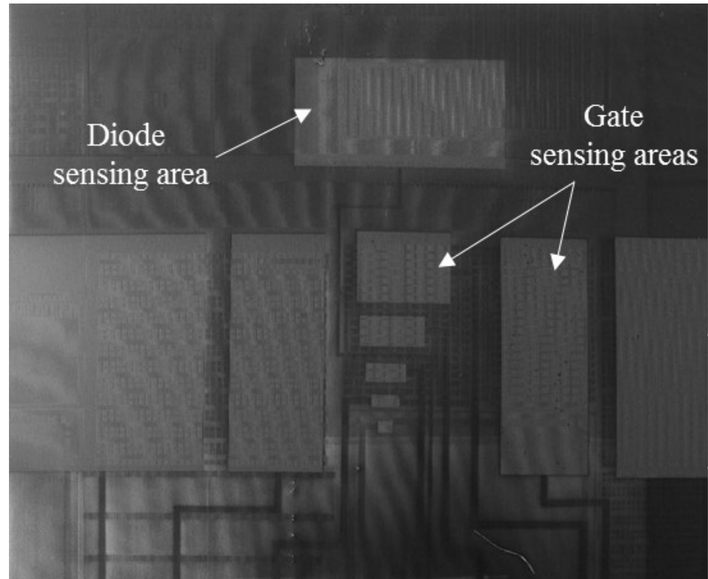

Figure 4. 26 Top down SEM image of the mixed type sensors in the vicinity of extended sensing areas

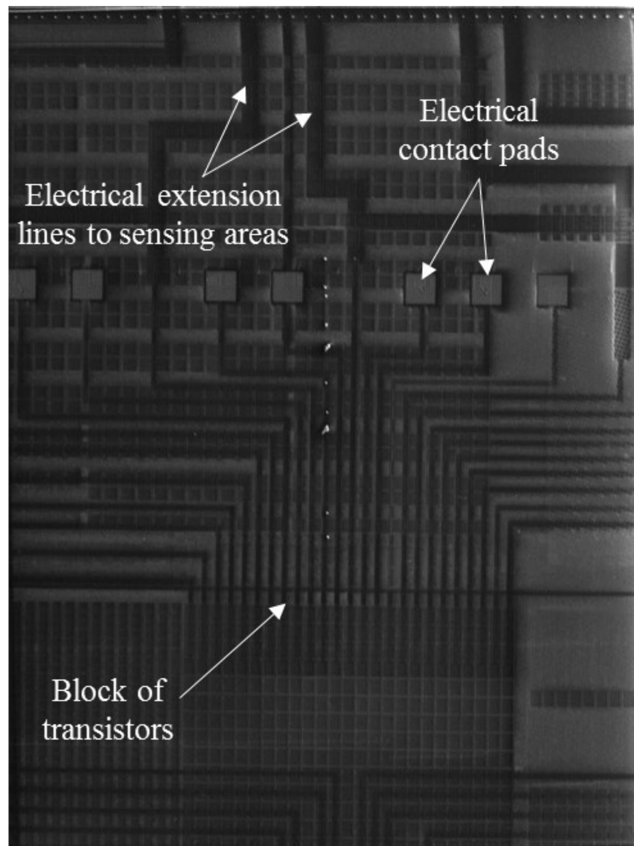

Figure 4. 27 Top down SEM image of the mixed type sensors in the vicinity of electrical contacts

4.5 Conclusion

Fabrication of the pH sensors, using industrial UTBB FDSOI transistors in the back end of line, has been successfully carried out both as a proof of concept extended gate sensor, and direct integration of the sensing functionality using capacitive divider circuit.

The simplified fabrication of the extended gate sensor is very important for quick proof of concept demonstration of the proposed new approach. The reduced process steps on top of the sensing film provide cleaner surface for the sensing purpose. External electrical connections between the sensing component and the transistor are required only during characterization of the sensor.

The fabrication process, for integration of a pH sensor in the BEOL of UTBB FDSOI, has been performed on a general purpose die. It has been accomplished in a small number of process steps employing different techniques such as using HD-4104 instead of silicon oxide passivation, and combining similar processes of different level processes.

Fabrication of sensors that can perform the pH sensing at the front gate (with a capacitive divider circuit) and at the gate protection diode has also been successfully achieved with a merged process flow, using the same set of masks.

CHAPTER FIVE

CHARACTERIZATION

The fabricated sensors, both in the proof of concept extended gate approach and in the back end of line of the UTBB FDSOI transistors, have been characterized for the main figures of merit such as sensitivity, response time, stability and repeatability. In the proof of concept sensors, however, more emphasis has been paid to sensitivity and repeatability, planning broader measurements on the final prototype of the sensor which is the sensor integrated in the back end of line.

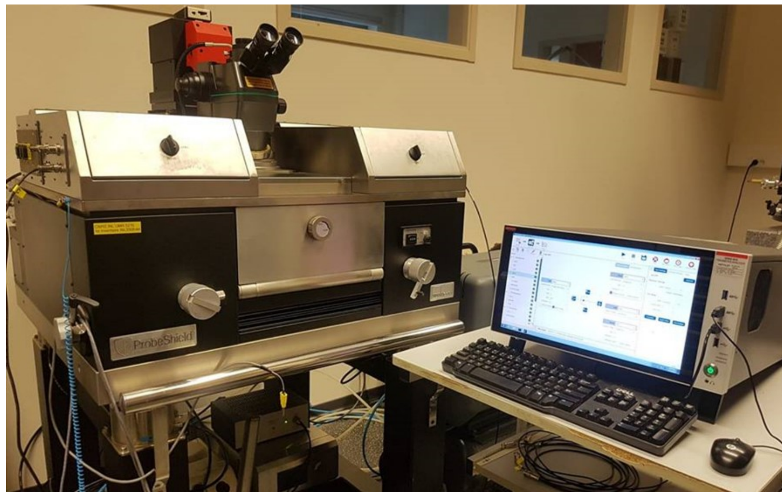

Figure 5. 1 The characterization bench

All tests were carried out in a laboratory of regulated atmosphere and temperature (20 °C). The electrical probe station has a chamber that can be closed isolating the test samples from ambient light. The electrical characterization bench, the SUSS Microtec probing station run by the Keithley 4200 semiconductor analyzing instrument, is shown above on figure 5.1.

5.1 Figures of Merit

The sensor's figures of merit are the parameters which indicate the sensor's performance from different perspectives. A large number of definitions of these parameters have been produced by different stakeholders, but somehow are harmonized by international organizations such as IUPAC, ISO, and IEC [207]. Some of the most important figures of merit selected for the description of the developed pH sensors are discussed below.

a. Sensitivity

In a more general sense, sensitivity can be defined as the slope of the linear fit for a given number of data pairs forming a linear calibration curve [208]. Specifically, for solid state pH sensors, the sensitivity is defined as the change in threshold voltage per unit change in pH value. For fixed bias operation of the sensor, the sensitivity can be described as the change in drain current per unit pH change.

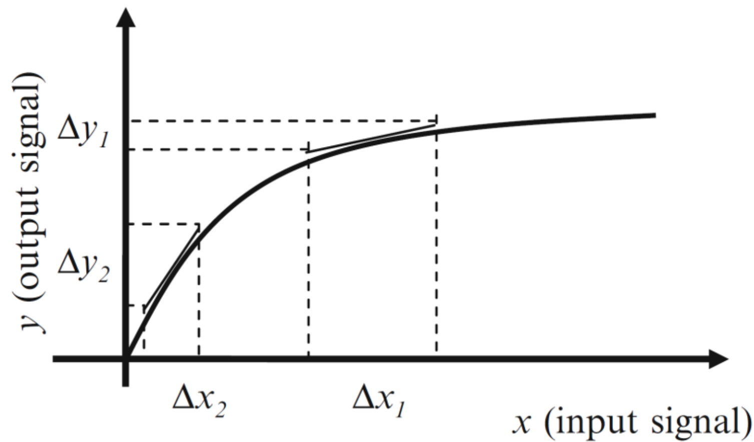

Figure 5. 2 Calibration curve of a sensor [209]

As can be seen on figure 5.2, the sensitivity is determined from the slope of the calibration curve, which is the ratio of the change in the output signal to an incremental change in input signal. The sensitivity may not be uniform throughout the operating range of the sensor. For instance, figure 5.2 depicts a higher sensitivity in the vicinity of ΔX_2 than that of ΔX_1. An ideal sensor has a uniform and high sensitivity in its operating range [209]. The parameter describing such uniformity of the sensitivity is called the linearity of the sensor. In other words, linearity of the sensor can be observed from the closeness of the calibration curve to a straight line.

b. Response time

With the highly growing demand and application of sensors in modern age, real time measurements are highly desirable. Response time defines the sensor's capability for such real time signal acquisition. It can also be a factor for the throughput of an analytical processing facility. The response time is itself defined as the time elapsed between the dispensing of the analyte onto the sensing film and the moment when the

sensor's output attains a practically constant value [9]. Chemical sensors demonstrating response times of less than 1-minute are generally considered as very good sensors.

c. Selectivity

This is perhaps the most critical feature of a sensor as it should, at least to an acceptable level, respond only to a specific analyte. Selectivity can be defined as the extent to which, in a given procedure, other substances affect the determination of a substance according to a given procedure [210]. Nonetheless, poorly selective sensors can be assembled into an array with an appropriate data processing, for measurement of several analyte concentrations. Although specificity is used by some authors as a synonym to selectivity, there are also authors who consider specificity as an ultimate selectivity, designating it as an absolute term [9].

d. Stability

Stability of a sensor is rather a broad concept dealing with the degree to which sensor characteristics remain constant over time [211]. Change of output in relatively longer time, which is also known as drift, is one type of stability issue. Drift can arise from property degradation of the sensing element due to prolonged exposure to analyte medium, or from aging of components. As a result, the stability of the sensor can be evaluated from drift characteristics.

e. Repeatability

Repeatability is used to evaluate the ability of the sensor to provide consistent results under the same circumstances, within short intervals of time [212]. In [210], repeatability is defined as the closeness or agreement between the results of successive measurements of the same measurand on identical test portions carried out under defined conditions.

Repeatability is closely related to precision which describes the capability of the sensor to give the same response when repetitively measuring the same measurand under the same conditions [209]. On the other hand, the capability of the sensor to provide the same result under different measurement conditions is referred at as reproducibility. For instance, if characterization of a sensor provides the same outputs when performed by different operators or at different laboratories, it is said to be reproducible.

f. Resolution

Resolution of a sensor is the capacity to measure splitted individual components of a composite signal [207]. Equivalently, it can also be defined as the smallest change of the sensor's stimuli which can produce a detectable change in sensor's output. In [209], resolution, also called as discrimination, is defined as the minimal change of the measurand that can produce a detectable change in the output signal. Given the fact that resolution is strongly limited by noise, we can evaluate the resolution from the sensitivity of the sensor and the signal to noise ratio of the sensor's output.

g. Accuracy and Precision

Accuracy of a sensing system may refer to accuracy of the measurement or accuracy of the measurement instrument. The former shows the closeness of the agreement between the result of a measurement and a true value of the measurand (VIM:1995), while the later indicates ability of a measuring instrument to give responses close to a true value [213].

Precision on the other hand represents the capacity of a sensor to give the same reading when repetitively measuring the same measurand under the same conditions. The precision is a statistical parameter and can be assessed by the standard deviation (or variance) of a set of readings of the system for similar inputs [213]. Figure 5.3 below shows the two parameters using an analogy with game of darts.

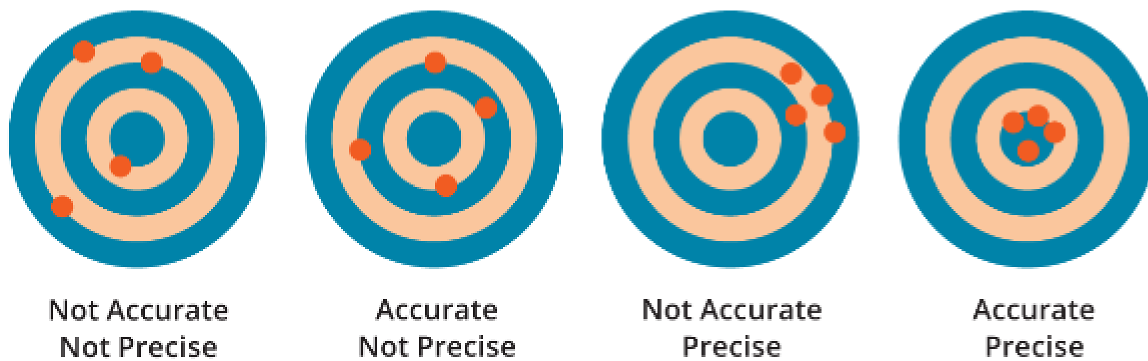

Figure 5. 3 Illustration of accuracy and precision using analogy with game of darts [214].

h. Hysteresis

This is a limiting factor on the accuracy of the sensor, yielding different outputs depending on the history of the sensor's operation. For example, in the case of pH sensing, hysteresis is the change in measured result

at the same pH value, but depending on the previous pH to which the sensor was exposed. For instance, the response of an ISFET at pH 9 is different when the measurement is taken just after pH 7 and after pH 10 if the sensor has hysteresis behavior. Figure 5.4 presents the hysteresis characteristics of a sensor.

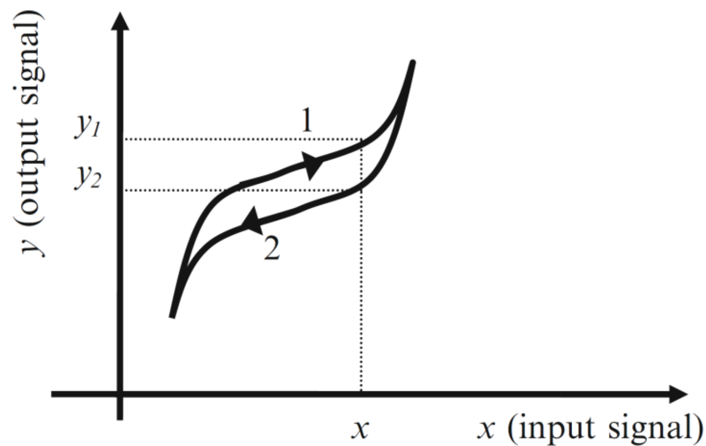

Figure 5. 4 Illustration of hysteresis behavior of a sensor [209]

5.2 Characterization Protocol

Characterization of both the transistors and the sensors was carried out using a SUSS MicroTec probstation, run by keithley 4200 semiconductor characterization system, under the Keithley Interactive Test Environment (KITE). This bench can measure current and voltage as small as few tens of femto amperes (fA) and micro volts (µV) respectively.

The characterization protocol is designed with a consideration of two very important constraints. The first constraint is that the bench can characterize, either of I-t or I-V test, only 1-device at a time. The second constraint is concerning the sensors that are integrated in the BEOL. In these devices, the sensing area of one sensor is 80 µm away from that of its neighboring sensor on the die. However, the smallest measurable pH solution spans an area in the order of millimeters. This poses a constraint towards systematic measurement of several sensors on the same die.

Dispensing of the pH solution (droplet) on the sensing area of the pH sensor was performed utilizing a micropipette. Upon completion of the measurement at a certain pH solution, removal of the solution from the sensing area was also made using micropipette. Depending on the level of droplet wetting (spreading to the electrical contacts), a 1 or 3 time wash has been carried out with the upcoming pH (pH of next solution for measurement), during the pH change.

The sensors were cleaned with acetone-isopropanol-deionized water and dried with nitrogen, and stored upon completion of the fabrication process. The characterization of the sensors was then made off-the-shelf, without any conditioning process of the sensing film. This is a very important performance achievement compared to literature reports in which the sensing film is conditioned by immersing the sensors in water for 12 hours and longer before starting the pH test [215], [216].

The main parameters (figures of merit) chosen for characterization of the fabricated pH sensors are sensitivity, response time, repeatability, resolution, stability (drift), and hysteresis. The protocol followed for evaluation of these parameters is presented below.

a. Sensitivity

The change in pH at the sensing film can be depicted as a change in threshold voltage or as a change in drain current of the transistor at a fixed bias. Since the pH sensitivity of the films are given in terms of surface potentials, more emphasis has been given for determination of sensitivity in terms of threshold voltage change as a function of pH. The protocol employed for such characterizations was:

i. Make electrical connection of the sensor
ii. Dispense the pH solution using micropipette
iii. Take I_D-V_{BG} sweeps at different times until practically repeatable curves are obtained
iv. Remove the pH solution with micropipette
v. Wash the sensing film 3-times with the pH solution of next test
vi. Repeat the same process from step (ii) to step (v), with the pH solution of next test

Fixed bias performance of the sensor is equivalently important since the sensor would finally be embedded in either of fixed current or fixed bias readout circuit. Therefore, for fixed bias sensitivity characterization, the protocol is as follows:

i. Make electrical connection, and apply proper biases to the sensor
ii. Dispense the pH solution using micropipette
iii. Launch the continuous drain current (I_D-t) measurement, and wait until stable output is measured
iv. Remove the pH solution with micropipette
v. Wash the sensing film 3-times with the pH solution of next test
vi. Repeat the same process from step (ii) to step (v), with the pH solution of next test

This second protocol of sensitivity evaluation gives the result as a change in drain current (in decades) for a certain change in pH. In addition to the sensitivity, the response time and stability of the sensor's output can also be observed at the same time.

b. Response time

The response time of the sensors has been measured to the best possible capability of the characterization system. The pH response has been recorded from a continuous drain current (I_D-t) monitoring, so that both the transient and stable drain current measurements have been made during and after dispensing the pH solution onto the sensor. The protocol for determining the response time is presented below.

i. Make electrical connection, and apply proper biases to the sensor.
ii. Launch the continuous drain current (I_D-t) measurement,
iii. Dispense the pH solution while the continuous drain current (I_D-t) measurement is running

c. Repeatability

In the second type of sensitivity measurement (fixed bias sensitivity), it needs to wait until practically stable output is obtained. This is equivalent to until repeatable drain current responses are attained. On the other hand, for sensitivity characterization in terms of shift in threshold voltage, the individual I_D-V_{BG} curves do not have sufficient information about the stability of the response. Therefore, several I_D-V_{BG} sweeps are taken until repeatability is reached.

d. Hysteresis

Hysteresis is one of the most commonly mentioned non-ideality factors of solid state pH sensors. This parameter which shows the offset in measured responses depending on history of the sensor's operation, is characterized with the protocol described here under.

i. Make electrical connection, and apply proper biases to the sensor.
ii. Dispense the pH solution using micropipette
iii. Launch continuous drain current (I_D-t) measurement, and wait until stable output is measured
iv. Remove the pH solution with micropipette
v. Wash the sensing film 3-times with the pH solution of next test

vi. Repeat process (ii) to (v), but with a solution of higher pH
vii. Repeat process (ii) to (v), again with a solution of higher pH (higher pH than step (vi))
viii. Repeat process (ii) to (v), with a solution of same pH as step (vi)
ix. Repeat process (ii) to (v), with a solution of same pH as step (v)
x. Compute hysteresis at pH value of step (vi)

The above protocol can equivalently be done in the reverse order. Instead of evaluating the hysteresis from drain current monitoring (sensing at fixed bias), it can also be determined from a fixed current characterization so that the hysteresis would be expressed in terms of offset in the shift in threshold voltage depending on the sensor's operation history.

e. Drift

This is a gradual change in the output of the sensor while the operating circumstance is maintained the same. Characterization of such a drift behavior can be accomplished following the protocol shown below.

i. Make electrical connection, and apply proper biases to the sensor.
ii. Dispense the pH solution using micropipette
iii. Launch continuous drain current (I_D-t) measurement, and measure the current for the duration of time planned for drift study

Resolution is calculated from the measured sensitivity and signal-to-noise ratio of the sensor's output, therefore there is no specific protocol attributed for resolution measurement. More details on the evaluation of this parameter is provided in section 5.4 of this chapter.

5.3 The Proof of Concept EG pH sensor

The sensitivity characterization of the extended gate pH sensors was carried out at 3- different pH values, but in somehow narrow pH range. The selected pH values of characterization are pH 6, pH 7.3, and pH 8. This characterization range is, however, sufficient for biomedical applications such as acidity monitoring of blood, and pH measurement of saliva [217]. Nevertheless, the sensor can be operated in wider pH range as both the sensing film and the transistor have wide linear operating ranges [45], [183]. Figure 5.5 presents the pH sensing characterization result of the proof of concept extended gate sensor. Since no patterning was employed on the surface of the sensor, the sensing area was equivalent to the area of the pH droplet which was around 4 mm^2.

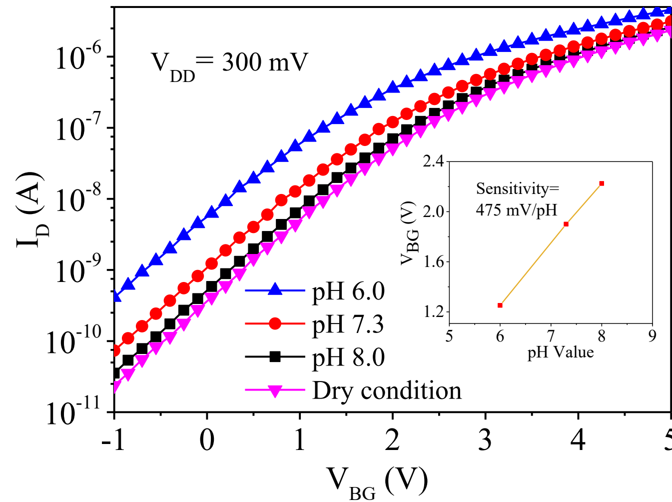

Figure 5. 5 pH sensitivity of the extended gate pH sensor

The extended gate sensor demonstrated a sensitivity of 475 mV/pH which is superior performance compared to state of the art solid state pH sensors. Nonetheless, the measured experimental sensitivity is less than the simulation result (ideally maximum sensitivity) which can be justified by the sub-Nernstian response of the sensing film and the signal loss on the external electrical connections between the transistor and the transduction component.

In addition to the high sensitivity, the very high I_{ON}/I_{OFF} ratio of the UTBB FDSOI industrial transistors provided us with a wide linear operating range and high signal to noise ratio (SNR).

At the different pH values, measurements were repeated to assess repeatability of the sensor's output. From such measurements, very good repeatability results were obtained during the first 3-minutes which is a remarkable performance compared to the work on literature [41] where initial drift was observed for 1 hour. Repeatability of the sensor's response at pH 8 is presented below on figure 5.6.

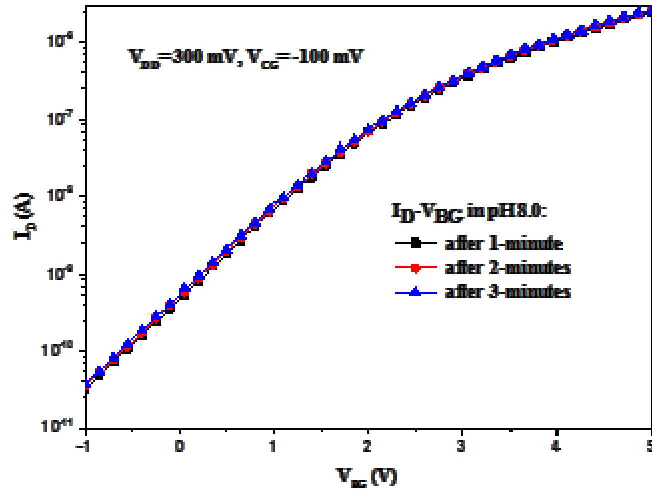

Figure 5. 6 Repeatability of the I_D-V_{BG} characteristics of the extended gate sensor at pH 8

The chronogram of the extended gate pH sensor, which shows the sensor's output as a function of time, is also presented on figure 5.7. Such diagrams are very important as they can depict the sensitivity, response time, repeatability, and stability of the sensor all in one diagram.

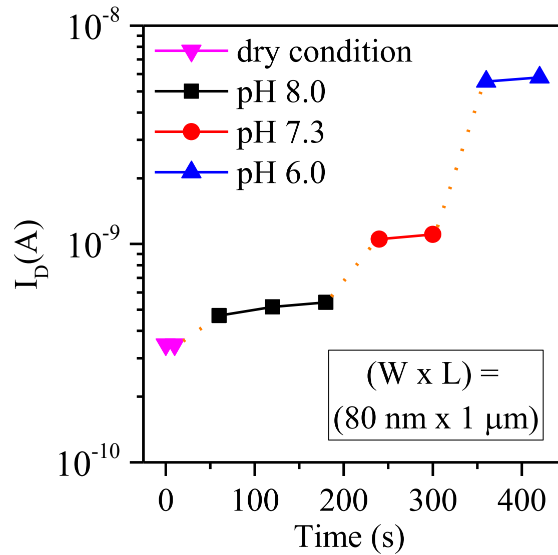

Figure 5. 7 Chronogram of the extended gate pH sensor's response

The performances obtained from the proof of concept pH sensor were so promising to the extent that it even demonstrated superiority over the state of the art. This led us to the integration of the sensor in the back end of line of the UTBB FDSOI devices.

The significance of the capacitive divider circuit, for biasing the sensors through a control gate, is characterized in the proof of concept extended gate pH sensors. The measurement result of the I-V characteristics is provided on figure 5.8 below. Very stable and repeatable characteristics were observed while a bias was applied at the control gate. When the control gate was disconnected (electrically floating), the stability of the I-V characteristics was lost. Therefore, application of a bias at the control gate is crucial for stable operation of the chemical sensors.

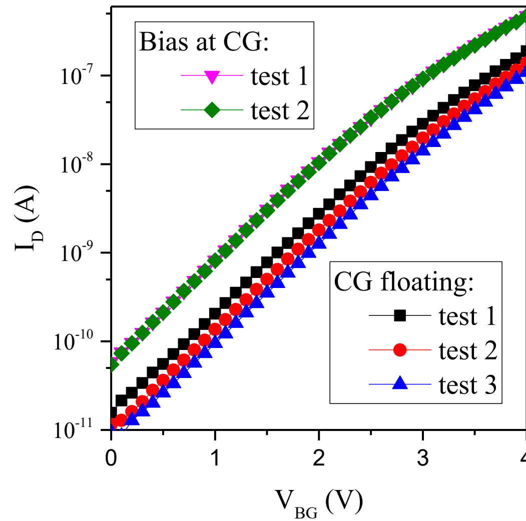

Figure 5. 8 Stability characterization with and without a bias at the control gate

5.4 The Sensor Integrated in BEOL

The pH sensors integrated in the back end of line of the FDSOI transistors were characterized at wider pH range. For sensitivity evaluation in terms of shift in threshold voltage as a function of change in pH, I_D-V_{BG} sweeps were taken at pH 4, pH 7 and pH 10. The measured response of the pH sensors integrated in BEOL is provided below on figure 5.9. These sensors were developed based on FDSOI devices of gate width and length 80 nm and 1 µm respectively. The sensing area was 29 µm x 70 µm.

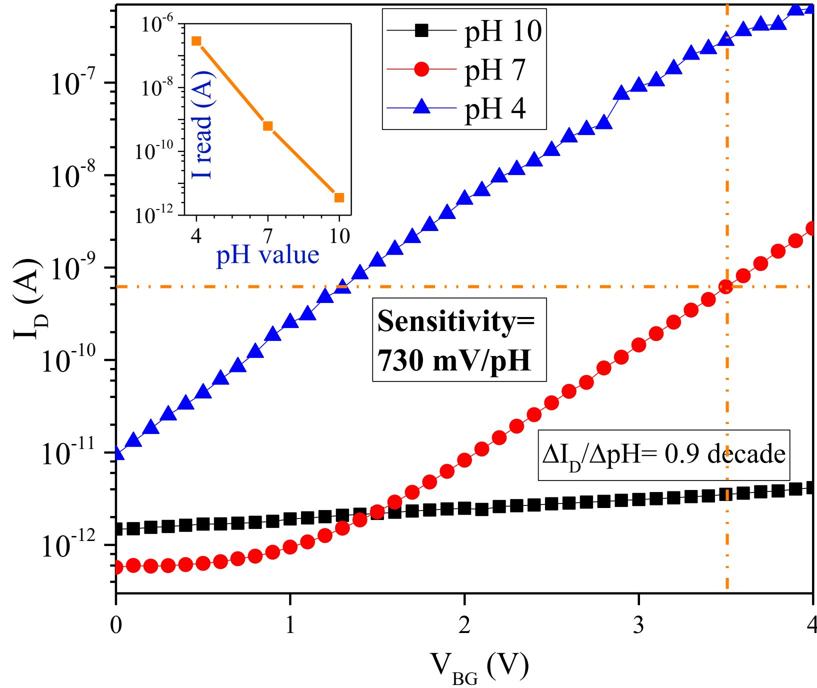

Figure 5. 9 Sensitivity of the BEOL integrated pH sensors

An experimental sensitivity of 730 mV/pH is obtained which is in confirmation with the mathematical model and the simulation result. This is more than 12-times higher than the Nernst limit, and superior to state of the art sensors [59], [74], [75], [77], [78], [218], [219].

The shift in threshold voltage of the sensors as a function of change in voltage at the control gate is also experimentally measured. In confirmation with the mathematical modeling and simulation results discussed in chapter-3, negligible modulation of the threshold voltage through the control gate voltage has been observed. The measurement result of this characteristics is shown on figure 5.10 below.

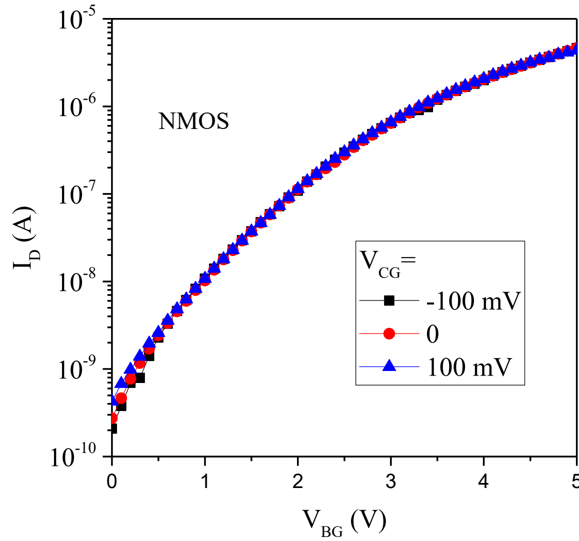

Figure 5. 10 Modulation of the BEOL integrated pH sensors' output through control gate

On the chronogram plot of these sensors, presented on figure 5.11 below, we can observe the fixed bias sensitivity, and repeatability of the output. It gave a fixed bias sensitivity of 0.9 decade/pH at V_{BG}= 3.5 V which is also a remarkable performance.

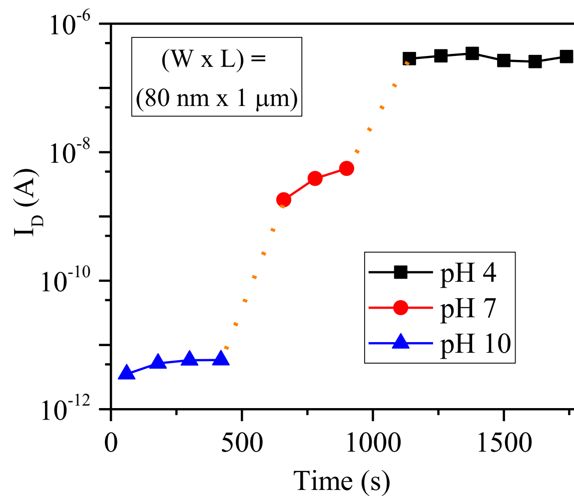

Figure 5. 11 Chronogram of the BEOL integrated sensors' response

The repeatability of the sensor's output at each pH value is depicted on the chronogram diagram of the sensors shown on figure 5.11. Very stable responses are observable at pH values of pH 4 and pH 10. At pH 7 on the other hand, less repeatability is observable. However, during later experiments, such phenomena

are observed sometimes that are expected to arise from external perturbations.

The last passivation process of the BEOL integrated sensors, for protecting the components from the liquid environment, was initially made with a cured AZ-1512 resist. But positive photoresists are not effective for such purposes as they do not have well cross linking molecules as in negative resists upon curing process. After few pH sensing characterizations of the samples, large amount of leakage current was observed on the sensors' pH response. Figure 5.12 shows the test result before and after normalization of the drain current at different pH. The normalization function is to account for the leakage drain current which in this case is a function of both the pH value and the applied voltage at the back gate.

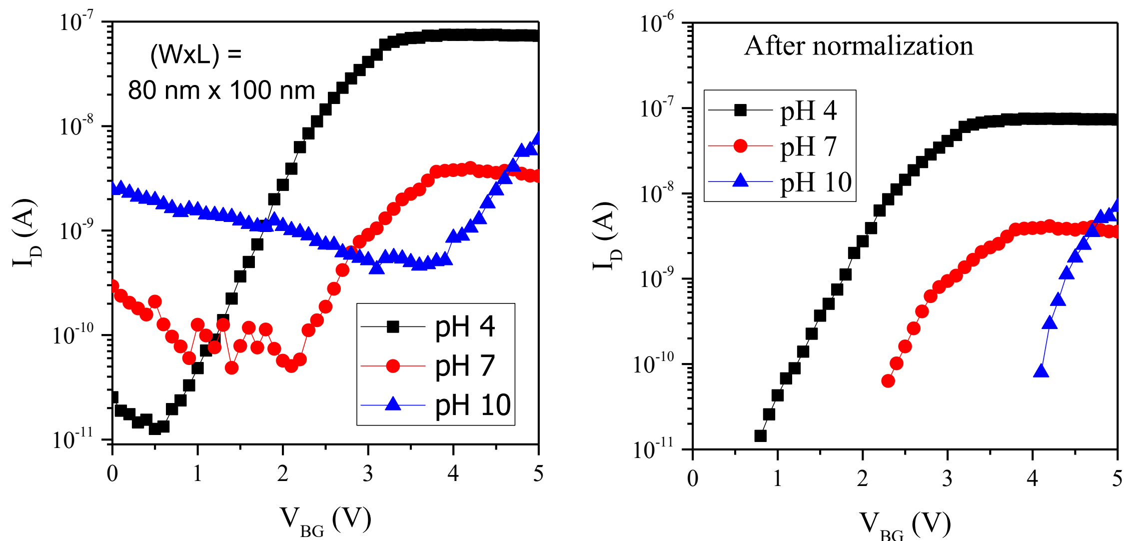

Figure 5. 12 pH response of sensors, before (left) and after (right) normalization function, with drain leakage current through cured AZ-1512 resist

The observation of leakage current through the passivation layer illustrated above has also been verified through measurement and comparison of the currents through drain (I_D), source (I_S), back gate (I_{BG}) and control gate (I_{CG}) metallic extensions, in dry condition and while pH solution is dispensed on the sensor. As the sensor is processed on n-type device, absolute values of source current (abs(I_S)) and control gate current (abs(I_{CG})) are used, for convenience in semi log plots.

Figure 5.13 illustrates a typical I-V characteristics of an n-type transistor, in which the magnitudes of drain current and source current are almost equal, and several orders higher than currents through other terminals of the transistor. Especially the control gate current is impressive in that such ultra-small currents are

expected through the capacitive (dielectric) structure of the sensor.

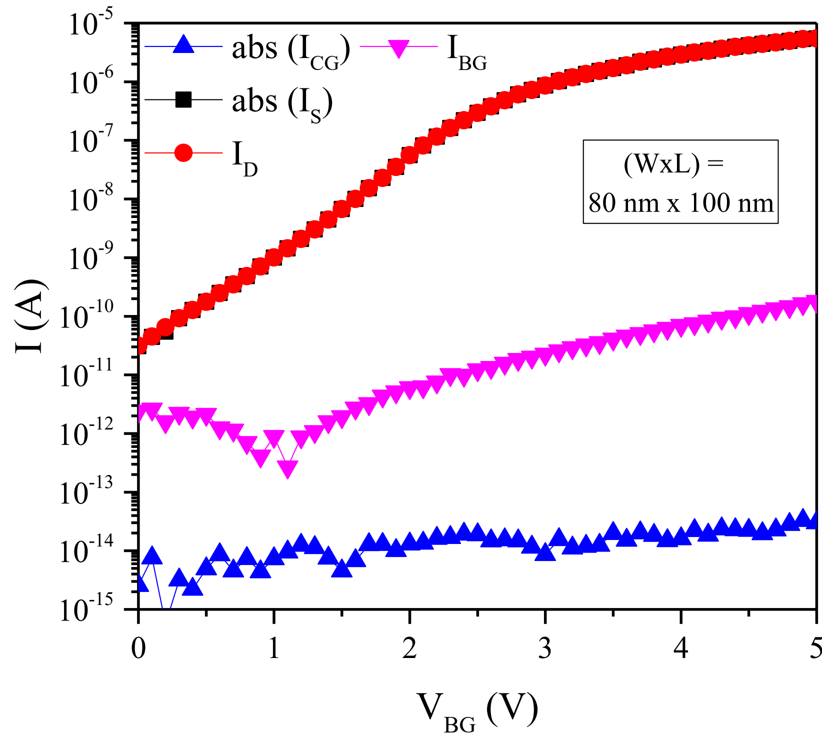

Figure 5. 13 Measured currents of the pH sensor through the drain, source, control gate and back gate in dry condition.

In contrary, when the pH solution was dispensed on the sample, high level of current leakage has occurred which can be observed from the unusual currents shown on figure 5.14. Up to 6-orders of higher current than the dry condition is recorded at the metallic extension of the control gate, which is not an expected value. There is also a huge difference in the magnitudes of drain and source currents, that also verifies the current leakage through the electrolyte past the passivating film. Therefore, such behaviors arise from the undesired shorting effect through the non-isolating passivating layer.

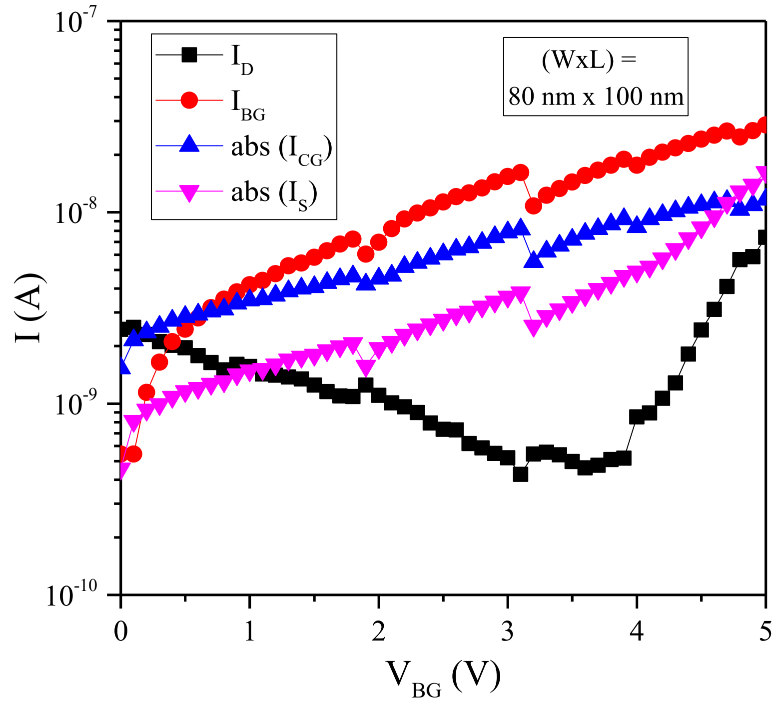

Figure 5. 14 Measured currents of the pH sensor through the drain, source, control gate and back gate in pH 10

Therefore, effective passivation should be employed to avoid leakage current and anomalous operation of chemical sensors. Consequently, cured HD-4104 was used for the passivation purpose instead of the hard baked AZ-1512 resist.

The pH sensing functionality was also demonstrated using p-type transistors. Figure 5.15 shows measured pH sensing characteristics of 2 different sensors having sensing area of 30 µm x 47 µm each, but had different gate dimensions. Nonetheless, the gate dimension does not affect the sensitivity as long as the coupling factor of the FDSOI, and the parameters of the capacitive divider circuit are the same. The expected high sensitivity and excellent repeatability have also been obtained. Despite the expected pH sensing performance, a big shift in threshold voltage has been observed in both sensors. This excessive shift in threshold voltage might have been caused by trapped charges during fabrication of the sensor.

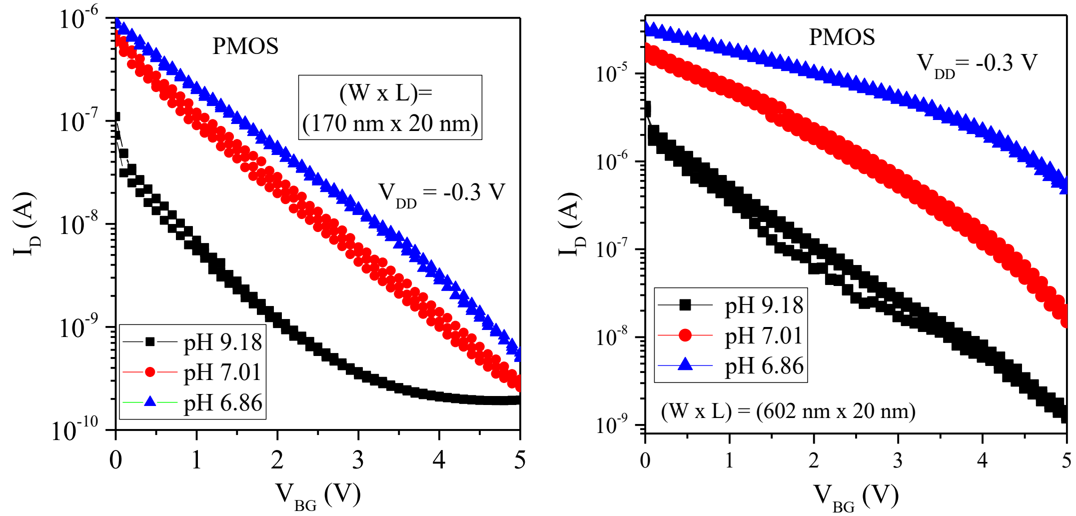

Figure 5. 15 Measured pH response of sensors developed based on p-type FDSOI devices

Highly attenuated sensitivities, much less than the theoretically achievable maximum response, can sometimes be observed as presented on figure 5.16 below. This effect may be caused by non-clean sensing surface which is for instance covered by a photoresist during the last fabrication process steps. Such issues can be circumvented by reducing the number of microfabrication process steps after the sensing film deposition. Effective cleaning procedures after each lithography step, such as cleaning in O_2 plasma, also help to have cleaner sensing films.

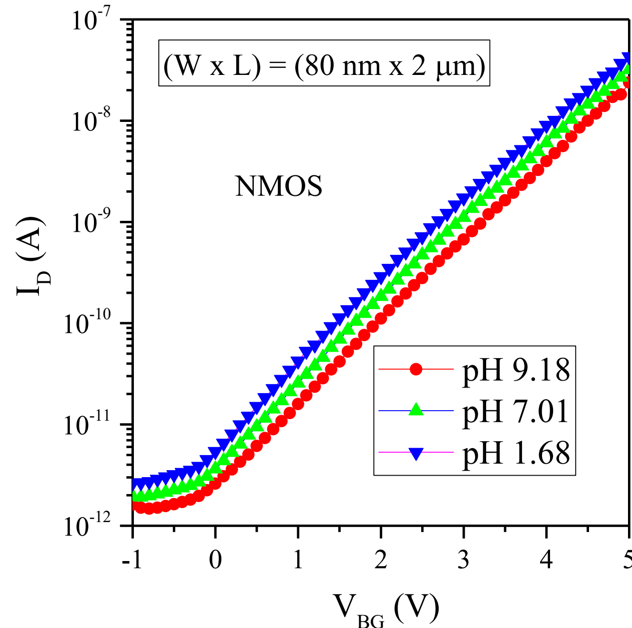

Figure 5. 16 Attenuated sensitivity of a pH sensor

On literature, fast response time is mentioned as one of the attractive features of the solid state pH sensors, although the evaluated response time is rarely available [77], [80]. Only a numerically simulated response time of a sensor based on tunnel field-effect transistors is reported in [220] where the fastest response time reported is 80 seconds. We determined the response time of the pH sensors to be 5 seconds which is 16 times faster than the reported result on literature. The experimental result of response time measurement of the BEOL integrated sensors is presented below on figure 5.17.

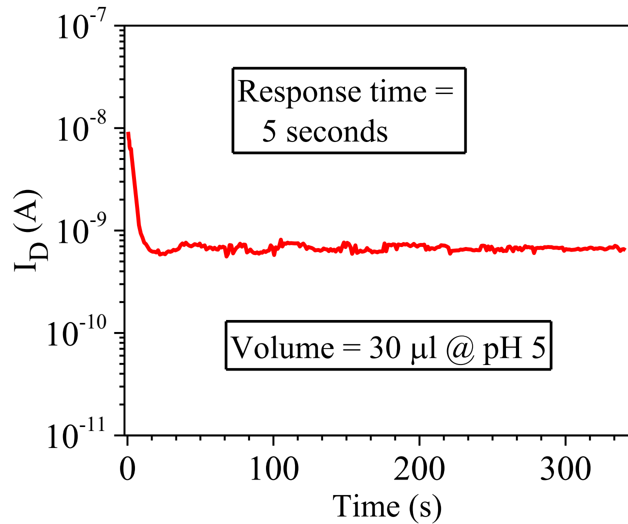

Figure 5. 17 Response time of the BEOL integrated sensors

The capability of the sensor to resolve tiny changes in pH is no less important than the sensitivity. This is because, sensitivity is merely a shift in the mean output response for a certain change in stimuli, while resolution depends on both sensitivity and signal to noise ratio. Consequently, the resolution of the sensors is computed from the sensitivity and the peak to peak noise, with an assumption that the smallest meaningful change in response is equal to 3 times more than the peak to peak noise. For instance, a peak to peak noise of magnitude 4.4 mV, for a sensor of 730 mV/pH is equivalent to a noise of (4.4 mV/730 mV.pH^{-1}) = 0.006 pH units. Assuming the smallest resolvable signal to be 3 times higher than this peak to peak noise, the resolution becomes (3 x 0.006 pH) = 0.018 pH. This way, a resolution of 0.018 pH is obtained which is also shown on figure 5.18 below. This computation of the resolution can similarly be computed from the noise on the drain current and fixed bias sensitivity.

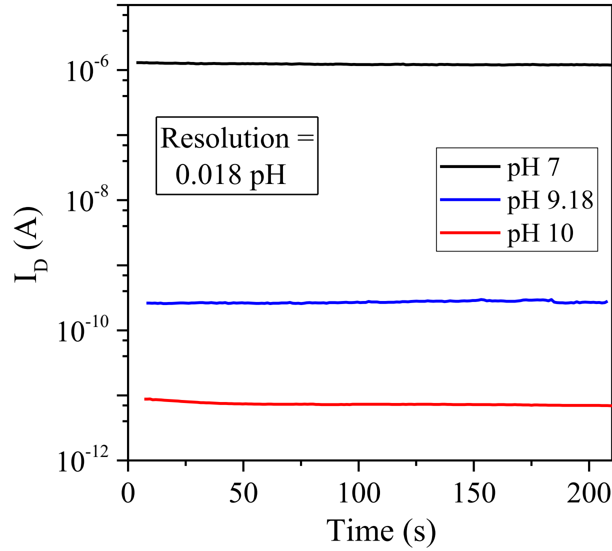

Figure 5. 18 Diagram showing the response for resolution computation of the BEOL integrated sensors

Real time devices are always constrained by some non-ideal conditions. In the case of solid state pH sensors, hysteresis and drift are the most frequently mentioned non idealities [40], [137], [139], [141], [143], [144], [221], [222]. We evaluated the hysteresis occurring in the pH sensors that we developed in the BEOL of UTBB FDSOI transistors. Monitoring the drain current at pH 9.18 following measurements at pH 7 and pH 10, the offset between the two measurements at pH 9.18 gave a hysteresis value of 0.03 pH. This hysteresis value is up to 4 times less than the hysteresis reported in [40], [78], [143], [223]. The measured result for hysteresis evaluation is provided below on figure 5.19.

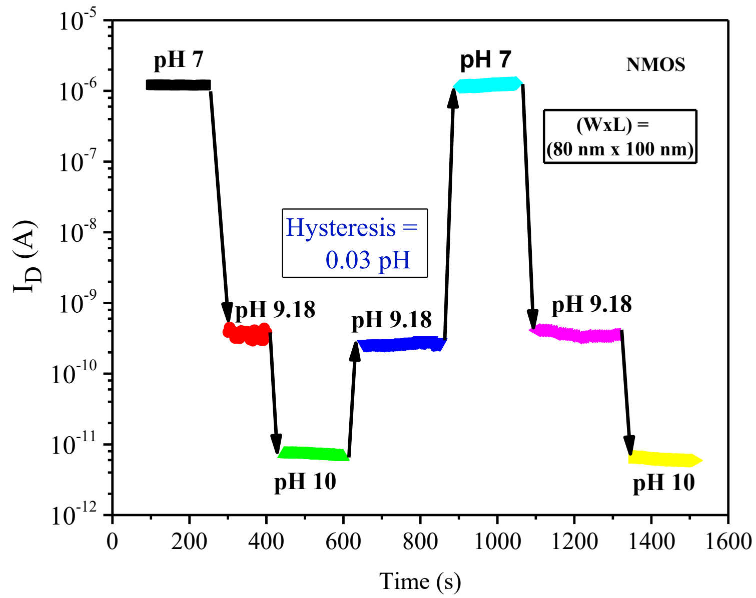

Figure 5. 19 Diagram showing the hysteresis of the BEOL integrated sensors

The stability of the sensor is also characterized by monitoring the change in drain current of the sensor for more than 4-hours. Very stable performance is obtained in which a drift of only 3% per hour is measured. This measurement result is indicated below on figure 3.20.

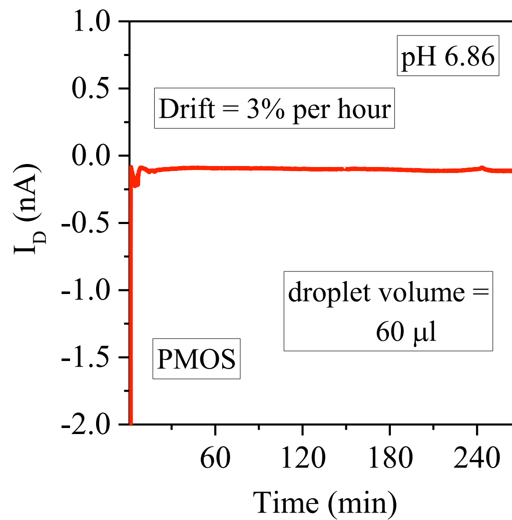

Figure 5. 20 Measured response of the sensor for drift study

5.5 Sensing at the Gate Protection Diode

Exploiting the extremely steep switching, as small as 9 mV/decade, ultrahigh sensitive pH sensors have been fabricated and tested in which the pH sensing is functionalized at the gate protection diode. The 9 mV/pH switching can provide a theoretically maximum sensitivity of 6.6 decade/pH (assuming a Nernstian responsive pH sensing film) which is more than 7-times higher than sensitivity of state of the art pH sensors.

A pH sensing characterization has been undertaken with (W x L = 170 nm x 100 nm) devices. The drain current was, however, 0.1 V which is small compared to the requirement for the DIBL effect to turn on the device very abruptly. From this measurement, pH sensing in very wide range (pH 1.68 to pH 12.46) has been obtained. Figure 5.21 illustrates this pH sensing experiment.

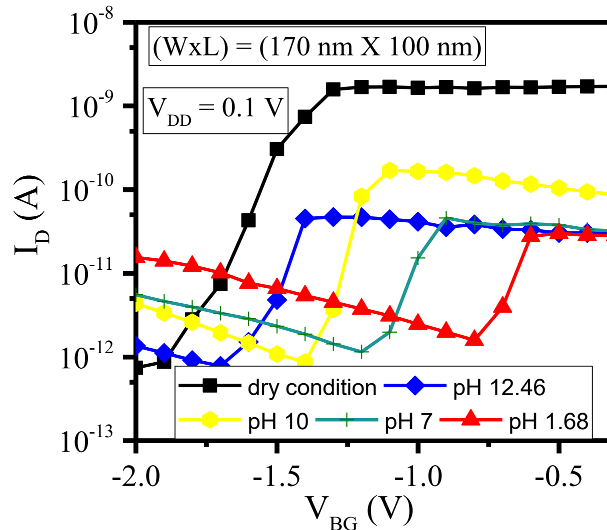

Figure 5. 21 pH response at lower drain voltage (V_{DD}=0.1 V)

Although the sensitivity on figure 5.21 is not as high as expected, the sensing performance in the wide pH range is very good. The linearity of this sensing response is presented below on figure 5.22.

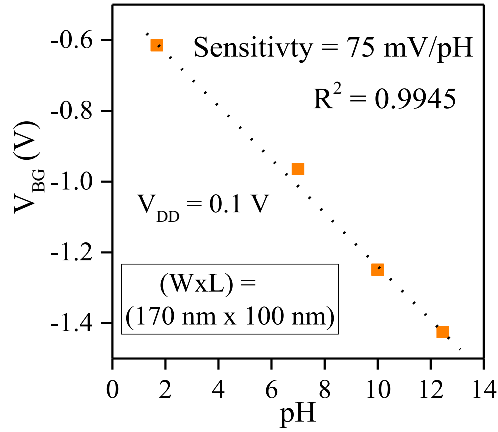

Figure 5. 22 Sensitivity and linearity of pH response at lower drain voltage (V_{DD}=0.1 V)

Increasing the drain voltage from 0.1 V to 0.6 V, steeper drain current switching has been obtained as illustrated on figure 5.23 below. Such steeper behaviors are required for the fixed bias ultrasensitive operation of the pH sensors.

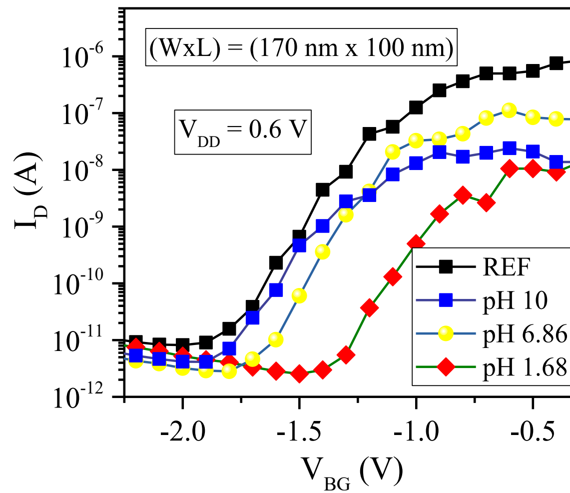

Figure 5. 23 pH response at higher drain voltage (V_{DD}=0.6 V)

The pH sensing characteristics at very short devices (W x L = 1 µm x 20 nm) is shown here under, on figure 5.24. Confirming the theory and experimental characterization of the DIBL effect presented in chapter 3, much steeper switching of the drain current is observed on sensors based on these very short devices (gate length = 20 nm).

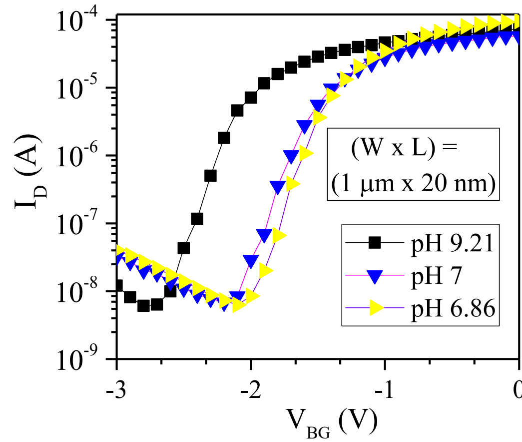

Figure 5. 24 pH response of short devices

The chronogram of these sensors, which are based on very short devices, is presented on figure 5.23. A very high fixed bias sensitivity of 1.25 decade/pH is demonstrated. This experimentally measured sensitivity, although less than the theoretically achievable maximum sensitivity which is 6.6 decade/pH, is higher than state of the art [203].

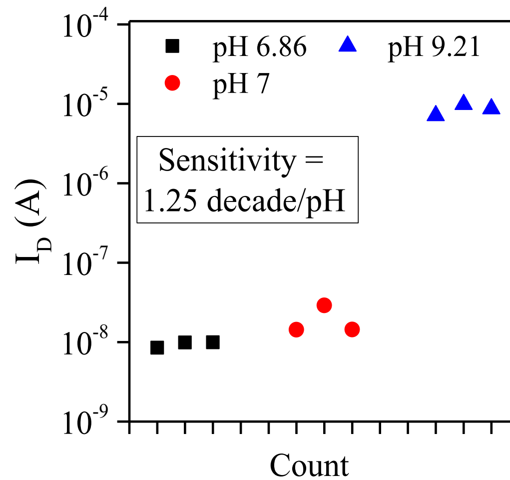

Figure 5. 25 Chronogram of sensors based on very short devices

The chronogram also shows that very good repeatability has been obtained with the measurements at each pH value. Moreover, the response time, hysteresis and drift characteristics of the sensors discussed in section 5.4 are believed to behave similarly in sensors where sensing is functionalized at the gate protection diode. This is because, those parameters are mostly determined by the phenomena at the electrolyte insulator interface, and this interface is the same in both configurations of the sensors.

5.6 Conclusion

Extended gate and BEOL integrated CMOS compatible pH sensors have been fabricated and characterized for the main figures of merit, such as sensitivity, repeatability and stability. Superior performances, compared to both the Nernstian response and to state of the art have been demonstrated. Experimental results are in confirmation with modeling and simulation which consolidates our approach of biasing the sensor through a capacitive divider circuit rather than the bulky reference electrode.

Not only in terms of sensitivity, but also the fast response time, excellent stability and reduced non-idealities validate the very good performance of the sensors. The role of the capacitive divider circuit is also experimentally validated enabling stable performance of the sensor at very low noise level, while also ensuring CMOS compatibility of the sensor.

The very novel approach of sensing through the gate protection diode, has also been successfully demonstrated. Although a theoretical fixed bias sensitivity reaching 6.6 decade/pH is achievable, we experimentally showed a sensitivity of 1.25 decade/pH which is higher than the state of the art sensitivity. Therefore, we successfully demonstrated ultrahigh sensitive, CMOS compatible pH sensors that have fast response time and stable performance.

CHAPTER SIX

CONCLUSION

Ultrasensitive and CMOS compatible pH sensors have been demonstrated with integration in the BEOL of industrial UTBB FDSOI transistors. A capacitive divider circuit is employed for biasing which ensures not only stable performance, but also CMOS compatibility of the sensor. The proposed approach and the experimental characterization have been validated by modeling and TCAD Sentaurus simulation. The sensitivity of our sensors, both for fixed current and fixed bias applications, are superior to the state of the art. Benchmarks are provided below on figures 6.1 and 6.2.

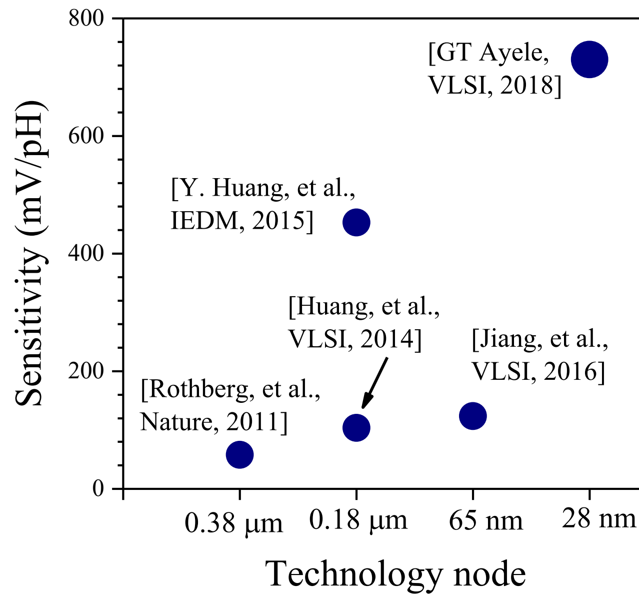

Figure 6. 1 Sensitivity benchmark of the sensor for fixed current readout

We also fabricated and tested pH sensors in which the detection is made at the gate protection diode rather than the front gate. Although the theoretical sensitivity can reach as high as 6.6 mV/decade, an experimental sensitivity of 1.25 decade/pH has been demonstrated. This is much higher than state of the art sensitivity which is less than 0.9 decade/pH.

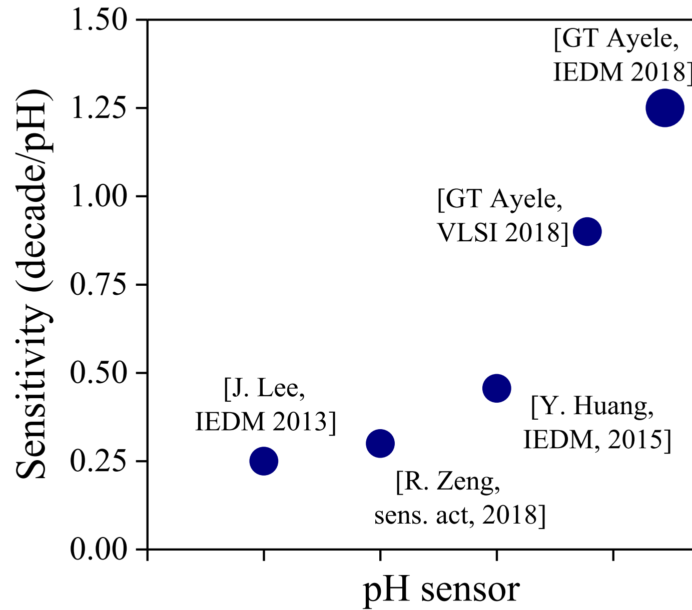

Figure 6. 2 Sensitivity benchmark of our sensor for fixed bias readout

6.1 Summary of the Thesis

The special feature of UTBB FDSOI transistors that there is a strong electrostatic coupling between the front gate and the back gate, and that the capacitances are asymmetric at those two gates, provides an intrinsic amplification opportunity. This is highly important for developing ultrasensitive sensors based on such technology. Moreover, the availability of two gates is beneficiary in order to functionalize the detection on one gate and to pursue the signal recording on the other. This eliminates the necessity of applying a variable bias at the front gate which would otherwise introduce a factor for variability and noise.

Integration of the sensors in the back end of line has several benefits over the direct exposure of the gate oxide to liquid environment. This encompasses the advantages of more reliability and sensor life time, compatibility with the standard CMOS process, and inclusion of capacitive divider circuit.

Operation of the MOSFETs without a proper front gate bias makes them vulnerable for undesired floating body effects [33]. The capacitive divider circuit helps to address these issues by biasing the front gate simultaneously with the sensing functionality at the same gate through capacitive coupling to a common BEOL metal. Therefore, the potential at the BEOL metal would be a weighted sum of the surface potential at the sensing gate and the applied bias at the control gate.

This proposed approach for developing ultrasensitive and CMOS compatible chemical and biosensors has been validated by modeling and simulation, followed by an experimental confirmation with a proof of concept extended gate pH sensor. Finally, the sensors have been integrated in the BEOL of the transistors which gave performances that confirm theoretical expectations, simulation works, and proof of concept results.

6.1.1 Modeling and Simulation

Analyzing the components of the sensor, the UTBB FDSOI, the capacitive divider circuit and the EI-interface, the output of the sensor is expressed as a function of the pH and the components parameters. The developed mathematical equation is a first report of a single complete equation describing the sensor output as a function of the solution pH and the design parameters of the capacitive divider circuit and the UTBB FDSOI transistors.

The mathematical modeling of the sensor is confirmed by numerical simulations with TCAD Sentaurus. For the simulation, the EI interface is modeled in two different ways─ sensing the surface potential and sensing the surface charge. Both cases provided results that are consistent with theoretical expectations and mathematical models.

6.1.2 EG pH Sensor

The modeling and simulation of the proposed sensor was further validated by a proof of concept extended gate pH sensor fabrication and characterization. These proof of concept EG sensors were developed by an isolated processing of the pH sensing component and making an external electrical connection for sensitivity characterizations. Therefore, it provides faster and simpler realization of the sensor without need of masks and patterning by lithography. In contrary, the external electrical connection during the characterization brings in more inconvenience and signal attenuation. But the approach is very good for simple and fast proof of concept validation.

The extended gate sensor demonstrated a sensitivity of 475 mV/pH which is superior performance compared to state of the art solid state pH sensors. Nonetheless, the measured experimental sensitivity is less than the simulation result (ideally maximum sensitivity) which can be justified by the sub-Nernstian response of the sensing film and the signal loss on the external electrical connections between the transistor and the

transduction component. The chronogram of the extended gate sensor shows its high sensitivity at fixed bias, and excellent stability (repeatability).

6.1.3 Sensor in BEOL of FDSOI

The proof of concept extended gate illustration was followed by integration of the sensors in the BEOL of the industrial UTBB FDSOI transistors. The theoretically expected sensitivity of 730 mV/pH has been obtained which is 12 times higher than the Nernst limit. The fixed bias sensitivity of these sensors, 0.9 decade/pH, is also superior to state of the art.

6.1.4 Sensing at Diode

A novel pH sensor, in which the detection is made at the gate protection diode, is successfully demonstrated. The abrupt current switching, which reaches 9 mV/decade, has the potential to increase the fixed bias sensitivity to 6.6 decade/pH. We experimentally demonstrated a sensitivity of 1.25 decade/pH which is superior to the state of the art sensitivity.

6.2 Original Contribution

It is for the first time that ultrasensitive and CMOS compatible pH sensors are integrated in the BEOL of industrial UTBB FDSOI devices which makes this work an original contribution. The ultrathin body and BOX enables effective coupling between the front gate and the back gate, and use of the back gate for signal recording at lower voltages. This provided the benefits of ultrahigh sensitivity and low voltage operation. On the other hand, the capacitive divider circuit was crucial for stable operation of the sensor, enabling CMOS compatibility at the same time.

In the modeling of such sensors, it is also only in this work that a single mathematical equation provided relating the sensor's output as a function of the solution pH and the design parameters of the UTBB FDSOI transistor and the capacitive divider circuit. A mathematical model is developed for describing the fixed bias sensitivity of an ISFET that is developed using any transistor type.

In addition to the above original works, we demonstrated for the first time the pH sensing functionality through the gate protection diode of the standard FDSOI. This is a novel work which is the very first report of its type. The significance of this work is incredible as it has the potential to increase the state of the art

sensitivity by more than 7-times (corresponding to 9 mV/decade current switching).

6.3 Perspective

In this PhD thesis, the special feature of UTBB FDSOI devices for sensing applications has been successfully demonstrated. It is therefore recommended to widen the use of this technology for sensing further chemical, bio, and other physico-chemical variables. Hence, we suggest to proceed with development of gas sensors based on the FDSOI technology in the BEOL of industrial UTBB FDSOI transistors. In addition to this, we suggest integration of biological ion (Na^+, K^+, Ca^{++}) sensors by functionalizing the bioreceptor films on the ISFET for multi-ion sensing chips.

The sensing areas of the sensors that are developed in this thesis range from (30 µm x 47 µm) to 9 mm^2. The requirement for larger sensing areas was to avoid undesired potential side reactions with the passivation material. More works, however, can be pursued to explore the smallest sensing area that gives an optimum sensitivity. A further study can be carried out to correlate the performance as a function of sensing area. Embedding the sensor in its own readout circuit and encapsulation, preferably with microfluidic structure on top of a sensor array for multi-ion detection, is also suggested as a perspective. Such developmental works enhance the immense potential for realizing highly miniaturized, CMOS integrable, label free, and highly sensitive chemical and biosensing solutions.

A very new approach, in which the pH sensing is functionalized at the gate protection diode, has also been demonstrated in this thesis. The highly steep I_D-V_{BG} characteristics, which reaches 9 mV/decade, has a potential to provide a fixed bias sensitivity of 6.6 decade/pH. This is more than 7-times higher than the thermionic (kT/q) limited field-effect devices. We obtained an experimental sensitivity of 1.25 decade/pH which is superior to conventional ISFETs, but still lower than the theoretically expected sensitivity. Thus, we recommend further works on this method of sensing to reach the theoretically anticipated performance. It can be reached developing the sensors based on short gate length (around 20 nm) devices, and operating them at relatively higher drain voltages (between 0.9 V and 1.3 V).

APPENDIX-I

RÉSUMÉ ÉTENDU

A1. Introduction

L'ère moderne marque le début de la quatrième révolution industrielle (Industrie 4.0), rendue possible par l'intégration du réseau informatique et du monde physique (système cyber-physique), communément appelé internet of things (IoT) [1]–[4]. L'intelligence artificielle (AI), big data, machine learning, et deep learning sont les autres technologies émergentes constituant la majorité des développements technologiques du futur proche [5], [6]. Les capteurs constituent la pierre angulaire de toutes ces technologies permettant la transmission en continu des données du monde physique au réseau informatique.

Le marché des capteurs a récemment connu une croissance spectaculaire alimentée par l'application remarquable de capteurs dans l'électronique de consommation, l'industrie de l'automatisation, les appareils portables, le secteur automobile et l'internet of things (IoT) de plus en plus adopté [1], [7]. Il s'appuie également sur des techniques innovantes de synthèse et de traitement de matériaux, ainsi que sur des technologies de fabrication telles que les complementary metal oxide semiconductor (CMOS) et les systèmes micro-électromécaniques (MEMS) [8], [9]. Ces technologies avancées ont permis le développement de capteurs dotés de caractéristiques typiques telles qu'une précision accrue, des dimensions miniaturisées, un coût très réduit et un temps de réponse rapide.

Le marché mondial des capteurs devrait connaître une croissance exponentielle avec un taux de croissance annuel composé de 11,3% sur la période 2016-2022, pour atteindre 241 milliards de dollars d'ici 2022 [8]. Le marché mondial de l'IoT, qui comprend non seulement les capteurs, mais également les services de connectivité et les plateformes IoT, devrait en revanche croître à un taux de croissance annuel composé de 20%, atteignant 7,1 billions de dollars en 2020 [10], [11]. L'agriculture et les soins de santé appartiennent aux principales industries qui pourraient largement utiliser l'IoT. Les capteurs chimiques, tels que les capteurs de pH, jouent un rôle important dans ce cas, car ils fournissent des informations cruciales telles que l'acidité du sol et le niveau de pH du fluide corporel. Le marché mondial des capteurs de pH devrait également connaître une croissance exponentielle, d'environ 4% du CAGR (compound annual growth rate) en 2017-2023, pour atteindre 1,8 milliard de dollars en 2023 [30].

Les ISFETs (ion-sensitive field-effect transistors) sont des capteurs ioniques à l'état solide dans lesquels le courant de drain est modulé par l'activité ionique d'une solution aqueuse. Le schéma de principe de la structure ISFET de base est présenté à la figure A-1. Ces capteurs chimiques CMOS offrent d'immenses avantages par rapport aux autres techniques de détection du pH. Parmi ces avantages, citons l'impédance d'entrée élevée, le courant continu et la bande passante basse fréquence [Matsuo et Wise, 1974], sa petite taille, sa fiabilité, son temps de réponse rapide et la possibilité de fabriquer une puce multicapteurs. Ils permettent également au traitement du signal sur puce d'atteindre une transformation d'impédance élevée à faible, une compensation de température et un multiplexage du signal [SD Moss, et al, 1978]. De plus, les ISFETs sont utiles pour la transformation d'impédance *in situ*, possibilité relativement facile de fabriquer des multi-sondes petites et robustes [PA Comte et J Janata, 1978].

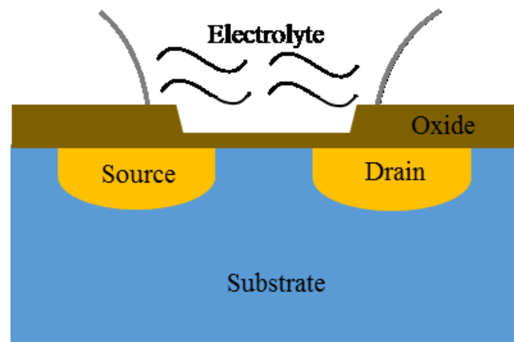

Figure A- 1 Schéma simplifié de l'ISFET

A2. Etat de l'art

En 1970, P. Bergveld a décrit l'ISFET (ion-sensitive field-effect transistor), dans lequel il expliquait la possibilité de moduler le courant de drain à travers la double couche formée à l'interface électrolyte-oxyde [25]. En retirant le métal de grille du MOSFET, il a exposé l'oxyde de grille du transistor à une solution aqueuse pour sonder la concentration molaire en ion sodium (Na^{+}) dans l'électrolyte (le diagramme schématique est présenté à la figure A-1). Sans l'utilisation d'électrode de référence, un courant de drain croissant linéairement a été signalé en fonction de la concentration molaire logarithmique de chlorure de sodium (NaCl).

Après près de 30 ans de recherche et de développement sur les ISFETs, différents groupes ont reporté une

sensibilité accrue dépassant la limite de Nernst. En 2012, K. B. Parizi et al. ont reporté une sensibilité de 130 mV / pH [74], bien que cette approche n'ait été ni approuvée ni suivie par d'autres travaux. Ils ont attribué l'incrément de sensibilité à une grille de détection agrandie d'un ISFET à grille étendue. Ils ont également évité l'utilisation de l'électrode de référence en utilisant un circuit de détection différentiel composé d'une paire de capteurs sensibles aux ions à canal n et p connectés en parallèle et polarisés en un point de polarisation de transconductance adapté [74]. L'inconvénient est que l'explication théorique de la sensibilité amplifiée n'est pas suffisante et que la zone de détection est trop grande (en cm^2).

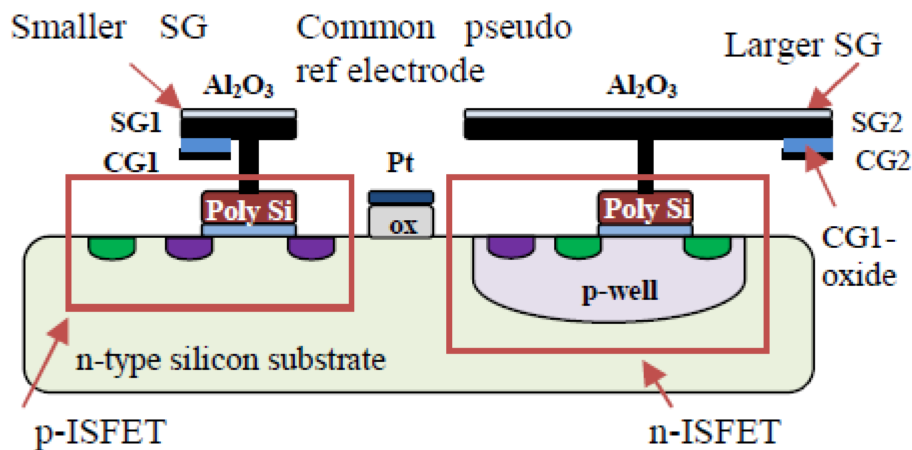

Figure A- 2 Schéma de principe de l'ISFET rapporté par [74]

En 2013, J. Lee et ses collaborateurs ont publié leurs travaux sur les circuits de biocapteurs hybrides SiNW/CMOS à deux compartiments fonctionnels [75]. Le premier compartiment consistait en un bloc SiNW complémentaire connecté en série (type n/p), qui détectait les biomolécules cibles et amplifiait le bio-signal, produisant une sensibilité élevée. Le deuxième compartiment est composé d'un bloc de circuit CMOS, qui amplifie davantage le biosignal et élimine le bruit sans sacrifier la sensibilité [75]. Ce travail a montré une grande sensibilité par rapport aux ISFET modernes, malgré le fait qu'il comprenait au total quatre dispositifs. Par conséquent, ce capteur est davantage un circuit qu'un appareil. Il comportait également la fonction d'annulation du bruit, considérée comme un atout supplémentaire. Enfin, faire passer tous ces dispositifs dans le liquide serait inefficace du point de vue de la polarisation du transistor.

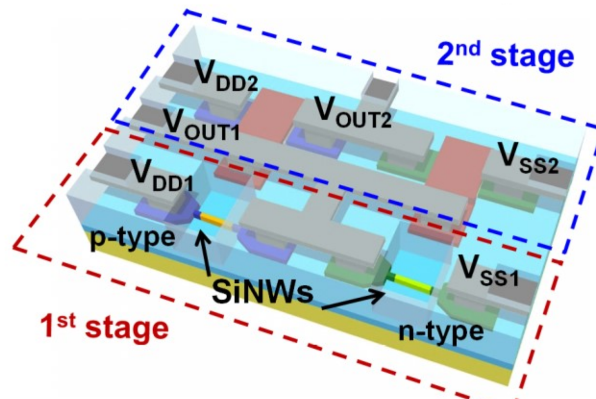

Figure A- 3 Schéma de principe de l'ISFET hybride SiNW/CMOS [75]

D'autre part, M. Spijkman et ses collaborateurs, utilisant la fonctionnalité de couplage capacitif des ISFETs à double grille, ont reporté une sensibilité accrue qui évolue linéairement avec un facteur de couplage capacitif de C_{top}/C_{bottom} [15]. L'amélioration a été obtenue en utilisant une monocouche auto-assemblée (SAM) d'acide octadécylphosphonique en tant que diélectrique à grille supérieure et une couche de SiO_2 de 1,2 µm du diélectrique à grille inférieure [76]. La variation linéaire de la sensibilité avec le rapport C_{top}/C_{bottom} est une caractéristique particulière des dispositifs SOI pour les applications de détection. En dépit de cet aspect important du travail, il présente quelques lacunes importantes. La première est la très faible pente sous le seuil des caractéristiques I_D-V_{BG} (moins de 1 décade de courant de drain pour une plage de tension supérieure à 15 V) de l'appareil qui rend le capteur vulnérable au bruit et nécessite un circuit de lecture strict. En deuxième lieu, la SAM est directement exposée à l'électrolyte, ce qui pose des problèmes de fiabilité et de stabilité du capteur. De plus, la sensibilité élevée est obtenue au dépit d'un diélectrique à grille inférieure très épais qui rend le capteur inadapté aux applications de détection de pointe à faible consommation d'énergie. Enfin, la tension de polarisation sur la grille avant a été appliquée via l'électrode de référence Ag/AgCl, ce qui rend le capteur inutilisable pour les capteurs évolutifs. Le schéma de l'ISFET à double

grille est illustré dans l'encadré de la figure A-4.

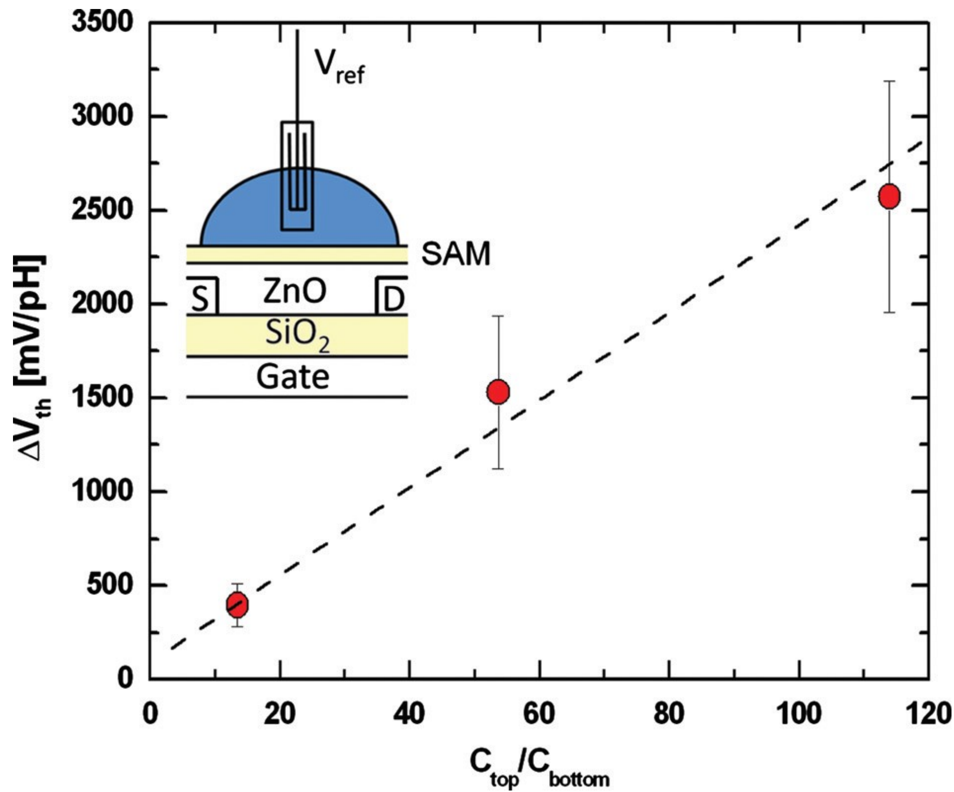

Figure A- 4 Mise à l'échelle de la sensibilité avec le rapport de capacité avec un encadré représentant le schéma de l'ISFET à double grille [76]

Hyun-June Jang et Won-Ju Cho ont également exploité la fonctionnalité de couplage capacitif issue de la structure de DG pour dépasser la limite de Nernst de la sensibilité des ISFETs. En 2014, ils ont rapporté leur travail sur DG ISFET à base de ultra thin body (UTB) à partir duquel les auteurs affirment non seulement une sensibilité bien accrue, mais également une composante de fuite fortement supprimée qui confère à l'ISFET une meilleure stabilité [77]. Ils ont fait valoir qu'un corps épais produit des facteurs non idéaux, tels qu'un rapport de couplage instable et des composants de fuite, dans la relation de couplage capacitif, entraînant une dégradation importante des performances du dispositif. Ils ont également mentionné que la sensibilité d'un dispositif UTB de 4,3 nm d'épaisseur était multipliée par deux, par rapport à un dispositif pour le corps de 85 nm, et que de plus grandes améliorations de la stabilité pouvaient être obtenues. Bien que ce travail paraisse excellent, il met trop l'accent sur l'étude de l'épaisseur du corps. Elle pourrait étudier l'effet des épaisseurs d'oxyde de grille avant et arrière, l'amplification intrinsèque dépendant davantage du rapport entre les capacités des grilles avant et arrière. Ils ont également utilisé une électrode de référence commerciale Ag/AgCl pour polariser la grille avant (à travers l'électrolyte), ce qui

rend leur ISFET à base d’UTB obscurci du point de vue de la miniaturisation.

La controverse sur l'utilisation de l'électrode de référence pour le fonctionnement de l'ISFET a commencé 4 ans après le premier rapport de l'ISFET et persiste jusqu'à présent [25], [26]. Lorsque le concept d'ISFET a été introduit tout au début, le principe de fonctionnement reposait sur la propriété des MOSFET selon laquelle les espèces ioniques incorporées dans le dispositif lors de la fabrication des MOSFET introduisent des variations de la tension de seuil (V_{th}) [145], de sorte qu’il n'avait pas d'électrode de référence. Bergveld a approuvé sa position concernant l'inutilité de l'électrode de référence pour les ISFETs dans ses travaux ultérieurs [41] en expliquant la capacité du champ localisé à moduler la tension de seuil des MOSFETs.

Des travaux de recherche et de développement ont été menés pour miniaturiser l'électrode de référence afin de réaliser un ISFET à l'échelle correspondante [146]. Dans certains travaux, la structure conventionnelle de l'électrode de référence est préservée tout en réduisant sa taille, mais ces électrodes ont une durée de vie très limitée. En effet, la durée pendant laquelle le contenu de la solution intérieure reste constant dépend du taux de transport de masse à travers la jonction et du volume du compartiment intérieur [146]. Une autre tentative consistait à réaliser une électrode de référence à l'état solide, également connue sous le nom de transistor à effet de champ de référence (REFET), qui ressemble à un ISFET, à la différence qu'il est recouvert d'un matériau insensible aux ions au niveau de la zone de détection [146]. Au contraire, certains groupes ont démontré le fonctionnement de leur ISFET sans électrode de référence [26], [161], [162].

Tout récemment, en 2018, R. Zeng et al. ont proposé une architecture interdigitée pour la détection et la polarisation de l'électrolyte, éliminant ainsi l'utilisation de l'électrode de référence [70]. Néanmoins, en observant plus précisément cette architecture et son schéma électrique, une fonctionnalité électrostatique équivalente peut être fournie par les extensions métalliques passivées de la grille de commande qui passent sous l'électrolyte dans le capteur de pH que nous avons développé dans les dispositifs BEOL de FDSOI. Ainsi, ce travail confirme notre approche consistant à utiliser le circuit diviseur capacitif pour polariser de manière capacitive non seulement le transistor, mais également l’électrolyte.

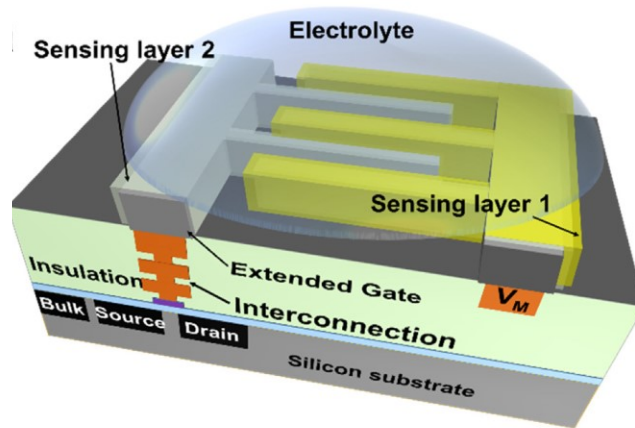

Figure A- 5 Schéma de principe du capteur à architecture interdigitée [70]

A3. Modélisation et simulation

Le capteur de pH est intégré dans le BEOL des transistors industriels UTBB FDSOI avec un circuit diviseur capacitif pour la polarisation de la grille avant à travers une grille de commande à couplage capacitif. La figure A-6 montre le schéma du capteur de pH dans lequel la détection du pH est poursuivie à la grille avant tandis que le signal est enregistré à la grille arrière. Le modèle électrostatique équivalent du capteur est également présenté à la Fig. A-6.

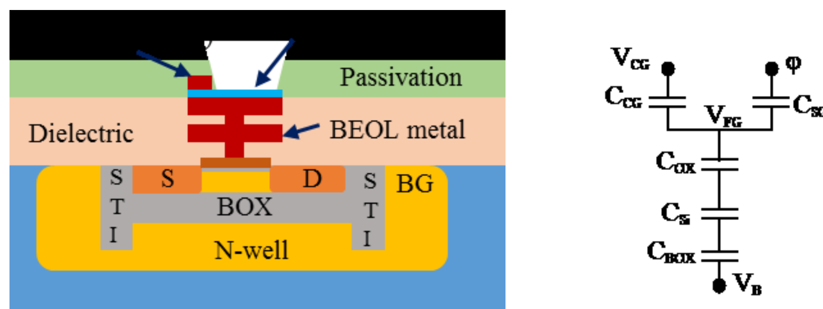

Figure A- 6 Schéma du capteur de pH intégré dans BEOL de FDSOI UTBB (à gauche) et son modèle électrostatique équivalent (à droite)

Par conséquent, en fonctionnalisant la détection du pH sur la grille avant des dispositifs FDSOI, la modification du potentiel de surface sur la grille avant est détectée sur la grille arrière amplifiée par le facteur de couplage (γ), donnant lieu à un capteur chimique à l'état solide à sensibilité ultra-élevée. En combinant les caractéristiques de sortie des composants du capteur, le décalage de la tension de seuil (pour les

dispositifs NMOS) au niveau de la grille arrière est représenté mathématiquement sur l'équation (A.1) ci-dessous en fonction du pH de la solution.

$$\Delta V_{th} = \left(2.3\ \frac{K_B T}{q} \alpha\right)\left(\frac{C_{OX}}{C_{BOX}}\right)\left(\frac{C_{CG}}{C_T}\Delta V_{CG} + \frac{C_{SG}}{C_T}\Delta pH\right) \quad \text{(A.1)}$$

Pour calculer la sensibilité du capteur de pH, qui correspond au rapport entre la variation de la tension de seuil et la variation du pH, la tension de la grille de commande doit être maintenue constante de sorte que le terme contenant (ΔV_{CG}) dans l'équation (A.1) devienne nul. En conséquence, la sensibilité est calculée par l'équation (A.2). Celle-ci est une description complète de la sensibilité de tels capteurs dans laquelle les effets du film de détection, du circuit diviseur capacitif et du facteur de couplage FDSOI sont tous inclus dans une équation.

$$\frac{\Delta V_{th}}{\Delta pH} = \left(\frac{C_{SG}}{C_T}\right)\left(\frac{C_{OX}}{C_{BOX}}\right)\left(2.3\ \frac{K_B T}{q} \alpha\right) \quad \text{(A.2)}$$

Sur les équations (A.1) et (A.2), le terme $\left(\frac{C_{SG}}{C_T}\right)$ vient du circuit diviseur capacitif qui prend une valeur comprise entre 0 et 1. Le circuit doit être conçu de telle sorte que $C_{SG} << C_T$, de sorte que le terme $\left(\frac{C_{SG}}{C_T}\right)$ soit très proche de l'unité, sinon il introduit une atténuation de la sensibilité.

En analysant les composants du capteur: le FDSOI UTBB, le circuit diviseur capacitif et l'interface EI, la sortie du capteur est exprimée en fonction des paramètres de pH et des composants. Cette modélisation mathématique du capteur est confirmée par une simulation numérique avec TCAD Sentaurus.

En modélisant l'adsorption des ions sur le film de détection sous forme de charges superficielles réparties, le décalage de tension au niveau de la grille arrière est simulé en fonction du changement de la densité de charges de surface au niveau de la grille de détection. Le résultat est présenté ci-dessous à la figure A-7. La simulation est également réalisée en modélisant le potentiel de surface à l'interface EI sous forme de tension variable. Tous les résultats de la simulation sont en confirmation avec les attentes théoriques et la modélisation mathématique.

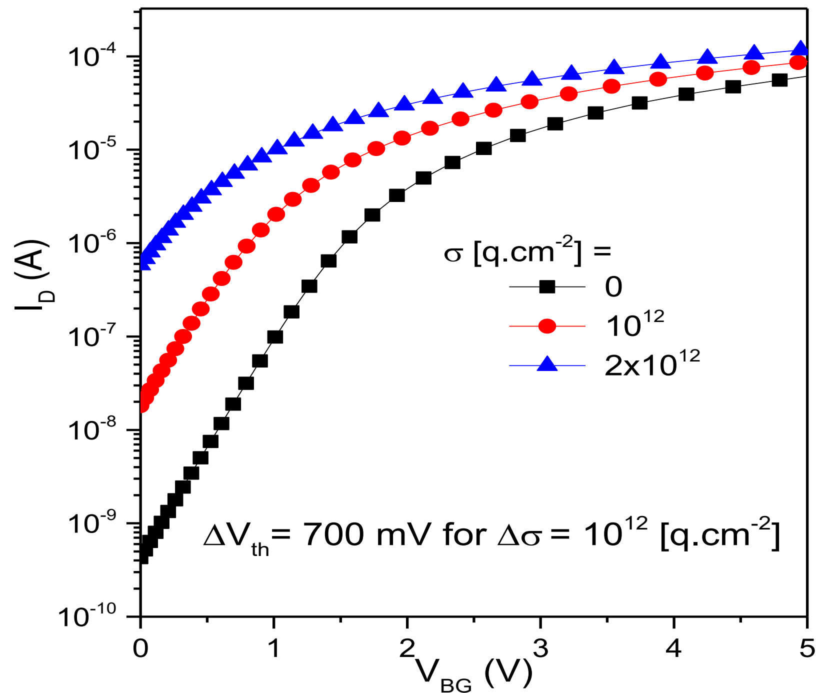

Figure A- 7 Résultat de la simulation du capteur à différentes densités de charge de surface

A4. Capteur de pH EG

La modélisation et la simulation du capteur proposé ont également été validées par une fabrication et une caractérisation du capteur de pH à grille étendue avec validation du concept. Ces capteurs EG de preuve de concept ont été développés par un traitement isolé du composant de détection du pH et par la réalisation d'une connexion électrique externe pour la caractérisation de la sensibilité. Par conséquent, il permet une réalisation plus rapide et plus simple du capteur sans nécessiter de masques ni de motifs par lithographie. Au contraire, la connexion électrique externe lors de la caractérisation apporte plus d'inconvénients et d'atténuation du signal. Mais l'approche est très bonne pour une validation simple et rapide de la preuve de concept.

Les composants de détection du pH des capteurs de pH EG ont été traités sur un substrat de Si de 750 µm, recouvert d'un SiO2 de 500 nm développé thermiquement. Une couche de métal Ti/Pt de 10 nm/80 nm a ensuite été déposée par évaporation par faisceau d'électrons [180]. Cette couche métallique sert d'extension du métal à grille flottante FDSOI pour le fonctionnement à grille étendue du capteur. On a déposé de l'oxyde d'aluminium (Al_2O_3) à 50 nm par dépôt de couche atomique (ALD) sur la couche métallique de Ti/Pt. Enfin,

nous avons appliqué de la laque d'argent pour compléter les connexions électriques externes entre la couche métallique Ti/Pt du composant de détection et la grille métallique flottante du FDSOI. Le schéma de principe de la connexion électrique et de la configuration du système pour la caractérisation de la détection du pH est présenté à la Fig. A-8.

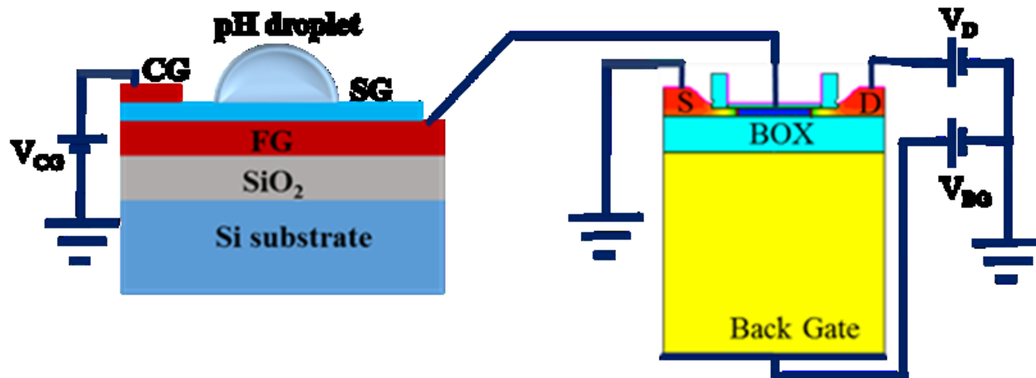

Figure A- 8 Schéma de principe du capteur de pH à grille étendue Proof of Concept

Le capteur à grille étendue a démontré une sensibilité de 475 mV/pH, ce qui représente une performance supérieure à celle des capteurs de pH à l'état solide de l'état de l'art. Néanmoins, la sensibilité expérimentale mesurée est inférieure au résultat de la simulation (idéalement maximale) qui peut être justifié par la réponse sous-Nernst du film de détection et par la perte de signal sur les connexions électriques externes entre le transistor et le composant de transduction.

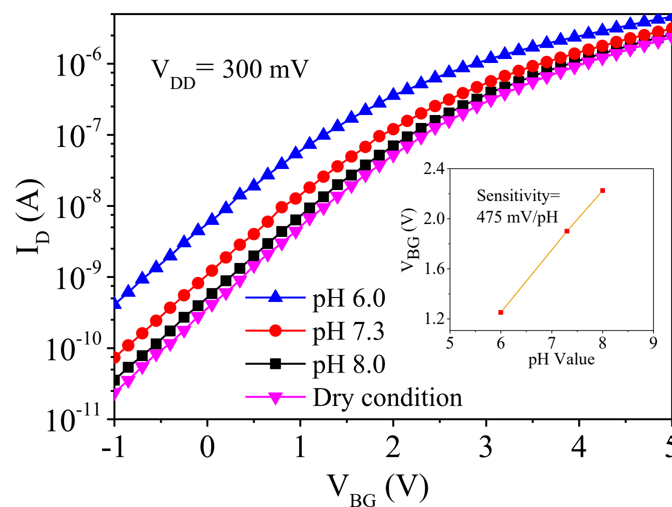

Figure A- 9 Sensibilité au pH du capteur de pH à grille étendue

Le chronogramme du capteur de grille étendue est illustré ci-dessous sur la figure A-10. Il montre la sensibilité du capteur de pH à biais fixe et la répétabilité des réponses du pH aux différentes valeurs de pH.

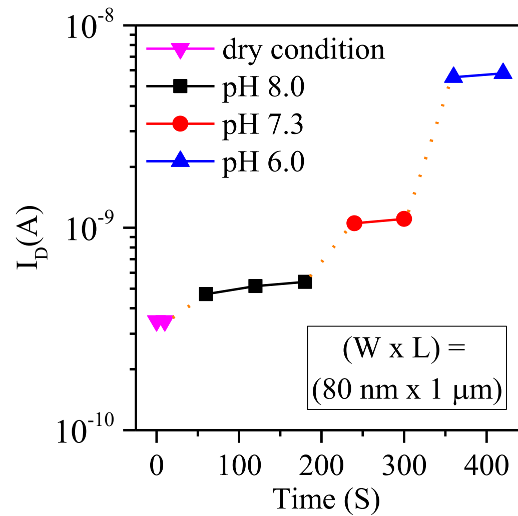

Figure A- 10 Chronogramme de la réponse du capteur de pH à grille étendue

A5. Capteur en BEOL de FDSOI

L'illustration de la grille étendue de validation de principe a été suivie de l'intégration des capteurs dans le BEOL des transistors industriels UTBB FDSOI. La sensibilité théoriquement attendue a été obtenue, soit 12 fois la limite de Nernst.

Le déroulement du processus résumé est présenté sous forme de diagramme sur la figure A-11 ci-dessous.

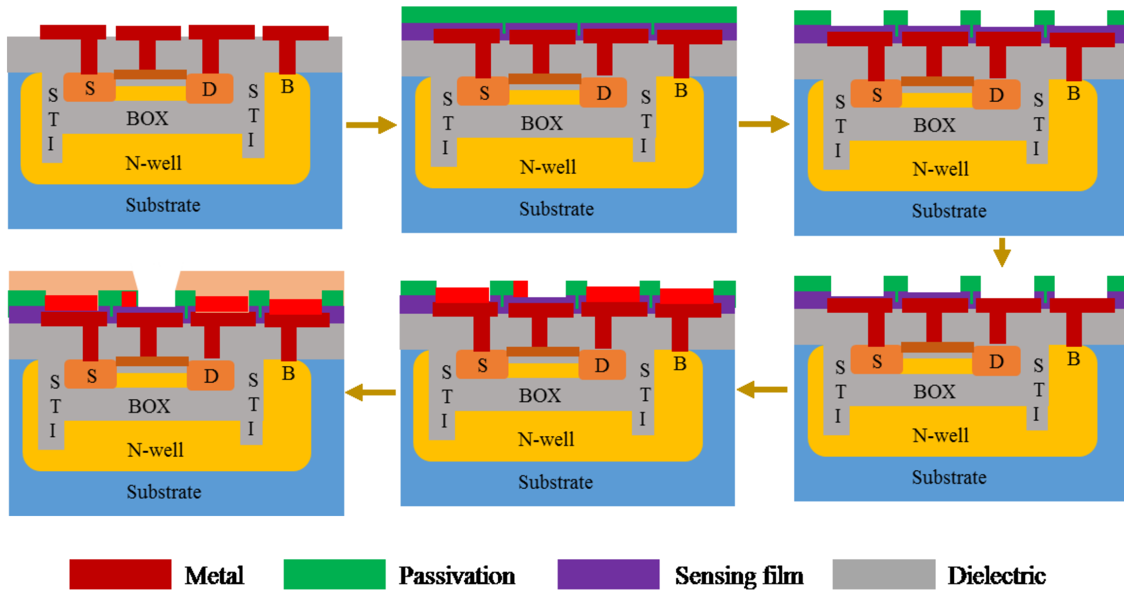

Figure A- 11 Process flow pour l'intégration des capteurs de pH dans le BEOL [203]

Le contour des capteurs fabriqués qui sont prêts pour la caractérisation, avec l'image optique comme encart et une gouttelette de pH distribuée sur la zone de détection, est présenté ci-dessous sur la figure A-13. Chaque capteur a une zone de détection de (29 µm x 70 µm).

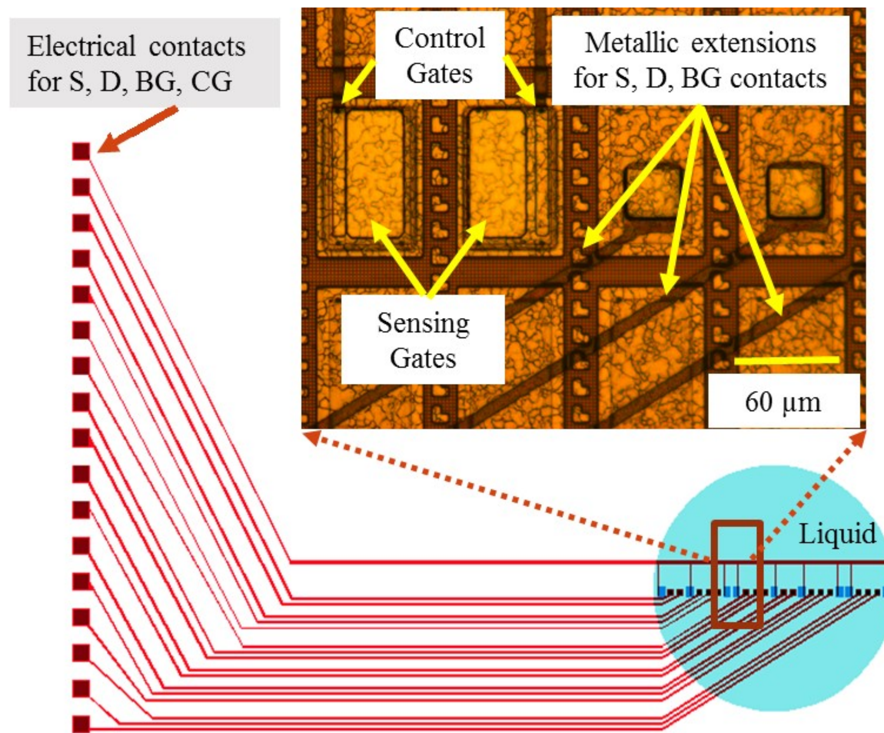

Figure A- 12 Contour des capteurs fabriqués, avec l'image optique comme encart et une gouttelette de pH distribuée sur la zone de détection [38]

Les capteurs de pH intégrés dans l'extrémité arrière de la ligne ont été caractérisés dans une plage de pH plus large (la réponse mesurée est indiquée ci-dessous sur la figure A-13). Pour l'évaluation de la sensibilité en termes de décalage de la tension de seuil en fonction du changement de pH, des balayages ID-VBG ont été effectués à pH 4, pH 7 et pH 10. Une sensibilité expérimentale de 730 mV/pH est obtenue, ce qui confirme le modèle mathématique et le résultat de la simulation. Ceci est plus de 12 fois supérieur à la limite de Nernst et supérieur aux capteurs de l'état de l'art.

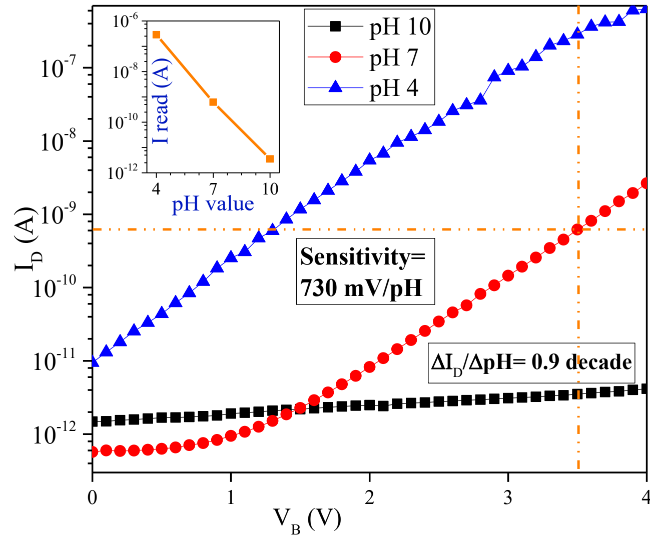

Figure A- 13 Sensibilité des capteurs de pH intégrés BEOL

A6. Détection à la diode

Une conception plus robuste a été adoptée pour intégrer des capteurs sur plus de dispositifs par puce et pour fonctionnaliser la détection au niveau de la grille avant ou de la diode de protection de la grille, le tout sur la même puce. Le bloc de transistors sélectionné et la structure d'extension métallique sont illustrés ci-dessous à la Fig. A-14.

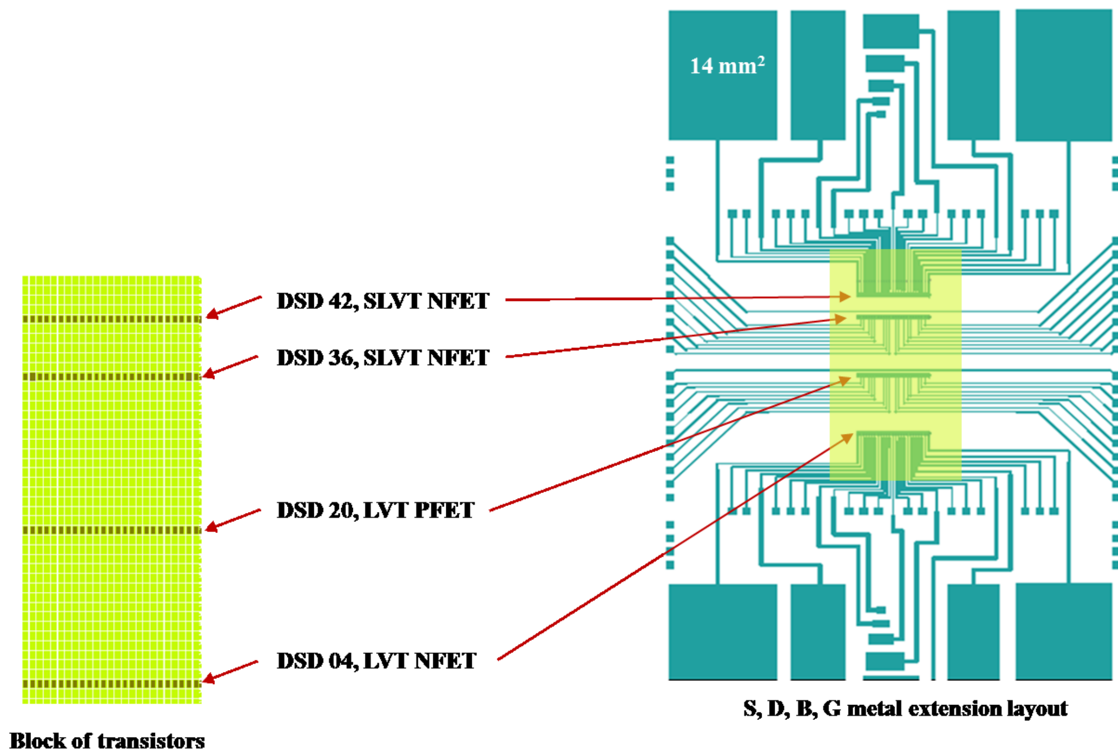

Figure A- 14 Les rangées sélectionnées de transistors (à gauche) et le contour des capteurs à la surface de la puce (à droite)

La figure A-15 montre le contour général du masque indiquant les différentes zones de détection, extensions métalliques et contacts électriques, grilles de contrôle, marques d'alignement, verniers, etc. Les 18 dispositifs des blocs DSD-04 et DSD-42 sont intégrés de façon que les capteurs basés sur ces transistors puissent détecter le pH à travers la grille avant ou la diode de protection de grille.

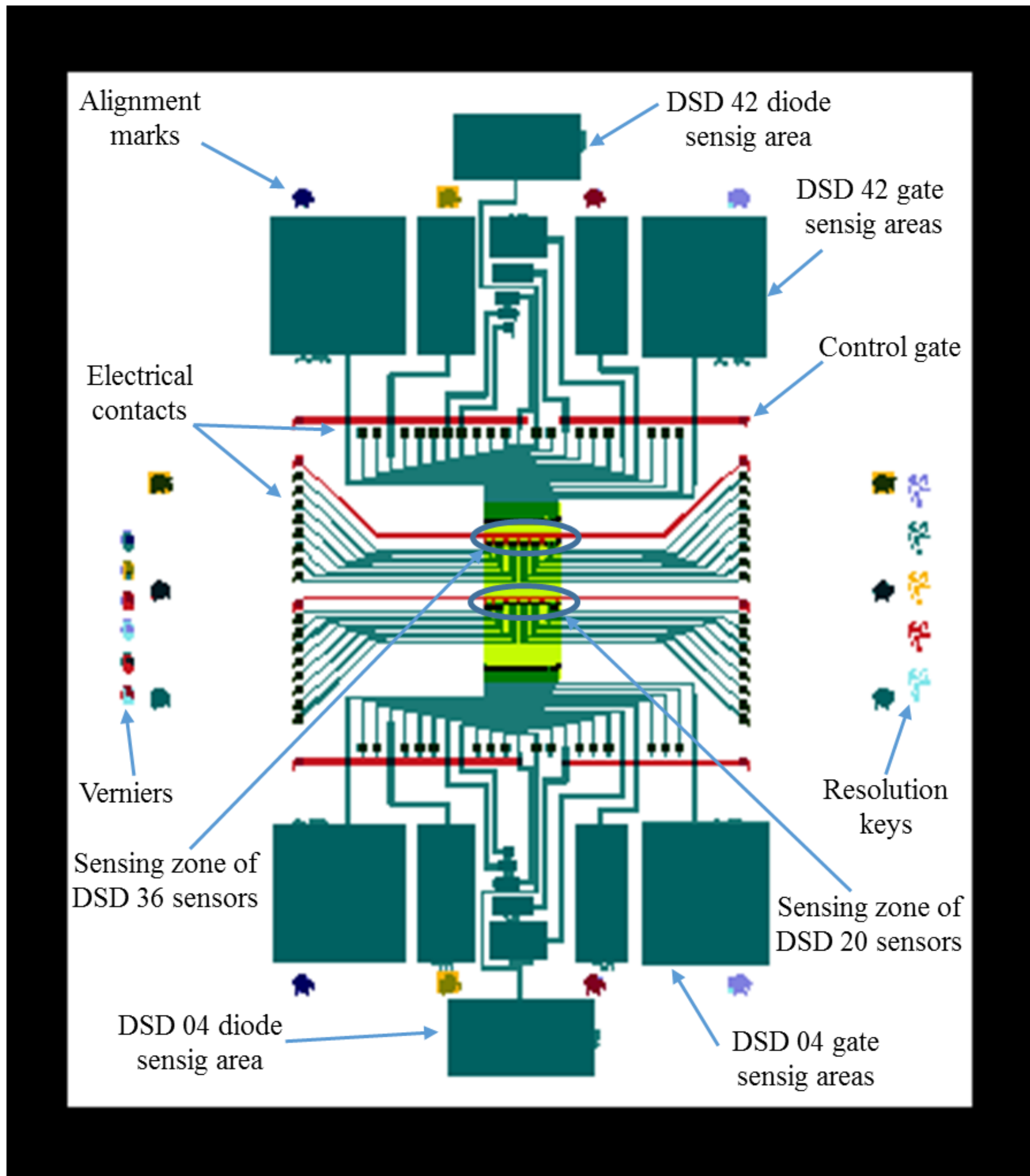

Figure A- 15 Disposition générale du masque

Le nouveau capteur de pH, dans lequel la détection est effectuée au niveau de la diode de protection, est démontré avec succès. La commutation de courant abrupte peut potentiellement augmenter la sensibilité de polarisation fixée à 6,6 decade/pH. Nous avons démontré expérimentalement une sensibilité de 1,25 decade/pH supérieure à la sensibilité de pointe.

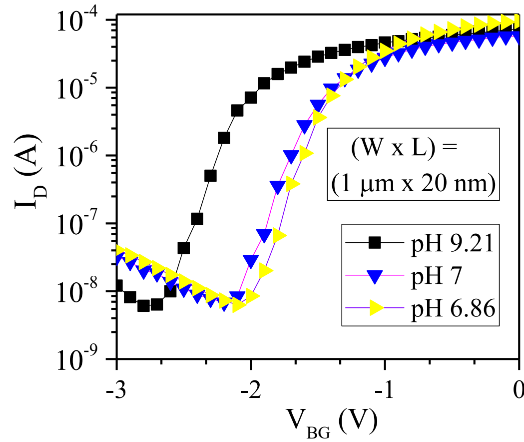

Figure A- 16 Réponse du pH lors de la détection à la diode de protection de grille

A7. Conclusion

Des capteurs ultra-sensibles et compatibles CMOS ont été démontrés avec l’intégration dans le BEOL de transistors industriels UTBB FDSOI. Un circuit diviseur capacitif est utilisé pour la polarisation, ce qui garantit non seulement des performances stables, mais également la compatibilité CMOS du capteur. L'approche proposée et la caractérisation expérimentale ont été validées par modélisation et simulation TCAD Sentaurus. La sensibilité de nos capteurs, aussi bien pour les applications à courant fixe que pour les applications à polarisation fixe, est supérieure à l’état de l’art. Les benchmarks sont fournis ci-dessous dans les figures A.17 et A.18.

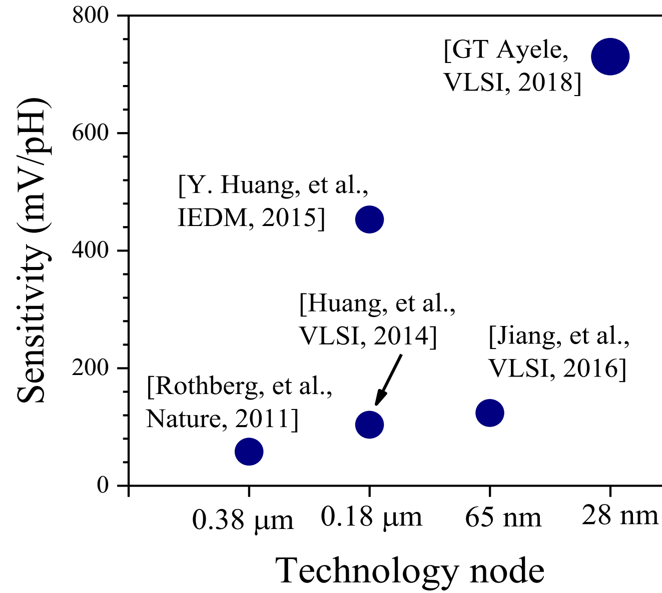

Figure A- 17 Benchmark de sensibilité du capteur pour la lecture de courant fixe.

La particularité des transistors UTBB FDSOI est l'existence d'un fort couplage électrostatique entre la grille avant et la grille arrière et que les capacités asymétriques sur ces deux grilles offrent une possibilité d'amplification intrinsèque. Ceci est très important pour le développement de capteurs ultrasensibles basés sur une telle technologie. De plus, la disponibilité de deux grilles est utile pour fonctionnaliser la détection sur une grille et poursuivre l'enregistrement du signal sur l'autre. Ceci élimine la nécessité d'appliquer un biais variable au niveau de la grille avant, ce qui introduirait autrement un facteur de variabilité et de bruit.

L'intégration des capteurs en bout de ligne présente plusieurs avantages par rapport à l'exposition directe de l'oxyde de grille à l'environnement liquide. Cela englobe les avantages de plus de fiabilité et de durée de vie, la compatibilité avec le processus CMOS standard et l'intégration d'un circuit diviseur capacitif.

Le fonctionnement des MOSFETs sans un biais approprié de la grille avant les rend vulnérables aux effets corporels flottants indésirables. Le circuit diviseur capacitif résout ces problèmes en polarisant la grille avant simultanément avec la fonctionnalité de détection sur la même grille par couplage capacitif à un métal BEOL commun. Par conséquent, le potentiel au niveau du métal BEOL serait une somme pondérée du potentiel de surface au niveau de la grille de détection et du biais appliqué au niveau de la grille de contrôle.

Cette approche proposée pour le développement de biocapteurs et de produits chimiques ultra sensibles et compatibles CMOS a été validée par modélisation et simulation, puis confirmée expérimentalement par un

capteur de pH à grille étendue avec validation du concept. Enfin, les capteurs ont été intégrés au BEOL des transistors, ce qui a permis d'obtenir des performances qui confirment les attentes théoriques, les travaux de simulation et les résultats de la preuve de concept.

Nous avons également fabriqué et testé des capteurs de pH dans lesquels la détection est effectuée au niveau de la diode de protection de la grille plutôt que de la grille avant. Bien que la sensibilité théorique puisse atteindre 6,6 decade/pH, une sensibilité expérimentale de 1,25 decade/pH a été démontrée. Ce résultat est plus élevé que la sensibilité de pointe qui est inférieure à 0,9 decade/pH.

Plusieurs contributions originales ont été faites dans cette thèse. C'est pour la première fois que des capteurs de pH ultra-sensibles et compatibles CMOS sont intégrés au BEOL des dispositifs industriels UTBB FDSOI. L'ultra thin body and BOX permet un couplage efficace entre la grille avant et la grille arrière et l'utilisation de la grille arrière pour l'enregistrement du signal à des tensions plus basses. Cela a offert les avantages d'une sensibilité ultra-élevée et d'un fonctionnement à basse tension. D'autre part, le circuit diviseur capacitif était crucial pour le fonctionnement stable du capteur, permettant à la fois la compatibilité CMOS. Dans la modélisation de tels capteurs, nous avons développé une seule équation mathématique liant la sortie du capteur en fonction du pH de la solution et les paramètres de conception du transistor UTBB FDSOI et du circuit diviseur capacitif. Nous avons également démontré pour la première fois la fonctionnalité de détection du pH à travers la diode de protection de grille du FDSOI standard.

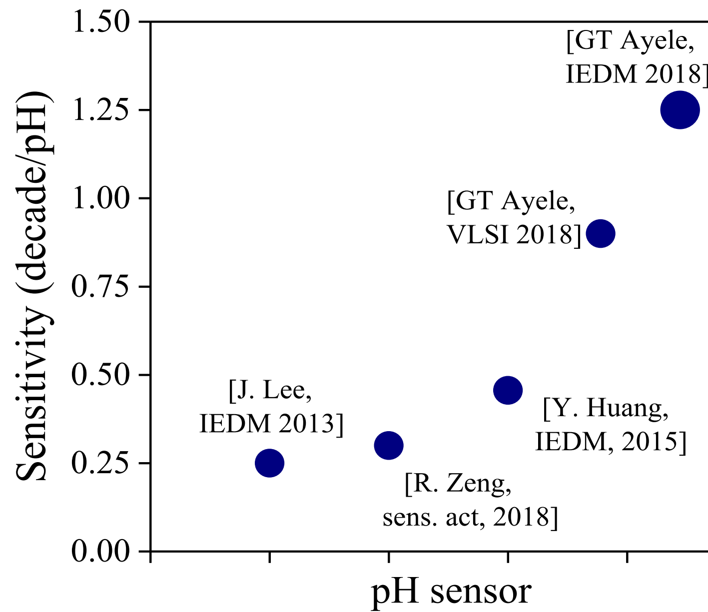

Figure A- 18 Benchmark de sensibilité de notre capteur pour la lecture de biais fixe.

En perspective, les travaux de développement suivants sont suggérés:

- Intégration du capteur dans son propre circuit de lecture et d'encapsulation,
- Intégration d'une structure micro fluidique au sommet d'un réseau de capteurs pour la détection multi-ions,
- Plus de capteurs sur la technologie FDSOI: capteurs de gaz, capteurs d'ions biologiques (Na^+, K^+, Ca^{++}), etc
- Etude rigoureuse et une modélisation de la cinétique de réaction à l'interface EI.

APPENDIX-II

SIMULATION CODES

The default code of TCAD Sentaurus has been followed for the development of the FDSOI transistor, except the user defined specifications. Below are the major user defined/adapted codes used for simulation of the sensor.

S-Process:

```
## ---------- Sensing Film Deposition --------------------------------
mask name= NFILM left= 0.0 right= 0.151 negative
etch material= {PolySilicon} rate= {$TPoly} type= anisotropic time= 1.2 mask= NFILM
deposit Nitride thickness= 0.006 anisotropic selective.material= {TiNitride} temperature= 500<C>
strip Photoresist
if { $debug } { WriteBND }

## ---------- Capacitive Divider Circuit --------------------------------
mask name= CDivider left= 0.0 right= 0.148 negative
deposit Oxide thickness= 0.001 anisotropic mask= CDivider
if { $debug } { WriteBND }

##---------------Remeshing for device simulation--------##
# clear the process simulation mesh
refinebox clear
refinebox !keep.lines
line clear
contact name= "ContGate"   point  xlo= -0.0136 ylo= 0.148 xhi= -0.0134 yhi= 0.150
contact name= "SENSGate"   point  xlo= -0.0336 ylo= -0.03 xhi= -0.0334 yhi= 0.028
contact name= "FloatGate"  point  x= -0.005  y=0.0
contact name= "drain"  point  x= -0.02  y= $Ymax-0.001  NickelSilicide adjacent.material= Silicon
```

```
contact name= "source" point  x= -0.02  y= -$Ymax+0.001 NickelSilicide adjacent.material= Silicon
contact name= "substrate" Silicon bottom
exit
```

S-Device:

```
struct tdr= n@node@ !gas
#define _VdLin_  -0.05
#define _VdSat_  @<-1*Vdd>@
#define _Vbg_    @<-1*Vbg>@
#define _WF_     4.71
#endif

Electrode {
  { Name="source"    Voltage= 0.0 }
  { Name="drain"     Voltage= 0.0 }
  { name="ContGate" voltage= @VCG@ Workfunction= _WF_ }
  { name="FloatGate" charge=0 FGcap= (value= @CAPACG@ name="ContGate") }
  { Name="substrate" Voltage= 0.0 }
}

Physics (MaterialInterface= "Nitride/Oxide"){
        Charge (
                Conc= @Chrg@
        )
}

#-- Vg sweep for Vd=VdLin
 NewCurrentFile= "IdVg_VdLin_"
 Load ( FilePrefix= "n@node@_VdLin" )
 Quasistationary(
```

```
    DoZero
    InitialStep= 1e-2 Increment= 1.1
    MinStep= 1e-6 MaxStep= 0.05
    Goal { Name= "substrate" Voltage= _Vbg_ }
  ){ Coupled { Poisson _CAR_ _DG_ } }

  #-- Vg sweep for Vd=VdSat
  NewCurrentFile= "IdVg_VdSat_"
  Load ( FilePrefix= "n@node@_VdSat" )
  Quasistationary(
    DoZero
    InitialStep= 1e-2 Increment= 1.1
    MinStep= 1e-6 MaxStep= 0.05
    Goal { Name= "ContGate" Voltage= -0.75 }
    Goal { Name= "substrate" Voltage= _Vbg_ }
  ){ Coupled { Poisson _CAR_ _DG_ } }

}
```

APPENDIX-III

MASKS USED FOR FABRICATION

Design 1:

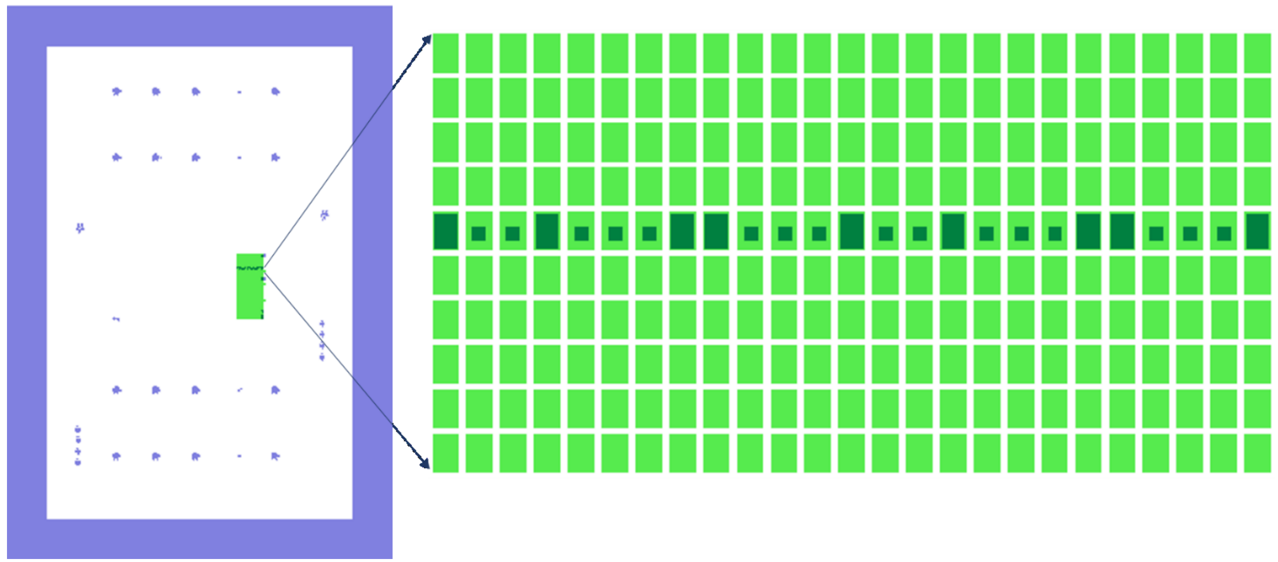

Figure C- 1 Mask UV-1

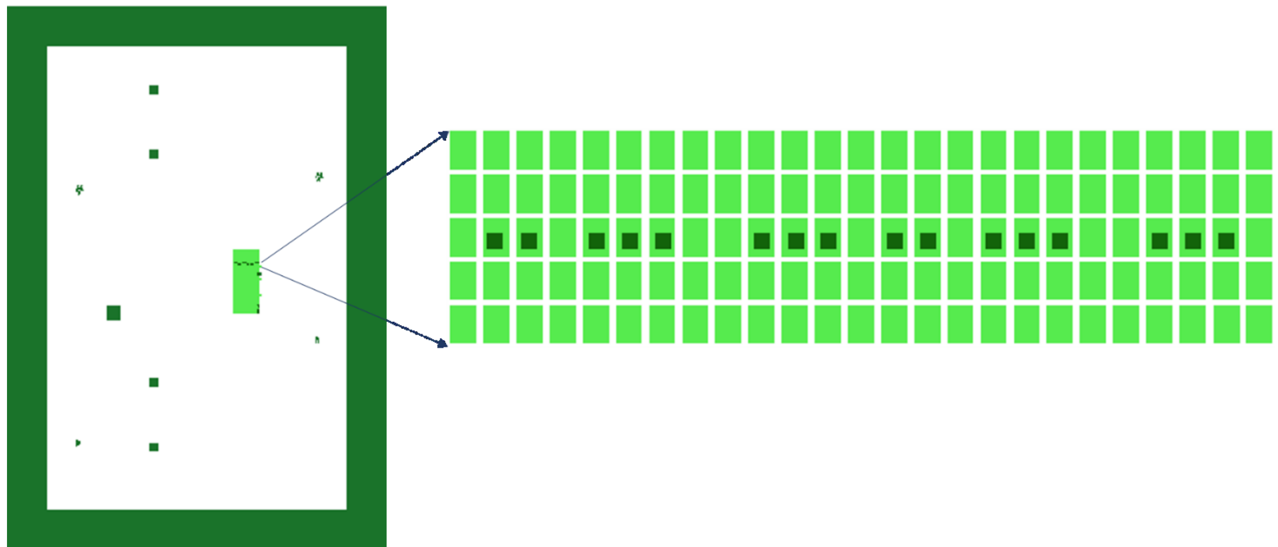

Figure C- 2 Mask UV-2

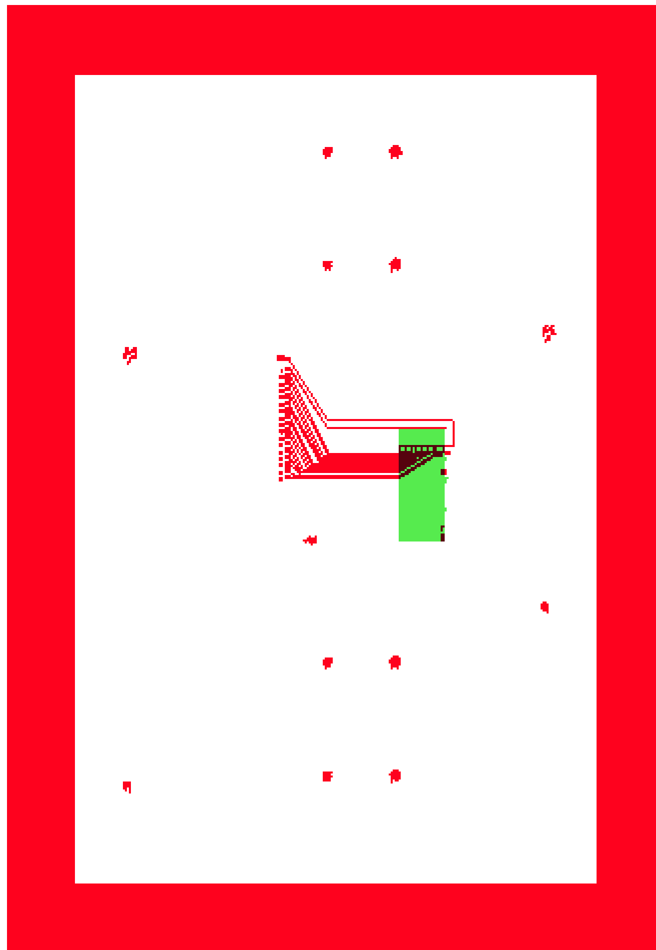

Figure C- 3 Mask UV-3

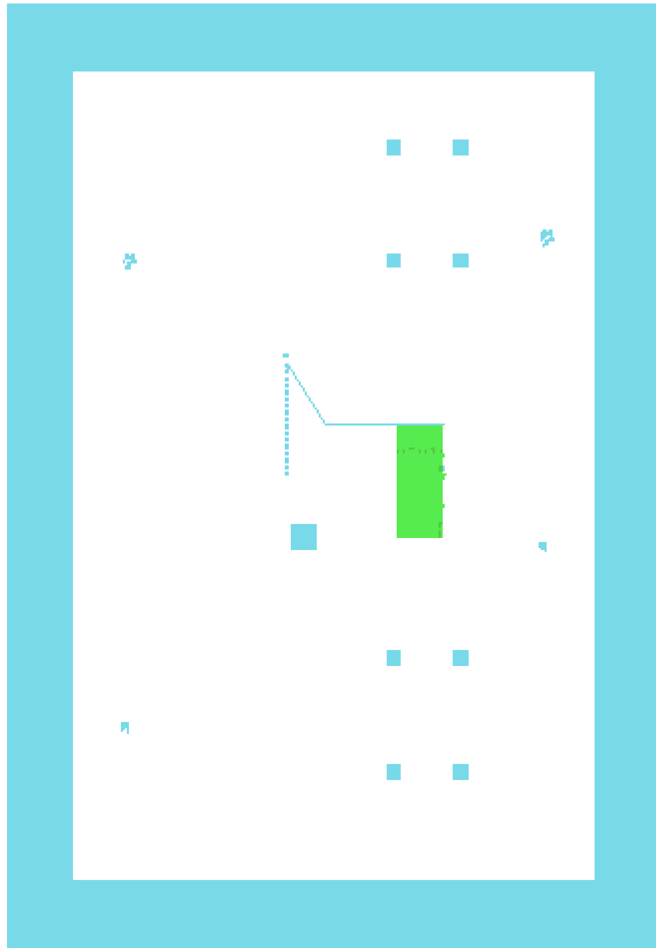

Figure C- 4 Mask UV-4

Design 2:

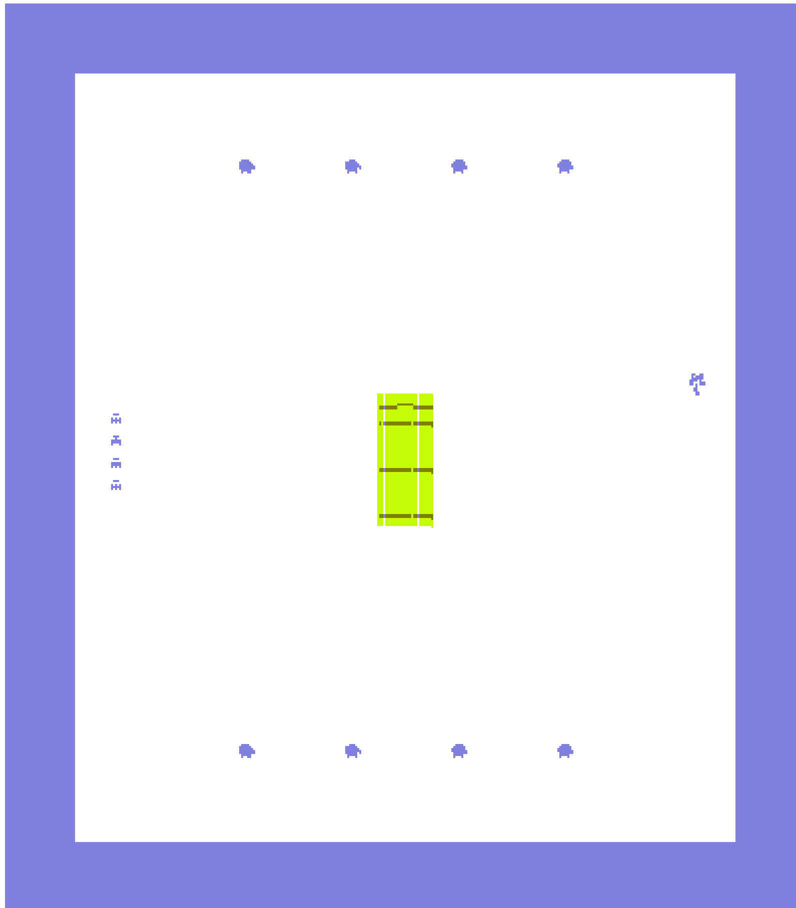

Figure C- 5 Mask UV-1

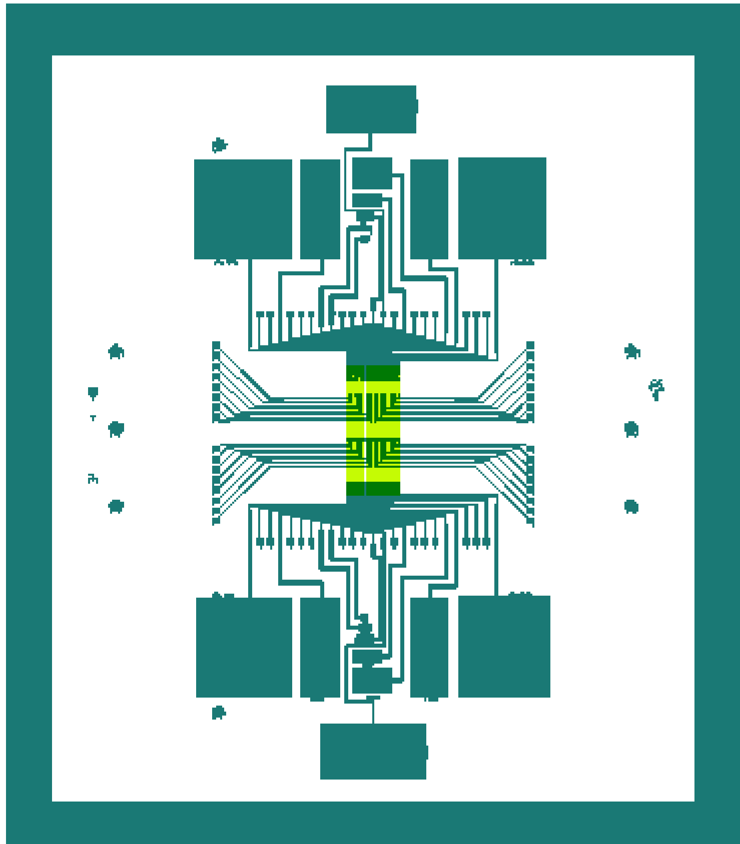

Figure C- 6 Mask UV-2

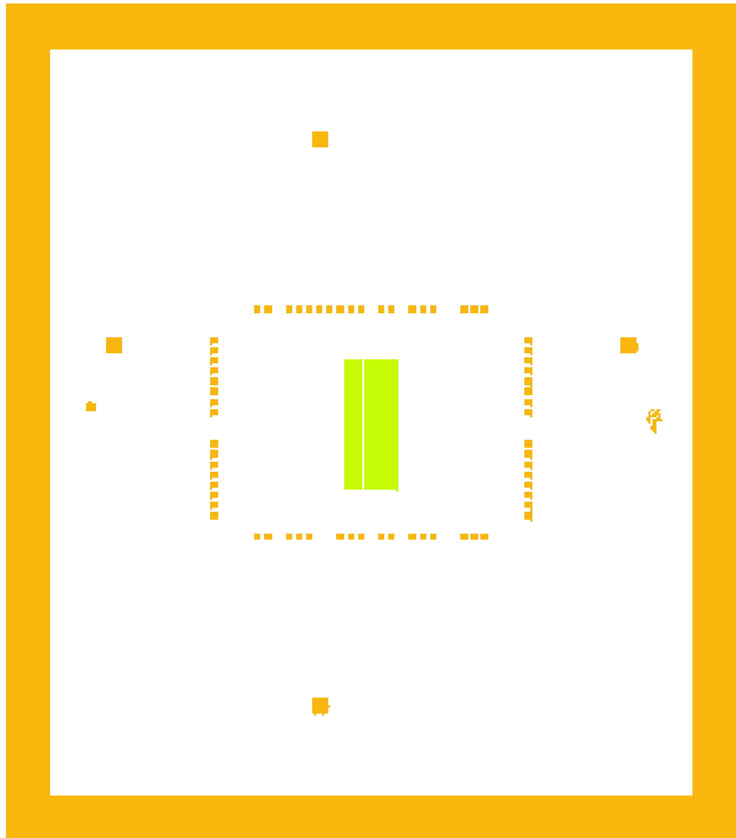

Figure C- 7 Mask UV-3

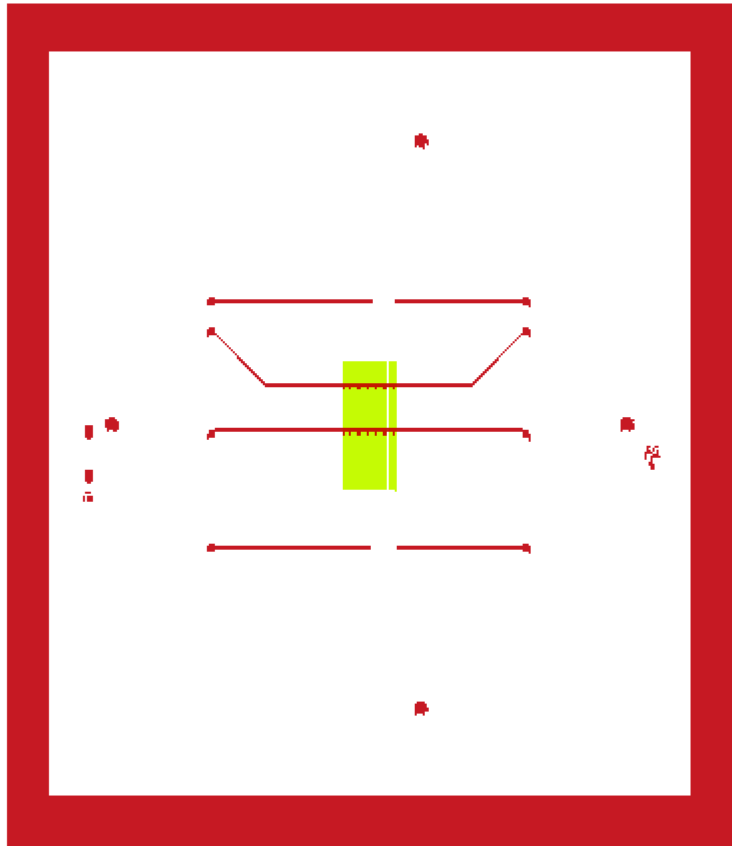

Figure C- 8 Mask UV-4

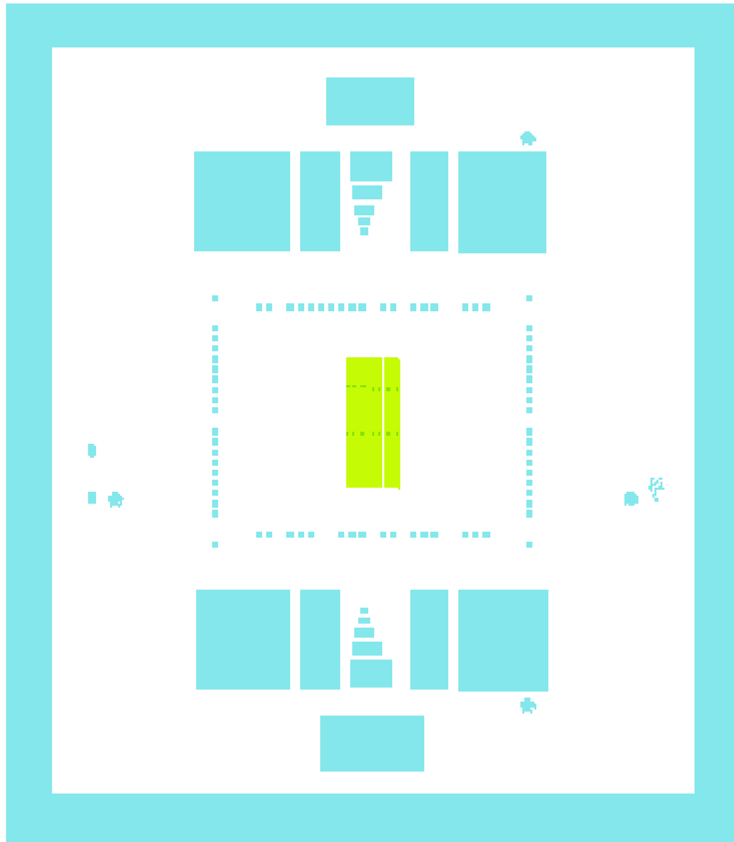

Figure C- 9 Mask UV-5

APPENDIX-IV

PUBLICATIONS

Journal Articles

1. **GT Ayele,** et al. "Ultrahigh-Sensitive CMOS pH Sensor Developed in the BEOL of Standard 28 nm UTBB FDSOI." *IEEE Journal of the Electron Devices Society* 6 (2018): 1026-1032.
2. Rahhal, Lama, **GT Ayele**, et al. "High sensitivity pH sensing on the BEOL of industrial FDSOI transistors." *Solid-State Electronics* 134 (2017): 22-29.

Conference Proceedings

1. **GT Ayele**, et al. "Highly Performant Integrated pH-Sensor Using the Gate Protection Diode in the BEOL of Industrial FDSOI." *2018 IEEE International Electron Devices Meeting*. IEEE, 2018.
2. **GT Ayele**, et al. "Ultrahigh-sensitive and CMOS compatible ISFET developed in BEOL of industrial UTBB FDSOI." *2018 IEEE Symposium on VLSI Technology*. IEEE, 2018.
3. **GT Ayele**, et al. "Development of ultrasensitive extended-gate Ion-sensitive-field-effect-transistor based on industrial UTBB FDSOI transistor." *Solid-State Device Research Conference (ESSDERC), 2017 47th European*. IEEE, 2017.

Poster Presentations

1. **GT Ayele**, et al., "*Developing Ultrasensitive and CMOS Compatible pH-Sensing ISFETs in the BEOL of Industrial UTBB FDSOI Transistors*," IEEE NANO 2018, 23-26 July 2018, Cork, Ireland.
2. **GT Ayele**, et al., " Development of ultrasensitive and CMOS compatible ISFETs based on FDSOI Technology," LN2 Colloque, 8-11 July 2018, Autran, France.

Patents

1. **GT Ayele**, and S. Monfray. "Ion-sensitive field-effect transistor (isfet) having higher sensitivity in response to dynamic biasing." U.S. Patent Application 15/631,078, filed December 27, 2018.
2. **GT Ayele**, and S. Monfray. "Detection device, in particular incorporated in a ph meter, and corresponding production process." U.S. Patent (Submitted).

References

[1] "Industry 4.0: Definition, Design Principles, Challenges, and the Future," *Cleverism*, 16-Jan-2017. [Online]. Available: https://www.cleverism.com/industry-4-0/. [Accessed: 25-Nov-2018].

[2] F. Shrouf, J. Ordieres, and G. Miragliotta, "Smart factories in Industry 4.0: A review of the concept and of energy management approached in production based on the Internet of Things paradigm," in *2014 IEEE International Conference on Industrial Engineering and Engineering Management*, 2014, pp. 697–701.

[3] J. Wan *et al.*, "Software-Defined Industrial Internet of Things in the Context of Industry 4.0," *IEEE Sens. J.*, vol. 16, no. 20, pp. 7373–7380, Oct. 2016.

[4] M. Wollschlaeger, T. Sauter, and J. Jasperneite, "The Future of Industrial Communication: Automation Networks in the Era of the Internet of Things and Industry 4.0," *IEEE Ind. Electron. Mag.*, vol. 11, no. 1, pp. 17–27, Mar. 2017.

[5] D. E. O'Leary, "Artificial Intelligence and Big Data," *IEEE Intell. Syst.*, vol. 28, no. 2, pp. 96–99, Mar. 2013.

[6] X. Wu, X. Zhu, G. Wu, and W. Ding, "Data mining with big data," *IEEE Trans. Knowl. Data Eng.*, vol. 26, no. 1, pp. 97–107, Jan. 2014.

[7] R. Bogue, "Towards the trillion sensors market," *Sens. Rev.*, vol. 34, no. 2, pp. 137–142, 2014.

[8] "Sensor Market by Type - Global Opportunity Analysis and Industry Forecast, 2014 - 2022," *Allied Market Research*. [Online]. Available: https://www.alliedmarketresearch.com/sensor-market. [Accessed: 20-Nov-2018].

[9] F.-G. Banica, *Chemical sensors and biosensors: fundamentals and applications*. John Wiley & Sons, 2012.

[10] C.-L. Hsu and J. C.-C. Lin, "An empirical examination of consumer adoption of Internet of Things services: Network externalities and concern for information privacy perspectives," *Comput. Hum. Behav.*, vol. 62, pp. 516–527, 2016.

[11] D. Lund, V. Turner, C. MacGillivray, and M. Morales, "Worldwide and Regional Internet of Things (IoT) 2014–2020 Forecast: A Virtuous Circle of Proven Value and Demand," p. 29.

[12] "Petr Vanysek, The glass pH electrode.pdf." .

[13] T. P. Jones and M. D. Porter, "Optical pH sensor based on the chemical modification of a porous polymer film," *Anal. Chem.*, vol. 60, no. 5, pp. 404–406, 1988.

[14] U.-W. Grummt, A. Pron, M. Zagorska, and S. Lefrant, "Polyaniline based optical pH sensor," *Anal. Chim. Acta*, vol. 357, no. 3, pp. 253–259, 1997.

[15] Z. Jin, Y. Su, and Y. Duan, "An improved optical pH sensor based on polyaniline," *Sens. Actuators B Chem.*, vol. 71, no. 1–2, pp. 118–122, 2000.

[16] A. Safavi and M. Bagheri, "Novel optical pH sensor for high and low pH values," *Sens. Actuators B Chem.*, vol. 90, no. 1–3, pp. 143–150, 2003.

[17] H. Oh, K. J. Lee, J. Baek, S. S. Yang, and K. Lee, "Development of a high sensitive pH sensor based on shear horizontal surface acoustic wave with ZnO nanoparticles," *Microelectron. Eng.*, vol. 111, pp. 154–159, Nov. 2013.

[18] Q. Y. Cai and C. A. Grimes, "A remote query magnetoelastic pH sensor," *Sens. Actuators B Chem.*, vol. 71, no. 1, pp. 112–117, Nov. 2000.

[19] C. Ruan, K. G. Ong, C. Mungle, M. Paulose, N. J. Nickl, and C. A. Grimes, "A wireless pH sensor based on the use of salt-independent micro-scale polymer spheres," *Sens. Actuators B Chem.*, vol. 96, no. 1, pp. 61–69, Nov. 2003.

[20] J. Z. Hilt, A. K. Gupta, R. Bashir, and N. A. Peppas, "Ultrasensitive Biomems Sensors Based on Microcantilevers Patterned with Environmentally Responsive Hydrogels," *Biomed. Microdevices*, vol. 5, no. 3, pp. 177–184, Sep. 2003.

[21] D. G. Hafeman, J. W. Parce, and H. M. McConnell, "Light-addressable potentiometric sensor for biochemical systems," *Science*, vol. 240, no. 4856, pp. 1182–1185, 1988.

[22] J. C. Owicki *et al.*, "The light-addressable potentiometric sensor: principles and biological applications," *Annu. Rev. Biophys. Biomol. Struct.*, vol. 23, no. 1, pp. 87–114, 1994.

[23] A. Seki, S. Ikeda, I. Kubo, and I. Karube, "Biosensors based on light-addressable potentiometric sensors for urea, penicillin and glucose," *Anal. Chim. Acta*, vol. 373, no. 1, pp. 9–13, 1998.

[24] T. Yoshinobu *et al.*, "The light-addressable potentiometric sensor for multi-ion sensing and imaging," *Methods*, vol. 37, no. 1, pp. 94–102, 2005.

[25] P. Bergveld, "Development of an Ion-Sensitive Solid-State Device for Neurophysiological Measurements," *IEEE Trans. Biomed. Eng.*, vol. BME-17, no. 1, pp. 70–71, Jan. 1970.

[26] T. Matsuo and K. D. Wise, "An integrated field-effect electrode for biopotential recording," *IEEE Trans. Biomed. Eng.*, no. 6, pp. 485–487, 1974.

[27] S. D. Moss, C. C. Johnson, and J. Janata, "Hydrogen, Calcium, and Potassium Ion-Sensitive FET Transducers: A Preliminary Report," *IEEE Trans. Biomed. Eng.*, vol. BME-25, no. 1, pp. 49–54, Jan. 1978.

[28] P. A. Comte and J. Janata, "A field effect transistor as a solid-state reference electrode," *Anal. Chim. Acta*, vol. 101, no. 2, pp. 247–252, 1978.

[29] E. H. Nicollian, J. R. Brews, and E. H. Nicollian, *MOS (metal oxide semiconductor) physics and technology*, vol. 1987. Wiley New York et al., 1982.

[30] "pH Sensor Market Report - Forecast to 2023 | MRFR." [Online]. Available: https://www.marketresearchfuture.com/reports/ph-sensor-market-5178. [Accessed: 20-Nov-2018].

[31] J.-P. Colinge, "Reduction of floating substrate effect in thin-film SOI MOSFETs," *Electron. Lett.*, vol. 22, no. 4, pp. 187–188, 1986.

[32] J. G. Fossum, R. Sundaresan, and M. Matloubian, "Anomalous subthreshold current—Voltage characteristics of n-channel SOI MOSFET's," *IEEE Electron Device Lett.*, vol. 8, no. 11, pp. 544–546, 1987.

[33] J.-P. Colinge, *Silicon-on-insulator technology: materials to VLSI: materials to Vlsi*. Springer Science & Business Media, 2004.

[34] C. G. Jakobson and Y. Nemirovsky, "1/f noise in ion sensitive field effect transistors from subthreshold to saturation," *IEEE Trans. Electron Devices*, vol. 46, no. 1, pp. 259–261, 1999.

[35] V. K. Khanna, "Remedial and adaptive solutions of ISFET non-ideal behaviour," *Sens. Rev.*, vol. 33, no. 3, pp. 228–237, Jun. 2013.

[36] K.-Y. Park, S.-B. Choi, M. Lee, B.-K. Sohn, and S.-Y. Choi, "ISFET glucose sensor system with fast recovery characteristics by employing electrolysis," *Sens. Actuators B Chem.*, vol. 83, no. 1, pp. 90–97, Mar. 2002.

[37] R. E. G. Van Hal, P. Bergveld, J. F. Engbersen, and D. N. Reinhoudt, "Characterization and testing of polymer-oxide adhesion to improve the packaging reliability of ISFETs," *Sens. Actuators B Chem.*, vol. 23, no. 1, pp. 17–26, 1995.

[38] G. T. Ayele *et al.*, "Ultrahigh-Sensitive CMOS pH Sensor Developed in the BEOL of Standard 28 nm UTBB FDSOI," *IEEE J. Electron Devices Soc.*, vol. 6, pp. 1026–1032, 2018.

[39] H. Abe, M. Esashi, and T. Matsuo, "ISFET's using inorganic gate thin films," *IEEE Trans. Electron Devices*, vol. 26, no. 12, pp. 1939–1944, Dec. 1979.

[40] J.-L. Chiang, S.-S. Jan, J.-C. Chou, and Y.-C. Chen, "Study on the temperature effect, hysteresis and drift of pH-ISFET devices based on amorphous tungsten oxide," *Sens. Actuators B Chem.*, vol. 76, no. 1, pp. 624–628, 2001.

[41] P. Bergveld, "Development, Operation, and Application of the Ion-Sensitive Field-Effect Transistor as a Tool for Electrophysiology," *IEEE Trans. Biomed. Eng.*, vol. BME-19, no. 5, pp. 342–351, Sep. 1972.

[42] J. N. Zemel, "Ion-sensitive field effect transistors and related devices," *Anal. Chem.*, vol. 47, no. 2, pp. 255A–268a, 1975.

[43] D. E. Yates, "The structure of the oxide/aqueous electrolyte interface," University of Melbourne Melbourne, 1975.

[44] S. D. Moss, J. Janata, and C. C. Johnson, “Potassium ion-sensitive field effect transistor,” *Anal. Chem.*, vol. 47, no. 13, pp. 2238–2243, 1975.

[45] T. Matsuo and M. Esashi, “Methods of ISFET fabrication,” *Sens. Actuators*, vol. 1, pp. 77–96, 1981.

[46] R. M. Cohen, R. J. Huber, J. Janata, R. W. Ure Jr, and S. D. Moss, “A study of insulator materials used in ISFET gates,” *Thin Solid Films*, vol. 53, no. 2, pp. 169–173, 1978.

[47] J. W. Perram, R. J. Hunter, and H. J. L. Wright, “The oxide-solution interface,” *Aust. J. Chem.*, vol. 27, no. 3, pp. 461–475, 1974.

[48] R. G. Kelly and A. E. Owen, “Microelectronic ion sensors: A critical survey,” *IEE Proc. -Solid-State Electron Devices*, vol. 132, no. 5, pp. 227–236, 1985.

[49] A. K. Covington and A. Sibbald, “Offset-gate chemical-sensitive field-effect transistors (OG-CHEMFETS) with electrolytically-programmable selectivity,” 4437969, Mar-1984.

[50] A. K. Covington and A. Sibbald, “Offset-gate chemical-sensitive field-effect transistors (OG-CHEMFETS) with electrolytically-programmable selectivity,” US4437969 A, 20-Mar-1984.

[51] J. van der spiegel, I. Lauks, P. Chan, and D. Babic, “The extended gate chemically sensitive field effect transistor as multi-species microprobe,” *Sens. Actuators*, vol. 4, no. Supplement C, pp. 291–298, Jan. 1983.

[52] L. Bousse, J. Shott, and J. D. Meindl, “A process for the combined fabrication of ion sensors and CMOS circuits,” *IEEE Electron Device Lett.*, vol. 9, no. 1, pp. 44–46, 1988.

[53] J. Bausells, J. Carrabina, A. Errachid, and A. Merlos, “Ion-sensitive field-effect transistors fabricated in a commercial CMOS technology,” *Sens. Actuators B Chem.*, vol. 57, no. 1–3, pp. 56–62, 1999.

[54] N. Y. Shen, Z. Liu, B. A. Minch, and E. C. Ken, “The chemoreceptive neuron MOS transistors (C/spl nu/MOS): a novel floating-gate device for molecular and chemical sensing,” in *TRANSDUCERS, Solid-State Sensors, Actuators and Microsystems, 12th International Conference on, 2003*, 2003, vol. 1, pp. 69–72 vol.1.

[55] A. Cohen, M. E. Spira, S. Yitshaik, G. Borghs, O. Shwartzglass, and J. Shappir, “Depletion type floating gate p-channel MOS transistor for recording action potentials generated by cultured neurons,” *Biosens. Bioelectron.*, vol. 19, no. 12, pp. 1703–1709, 2004.

[56] P. A. Hammond, D. Ali, and D. R. Cumming, “Design of a single-chip pH sensor using a conventional 0.6-/spl mu/m CMOS process,” *IEEE Sens. J.*, vol. 4, no. 6, pp. 706–712, 2004.

[57] M. J. Milgrew, M. O. Riehle, and D. R. S. Cumming, “A large transistor-based sensor array chip for direct extracellular imaging,” *Sens. Actuators B Chem.*, vol. 111, pp. 347–353, 2005.

[58] M. J. Milgrew, D. R. S. Cumming, and P. A. Hammond, “The fabrication of scalable multi-sensor arrays using standard CMOS technology [chemical sensors],” in *Custom Integrated Circuits Conference, 2003. Proceedings of the IEEE 2003*, 2003, pp. 513–516.

[59] J. M. Rothberg *et al.*, “An integrated semiconductor device enabling non-optical genome sequencing,” *Nature*, vol. 475, no. 7356, pp. 348–352, 2011.

[60] J. Bausells, J. Carrabina, A. Errachid, and A. Merlos, “Ion-sensitive field-effect transistors fabricated in a commercial CMOS technology,” *Sens. Actuators B Chem.*, vol. 57, no. 1–3, pp. 56–62, 1999.

[61] L.-L. Chi, J.-C. Chou, W.-Y. Chung, T.-P. Sun, and S.-K. Hsiung, “Study on extended gate field effect transistor with tin oxide sensing membrane,” *Mater. Chem. Phys.*, vol. 63, no. 1, pp. 19–23, 2000.

[62] L.-T. Yin, J.-C. Chou, W.-Y. Chung, T.-P. Sun, and S.-K. Hsiung, “Separate structure extended gate H+-ion sensitive field effect transistor on a glass substrate,” *Sens. Actuators B Chem.*, vol. 71, no. 1–2, pp. 106–111, 2000.

[63] Y.-L. Chin, J.-C. Chou, Z.-C. Lei, T.-P. Sun, W.-Y. Chung, and S.-K. Hsiung, “Titanium nitride membrane application to extended gate field effect transistor pH sensor using VLSI technology,” *Jpn. J. Appl. Phys.*, vol. 40, no. 11R, p. 6311, 2001.

[64] Y.-L. Chin, J.-C. Chou, T.-P. Sun, W.-Y. Chung, and S.-K. Hsiung, “A novel pH sensitive ISFET with on chip temperature sensing using CMOS standard process,” *Sens. Actuators B Chem.*, vol. 76, no. 1–3, pp. 582–593, 2001.

[65] Y.-L. Chin, J.-C. Chou, T.-P. Sun, H.-K. Liao, W.-Y. Chung, and S.-K. Hsiung, “A novel SnO2/Al discrete gate ISFET pH sensor with CMOS standard process,” *Sens. Actuators B Chem.*, vol. 75, no. 1–2, pp. 36–42, 2001.

[66] L.-T. Yin, J.-C. Chou, W.-Y. Chung, T.-P. Sun, and S.-K. Hsiung, “Study of indium tin oxide thin film for separative extended gate ISFET,” *Mater. Chem. Phys.*, vol. 70, no. 1, pp. 12–16, 2001.

[67] J.-C. Chen, J.-C. Chou, T.-P. Sun, and S.-K. Hsiung, “Portable urea biosensor based on the extended-gate field effect transistor,” *Sens. Actuators B Chem.*, vol. 91, no. 1–3, pp. 180–186, 2003.

[68] J.-C. Chou, P.-K. Kwan, and Z.-J. Chen, “SnO2 separative structure extended gate H+-ion sensitive field effect transistor by the sol–gel technology and the readout circuit developed by source follower,” *Jpn. J. Appl. Phys.*, vol. 42, no. 11R, p. 6790, 2003.

[69] P. D. Batista and M. Mulato, “ZnO extended-gate field-effect transistors as p H sensors,” *Appl. Phys. Lett.*, vol. 87, no. 14, p. 143508, 2005.

[70] R. Zeng, J. Zhang, C. Sun, M. Xu, S.-L. Zhang, and D. Wu, “A reference-less semiconductor ion sensor,” *Sens. Actuators B Chem.*, vol. 254, pp. 102–109, 2018.

[71] B. Zhao, T. Sai, A. Rahman, and K. Levon, “Floating-Gate Ion Sensitive Field-Effect Transistor for Chemical and Biological Sensing,” *MRS Online Proc. Libr. Arch.*, vol. 828, 2004.

[72] Y. Jiang *et al.*, “A 512$\times$ 576 65-nm CMOS ISFET sensor for food safety screening with 123.8 mV/pH sensitivity and 0.01 pH resolution,” in *VLSI Technology, 2016 IEEE Symposium on*, 2016, pp. 1–2.

[73] X. Huang, F. Wang, J. Guo, M. Yan, Y. Hao, and K. S. Yeo, “A 64$\times$ 64 1200fps CMOS ion-image sensor with suppressed fixed-pattern-noise for accurate high-throughput DNA sequencing,” in *VLSI Circuits Digest of Technical Papers, 2014 Symposium on*, 2014, pp. 1–2.

[74] K. B. Parizi, A. J. Yeh, A. S. Y. Poon, and H. S. P. Wong, “Exceeding Nernst limit (59mV/pH): CMOS-based pH sensor for autonomous applications,” in *2012 International Electron Devices Meeting*, 2012, pp. 24.7.1-24.7.4.

[75] J. Lee *et al.*, “A novel SiNW/CMOS hybrid biosensor for high sensitivity/low noise,” in *Electron Devices Meeting (IEDM), 2013 IEEE International*, 2013, pp. 14–5.

[76] M. Spijkman, E. C. P. Smits, J. F. M. Cillessen, F. Biscarini, P. W. M. Blom, and D. M. De Leeuw, “Beyond the Nernst-limit with dual-gate ZnO ion-sensitive field-effect transistors,” *Appl. Phys. Lett.*, vol. 98, no. 4, p. 043502, 2011.

[77] H.-J. Jang and W.-J. Cho, “Performance Enhancement of Capacitive-Coupling Dual-gate Ion-Sensitive Field-Effect Transistor in Ultra-Thin-Body,” *Sci. Rep.*, vol. 4, Jun. 2014.

[78] Y.-J. Huang *et al.*, “High performance dual-gate ISFET with non-ideal effect reduction schemes in a SOI-CMOS bioelectrical SoC,” in *Electron Devices Meeting (IEDM), 2015 IEEE International*, 2015, pp. 29–2.

[79] A. Al-Ahdal and C. Toumazou, “High gain ISFET based νMOS chemical inverter,” *Sens. Actuators B Chem.*, vol. 171, pp. 110–117, 2012.

[80] L. Rahhal *et al.*, “High sensitivity pH sensing on the BEOL of industrial FDSOI transistors,” *Solid-State Electron.*, vol. 134, no. Supplement C, pp. 22–29, Aug. 2017.

[81] C. Heitzinger and G. Klimeck, “Computational aspects of the three-dimensional feature-scale simulation of silicon-nanowire field-effect sensors for DNA detection,” *J. Comput. Electron.*, vol. 6, no. 1–3, pp. 387–390, 2007.

[82] P. R. Nair and M. A. Alam, “Design considerations of silicon nanowire biosensors,” *IEEE Trans. Electron Devices*, vol. 54, no. 12, pp. 3400–3408, 2007.

[83] E. Stern, A. Vacic, and M. A. Reed, “Semiconducting nanowire field-effect transistor biomolecular sensors,” *IEEE Trans. Electron Devices*, vol. 55, no. 11, pp. 3119–3130, 2008.

[84] X. P. Gao, G. Zheng, and C. M. Lieber, “Subthreshold regime has the optimal sensitivity for nanowire FET biosensors,” *Nano Lett.*, vol. 10, no. 2, pp. 547–552, 2009.

[85] O. Knopfmacher, D. Keller, M. Calame, and C. Schönenberger, “Dual gated silicon nanowire field effect transistors,” *Procedia Chem.*, vol. 1, no. 1, pp. 678–681, 2009.

[86] T. Kudo *et al.*, “Fabrication of Si nanowire field-effect transistor for highly sensitive, label-free biosensing,” *Jpn. J. Appl. Phys.*, vol. 48, no. 6S, p. 06FJ04, 2009.

[87] K. Nishiguchi, N. Clement, T. Yamaguchi, and A. Fujiwara, “Si nanowire ion-sensitive field-effect transistors with a shared floating gate,” *Appl. Phys. Lett.*, vol. 94, no. 16, p. 163106, 2009.

[88] O. Knopfmacher *et al.*, “Nernst limit in dual-gated Si-nanowire FET sensors,” *Nano Lett.*, vol. 10, no. 6, pp. 2268–2274, 2010.

[89] N. Clément, K. Nishiguchi, J. F. Dufreche, D. Guerin, A. Fujiwara, and D. Vuillaume, “A silicon nanowire ion-sensitive field-effect transistor with elementary charge sensitivity,” *Appl. Phys. Lett.*, vol. 98, no. 1, p. 014104, 2011.

[90] S. Kim *et al.*, “Silicon nanowire ion sensitive field effect transistor with integrated Ag/AgCl electrode: pH sensing and noise characteristics,” *Analyst*, vol. 136, no. 23, pp. 5012–5016, 2011.

[91] J. Y. Oh, H.-J. Jang, W.-J. Cho, and M. S. Islam, “Highly sensitive electrolyte-insulator-semiconductor pH sensors enabled by silicon nanowires with Al2O3/SiO2 sensing membrane,” *Sens. Actuators B Chem.*, vol. 171, pp. 238–243, 2012.

[92] M. Zaborowski, D. Tomaszewski, P. Dumania, and P. Grabiec, “From FinFET to nanowire ISFET,” in *Solid-State Device Research Conference (ESSDERC), 2012 Proceedings of the European*, 2012, pp. 165–168.

[93] V. Pachauri, K. Kern, and K. Balasubramanian, “Field-effect-based chemical sensing using nanowire-nanoparticle hybrids: The ion-sensitive metal-semiconductor field-effect transistor,” *Appl. Phys. Lett.*, vol. 102, no. 2, p. 023501, 2013.

[94] T. Rim *et al.*, “Improved electrical characteristics of honeycomb nanowire ISFETs,” *IEEE Electron Device Lett.*, vol. 34, no. 8, pp. 1059–1061, 2013.

[95] K. Kim, T. Rim, C. Park, D. Kim, M. Meyyappan, and J.-S. Lee, “Suspended honeycomb nanowire ISFETs for improved stiction-free performance,” *Nanotechnology*, vol. 25, no. 34, p. 345501, 2014.

[96] D. Nozaki, J. Kunstmann, F. Zörgiebel, and G. Cuniberti, “Influence of surface charge on the transport characteristics of nanowire-field effect transistors in liquid environments,” *Appl. Phys. Lett.*, vol. 106, no. 20, p. 203104, 2015.

[97] Y. Cui, Q. Wei, H. Park, and C. M. Lieber, “Nanowire nanosensors for highly sensitive and selective detection of biological and chemical species,” *Science*, vol. 293, no. 5533, pp. 1289–1292, 2001.

[98] D. Sarkar and K. Banerjee, “Proposal for tunnel-field-effect-transistor as ultra-sensitive and label-free biosensors,” *Appl. Phys. Lett.*, vol. 100, no. 14, p. 143108, 2012.

[99] D. Sarkar, W. Liu, X. Xie, A. C. Anselmo, S. Mitragotri, and K. Banerjee, “MoS2 field-effect transistor for next-generation label-free biosensors,” *ACS Nano*, vol. 8, no. 4, pp. 3992–4003, 2014.

[100] R. Narang, M. Saxena, and M. Gupta, “Comparative analysis of dielectric-modulated FET and TFET-based biosensor,” *IEEE Trans Nanotechnol*, vol. 14, no. 3, pp. 427–435, 2015.

[101] A. Gao, N. Lu, Y. Wang, and T. Li, “Robust ultrasensitive tunneling-FET biosensor for point-of-care diagnostics,” *Sci. Rep.*, vol. 6, p. 22554, 2016.

[102] P. Dwivedi and A. Kranti, “Applicability of Transconductance-to-Current ratio (gm/Ids) as a Sensing Metric for Tunnel FET Biosensors,” *IEEE Sens. J*, vol. 17, no. 4, pp. 1030–1036, 2017.

[103] R. Lee, D. W. Kwon, S. Kim, D. H. Kim, and B.-G. Park, “Investigation of Feasibility of Tunneling Field Effect Transistor (TFET) as Highly Sensitive and Multi-sensing Biosensors,” *J. Semicond. Technol. Sci.*, vol. 17, no. 1, pp. 141–146, 2017.

[104] Z. Lu *et al.*, “Realizing super-steep subthreshold slope with conventional FDSOI CMOS at low-bias voltages,” in *Electron Devices Meeting (IEDM), 2010 IEEE International*, 2010, pp. 16–6.

[105] K. Gopalakrishnan, P. B. Griffin, and J. D. Plummer, “I-MOS: A novel semiconductor device with a subthreshold slope lower than kT/q,” in *Electron Devices Meeting, 2002. IEDM’02. International*, 2002, pp. 289–292.

[106] E.-H. Toh *et al.*, “Impact ionization nanowire transistor with multiple-gates, silicon-germanium impact ionization region, and sub-5 mV/decade subtheshold swing,” in *Electron Devices Meeting, 2007. IEDM 2007. IEEE International*, 2007, pp. 195–198.

[107] A. Padilla, C. W. Yeung, C. Shin, C. Hu, and T.-J. K. Liu, “Feedback FET: A novel transistor exhibiting steep switching behavior at low bias voltages,” in *Electron Devices Meeting, 2008. IEDM 2008. IEEE International*, 2008, pp. 1–4.

[108] J. Zhang, M. De Marchi, P.-E. Gaillardon, and G. De Micheli, “A Schottky-barrier silicon FinFET with 6.0 mV/dec subthreshold slope over 5 decades of current,” in *Electron Devices Meeting (IEDM), 2014 IEEE International*, 2014, pp. 13–4.

[109] H. Kam, D. T. Lee, R. T. Howe, and T.-J. King, “A new nano-electro-mechanical field effect transistor (NEMFET) design for low-power electronics,” in *Electron Devices Meeting, 2005. IEDM Technical Digest. IEEE International*, 2005, pp. 463–466.

[110] S. Heinze, J. Tersoff, R. Martel, V. Derycke, J. Appenzeller, and P. Avouris, “Carbon nanotubes as Schottky barrier transistors,” *Phys. Rev. Lett.*, vol. 89, no. 10, p. 106801, 2002.

[111] S. Rigante *et al.*, “Low power finfet ph-sensor with high-sensitivity voltage readout,” in *Solid-State Device Research Conference (ESSDERC), 2013 Proceedings of the European*, 2013, pp. 350–353.

[112] S. Rigante *et al.*, “High-k dielectric FinFETs towards sensing integrated circuits,” in *Ultimate Integration on Silicon (ULIS), 2013 14th International Conference on*, 2013, pp. 73–76.

[113] S. Rigante *et al.*, "Integrated finfet based sensing in a liquid environment," in *Solid-State Sensors, Actuators and Microsystems (TRANSDUCERS & EUROSENSORS XXVII), 2013 Transducers & Eurosensors XXVII: The 17th International Conference on*, 2013, pp. 681–684.

[114] S. Rigante, M. Wipf, A. Bazigos, K. Bedner, D. Bouvet, and A. M. Ionescu, "Finfet with fully PH-responsive HFO 2 as highly stable biochemical sensor," in *Micro Electro Mechanical Systems (MEMS), 2014 IEEE 27th International Conference on*, 2014, pp. 1063–1066.

[115] M. Zaborowski, D. Tomaszewski, P. Dumania, and P. Grabiec, "From FinFET to nanowire ISFET," in *Solid-State Device Research Conference (ESSDERC), 2012 Proceedings of the European*, 2012, pp. 165–168.

[116] M. J. Schöning and A. Poghossian, "Recent advances in biologically sensitive field-effect transistors (BioFETs)," *Analyst*, vol. 127, no. 9, pp. 1137–1151, 2002.

[117] S. Caras and J. Janata, "Field effect transistor sensitive to penicillin," *Anal. Chem.*, vol. 52, no. 12, pp. 1935–1937, 1980.

[118] A. A. Shul'ga, A. C. Sandrovsky, V. I. Strikha, A. P. Soldatkin, N. F. Starodub, and A. V. El'Skaya, "Overall characterization of ISFET-based glucose biosensor," *Sens. Actuators B Chem.*, vol. 10, no. 1, pp. 41–46, 1992.

[119] D. G. Pijanowska and W. Torbicz, "pH-ISFET based urea biosensor," *Sens. Actuators B Chem.*, vol. 44, no. 1, pp. 370–376, Oct. 1997.

[120] S. Schütz *et al.*, "An insect-based BioFET as a bioelectronic nose," *Sens. Actuators B Chem.*, vol. 65, no. 1–3, pp. 291–295, 2000.

[121] A. B. Kharitonov, M. Zayats, L. Alfonta, E. Katz, and I. Willner, "A novel ISFET-based NAD+-dependent enzyme sensor for lactate," *Sens. Actuators B Chem.*, vol. 76, no. 1, pp. 203–210, Jun. 2001.

[122] B. H. van der Schoot and P. Bergveld, "ISFET based enzyme sensors," *Biosensors*, vol. 3, no. 3, pp. 161–186, 1987.

[123] A. Neidig, G. Popp, and G. Gilbers, "Chemically sensitive field effect transistor having electrode connections," Nov-1980.

[124] H.-H. Van den Vlekkert *et al.*, "A pH-isfet and an integrated ph-pressure sensor with back-side contacts," *Sens. Actuators*, vol. 14, no. 2, pp. 165–176, Jun. 1988.

[125] T. Sakai, I. Amemiya, S. Uno, and M. Katsura, "A Backside contact ISFET with a silicon-insulator-silicon structure," *Sens. Actuators B Chem.*, vol. 1, no. 1–6, pp. 341–344, Jan. 1990.

[126] P. Bergveld, "Thirty years of ISFETOLOGY: What happened in the past 30 years and what may happen in the next 30 years," *Sens. Actuators B Chem.*, vol. 88, no. 1, pp. 1–20, 2003.

[127] T. Katsube, I. Lauks, and J. N. Zemel, “pH-sensitive sputtered iridium oxide films,” *Sens. Actuators*, vol. 2, no. Supplement C, pp. 399–410, Jan. 1981.

[128] T.-F. Lu *et al.*, “Non-ideal effects improvement of SF6 plasma treated hafnium oxide film based on electrolyte–insulator–semiconductor structure for pH-sensor application,” *Microelectron. Reliab.*, vol. 50, no. 5, pp. 742–746, May 2010.

[129] K. A. Yusof, R. Abdul Rahman, M. A. Zulkefle, S. H. Herman, and W. F. H. Abdullah, “EGFET pH Sensor Performance Dependence on Sputtered TiO2 Sensing Membrane Deposition Temperature,” *J. Sens.*, vol. 2016, 2016.

[130] T.-M. Pan, M.-D. Huang, C.-W. Lin, and M.-H. Wu, “Development of high-κ HoTiO 3 sensing membrane for pH detection and glucose biosensing,” *Sens. Actuators B Chem.*, vol. 144, no. 1, pp. 139–145, 2010.

[131] T.-M. Pan, J.-C. Lin, M.-H. Wu, and C.-S. Lai, “Study of high-k Er2O3 thin layers as ISFET sensitive insulator surface for pH detection,” *Sens. Actuators B Chem.*, vol. 138, no. 2, pp. 619–624, May 2009.

[132] T.-M. Pan and K.-M. Liao, “Comparison of structural and sensing characteristics of Pr2O3 and PrTiO3 sensing membrane for pH-ISFET application,” *Sens. Actuators B Chem.*, vol. 133, no. 1, pp. 97–104, Jul. 2008.

[133] Y.-L. Chin, J.-C. Chou, T.-P. Sun, H.-K. Liao, W.-Y. Chung, and S.-K. Hsiung, “A novel SnO2/Al discrete gate ISFET pH sensor with CMOS standard process,” *Sens. Actuators B Chem.*, vol. 75, no. 1–2, pp. 36–42, 2001.

[134] H.-K. Liao, J.-C. Chou, W.-Y. Chung, T.-P. Sun, and S.-K. Hsiung, “Study of amorphous tin oxide thin films for ISFET applications,” *Sens. Actuators B Chem.*, vol. 50, no. 2, pp. 104–109, 1998.

[135] P. D. Batista, M. Mulato, C. de O. Graeff, F. J. R. Fernandez, and F. das C. Marques, “SnO2 extended gate field-effect transistor as pH sensor,” *Braz. J. Phys.*, vol. 36, no. 2A, pp. 478–481, 2006.

[136] K. R. Williams, K. Gupta, and M. Wasilik, “Etch rates for micromachining processing-Part II,” *J. Microelectromechanical Syst.*, vol. 12, no. 6, pp. 761–778, Dec. 2003.

[137] J.-C. Chou and C.-Y. Weng, “Sensitivity and hysteresis effect in Al 2 O 3 gate pH-ISFET,” *Mater. Chem. Phys.*, vol. 71, no. 2, pp. 120–124, 2001.

[138] L. Bousse, D. Hafeman, and N. Tran, “Time-dependence of the chemical response of silicon nitride surfaces,” *Sens. Actuators B Chem.*, vol. 1, no. 1–6, pp. 361–367, 1990.

[139] P. Hein and P. Egger, “Drift behaviour of ISFETs with Si3N4-SiO2 gate insulator,” *Sens. Actuators B Chem.*, vol. 14, no. 1–3, pp. 655–656, 1993.

[140] R. P. Buck, "Kinetics and drift of gate voltages for electrolyte-bathed chemically sensitive semiconductor devices," *Ieee Trans. Electron Devices*, vol. 29, no. 1, pp. 108–115, 1982.

[141] S. Jamasb, S. D. Collins, and R. L. Smith, "A physical model for threshold voltage instability in Si/sub 3/N/sub 4/-gate H/sup+/-sensitive FET's (pH ISFET's)," *IEEE Trans. Electron Devices*, vol. 45, no. 6, pp. 1239–1245, 1998.

[142] S. Jamasb, S. D. Collins, and R. L. Smith, "A physically-based model for drift in Al/sub 2/O/sub 3/-gate pH ISFET's," in *Solid State Sensors and Actuators, 1997. TRANSDUCERS'97 Chicago., 1997 International Conference on*, 1997, vol. 2, pp. 1379–1382.

[143] L. Bousse, S. Mostarshed, B. van der Schoot, and N. F. de Rooij, "Comparison of the hysteresis of Ta2O5 and Si3N4 pH-sensing insulators," *Sens. Actuators B Chem.*, vol. 17, no. 2, pp. 157–164, Jan. 1994.

[144] S. Jamasb, S. Collins, and R. L. Smith, "A physical model for drift in pH ISFETs," *Sens. Actuators B Chem.*, vol. 49, no. 1, pp. 146–155, 1998.

[145] R. G. Kelly, "Microelectronic approaches to solid state ion selective electrodes," *Electrochimica Acta*, vol. 22, no. 1, pp. 1–8, 1977.

[146] J. Janata, "Historical review. Twenty years of ion-selective field-effect transistors," *Analyst*, vol. 119, no. 11, pp. 2275–2278, 1994.

[147] M. Yano, K. Shimada, K. Shibatani, and T. Makimoto, "Reference electrode of insulated gate field effect transistor," May-1981.

[148] S. Tahara, M. Yoshii, and S. Oka, "Electrochemical reference electrode for the ion-selective field effect transistor," *Chem. Lett.*, vol. 11, no. 3, pp. 307–310, 1982.

[149] P. Bergveld, "The impact of MOSFET-based sensors," *Sens. Actuators*, vol. 8, no. 2, pp. 109–127, 1985.

[150] A. van den Berg, P. Bergveld, D. N. Reinhoudt, and E. J. Sudhölter, "Sensitivity control of ISFETs by chemical surface modification," *Sens. Actuators*, vol. 8, no. 2, pp. 129–148, 1985.

[151] M. Chudy, W. Wroblewski, and Z. Brzózka, "Towards REFET," *Sens. Actuators B Chem.*, vol. 57, no. 1–3, pp. 47–50, 1999.

[152] L. Shepherd, P. Georgiou, and C. Toumazou, "A novel voltage-clamped CMOS ISFET sensor interface," in *2007 IEEE International Symposium on Circuits and Systems*, 2007, pp. 3331–3334.

[153] P. Bergveld, A. Van Den Berg, P. D. Van Der Wal, M. Skowronska-Ptasinska, E. J. R. Sudhölter, and D. N. Reinhoudt, "How electrical and chemical requirements for refets may coincide," *Sens. Actuators*, vol. 18, no. 3, pp. 309–327, Jul. 1989.

[154] P. A. Hammond, D. Ali, and D. R. S. Cumming, "Design of a single-chip pH sensor using a conventional 0.6-/spl mu/m CMOS process," *IEEE Sens. J.*, vol. 4, no. 6, pp. 706–712, Dec. 2004.

[155] M. J. Milgrew, D. R. S. Cumming, and P. A. Hammond, "The fabrication of scalable multi-sensor arrays using standard CMOS technology [chemical sensors]," in *Proceedings of the IEEE 2003 Custom Integrated Circuits Conference, 2003.*, 2003, pp. 513–516.

[156] Y. H. Ghallab, W. Badawy, and K. V. I. S. Kaler, "A novel pH sensor using differential ISFET current mode read-out circuit," in *Proceedings International Conference on MEMS, NANO and Smart Systems*, 2003, pp. 255–258.

[157] E. Salm *et al.*, "Electrical detection of nucleic acid amplification using an on-chip quasi-reference electrode and a PVC REFET," *Anal. Chem.*, vol. 86, no. 14, pp. 6968–6975, 2014.

[158] A. Morgenshtein, L. Sudakov-Boreysha, U. Dinnar, C. G. Jakobson, and Y. Nemirovsky, "Wheatstone-Bridge readout interface for ISFET/REFET applications," *Sens. Actuators B Chem.*, vol. 98, no. 1, pp. 18–27, Mar. 2004.

[159] T. Matsuo, H. Nakajima, T. Osa, and J. Anzai, "Parylene-gate isfet and chemical modification of its surface with crown ether compounds," *Sens. Actuators*, vol. 9, no. 2, pp. 115–123, Apr. 1986.

[160] H. H. van den Vlekkert, N. F. de Rooij, A. van den Berg, and A. Grisel, "Multi-ion sensing system based on glass-encapsulated pH-ISFETs and a pseudo-REFET," *Sens. Actuators B Chem.*, vol. 1, no. 1, pp. 395–400, Jan. 1990.

[161] Q. Zhang *et al.*, "Surface functionalization of ion-sensitive floating-gate field-effect transistors with organic electronics," *IEEE Trans. Electron Devices*, vol. 62, no. 4, pp. 1291–1298, 2015.

[162] P. Bergveld, "Thirty years of ISFETOLOGY: What happened in the past 30 years and what may happen in the next 30 years," *Sens. Actuators B Chem.*, vol. 88, no. 1, pp. 1–20, 2003.

[163] Y. Wang *et al.*, "Supercapacitor devices based on graphene materials," *J. Phys. Chem. C*, vol. 113, no. 30, pp. 13103–13107, 2009.

[164] E. Frackowiak, "Carbon materials for supercapacitor application," *Phys. Chem. Chem. Phys.*, vol. 9, no. 15, pp. 1774–1785, 2007.

[165] L. L. Zhang and X. S. Zhao, "Carbon-based materials as supercapacitor electrodes," *Chem. Soc. Rev.*, vol. 38, no. 9, pp. 2520–2531, 2009.

[166] T. M. Squires and M. Z. Bazant, "Induced-charge electro-osmosis," *J. Fluid Mech.*, vol. 509, pp. 217–252, 2004.

[167] E. Garcia-Cordero *et al.*, "Three-Dimensional Integrated Ultra-Low Volume Passive Microfluidics With Ion Sensitive Field Effect Transistors For Multi-Parameter Wearable Sweat Analyzers," *ACS Nano*, 2018.

[168] F. Bellando, E. Garcia-Cordero, F. Wildhaber, J. Longo, H. Guérin, and A. M. Ionescu, "Lab on skin^{TM}: 3D monolithically integrated zero-energy micro/nanofludics and FD SOI ion sensitive FETs

for wearable multi-sensing sweat applications," in *2017 IEEE International Electron Devices Meeting (IEDM)*, 2017, pp. 18–1.

[169] S. Srinivasan, "Electrode/electrolyte interfaces: Structure and kinetics of charge transfer," in *Fuel Cells*, Springer, 2006, pp. 27–92.

[170] H. von Helmholtz, "Ueber einige Gesetze der Vertheilung elektrischer Ströme in körperlichen Leitern, mit Anwendung auf die thierisch-elektrischen Versuche (Schluss.)," *Ann. Phys.*, vol. 165, no. 7, pp. 353–377, 1853.

[171] O. Stern, "Zur theorie der elektrolytischen doppelschicht," *Z. Für Elektrochem. Angew. Phys. Chem.*, vol. 30, no. 21–22, pp. 508–516, 1924.

[172] D. C. Grahame, "The Electrical Double Layer and the Theory of Electrocapillarity.," *Chem. Rev.*, vol. 41, no. 3, pp. 441–501, Dec. 1947.

[173] D. E. Yates, S. Levine, and T. W. Healy, "Site-binding model of the electrical double layer at the oxide/water interface," *J. Chem. Soc. Faraday Trans. 1 Phys. Chem. Condens. Phases*, vol. 70, no. 0, pp. 1807–1818, 1974.

[174] R. E. G. Van Hal, J. C. Eijkel, and P. Bergveld, "A general model to describe the electrostatic potential at electrolyte oxide interfaces," *Adv. Colloid Interface Sci.*, vol. 69, no. 1–3, pp. 31–62, 1996.

[175] Y. G. Berube and P. L. de Bruyn, "Adsorption at the rutile-solution interface: I. Thermodynamic and experimental study," *J. Colloid Interface Sci.*, vol. 27, no. 2, pp. 305–318, 1968.

[176] S. Levine and A. L. Smith, "Theory of the differential capacity of the oxide/aqueous electrolyte interface," *Discuss. Faraday Soc.*, vol. 52, pp. 290–301, 1971.

[177] J. W. Perram, R. J. Hunter, and H. J. L. Wright, "Charge and potential at the oxide/solution interface," *Chem. Phys. Lett.*, vol. 23, no. 2, pp. 265–269, 1973.

[178] D. E. Yates, S. Levine, and T. W. Healy, "Site-binding model of the electrical double layer at the oxide/water interface," *J. Chem. Soc. Faraday Trans. 1 Phys. Chem. Condens. Phases*, vol. 70, pp. 1807–1818, 1974.

[179] J. A. Davis, R. O. James, and J. O. Leckie, "Surface ionization and complexation at the oxide/water interface: I. Computation of electrical double layer properties in simple electrolytes," *J. Colloid Interface Sci.*, vol. 63, no. 3, pp. 480–499, 1978.

[180] G. T. Ayele *et al.*, "Development of ultrasensitive extended-gate Ion-sensitive-field-effect-transistor based on industrial UTBB FDSOI transistor," in *2017 47th European Solid-State Device Research Conference (ESSDERC)*, 2017, pp. 264–267.

[181] W. A. Vitale *et al.*, "A Steep-Slope Transistor Combining Phase-Change and Band-to-Band-Tunneling to Achieve a sub-Unity Body Factor," *Sci. Rep.*, vol. 7, Mar. 2017.

[182] X. P. Gao, G. Zheng, and C. M. Lieber, "Subthreshold regime has the optimal sensitivity for nanowire FET biosensors," *Nano Lett.*, vol. 10, no. 2, pp. 547–552, 2009.

[183] T. Skotnicki and S. Monfray, "UTBB FDSOI: Evolution and opportunities," in *2015 45th European Solid State Device Research Conference (ESSDERC)*, 2015, pp. 76–79.

[184] J.-P. Noel *et al.*, "Multi-$ V_ ${$T$}$ $ UTBB FDSOI device architectures for low-power CMOS circuit," *IEEE Trans. Electron Devices*, vol. 58, no. 8, pp. 2473–2482, 2011.

[185] L. Grenouillet *et al.*, "UTBB FDSOI transistors with dual STI for a multi-V t strategy at 20nm node and below," in *Electron Devices Meeting (IEDM), 2012 IEEE International*, 2012, pp. 3–6.

[186] T. Ernst *et al.*, "Ultimately thin double-gate SOI MOSFETs," *IEEE Trans. Electron Devices*, vol. 50, no. 3, pp. 830–838, 2003.

[187] H.-J. Jang and W.-J. Cho, "Performance enhancement of capacitive-coupling dual-gate ion-sensitive field-effect transistor in ultra-thin-body," *Sci. Rep.*, vol. 4, p. 5284, 2014.

[188] M. Spijkman, E. C. P. Smits, J. F. M. Cillessen, F. Biscarini, P. W. M. Blom, and D. M. De Leeuw, "Beyond the Nernst-limit with dual-gate ZnO ion-sensitive field-effect transistors," *Appl. Phys. Lett.*, vol. 98, no. 4, p. 043502, 2011.

[189] H.-K. Lim and J. G. Fossum, "Threshold voltage of thin-film silicon-on-insulator (SOI) MOSFET's," *IEEE Trans. Electron Devices*, vol. 30, no. 10, pp. 1244–1251, 1983.

[190] D.-I. Moon, J.-W. Han, and M. Meyyappan, "Comparative Study of Field Effect Transistor Based Biosensors," *IEEE Trans. Nanotechnol.*, vol. 15, no. 6, pp. 956–961, 2016.

[191] C. Lombardi, S. Manzini, A. Saporito, and M. Vanzi, "A physically based mobility model for numerical simulation of nonplanar devices," *IEEE Trans. Comput.-Aided Des. Integr. Circuits Syst.*, vol. 7, no. 11, pp. 1164–1171, Nov. 1988.

[192] S.-L. Li *et al.*, "Thickness-Dependent Interfacial Coulomb Scattering in Atomically Thin Field-Effect Transistors," *Nano Lett.*, vol. 13, no. 8, pp. 3546–3552, Aug. 2013.

[193] M. V. Fischetti, D. A. Neumayer, and E. A. Cartier, "Effective electron mobility in Si inversion layers in metal–oxide–semiconductor systems with a high-κ insulator: The role of remote phonon scattering," *J. Appl. Phys.*, vol. 90, no. 9, pp. 4587–4608, Oct. 2001.

[194] D. L. Harame, L. J. Bousse, J. D. Shott, and J. D. Meindl, "Ion-sensing devices with silicon nitride and borosilicate glass insulators," *IEEE Trans. Electron Devices*, vol. 34, no. 8, pp. 1700–1707, 1987.

[195] S. G. Chamberlain and S. Ramanan, "Drain-induced barrier-lowering analysis in VSLI MOSFET devices using two-dimensional numerical simulations," *IEEE Trans. Electron Devices*, vol. 33, no. 11, pp. 1745–1753, Nov. 1986.

[196] N. Arora, *Mosfet Modeling for VLSI Simulation: Theory and Practice*. World Scientific, 2007.

[197] "SOI device with reduced drain induced barrier lowering," 19-Aug-2004.

[198] A. A. Mutlu and M. Rahman, "Two-dimensional analytical model for drain induced barrier lowering (DIBL) in short channel MOSFETs," in *Proceedings of the IEEE SoutheastCon 2000. "Preparing for The New Millennium" (Cat. No.00CH37105)*, 2000, pp. 340–344.

[199] R. Koh, "Buried Layer Engineering to Reduce the Drain-Induced Barrier Lowering of Sub-0.05 µm SOI-MOSFET," *Jpn. J. Appl. Phys.*, vol. 38, no. 4S, p. 2294, Apr. 1999.

[200] T. Tsuchiya, Y. Sato, and M. Tomizawa, "Three mechanisms determining short-channel effects in fully-depleted SOI MOSFETs," *IEEE Trans. Electron Devices*, vol. 45, no. 5, pp. 1116–1121, May 1998.

[201] C.- Chang, D.-S. Day, and S. Chan, "An analytical two-dimensional simulation for the GaAs MESFET drain-induced barrier lowering: a short-channel effect," *IEEE Trans. Electron Devices*, vol. 37, no. 5, pp. 1182–1186, May 1990.

[202] S. G. Chamberlain and S. Ramanan, "Drain-induced barrier-lowering analysis in VSLI MOSFET devices using two-dimensional numerical simulations," *IEEE Trans. Electron Devices*, vol. 33, no. 11, pp. 1745–1753, Nov. 1986.

[203] G. T. Ayele *et al.*, "Ultrahigh-sensitive and CMOS compatible ISFET developed in BEOL of industrial UTBB FDSOI," in *2018 IEEE Symposium on VLSI Technology*, 2018, pp. 97–98.

[204] "HD – 4100 SERIES Photodefineable, negative, solvent | HD MicroSystems™." [Online]. Available: http://www.hdmicrosystems.com/ec/liquid-polyimides-and-pbo-precursors/products/sub-products/hd-4100-series.html. [Accessed: 14-Nov-2018].

[205] "Photoresist AZ 1512HS Photoresists MicroChemicals GmbH." [Online]. Available: https://www.microchemicals.com/products/photoresists/az_1512_hs.html. [Accessed: 26-Nov-2018].

[206] K. R. Williams, K. Gupta, and M. Wasilik, "Etch rates for micromachining processing-Part II," *J. Microelectromechanical Syst.*, vol. 12, no. 6, pp. 761–778, 2003.

[207] S. L. Ellison, "K. Danzer: Analytical chemistry. Theoretical and metrological fundamentals," *Anal. Bioanal. Chem.*, vol. 392, no. 1, pp. 23–24, 2008.

[208] H.-P. Loock and P. D. Wentzell, "Detection limits of chemical sensors: Applications and misapplications," *Sens. Actuators B Chem.*, vol. 173, pp. 157–163, Oct. 2012.

[209] K. Kalantar-zadeh, "Sensors Characteristics," in *Sensors*, Springer, 2013, pp. 11–28.

[210] "Analytical Measurement Terminology: Handbook of Terms Used in Quality Assurance of Analytical Measurement | E. Prichard | download." [Online]. Available: http://b-ok.cc/book/561897/9b88eb. [Accessed: 15-Nov-2018].

[211] "Uniformity, Repeatability, Stability, and Accuracy." [Online]. Available: https://www.apogeeinstruments.com/uniformity-repeatability-stability-and-accuracy. [Accessed: 15-Nov-2018].

[212] "ISO 5725-1:1994," *ISO*. [Online]. Available: http://www.iso.org/cms/render/live/en/sites/isoorg/contents/data/standard/01/18/11833.html. [Accessed: 15-Nov-2018].

[213] P. J. Potts, "A glossary of terms and definitions used in analytical chemistry," *Geostand. Newsl.*, vol. 21, no. 1, pp. 157–161, 1997.

[214] "Backyard Engineers - Lesson 3: Accuracy and Precision | Filament Games." [Online]. Available: https://www.filamentlearning.com/backyard-engineers-lesson-3-accuracy-and-precision. [Accessed: 15-Feb-2019].

[215] L. C. Yen, M. T. Tang, C. Y. Tan, T. M. Pan, and T. S. Chao, "Effect of Sensing Film Thickness on Sensing Characteristics of Dual-Gate Poly-Si Ion-Sensitive Field-Effect-Transistors," *IEEE Electron Device Lett.*, vol. 35, no. 12, pp. 1302–1304, Dec. 2014.

[216] H. Abe, M. Esashi, and T. Matsuo, "ISFET's using inorganic gate thin films," *IEEE Trans. Electron Devices*, vol. 26, no. 12, pp. 1939–1944, 1979.

[217] S. Baliga, S. Muglikar, and R. Kale, "Salivary pH: A diagnostic biomarker," *J. Indian Soc. Periodontol.*, vol. 17, no. 4, pp. 461–465, 2013.

[218] Y. Jiang *et al.*, "A 512$\times$ 576 65-nm CMOS ISFET sensor for food safety screening with 123.8 mV/pH sensitivity and 0.01 pH resolution," in *VLSI Technology, 2016 IEEE Symposium on*, 2016, pp. 1–2.

[219] X. Huang, F. Wang, J. Guo, M. Yan, Y. Hao, and K. S. Yeo, "A 64$\times$ 64 1200fps CMOS ion-image sensor with suppressed fixed-pattern-noise for accurate high-throughput DNA sequencing," in *VLSI Circuits Digest of Technical Papers, 2014 Symposium on*, 2014, pp. 1–2.

[220] D. Sarkar and K. Banerjee, "Proposal for tunnel-field-effect-transistor as ultra-sensitive and label-free biosensors," *Appl. Phys. Lett.*, vol. 100, no. 14, p. 143108, 2012.

[221] L. Bousse, H. H. Van Den Vlekkert, and N. F. De Rooij, "Hysteresis in Al2O3-gate ISFETs," *Sens. Actuators B Chem.*, vol. 2, no. 2, pp. 103–110, 1990.

[222] J.-C. Chou and W.-L. Hsia, "Study on the characteristics of the measurement system for pH array sensors," *Proc World Acad Sci Eng Technol*, vol. 53, pp. 354–7, 2009.

[223] J. C. Chou and Y. F. Wang, "Preparation and study on the drift and hysteresis properties of the tin oxide gate ISFET by the sol–gel method," *Sens. Actuators B Chem.*, vol. 86, no. 1, pp. 58–62, 2002.